ACS OMEGA

Article

Cite This: ACS Omega 2019, 4, 13520−13529

http://pubs.acs.org/journal/acsodf

Thermodynamically Consistent Methodology for Estimation of Diffusivities of Mixtures of Guest Molecules in Microporous Materials

Rajamani Krishna*

Van 't Hoff Institute for Molecular Sciences, University of Amsterdam, Science Park 904, 1098 XH Amsterdam, The Netherlands

Supporting Information

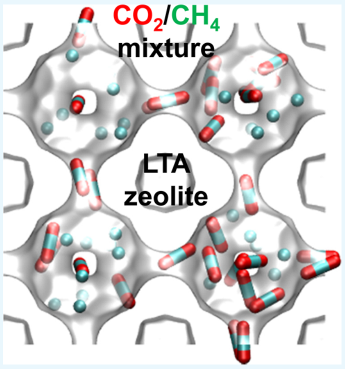

ABSTRACT: The Maxwell−Stefan (M−S) formulation, that is grounded in the theory of irreversible thermodynamics, is widely used for describing mixture diffusion in microporous crystalline materials such as zeolites and metal−organic frameworks (MOFs). Binary mixture diffusion is characterized by a set of three M−S diffusivities: $Đ_1$, $Đ_2$, and $Đ_{12}$. The M−S diffusivities $Đ_1$ and $Đ_2$ characterize interactions of guest molecules with pore walls. The exchange coefficient $Đ_{12}$ quantifies correlation effects that result in slowing-down of the more mobile species due to correlated molecular jumps with tardier partners. The primary objective of this article is to develop a methodology for estimating $Đ_1$, $Đ_2$, and $Đ_{12}$ using input data for the constituent unary systems. The dependence of the unary diffusivities $Đ_1$ and $Đ_2$ on the pore occupancy, θ, is quantified using the quasi-chemical theory that accounts for repulsive, or attractive, forces experienced by a guest molecule with the nearest neighbors. For binary mixtures, the same occupancy dependence of $Đ_1$ and $Đ_2$ is assumed to hold; in this case, the occupancy, θ, is calculated using the ideal adsorbed solution theory. The exchange coefficient $Đ_{12}$ is estimated from the data on unary self-diffusivities. The developed estimation methodology is validated using a large data set of M−S diffusivities determined from molecular dynamics simulations for a wide variety of binary mixtures (H_2/CO_2, Ne/CO_2, CH_4/CO_2, CO_2/N_2, H_2/CH_4, H_2/Ar, CH_4/Ar, Ne/Ar, CH_4/C_2H_6, CH_4/C_3H_8, and C_2H_6/C_3H_8) in zeolites (MFI, BEA, ISV, FAU, NaY, NaX, LTA, CHA, and DDR) and MOFs (IRMOF-1, CuBTC, and MgMOF-74).

1. INTRODUCTION

Many separation and reaction processes use microporous crystalline materials such as zeolites (alumino-silicates), metal−organic frameworks (MOFs), and zeolitic imidazolate frameworks (ZIFs) as perm-selective membrane layers, adsorbents, or catalysts.[1−8] Separation of nitrogen/oxygen, nitrogen/methane, and propene/propane mixtures in adsorbers packed with LTA-4A, CHA, or ZIF-8 are essentially driven by differences in the pore diffusivities of the guest constituents.[9−16] The conversion and selectivity of several heterogeneous catalytic reactions are influenced by intraparticle transport of reactants and products.[17−19] Pore diffusion characteristics have a significant influence on membrane separation selectivities.[4,20−25]

Mixture diffusion in microporous materials is characterized by the fact that the mobility of any guest constituent is influenced by its partner species;[20,26] the proper modeling of such influences is essential for process development and design.[6,15] It is a common practice to model n-component mixture diffusion by adopting the Maxwell−Stefan (M−S) formulation,[1,6,7,27,28] that has its foundations in the theory of nonequilibrium thermodynamics. The dependence of the intracrystalline molar fluxes, N_i, on the chemical potential gradients is written in the following form

$$-\rho \frac{q_i}{RT}\frac{d\mu_i}{dz} = \sum_{\substack{j=1\\ j\neq i}}^{n} \frac{x_j N_i - x_i N_j}{Đ_{ij}} + \frac{N_i}{Đ_i}; \qquad i = 1,2, ..n \tag{1}$$

In eq 1, R is the gas constant, ρ represents the material framework density, and the component loadings, and q_i are defined in terms of moles per kg of framework material. The x_i in eq 1 is the mole fractions of the adsorbed phase components

$$x_i = q_i/q_t; \qquad q_t = q_1 + q_2 + ...q_n; \qquad i = 1,2, ..n \tag{2}$$

Two distinct sets of M−S diffusivities are defined by eq 1, that is phenomenological in nature.[29] The $Đ_i$ characterize interactions between species i with the pore walls. As established in earlier works,[23,28] the important advantage of the M−S formulation is that the $Đ_i$ can be identified with the corresponding unary diffusivities, provided the diffusivity data are compared at the same adsorption potential, $\pi A/RT$, where A represents the surface area per kg of framework material, and π is the spreading pressure, defined by the Gibbs adsorption equation[3,30,31]

Received: June 23, 2019
Accepted: July 26, 2019
Published: August 2, 2019

DOI: 10.1021/acsomega.9b01873
ACS Omega 2019, 4, 13520−13529

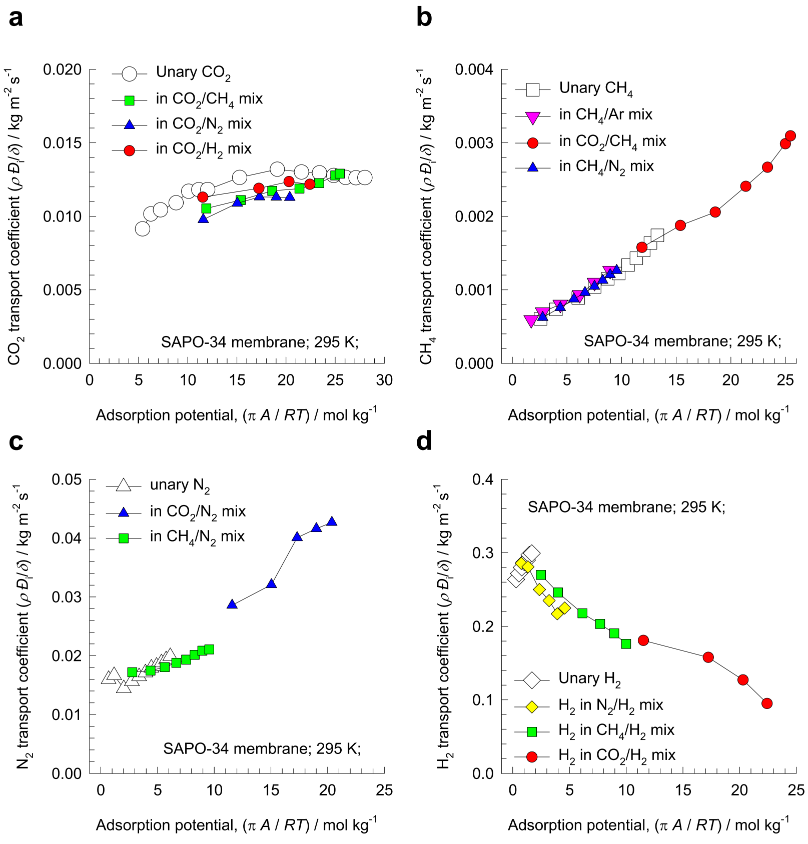

Figure 1. Experimental data of Li et al.[25,33,34] for transport coefficients $\rho Đ_i/\delta$ of (a) CO_2, (b) CH_4, (c) N_2, and (d) H_2 determined for unary and equimolar binary CO_2/H_2, CO_2/CH_4, CO_2/N_2, CH_4/Ar, CH_4/N_2, CH_4/H_2, and N_2/H_2 mixture permeation across SAPO-34 membrane at 295 K. The data are plotted as a function of the adsorption potential, $\pi A/RT$, calculated for conditions prevailing at the upstream face of the membrane; the calculation details are provided in an earlier work.[23]

$$A\,\mathrm{d}\pi = \sum_{i=1}^{n} q_i\,\mathrm{d}\mu_i \tag{3}$$

The ideal adsorbed solution theory (IAST) of Myers and Prausnitz[32] enables the calculation of the adsorption potential, $\pi A/RT$;[23,28] details are provided in the Supporting Information.

As illustration, Figure 1 presents plots of the transport coefficients, $\rho Đ_i/\delta$, of CO_2, CH_4, N_2, and H_2 determined for unary and equimolar binary (CO_2/H_2, CO_2/CH_4, CO_2/N_2, CH_4/Ar, CH_4/N_2, CH_4/H_2, and N_2/H_2) mixture permeation across a SAPO-34 membrane of thickness δ.[23,25,33,34] SAPO-34 has the same structural topology as CHA zeolite, consisting of cages of volume 316 Å^3, separated by 8-ring windows of 3.8 × 4.2 Å size.[23] Compared at the same value of $\pi A/RT$, the magnitude of $\rho Đ_i/\delta$ for a binary mixture is comparable to that for the corresponding pure component. Also noteworthy, from the data in Figure 1 is that the dependence of $\rho Đ_i/\delta$ on $\pi A/RT$ is distinctly different for each guest molecule.

The exchange coefficients, $Đ_{ij}$, defined by the first right member of eq 1 reflect how the facility for transport of species i correlates with that of species j. The Onsager reciprocal relations impose the symmetry constraint

$$Đ_{ij} = Đ_{ji} \tag{4}$$

The magnitude of $Đ_i$ relative to that of $Đ_{ij}$ determines the extent to which the flux of species i is influenced by the chemical potential gradient of species j. The larger the degree of correlations, $Đ_i/Đ_{ij}$, the stronger is the influence of diffusional "coupling". Generally speaking, the more strongly adsorbed tardier partner species will have the effect of slowing down the less strongly adsorbed more mobile partner in the mixture.

For estimation of the exchange coefficient, $Đ_{ij}$, the following interpolation formula has been suggested in the literature.[28,35]

$$Đ_{ij} = (Đ_{ii})^{x_i/(x_i+x_j)}(Đ_{jj})^{x_j/(x_i+x_j)} \tag{5}$$

where the $Đ_{ii}$ and $Đ_{jj}$ represent the self-exchange coefficients, that are accessible from molecular dynamics (MD) simulations of self-diffusivities for the constituent unary systems,[26] as will be discussed in a subsequent section. Equation 5 is essentially an adaptation of the interpolation formula for estimation of the M−S diffusivity for binary fluid mixtures.[36]

Specifically, for a binary mixture, that is $n = 2$, the M−S eq 1 can be rewritten to evaluate the fluxes N_i explicitly by defining a 2 × 2 dimensional square matrix $[\Lambda]$

$$N_i = -\rho \sum_{j=1}^{2} \Lambda_{ij} \frac{q_j}{RT}\frac{\mathrm{d}\mu_j}{\mathrm{d}z}; \qquad i = 1,2 \tag{6}$$

The elements of $[\Lambda]$ are directly accessible from MD simulations[28,35,37,38] by monitoring the individual molecular displacements

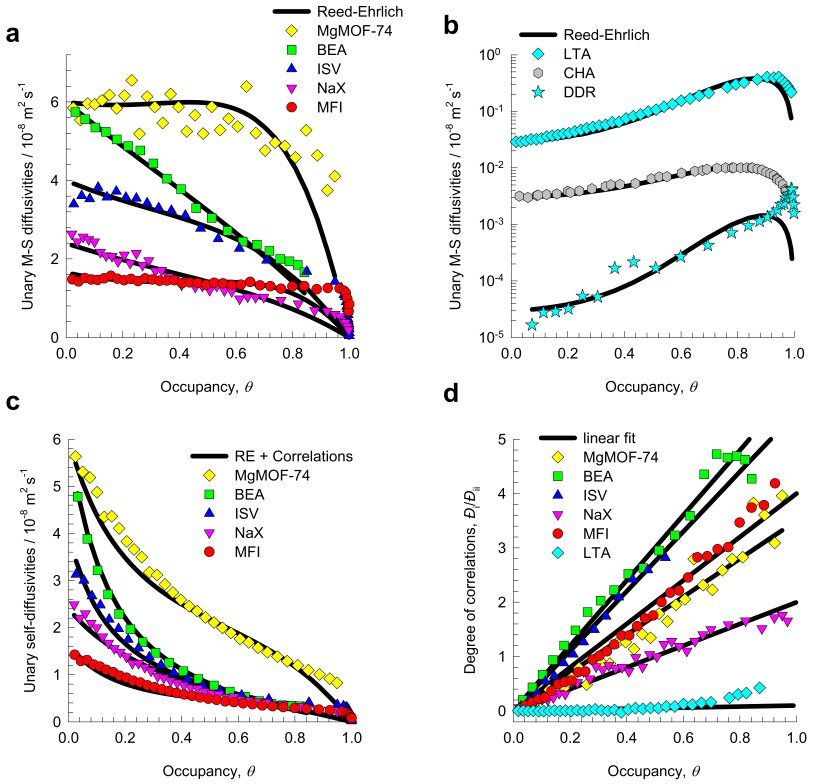

Figure 2. MD simulations of (a,b) Maxwell−Stefan diffusivity, $Đ_i$, (c) self-diffusivities $D_{i,\mathrm{self}}$, and (d) degree of correlations, $Đ_i/Đ_{ii}$ for CH_4 in a variety of host structures plotted as a function of the occupancy, θ, determined from eq 10, where q_{sat} and π are determined from the unary isotherm fits that are specified in the Supporting Information accompanying this article.

$$\Lambda_{ij} = \frac{1}{2}\lim_{\Delta t\to\infty}\frac{1}{n_j}\frac{1}{\Delta t}\left\langle\left(\sum_{l=1}^{n_i}(\mathbf{r}_{l,i}(t+\Delta t)-\mathbf{r}_{l,i}(t))\right)\left(\sum_{k=1}^{n_j}(\mathbf{r}_{k,j}(t+\Delta t)-\mathbf{r}_{k,j}(t))\right)\right\rangle \tag{7}$$

In 7 n_i and n_j represent the number of molecules of species i and j, respectively, and $\mathbf{r}_{l,i}(t)$ is the position of molecule l of species i at any time t.

Combining eq 1 with eq 6, the following explicit expression for calculation of the elements of the 2 × 2 dimensional square matrix $[\Lambda]$ can be derived

$$[\Lambda] = \frac{1}{1+\frac{x_1Đ_2}{Đ_{12}}+\frac{x_2Đ_1}{Đ_{12}}}\begin{bmatrix} Đ_1\left(1+\frac{x_1Đ_2}{Đ_{12}}\right) & \frac{x_1Đ_1Đ_2}{Đ_{12}} \\ \frac{x_2Đ_1Đ_2}{Đ_{12}} & Đ_2\left(1+\frac{x_2Đ_1}{Đ_{12}}\right)\end{bmatrix} \tag{8}$$

The primary objective of this article is to seek validation of the predictive capability of the Maxwell−Stefan formulation by comparing each of the four elements, Λ_{ij}, determined from MD simulations using eq 7, with the estimations using eqs 5 and 8; the required data inputs for $Đ_1$, $Đ_2$, $Đ_{11}$, and $Đ_{22}$ are determined from MD simulations for the constituent pure components. To meet the stated objective, use is made of the MD simulation data base compiled in an earlier work[28] for a variety of binary mixtures (H_2/CO_2, Ne/CO_2, CH_4/CO_2, CO_2/N_2, H_2/CH_4, H_2/Ar, CH_4/Ar, Ne/Ar, CH_4/C_2H_6, CH_4/C_3H_8, and C_2H_6/C_3H_8) in different host materials. The host materials were chosen to represent a variety of pore sizes, topologies, and connectivities: one-dimensional (1D) channels (e.g., AFI, MgMOF-74), intersecting channels (MFI, BEA, ISV), cages separated by narrow windows (LTA, CHA, DDR), cavities with large windows (FAU, NaY, NaX, IRMOF-1, CuBTC). The Supporting Information provides structural details for all of the host materials considered in this article.

2. RESULTS AND DISCUSSIONS

2.1. Occupancy Dependence of Unary Diffusivities.

For any guest molecule, the loading dependence of $Đ_i$ is strongly influenced also by the pore topology and connectivity and molecule−molecule interactions.[7,8,23,28,39−43] As an illustration, Figure 2a,b presents data on $Đ_i$ for the guest species CH_4 in a variety of host structures, determined from MD simulations of molecular displacements using the following formula in each of the coordinate direction

$$Đ_i = \frac{1}{2}\lim_{\Delta t\to\infty}\frac{1}{n_i}\frac{1}{\Delta t}\left\langle\left(\sum_{l=1}^{n_i}(\mathbf{r}_{l,i}(t+\Delta t)-\mathbf{r}_{l,i}(t))\right)^2\right\rangle \tag{9}$$

The M−S diffusivity, $Đ_i$ displays a wide variety of dependencies on the fractional occupancy, θ, that serves as a convenient and practical proxy for the adsorption potential

$$\theta \equiv 1-\exp\left(-\frac{\pi A}{q_{\mathrm{sat}}RT}\right) \tag{10}$$

where q_{sat} is the saturation capacity.[23,28] The calculations of the adsorption potential in eq 10 use dual-site Langmuir−

DOI: 10.1021/acsomega.9b01873
ACS Omega 2019, 4, 13520−13529

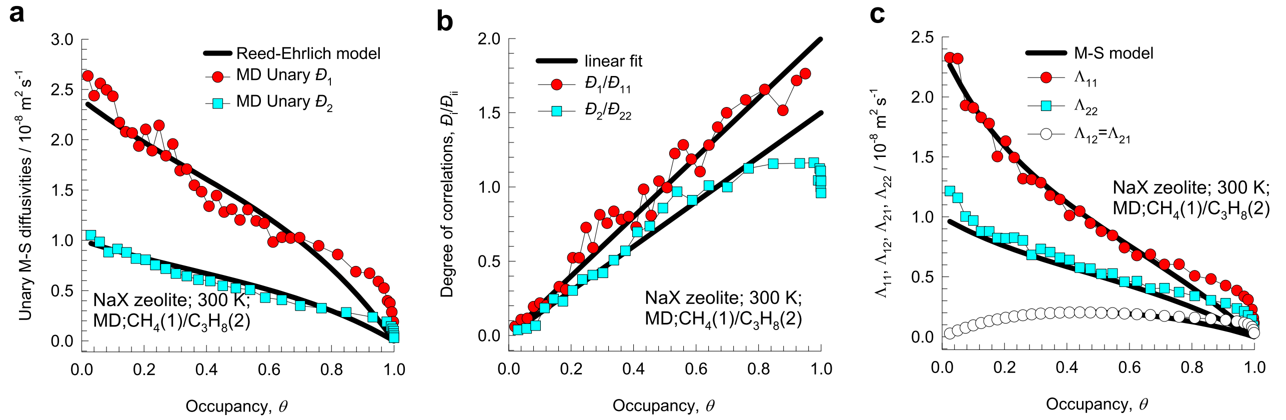

Figure 3. (a,b) MD simulated values of (a) $Đ_1$, $Đ_2$ and (b) $Đ_1/Đ_{11}$, $Đ_2/Đ_{22}$ for guest molecules CH_4 and C_3H_8 in NaX zeolite (86 Al) at 300 K. The continuous solid lines are the fits of the unary diffusivities. (c) MD simulation data for Λ_{11}, $\Lambda_{12} = \Lambda_{21}$, and Λ_{22} for equimolar ($q_1 = q_2$) binary $CH_4(1)/C_3H_8(2)$ mixtures in NaX zeolite (86 Al) at 300 K, compared with the estimations (shown by continuous solid lines) using eqs 5 and 8.

Freundlich fits of the unary isotherms that are determined from configurational-bias Monte Carlo (CBMC) simulations[44−48] for each guest/host combination; details are provided in the Supporting Information.

For CH_4/BEA and CH_4/NaX, the $Đ_i$ appears to decrease almost linearly with occupancy θ till pore saturation conditions, $\theta = 1$, are reached. An appropriate model to describe this occupancy dependence is

$$Đ_i = Đ_i(0)(1 - \theta) \tag{11}$$

where $Đ_i(0)$ is the M−S diffusivity at "zero-loading". Equation 11 is essentially based on a hopping model in which one molecule at any time can jump from one sorption site to an adjacent one, provided it is not already occupied.[23,28,49,50] Using a simple two-dimensional square lattice model, the M−S diffusivity in the limit of vanishingly small occupancies, $Đ_i(0) = \frac{1}{\zeta}\nu_i(0)\lambda^2$, where $\zeta = 4$ is the coordination number of the 2D array of lattice sites, λ is the jump distance on the square lattice, and $\nu_i(0)$ is the jump frequency at vanishingly small occupancy.[50]

More generally, molecule−molecule interactions serve to influence the jump frequencies by a factor that depends on the energy of interaction, w. For repulsive interactions, $w > 0$, whereas for attractive interactions, $w < 0$. Using the quasi-chemical approach of Reed and Ehrlich[51] to quantify such interactions, the following expression is obtained for the occupancy dependence of the M−S diffusivities[50,52,53]

$$Đ_i = Đ_i(0)\left(\frac{1+\beta}{2(1-\theta)}\right)^{-\zeta}\left(1 + \frac{(\beta - 1 + 2\theta)\phi}{2(1-\theta)}\right)^{\zeta-1} \tag{12}$$

In 12 the following dimensionless parameters are defined

$$\beta = \sqrt{1 - 4\theta(1-\theta)(1 - 1/\phi)}; \qquad \phi = \exp(w/RT) \tag{13}$$

In the limiting case of negligible molecule−molecule interactions, $w = 0$, $\phi = 1$, $\beta = 1$, eqs 12 and 13 degenerate to yield eq 11. The continuous solid lines in Figure 2a,b are fits of the MD simulated $Đ_i$ by fitting the sets of parameters: $Đ_i(0)$, and $\phi = \phi_0\exp(-a\theta)$. For all of the guest/host combinations, eqs 12 and 13 provide good descriptions of the occupancy dependencies; see Figures S38−S108 of the Supporting Information.

Applying eq 1 to a binary mixture consisting of tagged and untagged species i, that are otherwise identical,[7,50,54] we can derive the following relation between the self-diffusivity, $D_{i,\text{self}}$ and the M−S diffusivity, $Đ_i$

$$\frac{1}{D_{i,\text{self}}} = \frac{1}{Đ_i} + \frac{1}{Đ_{ii}} = \frac{1}{Đ_i}\left(1 + \frac{Đ_i}{Đ_{ii}}\right) \tag{14}$$

The self-diffusivities, $D_{i,\text{self}}$ may be computed from MD simulations by analyzing the mean square displacement of each species, i for each coordinate direction[7]

$$D_{i,\text{self}} = \frac{1}{2n_i}\lim_{\Delta t\to\infty}\frac{1}{\Delta t}\left\langle\left(\sum_{l=1}^{n_i}(\mathbf{r}_{l,i}(t+\Delta t) - \mathbf{r}_{l,i}(t))^2\right)\right\rangle \tag{15}$$

By combination of eqs 9, 14, and 15, we can determine the degrees of correlations due to self-exchange, $Đ_i/Đ_{ii}$. Figure 2c,d presents MD simulated data on $D_{i,\text{self}}$ and $Đ_i/Đ_{ii}$ for CH_4 in different host materials: MgMOF-74 (1D channels of 11 Å), BEA (intersecting channels of 6.5 Å), ISV (intersecting channels of 6.5 Å), NaX (790 Å^3 cages separated by 7.4 Å windows), MFI (intersecting channels of 5.5 Å), and LTA (743 Å^3 cages separated by 4.2 Å windows). It is also to be noted that the size of the 1D channels of MgMOF-74 are large enough to preclude single-file diffusion of guest molecules. The degree of correlations is the lowest for the LTA zeolite because the guest molecules jump one-at-a-time across the narrow 4.2 Å windows;[6,55,56] the same characteristics are valid for other cage-window structures with narrow windows, such as CHA, DDR, and ZIF-8.[24,57−59] The variation of $Đ_i/Đ_{ii}$ with occupancy is practically linear,[23,28] and the solid lines in Figure 2d are the linear fits

$$Đ_i/Đ_{ii} = b\theta \tag{16}$$

Equation 16 provides a good description of the occupancy dependence of the degrees of correlations due to self-exchange for all guest/host combinations; see Figures S38−S108 of the Supporting Information.

2.2. Occupancy Dependence of [Λ] for Binary Mixture Diffusion.

Having established and quantified the occupancy dependence of $Đ_i$ and $Đ_i/Đ_{ii}$ for each guest/host combination, we are in a position to compare the estimations of Λ_{ij} for binary mixtures using eqs 5 and 8 with the corresponding MD simulated values by monitoring molecular

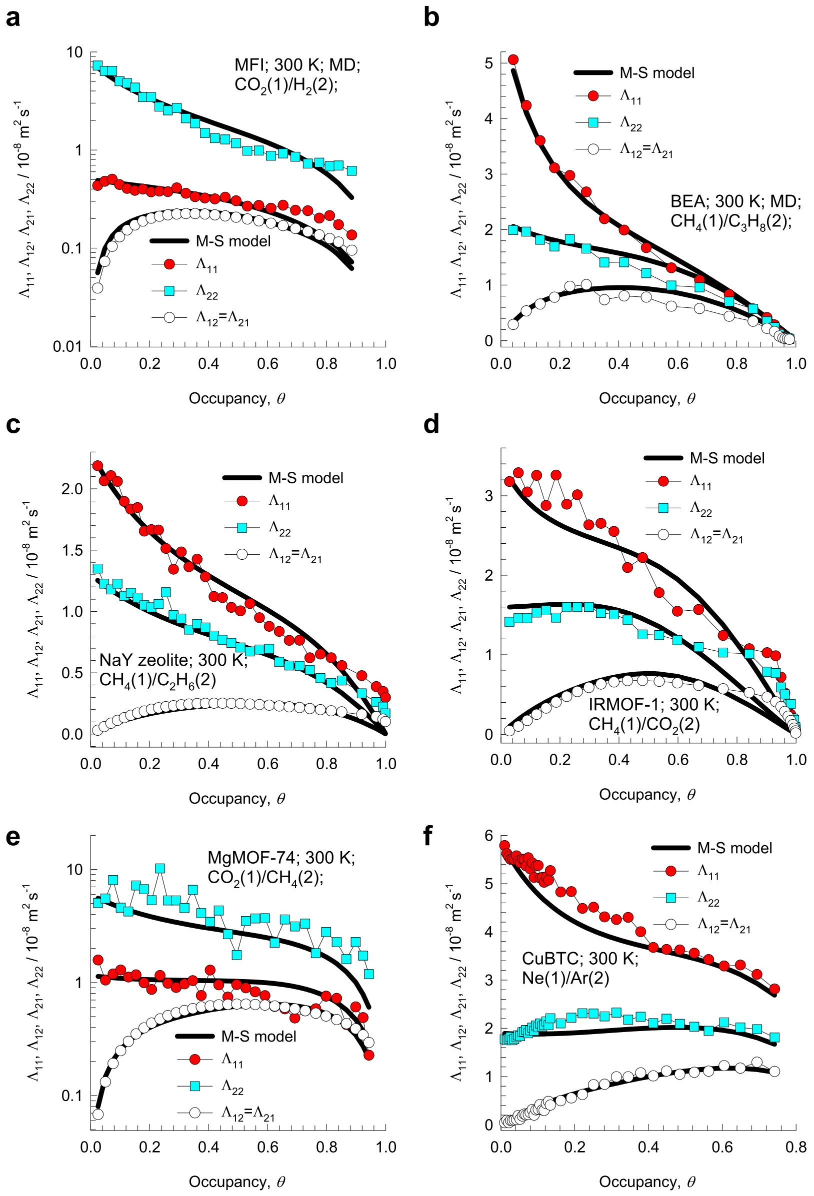

Figure 4. MD simulation data for Λ_{11}, $\Lambda_{12} = \Lambda_{21}$, and Λ_{22} for equimolar ($q_1 = q_2$) binary (a) $CO_2(1)/H_2(2)$ in MFI zeolite, (b) $CH_4(1)/C_3H_8(2)$ in BEA zeolite, (c) $CH_4(1)/C_2H_6(2)$ in NaY zeolite (48 Al), (d) $CH_4(1)/CO_2(2)$ in IRMOF-1, (e) $CO_2(1)/CH_4(2)$ in MgMOF-74, and (f) Ne(1)/Ar(2) in CuBTC at 300 K, compared with the estimations (shown by continuous solid lines) using eqs 5, and 8.

displacements and use of eq 7; Figures S38−S108 provide detailed comparisons for each mixture/host combination that was investigated. Figure 3 provides an illustration of the estimation procedure for $CH_4(1)/C_3H_8(2)$ mixture diffusion in NaX zeolite. Figure 3a show the Reed−Ehrlich model fits for the unary diffusivities $Đ_1$, $Đ_2$ for CH_4 and C_3H_8 in NaX. The linear fits for the degrees of self-exchange $Đ_1/Đ_{11}$ and $Đ_2/Đ_{22}$ are shown in Figure 3b. In Figure 3c, the MD simulation data for Λ_{11}, $\Lambda_{12} = \Lambda_{21}$, and Λ_{22} for equimolar ($q_1 = q_2$) binary $CH_4(1)/C_3H_8(2)$ mixtures are compared with the estimations (shown by the continuous solid lines) using eqs 5 and 8. The Maxwell−Stefan formulation provides very good estimates of dependence of each Λ_{ij} on the occupancy θ, calculated using eq 10, wherein the saturation capacity for the mixture is determined from

$$\frac{1}{q_{sat}} = \frac{x_1}{q_{1,sat}} + \frac{x_2}{q_{2,sat}} \tag{17}$$

where $q_{1,sat}$ and $q_{2,sat}$ are the saturation capacities of components 1 and 2, respectively. Equation 17 can be derived from the IAST, as detailed in the Supporting Information.

Similar good estimates of the M−S model are established in Figure 4 for six other equimolar ($q_1 = q_2$) binary mixtures: CO_2/H_2 in MFI, CH_4/C_3H_8 in BEA, CH_4/C_2H_6 in NaY, CH_4/CO_2 in IRMOF-1, CO_2/CH_4 in MgMOF-74, and Ne/Ar in CuBTC.

A different test of the predictive capability of M−S formulation is to consider diffusion in binary mixtures for which the total loading $q_1 + q_2$ is held constant, and the mole fraction of component 1 in the adsorbed mixture, x_1, is varied from 0 to 1.[60] One of the earliest investigations of this type were reported by Snurr and Kärger[61] for CH_4/CF_4 diffusion in MFI zeolite at a total loading of 12 molecules uc^{-1}.

Figure 5 compares the MD simulation data for Λ_{ij} for binary Ne(1)/Ar(2) mixtures of varying composition x_1 in MFI, LTA, CHA, and DDR zeolites. In all four cases, eqs 5,

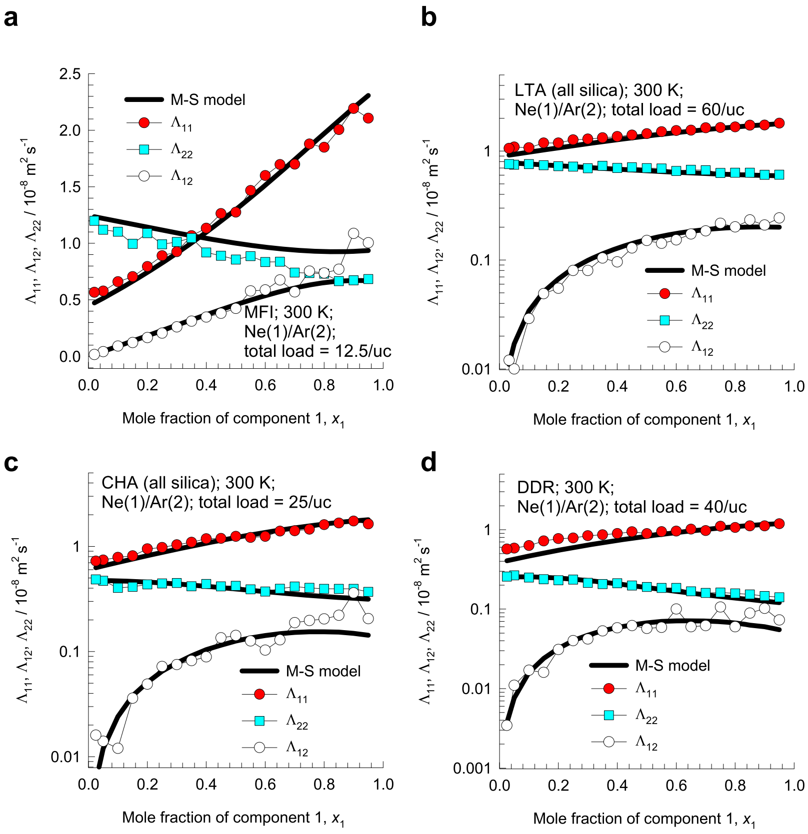

Figure 5. MD simulation data for Λ_{11}, Λ_{12}, and Λ_{22} for binary Ne(1)/Ar(2) mixtures of varying composition at constant total loading $q_t = q_1 + q_2$ in (a) MFI zeolite (q_t = 12.5 molecules uc^{-1}), (b) LTA all-silica zeolite (q_t = 60 molecules uc^{-1}), (c) CHA all-silica zeolite (q_t = 25 molecules uc^{-1}), and (d) DDR zeolite (q_t = 40 molecules uc^{-1}) at 300 K, compared with the estimations (shown by continuous solid lines) using eqs 5, and 8. Note that $\Lambda_{21} = (x_2/x_1)\Lambda_{12}$ has not been plotted because it is not independent.

and 8 provide good predictions of the variation of Λ_{ij} with composition. It is also to be noted that the off-diagonal elements Λ_{12} for LTA, CHA, and DDR zeolites are significantly lower, by about an order of magnitude, than the diagonal elements, Λ_{11} and Λ_{22}. For cage-type zeolites such as LTA, CHA, DDR, ERI with 8-ring windows in the 3.3−4.5 Å size range, the degree of correlations $Đ_i/Đ_{ii}$ are negligibly small because the guest molecules jump one-at-a-time across the narrow windows.[20,26−28,55,62]

Further evidence of the good predictive capability of the M−S formulation is provided in Figures S38−S108.

2.3. Preferential Perching of CO_2 in Window Regions of Cage-Type Zeolites. For separation of CO_2 from gaseous mixtures containing CH_4, H_2, N_2, Ar, or Ne, cage-type zeolites such as DDR CHA, LTA, and ERI are of practical interest.[8,24,30,31,46,47,55,56] These materials consist of cages separated by narrow windows, in the 3.3−4.5 Å range. CBMC simulations[59] show that the window regions of cage-type zeolites have a significantly higher proportion of CO_2 than within the cages. For all four zeolites, CO_2 has the highest probability, about 30−40%, of locating at the window regions.[59] The preferential perching of CO_2 in the window regions, evidenced by the computational snapshot for CHA (see Figure 6a), has the effect of hindering the intercage hopping of partner molecules.

Figure 6b−d compare the MD simulation data for Λ_{11} and Λ_{22} for equimolar ($q_1 = q_2$) binary CO_2(1)/Ne(2) mixtures in LTA, CHA, and DDR zeolite, with the estimations using eq 8, assuming that the degrees of correlations are negligible, that is $Đ_i/Đ_{ii} \to 0$. For all three zeolites, the MD simulation data for Λ_{22} are significantly lower than the predictions using eq 8; the M−S formulation does not cater for hindering effects caused due to segregated mixture adsorption. Experimental evidence of the importance of hindering effects is provided in published works on CO_2/CH_4 and CO_2/N_2 mixture permeation across the DDR membrane.[38,63,64] Analogous hindering effects are also evidenced for CO_2/CH_4 mixture permeation across ZIF-8 membranes.[24]

Preferential location of branched alkanes and aromatics at the intersections of MFI zeolite often cause intersection-blocking and loss of connectivity;[55,65,66] this leads to failure of the predictions of the M−S model.[67]

2.4. Molecular Clustering Due to Hydrogen Bonding. For water/methanol and water/ethanol mixture diffusion in microporous materials, molecular simulations[62,68−71] demonstrate the occurrence of molecular clustering due to hydrogen bonding. As a consequence of cluster formation, the diffusivities of either guest molecule in the mixture is significantly lower than the corresponding unary diffusivities. As illustration of mutual-slowing down effects, Figure 7 presents MD data on the self-diffusivities, $D_{i,self}$, in water/methanol mixtures in CHA, DDR, and LTA zeolites, plotted as a function of the mole fraction of water in the adsorbed phase, x_1. Each of the diffusivities is lowered due to the presence of its partner species. Experimental evidence of mutual-slowing down effects are available for water/alcohol permeation across CHA,[72,73] H-SOD,[74] and DDR[71,75] membranes. Further research is necessary to generalize the

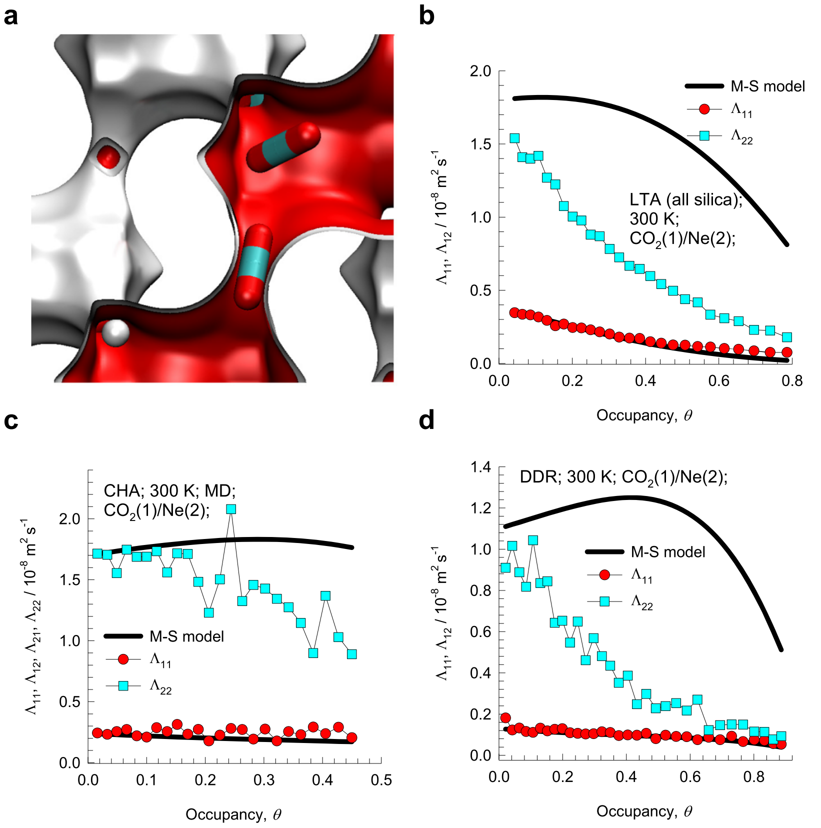

Figure 6. (a) Computational snapshot showing the preferential perching of CO_2 at the window regions of CHA zeolite.[59] (b–d) MD simulation data for Λ_{11} and Λ_{22} for equimolar ($q_1 = q_2$) binary $CO_2(1)/Ne(2)$ mixtures at 300 K (b) LTA all-silica zeolite, (c) CHA all-silica zeolite, and (d) DDR zeolite, compared with the estimations (shown by continuous solid lines) using eq 8 and assuming that the degrees of correlations are negligible, that is $Đ_i/Đ_{ii} \to 0$.

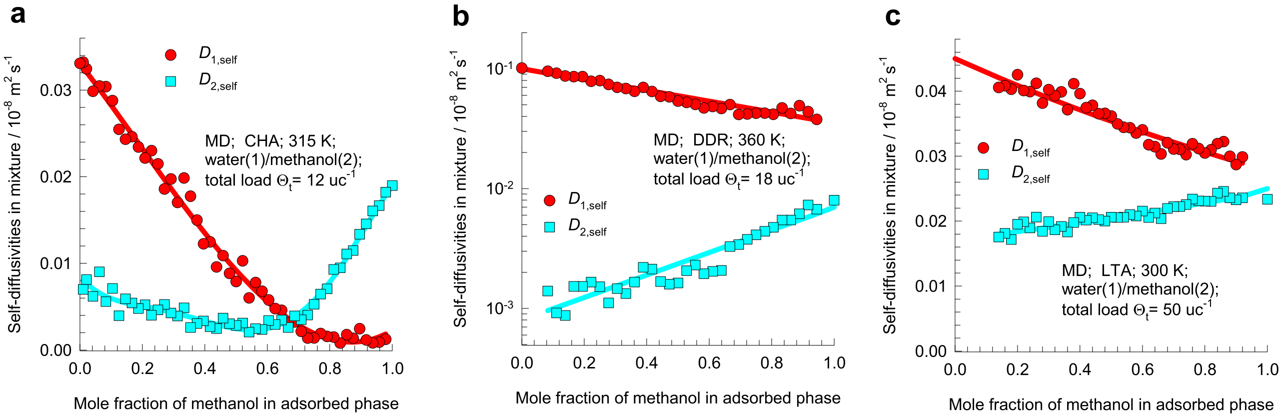

Figure 7. MD simulations of self-diffusivities, $D_{i,\mathrm{self}}$, of water(1)/methanol(2) mixtures of varying composition in (a) CHA, (b) DDR, and (c) LTA zeolites, plotted as a function of the mole fraction of water in the adsorbed phase, x_1. In the MD simulations, the total loading, Θ_t, expressed as molecules uc^{-1}, is held constant; the values Θ_t are specified. The MD data are culled from our previous publications.[69−71]

M−S formulation in a manner that explicitly allows for cluster formation, by defining a cluster to be a pseudospecies in the mixture.

3. CONCLUSIONS

The capability of eqs 5 and 8 for the estimation of the elements of the square matrix of M−S diffusivities, Λ_{ij}, characterizing mixture diffusion, using input based on unary systems is tested using a large database obtained from MD simulations for a wide variety of guest/host combinations. The key to the estimation methodology is that the estimates are based on comparing the mixture diffusion data with those of the constituent unaries at the same fractional occupancy, θ, that is calculated on the basis of the adsorption potential using eq 10. For the majority of binary mixtures investigated, 70 in total, summarized in Figures S38−S108, the MD-simulated Λ_{ij} data are in good agreement with the estimations using the M−S theory. The predictions of the M−S formulation are found to be poor for diffusion of CO_2-bearing mixture in cage-type zeolites (LTA, CHA, DDR) wherein the preferential perching of CO_2 at the window regions hinders the intercage hopping of partner molecules. The M−S predictions also fail

DOI: 10.1021/acsomega.9b01873
ACS Omega 2019, 4, 13520−13529

to capture molecular clustering effects in water/alcohol systems that are engendered due to hydrogen bonding.[62]

■ ASSOCIATED CONTENT

Ⓢ Supporting Information

The Supporting Information is available free of charge on the ACS Publications website at DOI: 10.1021/acsomega.9b01873.

> Structural details for zeolites and MOFs considered and analyzed in this article, dual-Langmuir−Freundlich data fits of unary isotherms for each guest/host combination, IAST calculation procedure for the spreading pressure and the fractional occupancy, θ, and MD simulation data (a total of 70 data sets) for Λ_{ij}, along with comparisons with estimates using eqs 5, and 8 (PDF)

■ AUTHOR INFORMATION

Corresponding Author

*E-mail: r.krishna@contact.uva.nl.

ORCID

Rajamani Krishna: 0000-0002-4784-8530

Notes

The author declares no competing financial interest.

■ ACKNOWLEDGMENTS

The generous assistance of Dr. Jasper van Baten, Amster-CHEM, in performing the CBMC and MD simulations is gratefully acknowledged.

■ NOMENCLATURE

Latin alphabet

A	surface area per kg of framework, m^2 kg^{-1}
$Đ_i$	Maxwell−Stefan diffusivity for molecule−wall interaction, m^2 s^{-1}
$Đ_i(0)$	M−S diffusivity at zero-loading, m^2 s^{-1}
$Đ_{ij}$	M−S exchange coefficient, m^2 s^{-1}
$Đ_{ii}$	M−S self-exchange coefficient, m^2 s^{-1}
$D_{i,\mathrm{self}}$	self-diffusivity of species i, m^2 s^{-1}
n	number of species in the mixture, dimensionless
n_i	number of molecules of species i in simulation box, dimensionless
N_i	molar flux of species i with respect to framework, mol m^{-2} s^{-1}
p_i	partial pressure of species i, Pa
q_i	component molar loading of species i, mol kg^{-1}
$q_{i,\mathrm{sat}}$	molar loading of species i at saturation, mol kg^{-1}
q_t	total molar loading in mixture, mol kg^{-1}
$\mathbf{r}_{l,i}(t)$	position vector for molecule l of species i at any time t, m
R	gas constant, 8.314 J mol^{-1} K^{-1}
T	absolute temperature, K
x_i	mole fraction of species i in adsorbed phase, dimensionless
z	distance coordinate, m

Greek alphabet

β	parameter defined b eq 13, dimensionless
δ	thickness of membrane, m
δ_{ij}	Kronecker delta, dimensionless
ζ	coordination number defined in eq 12, dimensionless
λ	jump distance in lattice model, m
$[\Lambda]$	matrix of Maxwell−Stefan diffusivities, m^2 s^{-1}
μ_i	molar chemical potential of component i, J mol^{-1}
π	spreading pressure, N m^{-1}
Π_i	permeance of species i for zeolite membrane, mol m^{-2} s^{-1} Pa^{-1}
θ	fractional occupancy, dimensionless
ν	jump frequency, s^{-1}
ρ	framework density, kg m^{-3}

Subscripts

1	referring to component 1
2	referring to component 2
i	referring to component i
t	referring to total mixture
sat	referring to saturation conditions

■ REFERENCES

(1) Kärger, J.; Ruthven, D. M. Diffusion in nanoporous materials: fundamental principles, insights and challenges. *New J. Chem.* **2016**, *40*, 4027−4048.

(2) Keil, F. J.; Krishna, R.; Coppens, M. O. Modeling of diffusion in zeolites. *Rev. Chem. Eng.* **2000**, *16*, 71−197.

(3) Ruthven, D. M. *Principles of Adsorption and Adsorption Processes*; John Wiley: New York, 1984; pp 1−433.

(4) Caro, J.; Noack, M. Zeolite membranes - Recent Developments and Progress. *Microporous Mesoporous Mater.* **2008**, *115*, 215−233.

(5) Caro, J. Are MOF membranes better in gas separation than those made of zeolites? *Curr. Opin. Chem. Eng.* **2011**, *1*, 77−83.

(6) Krishna, R. The Maxwell-Stefan Description of Mixture Diffusion in Nanoporous Crystalline Materials. *Microporous Mesoporous Mater.* **2014**, *185*, 30−50.

(7) Krishna, R. Describing the Diffusion of Guest Molecules inside Porous Structures. *J. Phys. Chem. C* **2009**, *113*, 19756−19781.

(8) Krishna, R. Methodologies for Screening and Selection of Crystalline Microporous Materials in Mixture Separations. *Sep. Purif. Technol.* **2018**, *194*, 281−300.

(9) Ruthven, D. M.; Farooq, S.; Knaebel, K. S. *Pressure Swing Adsorption*; VCH Publishers: New York, 1994; pp 1−352.

(10) Yang, R. T. *Gas Separation by Adsorption Processes*; Boston: Butterworth, 1987; pp 1−352.

(11) Yang, R. T. *Adsorbents: Fundamentals and Applications*; John Wiley & Sons, Inc.: Hoboken, New Jersey, 2003; pp 1−410.

(12) Krishna, R. Tracing the Origins of Transient Overshoots for Binary Mixture Diffusion in Microporous Crystalline Materials. *Phys. Chem. Chem. Phys.* **2016**, *18*, 15482−15495.

(13) Krishna, R. A Maxwell-Stefan-Glueckauf Description of Transient Mixture Uptake in Microporous Adsorbents. *Sep. Purif. Technol.* **2018**, *191*, 392−399.

(14) Krishna, R. Methodologies for Evaluation of Metal-Organic Frameworks in Separation Applications. *RSC Adv.* **2015**, *5*, 52269−52295.

(15) Krishna, R. Highlighting the Influence of Thermodynamic Coupling on Kinetic Separations with Microporous Crystalline Materials. *ACS Omega* **2019**, *4*, 3409−3419.

(16) Krishna, R. Maxwell-Stefan modelling of mixture desorption kinetics in microporous crystalline materials. *Sep. Purif. Technol.* **2019**, *229*, 115790.

(17) Hansen, N.; Krishna, R.; van Baten, J. M.; Bell, A. T.; Keil, F. J. Analysis of Diffusion Limitation in the Alkylation of Benzene over H-ZSM-5 by Combining Quantum Chemical Calculations, Molecular Simulations, and a Continuum Approach. *J. Phys. Chem. C* **2009**, *113*, 235−246.

(18) Hansen, N.; Krishna, R.; van Baten, J. M.; Bell, A. T.; Keil, F. J. Reactor simulation of benzene ethylation and ethane dehydrogenation catalyzed by ZSM-5: A multiscale approach. *Chem. Eng. Sci.* **2010**, *65*, 2472−2480.

(19) Krishna, R.; Baur, R.; Van Baten, J. M. Highlighting Diffusional Coupling Effects in Zeolite Catalyzed Reactions by Combining the

Maxwell-Stefan and Langmuir-Hinshelwood Formulations. *React. Chem. Eng.* **2017**, *2*, 324−336.

(20) Krishna, R. Using the Maxwell-Stefan formulation for highlighting the influence of interspecies (1−2) friction on binary mixture permeation across microporous and polymeric membranes. *J. Membr. Sci.* **2017**, *540*, 261−276.

(21) Bux, H.; Chmelik, C.; Krishna, R.; Caro, J. Ethene/Ethane Separation by the MOF Membrane ZIF-8: Molecular Correlation of Permeation, Adsorption, Diffusion. *J. Membr. Sci.* **2011**, *369*, 284−289.

(22) Bux, H.; Chmelik, C.; Van Baten, J. M.; Krishna, R.; Caro, J. Novel MOF-Membrane for Molecular Sieving Predicted by IR-Diffusion Studies and Molecular Modeling. *Adv. Mater.* **2010**, *22*, 4741−4743.

(23) Krishna, R. Thermodynamic Insights into the Characteristics of Unary and Mixture Permeances in Microporous Membranes. *ACS Omega* **2019**, *4*, 9512−9521.

(24) Chmelik, C.; van Baten, J.; Krishna, R. Hindering effects in diffusion of CO2/CH4 mixtures in ZIF-8 crystals. *J. Membr. Sci.* **2012**, *397-398*, 87−91.

(25) Li, S.; Falconer, J. L.; Noble, R. D.; Krishna, R. Interpreting Unary, Binary, and Ternary Mixture Permeation Across a SAPO-34 Membrane with Loading-Dependent Maxwell−Stefan Diffusivities. *J. Phys. Chem. C* **2007**, *111*, 5075−5082.

(26) Krishna, R.; van Baten, J. M. Maxwell-Stefan modeling of slowing-down effects in mixed gas permeation across porous membranes. *J. Membr. Sci.* **2011**, *383*, 289−300.

(27) Krishna, R. Diffusion in Porous Crystalline Materials. *Chem. Soc. Rev.* **2012**, *41*, 3099−3118.

(28) Krishna, R. Occupancy Dependency of Maxwell-Stefan Diffusivities in Ordered Crystalline Microporous Materials. *ACS Omega* **2018**, *3*, 15743−15753.

(29) Skoulidas, A. I.; Sholl, D. S.; Krishna, R. Correlation Effects in Diffusion of CH4/CF4Mixtures in MFI Zeolite. A Study Linking MD Simulations with the Maxwell−Stefan Formulation. *Langmuir* **2003**, *19*, 7977−7988.

(30) Krishna, R.; van Baten, J. M.; Baur, R. Highlighting the origins and consequences of thermodynamic non-idealities in mixture separations using zeolites and metal-organic frameworks. *Microporous Mesoporous Mater.* **2018**, *267*, 274−292.

(31) Krishna, R.; Van Baten, J. M. Investigating the non-idealities in adsorption of CO2-bearing mixtures in cation-exchanged zeolites. *Sep. Purif. Technol.* **2018**, *206*, 208−217.

(32) Myers, A. L.; Prausnitz, J. M. Thermodynamics of mixed-gas adsorption. *AIChE J.* **1965**, *11*, 121−127.

(33) Li, S.; Falconer, J. L.; Noble, R. D.; Krishna, R. Modeling Permeation of CO2/CH4, CO2/N2, and N2/CH4Mixtures Across SAPO-34 Membrane with the Maxwell−Stefan Equations. *Ind. Eng. Chem. Res.* **2007**, *46*, 3904−3911.

(34) Krishna, R.; Li, S.; van Baten, J. M.; Falconer, J. L.; Noble, R. D. Investigation of slowing-down and speeding-up effects in binary mixture permeation across SAPO-34 and MFI membranes. *Sep. Purif. Technol.* **2008**, *60*, 230−236.

(35) Krishna, R.; van Baten, J. M. Unified Maxwell-Stefan description of binary mixture diffusion in micro- and meso-porous materials. *Chem. Eng. Sci.* **2009**, *64*, 3159−3178.

(36) Krishna, R. Diffusing Uphill with James Clerk Maxwell and Josef Stefan. *Chem. Eng. Sci.* **2019**, *195*, 851−880.

(37) Krishna, R.; van Baten, J. M. Describing Mixture Diffusion in Microporous Materials under Conditions of Pore Saturation. *J. Phys. Chem. C* **2010**, *114*, 11557−11563.

(38) Krishna, R.; van Baten, J. M. Onsager coefficients for binary mixture diffusion in nanopores. *Chem. Eng. Sci.* **2008**, *63*, 3120−3140.

(39) Düren, T.; Jakobtorweihen, S.; Keil, F. J.; Seaton, N. A. Grand canonical molecular dynamics simulations of transport diffusion in geometrically heterogeneous pores. *Phys. Chem. Chem. Phys.* **2003**, *5*, 369−375.

(40) Beerdsen, E.; Dubbeldam, D.; Smit, B. Loading Dependence of the Diffusion Coefficient of Methane in Nanoporous Materials. *J. Phys. Chem. B* **2006**, *110*, 22754−22772.

(41) Beerdsen, E.; Dubbeldam, D.; Smit, B. Understanding Diffusion in Nanoporous Materials. *Phys. Rev. Lett.* **2006**, *96*, 044501.

(42) Krishna, R.; van Baten, J. M. Diffusion of Alkane Mixtures in Zeolites: Validating the Maxwell−Stefan Formulation Using MD Simulations. *J. Phys. Chem. B* **2005**, *109*, 6386−6396.

(43) Krishna, R.; van Baten, J. M. A rationalization of the Type IV loading dependence in the Kärger-Pfeifer classification of self-diffusivities. *Microporous Mesoporous Mater.* **2011**, *142*, 745−748.

(44) Vlugt, T. J. H.; Krishna, R.; Smit, B. Molecular Simulations of Adsorption Isotherms for Linear and Branched Alkanes and Their Mixtures in Silicalite. *J. Phys. Chem. B* **1999**, *103*, 1102−1118.

(45) Dubbeldam, D.; Calero, S.; Vlugt, T. J. H.; Krishna, R.; Maesen, T. L. M.; Smit, B. United Atom Force Field for Alkanes in Nanoporous Materials. *J. Phys. Chem. B* **2004**, *108*, 12301−12313.

(46) Krishna, R.; van Baten, J. M. In silico screening of zeolite membranes for CO2 capture. *J. Membr. Sci.* **2010**, *360*, 323−333.

(47) Krishna, R.; van Baten, J. M. In silico screening of metal-organic frameworks in separation applications. *Phys. Chem. Chem. Phys.* **2011**, *13*, 10593−10616.

(48) Smit, B.; Maesen, T. L. M. Molecular Simulations of Zeolites: Adsorption, Diffusion, and Shape Selectivity. *Chem. Rev.* **2008**, *108*, 4125−4184.

(49) Krishna, R.; Baur, R. Modelling issues in zeolite based separation processes. *Sep. Purif. Technol.* **2003**, *33*, 213−254.

(50) Krishna, R. The Maxwell-Stefan Description of Mixture Permeation across Nanoporous Graphene Membranes. *Chem. Eng. Res. Des.* **2018**, *133*, 316−325.

(51) Reed, D. A.; Ehrlich, G. Surface diffusion, atomic jump rates and thermodynamics. *Surf. Sci.* **1981**, *102*, 588−609.

(52) Krishna, R.; Paschek, D.; Baur, R. Modeling the occupancy dependence of diffusivities in zeolites. *Microporous Mesoporous Mater.* **2004**, *76*, 233−246.

(53) Krishna, R.; van Baten, J. M. A molecular dynamics investigation of a variety of influences of temperature on diffusion in zeolites. *Microporous Mesoporous Mater.* **2009**, *125*, 126−134.

(54) Krishna, R.; van Baten, J. M. Investigating the potential of MgMOF-74 membranes for CO2 capture. *J. Membr. Sci.* **2011**, *377*, 249−260.

(55) Krishna, R.; van Baten, J. M. Using Molecular Dynamics Simulations for Elucidation of Molecular Traffic in Ordered Crystalline Microporous Materials. *Microporous Mesoporous Mater.* **2018**, *258*, 151−169.

(56) Krishna, R.; van Baten, J. M. A molecular dynamics investigation of the diffusion characteristics of cavity-type zeolites with 8-ring windows. *Microporous Mesoporous Mater.* **2011**, *137*, 83−91.

(57) Chmelik, C.; Kärger, J. The predictive power of classical transition state theory revealed in diffusion studies with MOF ZIF-8. *Microporous Mesoporous Mater.* **2016**, *225*, 128−132.

(58) Lauerer, A.; Binder, T.; Chmelik, C.; Miersemann, E.; Haase, J.; Ruthven, D. M.; Kärger, J. Uphill diffusion and overshooting in the adsorption of binary mixtures in nanoporous solids. *Nat. Commun.* **2015**, *6*, 7697.

(59) Krishna, R.; van Baten, J. M. Segregation effects in adsorption of CO2-containing mixtures and their consequences for separation selectivities in cage-type zeolites. *Sep. Purif. Technol.* **2008**, *61*, 414−423.

(60) Paschek, D.; Krishna, R. Diffusion of binary mixtures in zeolites: Kinetic Monte Carlo versus molecular dynamics simulations. *Langmuir* **2001**, *17*, 247−254.

(61) Snurr, R. Q.; Kärger, J. Molecular simulations and NMR measurements of binary diffusion in zeolites. *J. Phys. Chem. B* **1997**, *101*, 6469−6473.

(62) Krishna, R.; van Baten, J. M. Investigating the influence of diffusional coupling on mixture permeation across porous membranes. *J. Membr. Sci.* **2013**, *430*, 113−128.

(63) van den Bergh, J.; Zhu, W.; Groen, J. C.; Kapteijn, F.; Moulijn, J. A.; Yajima, K.; Nakayama, K.; Tomita, T.; Yoshida, S. Natural Gas Purification with a DDR Zeolite Membrane; Permeation Modelling with Maxwell-Stefan Equations. *Stud. Surf. Sci. Catal.* **2007**, *170*, 1021−1027.

(64) van den Bergh, J.; Zhu, W.; Gascon, J.; Moulijn, J. A.; Kapteijn, F. Separation and permeation characteristics of a DD3R zeolite membrane. *J. Membr. Sci.* **2008**, *316*, 35−45.

(65) Fernandez, M.; Kärger, J.; Freude, D.; Pampel, A.; van Baten, J. M.; Krishna, R. Mixture Diffusion in Zeolites Studied by MAS PFG NMR and Molecular Simulation. *Microporous Mesoporous Mater.* **2007**, *105*, 124−131.

(66) Krishna, R.; Vlugt, T. J. H.; Smit, B. Influence of Isotherm Inflection on Diffusion in Silicalite. *Chem. Eng. Sci.* **1999**, *54*, 1751−1757.

(67) Krishna, R.; Van Baten, J. M. Elucidating Traffic Junction Effects in MFI Zeolite using Kinetic Monte Carlo Simulations. *ACS Omega* **2019**, *4*, 10761−10766.

(68) Krishna, R.; van Baten, J. M. Highlighting a variety of unusual characteristics of adsorption and diffusion in microporous materials induced by clustering of guest molecules. *Langmuir* **2010**, *26*, 8450−8463.

(69) Krishna, R.; van Baten, J. M. Hydrogen Bonding Effects in Adsorption of Water−Alcohol Mixtures in Zeolites and the Consequences for the Characteristics of the Maxwell−Stefan Diffusivities. *Langmuir* **2010**, *26*, 10854−10867.

(70) Krishna, R.; van Baten, J. M. Highlighting Pitfalls in the Maxwell-Stefan Modeling of Water-Alcohol Mixture Permeation across Pervaporation Membranes. *J. Membr. Sci.* **2010**, *360*, 476−482.

(71) Krishna, R.; van Baten, J. M. Mutual slowing-down effects in mixture diffusion in zeolites. *J. Phys. Chem. C* **2010**, *114*, 13154−13156.

(72) Hasegawa, Y.; Abe, C.; Nishioka, M.; Sato, K.; Nagase, T.; Hanaoka, T. Formation of high flux CHA-type zeolite membranes and their application to the dehydration of alcohol solutions. *J. Membr. Sci.* **2010**, *364*, 318−324.

(73) Sato, K.; Sugimoto, K.; Shimotsuma, N.; Kikuchi, T.; Kyotani, T.; Kurata, T. Development of practically available up-scaled high-silica CHA-type zeolite membranes for industrial purpose in dehydration of N-methyl pyrrolidone solution. *J. Membr. Sci.* **2012**, *409-410*, 82−95.

(74) Khajavi, S.; Jansen, J. C.; Kapteijn, F. Application of hydroxy sodalite films as novel water selective membranes. *J. Membr. Sci.* **2009**, *326*, 153−160.

(75) Kuhn, J.; Castillo-Sanchez, J. M.; Gascon, J.; Calero, S.; Dubbeldam, D.; Vlugt, T. J. H.; Kapteijn, F.; Gross, J. Adsorption and Diffusion of Water, Methanol, and Ethanol in All-Silica DD3R: Experiments and Simulation. *J. Phys. Chem. C* **2009**, *113*, 14290−14301.

A Thermodynamically Consistent Methodology for Estimation of Diffusivities of Mixtures of Guest Molecules in Microporous Materials

Rajamani Krishna*
Van 't Hoff Institute for Molecular Sciences
University of Amsterdam
Science Park 904
1098 XH Amsterdam, The Netherlands
email: r.krishna@contact.uva.nl

Table of Contents

1 Preamble

The Supporting Information accompanying our article *A Thermodynamically Consistent Methodology for Estimation of Diffusivities of Mixtures of Guest Molecules in Microporous Materials* provides (a) structural details for zeolites and MOFs considered and analyzed in this article, (b) dual-Langmuir-Freundlich data fits of unary isotherms, (c) the IAST calculation procedure for the spreading pressure, and its proxy θ, using the unary adsorption isotherm fits, (d) MD simulation data (a total of 70 data sets) for Λ_{ij}, along with comparisons with estimates using the methodology developed in this work.

The MD data analyzed in this publication is the same as presented in our earlier publication[1] entitled *Occupancy Dependency of Maxwell-Stefan Diffusivities in Ordered Crystalline Micro-porous Materials*.

For ease of reading, the Supporting Information is written as a stand-alone document; as a consequence, there is some overlap of material with the main manuscript.

2 Structural details of microporous crystalline materials

A wide variety of ordered crystalline microporous materials is used in several applications in separation applications.[2-5] These include zeolites (crystalline aluminosilicates), carbon nanotubes (CNTs), metal-organic frameworks (MOFs), and zeolitic imidazolate frameworks (ZIFs).

A number of different channel topologies and connectivities are encountered in zeolites, MOFs, and ZIFs; these can be divided into five broad classes;

1. One-dimensional (1D) channels (e.g. AFI, LTL, TON, MTW, Co-BDP, $Fe_2(BDP)_3$, MgMOF-74, NiMOF-74, Zn-MOF-74, MIL-47, MIL-53(Cr), BTP-COF); see Figure S1.
2. 1D channels with side pockets (e.g. MOR, FER); see Figure S2.
3. Intersecting channels (e.g. MFI, ISV, BEA, BOG, Zn(bdc)dabco, Co(bdc)dabco); see Figure S3
4. Cages separated by narrow windows (e.g. LTA (all-silica), LTA-4A, LTA-5A, CHA, DDR, ERI, TSC, ZIF-8); see Figure S4.
5. Cavities with large windows (e.g. FAU (all-silica), NaY, NaX, IRMOF-1, CuBTC, MOF-177); see Figure S5.

The crystallographic data are available on the zeolite atlas website of the International Zeolite Association (IZA).[6, 7] Further details on the structure, landscape, pore dimensions of a very wide variety of micro-porous materials are available in the published literature.[8-15] Table S1, Table S2, Table S3, and Table S4 provide some salient structural information on various zeolites and MOFs of interest.

In comparison to traditionally used porous materials such as zeolites, MOFs and ZIFs offer significantly higher surface areas and porosities. This is underscored in the data presented in Figure S6 for surface areas, pore volumes, characteristic dimensions, and framework densities of some representative zeolites, MOFs and ZIFs. The commonly used Faujasite zeolite (FAU), for example, has a characteristic size (window aperture) of 7.4 Å, a pore volume of 0.33 cm^3/g, and a surface area of 980

m^2/g. MFI zeolite (also known as silicalite-1, and ZSM-5) has a channel dimension of 5.5 Å, pore volume of 0.165 cm^3 g^{-1}, and surface area of 490 m^2 g^{-1}. The accessible pore volumes of MOFs are commonly in the 0.5 – 2 cm^3/g range. Furthermore, significantly higher surface areas are available with MOFs; for example MOF-177 has an area of 4800 m^2/g. The pore dimensions of MOFs are also often significantly larger; MgMOF-74 has one-dimensional hexagonal-shaped channels of approximately 11 Å diameter. In the ensuing discussions, we use the terminology “open” structures to describe materials that have high pore volumes.

2.1 List of Tables for Structural details of microporous crystalline materials

Table S1. Salient structural information on zeolites.

Structure	Topology	Fractional pore volume, ϕ	Pore volume/ cm^3/g	Framework density/ kg/m^3
AFI	12-ring 1D channels of 7.3 Å size	0.274	0.159	1730
BEA	Intersecting channels of two sizes: 12-ring of 6.1 Å - 6.8 Å and 10-ring of 5.6 Å – 6.7 Å	0.408	0.271	1509
BOG	Intersecting channels: 12-ring 6.8 Å -7.4 Å and 10-ring of 5.6 Å - 5.8 Å	0.374	0.241	1996
CHA	316 Å^3 cages separated by 3.77 Å × 4.23 Å size windows	0.382	0.264	1444
DDR	277.8 Å^3 cages separated by 3.65 Å × 4.37 Å size windows	0.245	0.139	1760
ERI	408 Å^3 cages separated by 3.8 Å – 4.9 Å size windows	0.363	0.228	1595
FAU (all silica)	790 Å^3 cages separated by 7.4 Å size windows	0.439	0.328	1338
FER	10-ring 1D main channels of 4.2 Å -5.4 Å size, connected with 8-ring side pockets of 3.5 Å -4.8 Å size	0.283	0.160	1772
ISV	Intersecting channels of two sizes: 12-ring of 6.1 Å -6.5 Å and 12-ring of 5.9 Å - 6.6 Å	0.426	0.278	1533
LTL	12-ring 1D channels of 7.1 Å size	0.277	0.170	1627
LTA (all silica)	743 Å^3 cages separated by 4.11 Å × 4.47 Å size windows	0.399	0.310	1285
LTA-4A	694 Å^3 cages separated by 4 Å × 4.58 Å size windows	0.38	0.25	1530
LTA-5A	702 Å^3 cages separated by 4 Å × 4.58 Å size windows	0.38	0.25	1508
MFI	10-ring intersecting channels of 5.4 Å – 5.5 Å and 5.4 Å – 5.6 Å size	0.297	0.165	1796
MOR	12-ring 1D main channels of 6.5 Å -7 Å size, connected with 8-ring side pockets of 2.6 Å -5.7 Å size	0.285	0.166	1715
MTW	12-ring 1D channels of 5.6 Å -6 Å size	0.215	0.111	1935

Structural details of microporous crystalline materials

NaY	790 Å^3 cages separated by 7.4 Å size windows	0.41	0.303	1347
NaX	790 Å^3 cages separated by 7.4 Å size windows	0.40	0.280	1421
TON	10-ring 1D channels of 4.6 Å -5.7 Å size	0.190	0.097	1969

Table S2. Pore volumes, surface areas, and characteristic (Delaunary) dimenions for zeolites

Structure	**Pore volume** / cm^3 g^{-1}	**Surface area** / m^2 g^{-1}	**Delaunay diameter**/ Å
MFI	0.165	487.2	5.16
ISV	0.278	911.4	5.96
BEA	0.271	922.7	5.87
BOG	0.241	758.4	5.02
GME	0.265	717.6	7.09
LTL	0.170	520.6	7.26
MOR	0.166	416.7	7.47
FER	0.160	402.5	6.44
FAU (all silica)	0.328	1086	4.65
LTA (all silica)	0.310	896	7.37
CHA	0.264	757.5	3.98
ERI	0.228	635.3	4.10
DDR	0.139	350	4.02
AFX	0.246	674.5	3.77

Structural details of microporous crystalline materials

Table S3. Salient structural information on MOFs, ZIFs, and COFs.

Structure	Topology	Fractional pore volume, ϕ	Pore volume/ cm^3/g	Framework density/ kg/m^3
CuBTC	Large cages are inter-connected by 9 Å windows of square cross-section. The large cages are also connected to tetrahedral-shaped pockets of ca. 6 Å size through triangular-shaped windows of 4.6 Å size	0.759	0.863	879
IRMOF-1	Two alternating, inter-connected, cavities of 10.9 Å and 14.3 Å with window size of 8 Å.	0.812	1.369	593
Zn(bdc)dabco	There exist two types of intersecting channels of about 7.5 Å × 7.5 Å along the x-axis and channels of 3.8 Å × 4.7 Å along y and z axes.	0.662	0.801	826
Co(bdc)dabco	There exist two types of intersecting channels of about 7.6 Å × 7.6 Å along the x-axis and channels of 3.7 Å × 5.1 Å along y and z axes.	0.648	0.796	814
MOF-177	Six diamond-shaped channels (upper) with diameter of 10.8 Å surround a pore containing eclipsed BTB^{3-} moieties.	0.840	1.968	427
MgMOF-74	1D hexagonal-shaped channels of 11 Å	0.708	0.782	905
MIL-47	1D diamond-shaped channels of 8.5 Å	0.608	0.606	1004
MIL-53 (Cr)-lp	1D lozenge-shaped channels of 8.5 Å	0.539	0.518	1041
ZIF-8	1168 $Å^3$ cages separated by 3.26 Å size windows	0.476	0.515	924

Structural details of microporous crystalline materials

Table S4. Pore volumes, surface areas, and characteristic (Delaunary) dimenions for MOFs, ZIFs, and BTP-COF.

Structure	**Pore volume** / $cm^3\ g^{-1}$	**Surface area** / $m^2\ g^{-1}$	**Delaunay diameter**/ Å
IRMOF1	1.369	3522.2	7.38
CuBTC	0.848	2097.0	6.23
MIL47	0.606	1472.8	8.03
MIL53(Cr)-lp	0.518	1280.5	7.40
Zn(BDC)dabco	0.801	2022.5	8.32
Co(BDC)dabco	0.796		8.35
ZIF-8	0.515	1164.7	3.26
MOF-177	1.968	4781.0	10.1
MgMOF-74	0.782	1640.0	10.66

2.2 List of Figures for Structural details of microporous crystalline materials

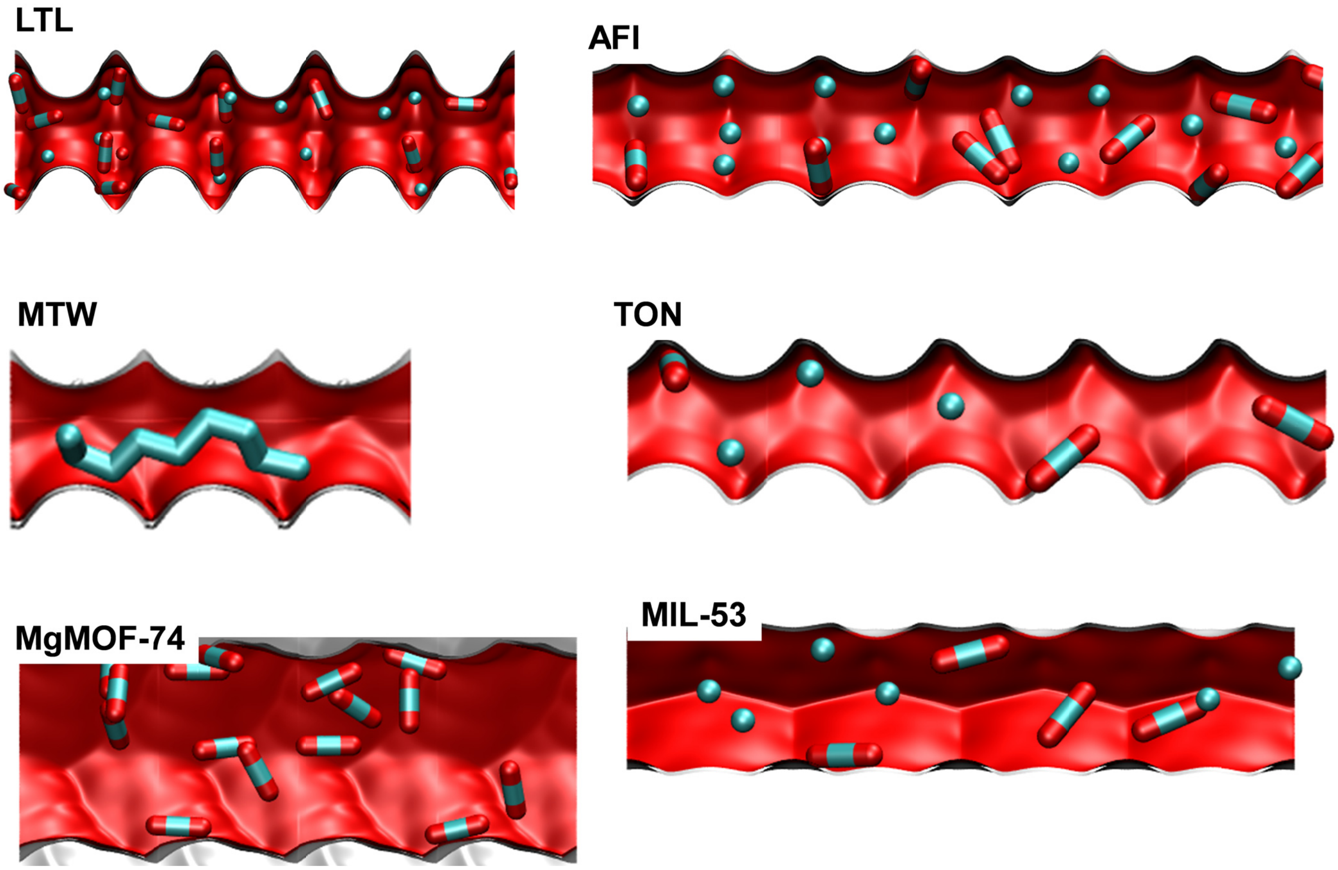

Figure S1. Examples of one-dimensional (1D) channel structures: AFI, MgMOF-74, and MIL-53(Cr)-lp, BTP-COF, and $Fe_2(BDP)_3$.

Structural details of microporous crystalline materials

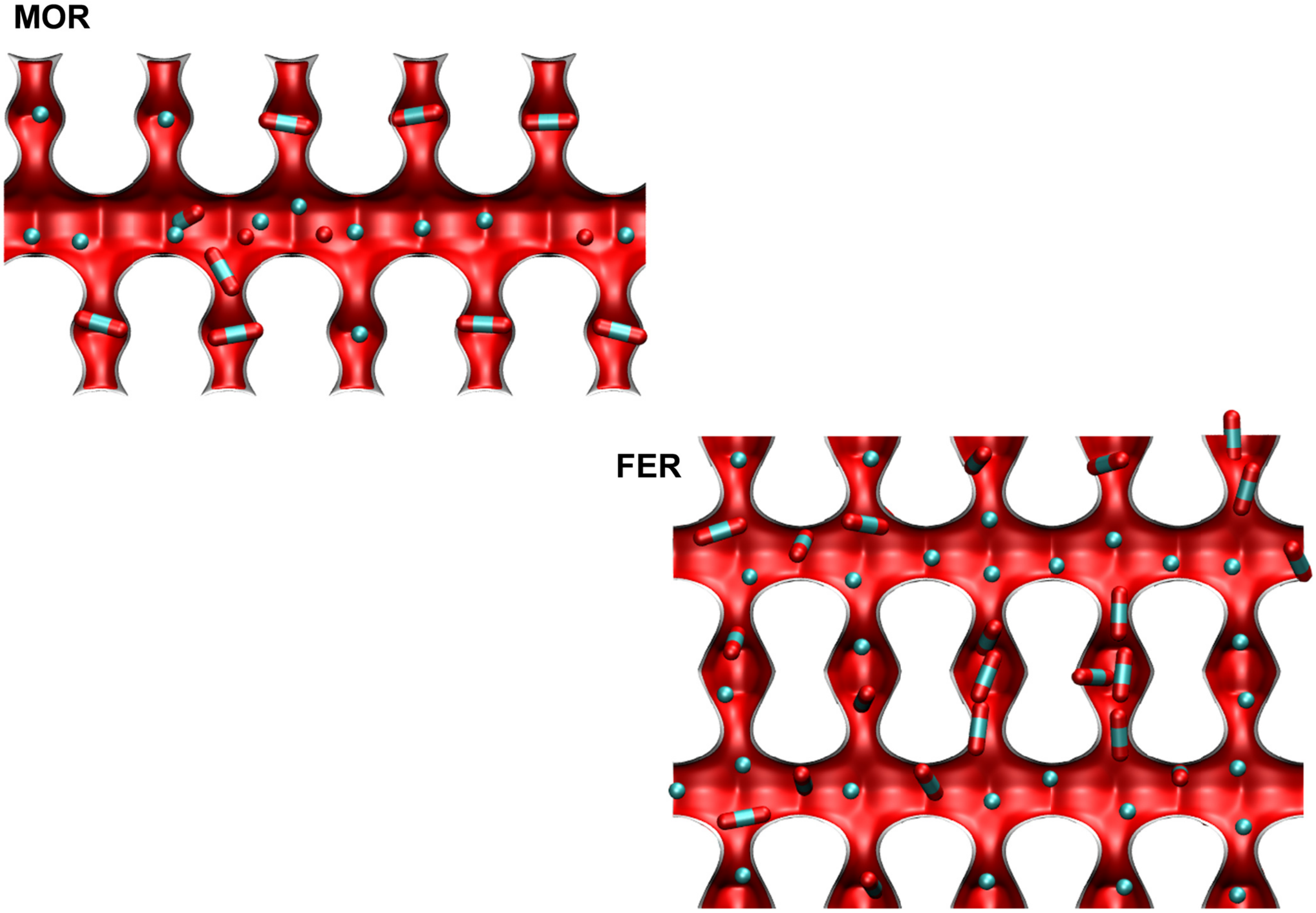

Figure S2. Examples of 1D channel structures with side pockets: MOR and FER.

Structural details of microporous crystalline materials

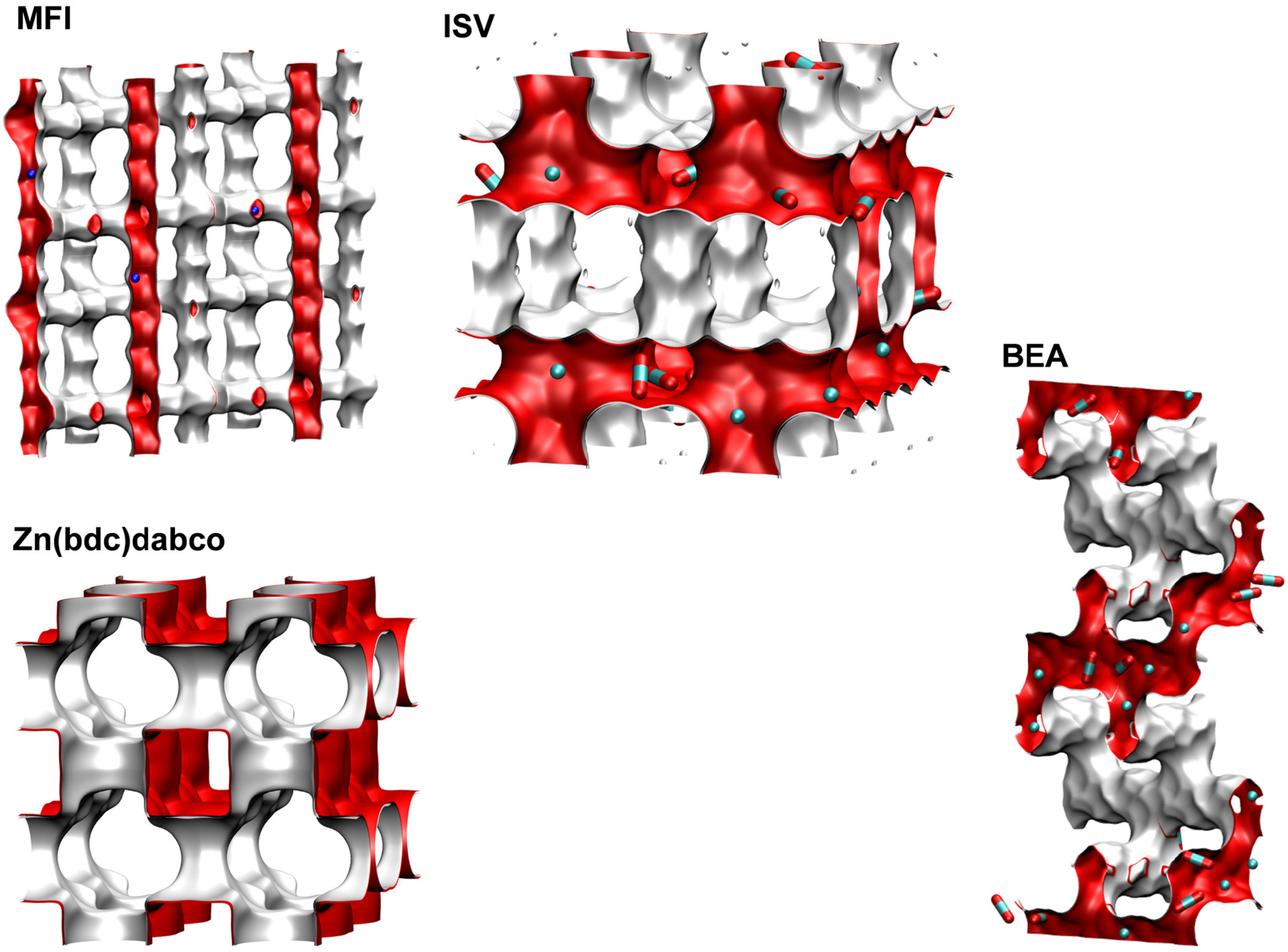

Figure S3. Examples of structures consisting of intersecting channels: MFI, ISV, BEA, and Zn(bdc)dabco.

Structural details of microporous crystalline materials

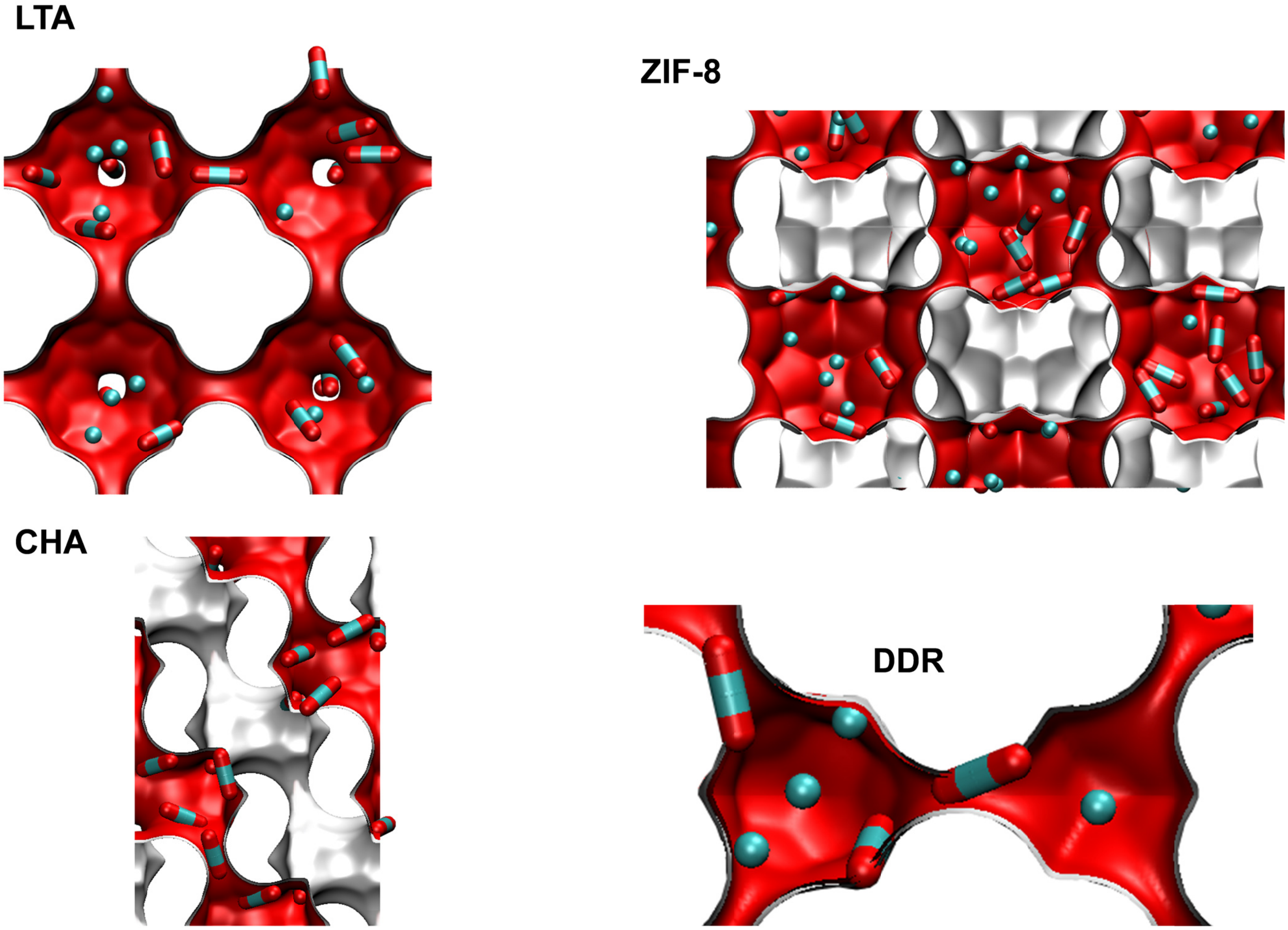

Figure S4. Structures consisting of cages separated by narrow windows: LTA, CHA, DDR, and ZIF-8.

Structural details of microporous crystalline materials

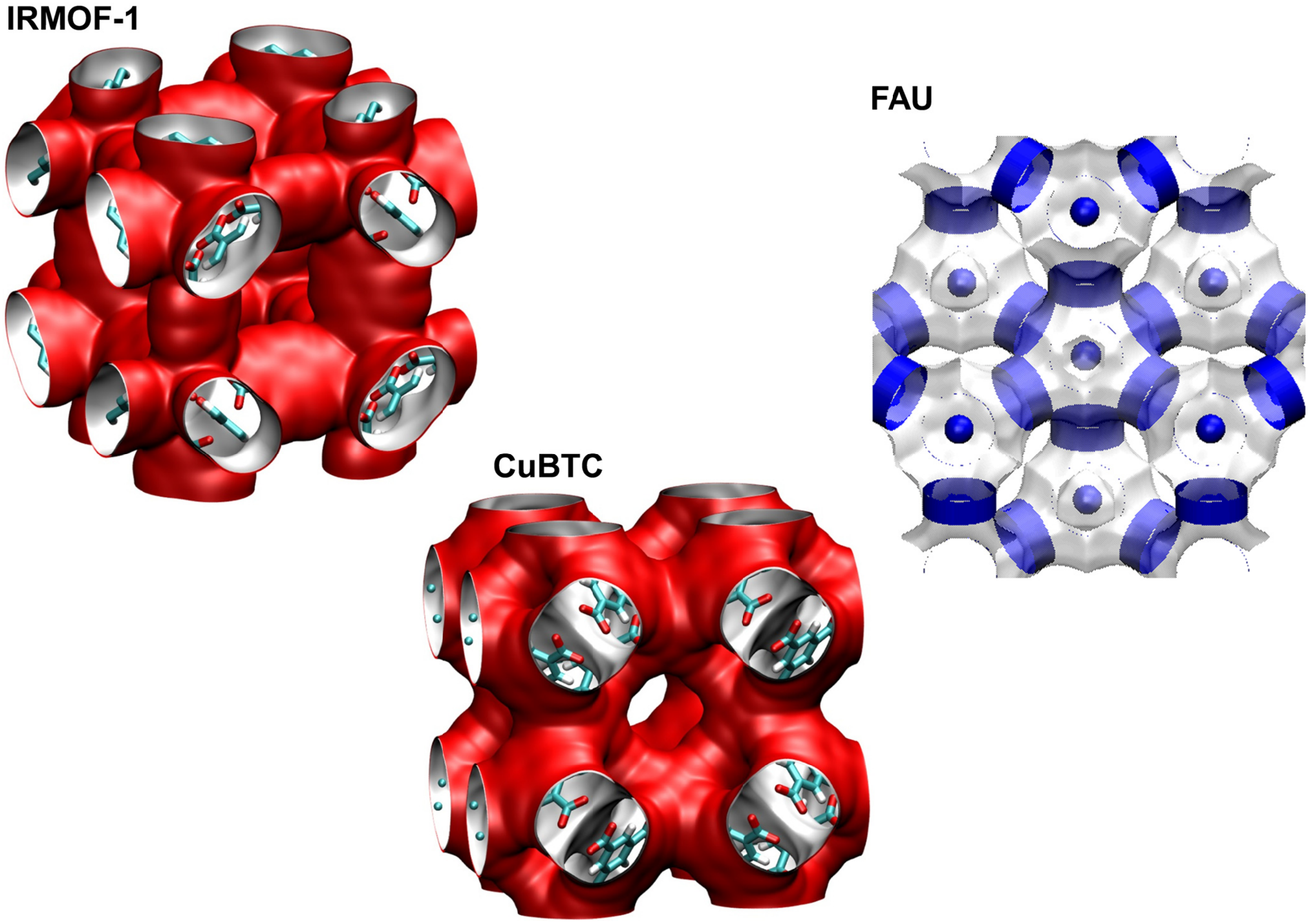

Figure S5. "Open" structures that consist of cages separated by large windows: IRMOF-1, CuBTC, and FAU.

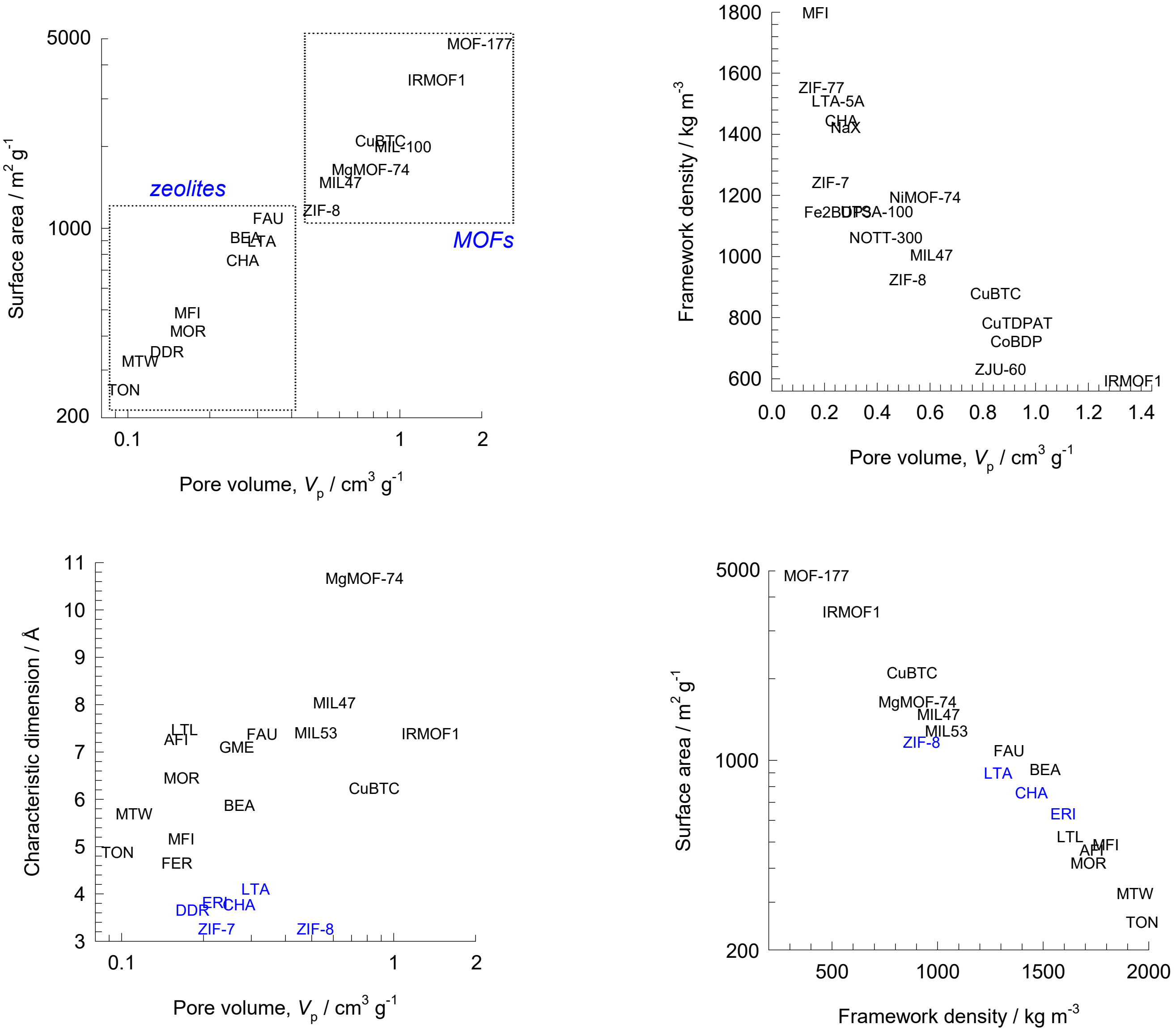

Figure S6. Comparison of surface area, pore volumes, framework densities, fractional pore volumes, and characteristic dimensions of some representative zeolites, MOFs and ZIFs.

3 Thermodynamics of Mixture Adsorption in Micro-porous Materials

Within microporous crystalline materials, the guest molecules exist in the adsorbed phase, and the thermodynamics of mixture adsorption has an important bearing on the diffusion characteristics of guest molecules. For that reason, we provide below a brief summary of the Ideal Adsorbed Solution Theory (IAST) theory of Myers and Prausnitz.[16]

3.1 Brief outline of IAS theory

The Gibbs adsorption equation[17] in differential form is

$$A d\pi = \sum_{i=1}^{n} q_i d\mu_i \tag{S1}$$

The quantity A is the surface area per kg of framework, with units of m^2 per kg of the framework of the crystalline material; q_{i} is the molar loading of component i in the adsorbed phase with units moles per kg of framework; μ_{i} is the molar chemical potential of component i. The spreading pressure π has the same units as surface tension, i.e. N m^{-1}.

The chemical potential of any component in the adsorbed phase, μ_{i}, equals that in the bulk fluid phase. If the partial fugacities in the bulk fluid phase are f_{i}, we have

$$d\mu_i = RTd \ln f_i \tag{S2}$$

where R is the gas constant (= 8.314 J mol^{-1} K^{-1}).

Briefly, the basic equation of Ideal Adsorbed Solution Theory (IAST) theory of Myers and Prausnitz[16] is the analogue of Raoult's law for vapor-liquid equilibrium, i.e.

$$f_i = P_i^0 x_i; \quad i = 1,2,..n \tag{S3}$$

where x_{i} is the mole fraction in the adsorbed phase

$$x_i = \frac{q_i}{q_1 + q_2 + ...q_n} \tag{S4}$$

and P_i^0 is the pressure for sorption of every component i, which yields the same spreading pressure, π for each of the pure components, as that for the mixture:

$$\frac{\pi A}{RT} = \int_0^{P_1^0} \frac{q_1^0(f)}{f} df = \int_0^{P_2^0} \frac{q_2^0(f)}{f} df = \int_0^{P_3^0} \frac{q_3^0(f)}{f} df = ... \tag{S5}$$

where $q_i^0(f)$ is the *pure* component adsorption isotherm. For *n*-component adsorption, there are a set of *n*-1 independent equalities in Equations (S5). The units of $\frac{\pi A}{RT}$, also called the adsorption potential,[18] are mol kg^{-1}. Each of the integrals in Equation (S5) can be evaluated analytically.

The unary isotherms may be described by say the dual-Langmuir-Freundlich model

$$q^0(f) = q_{A,sat} \frac{b_A f^{\nu A}}{1 + b_A f^{\nu A}} + q_{B,sat} \frac{b_B f^{\nu B}}{1 + b_B f^{\nu B}} \tag{S6}$$

For the dual-site Langmuir-Freundlich isotherm, the integration yields for component *i*,

$$\frac{\pi A}{RT} = \int_{f=0}^{P_i^0} \frac{q^0(f)}{f} df = \frac{q_{A,sat}}{\nu_A} \ln\left(1 + b_A \left(P_i^0\right)^{\nu_A}\right) + \frac{q_{B,sat}}{\nu_B} \ln\left(1 + b_B \left(P_i^0\right)^{\nu_B}\right) \tag{S7}$$

Invoking equation (S3) to express the sorption pressures in terms of the partial fugacities and component mole fractions we obtain

$$\frac{\pi A}{RT} = \int_{f=0}^{P_i^0} \frac{q^0(f)}{f} df = \frac{q_{A,sat}}{\nu_A} \ln\left(1 + b_A \left(\frac{f_i}{x_i}\right)^{\nu_A}\right) + \frac{q_{B,sat}}{\nu_B} \ln\left(1 + b_B \left(\frac{f_i}{x_i}\right)^{\nu_B}\right) \tag{S8}$$

For a specified set of partial fugacities f_i in the bulk fluid phase, a total of *n* in number, the right hand side of equation (S8) is a function of the mole fraction in the adsorbed phase x_i. For *n*-component adsorption, there are *n*-1 independent mole fractions x_i that are determined by solving the set of *n*-1 independent equalities in Equations (S5). These constraints may be solved using a suitable equation solver to determine the x_1, x_2, x_3,.. x_{n-1}, and $x_n = 1 - x_1 - x_2 - ... - x_{n-1}$. In all of the calculations presented in this article, the set of *n*-1 non-linear equations were solved using the Given-Find solve block of MathCad 15.[19] For a binary mixture, a simple root finder is required to solve a single non-linear equation.

From knowledge of the adsorbed phase mole fractions x_i, the sorption pressures P_1^0, P_2^0, P_3^0,.. P_n^0 are then determined from

$$P_i^0 = \frac{f_i}{x_i}; \quad i = 1, 2, \ldots n \tag{S9}$$

A key assumption of the IAST is that the enthalpies and surface areas of the adsorbed molecules do not change upon mixing. If the total mixture loading is q_t, the area covered by the adsorbed mixture is $\frac{A}{q_t}$ with units of m^2 (mol mixture)$^{-1}$. Therefore, the assumption of no surface area change due to mixture adsorption translates as $\frac{A}{q_t} = \frac{Ax_1}{q_1^0\left(P_1^0\right)} + \frac{Ax_2}{q_2^0\left(P_2^0\right)} + \cdots \frac{Ax_n}{q_n^0\left(P_n^0\right)}$; the total mixture loading is q_t is calculated from

$$q_t = q_1 + q_2 \ldots + q_n = \frac{1}{\frac{x_1}{q_1^0(P_1^0)} + \frac{x_2}{q_2^0(P_2^0)} + \ldots . + \frac{x_n}{q_n^0(P_n^0)}} \tag{S10}$$

in which $q_1^0(P_1^0)$, $q_2^0(P_2^0)$,... $q_n^0(P_n^0)$ are determined from the unary isotherm fits, using the sorption pressures for each component P_1^0, P_2^0, P_3^0,.. P_n^0 that are available from the solutions of Equations (S5), (S8), and (S9).

From knowledge of the adsorption potential, $\frac{\pi A}{RT}$, the fractional occupancy for mixture adsorption is then calculated using

$$\theta = 1 - \exp\left(-\frac{\pi A}{q_{sat,mix} RT}\right) \tag{S11}$$

For a binary mixture, the saturation capacity $q_{sat,mix}$ is calculated from the saturation capacities of the constituent guests

$$q_{sat,mix} = \frac{1}{\frac{x_1}{q_{1,sat}} + \frac{x_2}{q_{2,sat}}}; \quad q_{1,sat} = q_{1,A,sat} + q_{1,B,sat}; \quad q_{2,sat} = q_{2,A,sat} + q_{2,B,sat} \tag{S12}$$

where

$$x_1 = \frac{q_1}{q_1 + q_2}; \quad x_2 = \frac{q_2}{q_1 + q_2} \tag{S13}$$

are the mole fractions in the adsorbed mixture. For equimolar mixtures, $x_1 = x_2 = 0.5$, equation (S13) simplifies to yield $q_{sat,mix} = \frac{2}{\frac{1}{q_{1,sat}} + \frac{1}{q_{2,sat}}}$.

The fundamental justification of Equation (S12) is provided by applying equation (S10) to pore saturation conditions.

Equations (S11) is the appropriate generalization of Equation (S26), derived in the following section for the mixed-gas Langmuir model. It is also to be noted that equation (15) of our earlier publication[1] has a typographical error in the calculation of $q_{sat,mix}$; the correct form is given by equation (S12).

For the special case of unary diffusion wherein the unary adsorption isotherm is described by the dual-Langmuir-Freundlich isotherm, equation (S6), the fractional occupancy can be determined as follows

$$\begin{aligned} &\frac{\pi A}{RT} = \frac{q_{A,sat}}{\nu_A} \ln\left(1 + b_A \left(P_i^0\right)^{\nu_A}\right) + \frac{q_{B,sat}}{\nu_B} \ln\left(1 + b_B \left(P_i^0\right)^{\nu_B}\right); \quad q_{i,sat} = q_{A,sat} + q_{B,sat} \\ &\theta_i = 1 - \exp\left(-\frac{\pi A}{q_{i,sat} RT}\right); \quad \text{unary adsorption of species i} \end{aligned} \tag{S14}$$

3.2 IAST model: 1-site Langmuir isotherms

The IAST procedure will be applied for binary mixture adsorption in which the unary isotherms are described by the 1-site Langmuir model in which the saturation capacities of components 1 and 2 are identical to each other, i.e. $q_{1,sat} = q_{2,sat} = q_{sat}$:

$$q^0(f) = q_{sat}\frac{bf}{1+bf}; \quad \theta = \frac{bf}{1+bf} \tag{S15}$$

where we define the fractional *occupancy* of the adsorbate molecules, $\theta = q^0(f)/q_{sat}$. The superscript 0 is used to emphasize that $q^0(f)$ relates the *pure component* loading to the bulk fluid fugacity.

For unary adsorption, the adsorption potential for a 1-site Langmuir isotherm can be calculated analytically

$$\frac{\pi A}{RT} = q_{sat}\ln\left(1+bP^0\right) \tag{S16}$$

The objective is to determine the molar loadings, q_1, and q_2, in the adsorbed phase.

Performing the integration of Equation (S5) results in an expression relating the sorption pressures P_i^0 of the two species

$$\begin{aligned} &\frac{\pi A}{RT} = q_{sat}\ln\left(1+b_1P_1^0\right) = q_{sat}\ln\left(1+b_2P_2^0\right) \\ &b_1P_1^0 = b_2P_2^0 = \exp\left(\frac{\pi A}{q_{sat}RT}\right) - 1 \end{aligned} \tag{S17}$$

The adsorbed phase mole fractions of component 1, and component 2 are given by equation (S9)

$$x_1 = \frac{f_1}{P_1^0}; \quad x_2 = 1 - x_1 = \frac{f_2}{P_2^0} \tag{S18}$$

Combining equations (S17), and (S18):

$$\begin{aligned} &\exp\left(\frac{\pi A}{q_{sat}RT}\right) - 1 = b_1\frac{f_1}{x_1} = b_2\frac{f_2}{1-x_1} \\ &\frac{\pi A}{q_{sat}RT} = \ln\left(1+b_1\frac{f_1}{x_1}\right) = \ln\left(1+b_2\frac{f_2}{x_2}\right) \end{aligned} \tag{S19}$$

The adsorbed phase mole fractions can be determined

$$\frac{x_1}{x_2} = \frac{q_1}{q_2} = \frac{b_1f_1}{b_2f_2}; \quad x_1 = \frac{q_1}{q_t} = \frac{b_1f_1}{b_1f_1+b_2f_2}; \quad x_2 = \frac{q_2}{q_t} = \frac{b_2f_2}{b_1f_1+b_2f_2} \tag{S20}$$

Once x_1, and $x_2 = 1 - x_1$ are determined, the sorption pressures can be calculated:

$$P_1^0 = \frac{f_1}{x_1}; \quad P_2^0 = \frac{f_2}{x_2} = \frac{f_2}{1-x_1} \tag{S21}$$

From equations (S17), (S20), and (S21) we get

$$\begin{gathered} b_i P_1^0 = \frac{b_1 f_1}{x_1} = b_2 P_2^0 = \frac{b_2 f_2}{x_2} = b_1 f_1 + b_2 f_2 \\ 1 + b_i P_1^0 = 1 + b_2 P_2^0 = 1 + b_1 f_1 + b_2 f_2 \end{gathered} \tag{S22}$$

Combining equations (S19), and (S22) we get the following expression for the adsorption potential for the mixture

$$\frac{\pi A}{RT} = q_{sat} \ln\left(1 + b_1 f_1 + b_2 f_2\right) \tag{S23}$$

The total amount adsorbed, $q_t = q_1 + q_2$ can be calculated from Equation (S10)

$$q_t = q_1 + q_2 = q_{sat} \frac{b_1 P_1^0}{1 + b_1 P_1^0} = q_{sat} \frac{b_2 P_2^0}{1 + b_2 P_2^0} = q_{sat} \frac{b_1 f_1 + b_2 f_2}{1 + b_1 f_1 + b_2 f_2} \tag{S24}$$

Combining equations (S20), and (S24) we obtain the following explicit expressions for the component loadings, and fractional occupancies

$$\theta_1 = \frac{q_1}{q_{sat}} = \frac{b_1 f_1}{1 + b_1 f_1 + b_2 f_2}; \quad \theta_2 = \frac{q_2}{q_{sat}} = \frac{b_2 f_2}{1 + b_1 f_1 + b_2 f_2} \tag{S25}$$

Equation (S25) is commonly referred to as the mixed-gas Langmuir model.

From equations (S17), (S24), and (S25) we derive the following expression for the total occupancy of the mixture

$$\theta = \theta_1 + \theta_2 = \frac{q_t}{q_{sat}} = 1 - \exp\left(-\frac{\pi A}{q_{sat} RT}\right) = \frac{b_1 f_1 + b_2 f_2}{1 + b_1 f_1 + b_2 f_2} \tag{S26}$$

For *unary* adsorption of component *i*, say, $f_i = P_i^0$, the occupancy of component 1 is

$$\theta_i = 1 - \exp\left(-\frac{\pi A}{q_{sat} RT}\right) = \frac{b_i f_i}{1 + b_i f_i}; \quad \text{unary adsorption of species i} \tag{S27}$$

From equations (S26), and (S27) we may also conclude the *occupancy* may be considered to be the appropriate *proxy* for the spreading pressure. The conclusion that we draw from the foregoing analysis is that the equalities of spreading pressures for unary adsorption of component 1, unary adsorption of component 2, and binary 1-2 mixture adsorption also implies the corresponding equalities of the corresponding *occupancies* for unary adsorption of component 1, unary adsorption of component 2, and binary 1-2 mixture adsorption.

4 The Maxwell-Stefan formulation for diffusion in micropores

Within micro-porous crystalline materials, such as zeolites, metal-organic frameworks (MOFs), and zeolitic imidazolate frameworks (ZIFs), the guest molecules exist in the adsorbed phase. The Maxwell-Stefan (M-S) equations for *n*-component diffusion in porous materials is applied in the following manner[8, 10, 20-25]

$$-\rho \frac{q_i}{RT}\frac{d\mu_i}{dz} = \sum_{\substack{j=1\\ j\neq i}}^{n} \frac{x_j N_i - x_i N_j}{Đ_{ij}} + \frac{N_i}{Đ_i}; \quad i = 1,2,..n \tag{S28}$$

where ρ is the framework density with units of kg m^{-3}, and the fluxes N_i are the number of moles of species *i* transported per m^2 of crystalline material per second. The mole fractions of the components in the adsorbed phase, $x_i = q_i / q_t$ where q_i is the molar loading of adsorbate, and q_t is the *total* mixture loading $q_t = \sum_{i=1}^{n} q_i$.

The Maxwell-Stefan diffusion formulation (S28) is consistent with the theory of irreversible thermodynamics. The Onsager Reciprocal Relations imply that the M-S pair diffusivities are symmetric

$$Đ_{ij} = Đ_{ji} \tag{S29}$$

An important, persuasive, argument for the use of the M-S formulation for mixture diffusion is that the M-S diffusivity $Đ_i$ in mixtures can be estimated using information on the loading dependence of the corresponding unary diffusivity values. Put another way, the M-S diffusivity $Đ_i$ can be estimated from experimental data on *unary* diffusion in the porous material.

The M-S diffusivity $Đ_{ij}$ has the units m^2 s^{-1} and the physical significance of an *inverse* drag coefficient. At the molecular level, the $Đ_{ij}$ reflect how the facility for transport of species *i correlates* with that of species *j*; they are also termed *exchange coefficients*.

4.1 Thermodynamic correction factors

At thermodynamic equilibrium, the chemical potential of component *i* in the bulk fluid mixture equals the chemical potential of that component in the adsorbed phase. For the bulk fluid phase mixture we have

$$\frac{1}{RT}\frac{d\mu_i}{dz}=\frac{d\ln f_i}{dz}=\frac{1}{f_i}\frac{df_i}{dz};\qquad i=1,2,..n \tag{S30}$$

The chemical potential gradients $d\mu_i/dz$ can be related to the gradients of the molar loadings, q_i, by defining thermodynamic correction factors Γ_{ij}

$$\frac{q_i}{RT}\frac{d\mu_i}{dz}=\sum_{j=1}^{n}\Gamma_{ij}\frac{dq_j}{dz};\quad \frac{c_i}{RT}\frac{d\mu_i}{dz}=\sum_{j=1}^{n}\Gamma_{ij}\frac{dc_j}{dz};\qquad \Gamma_{ij}=\frac{q_i}{f_i}\frac{\partial f_i}{\partial q_j}=\frac{c_i}{p_i}\frac{\partial f_i}{\partial c_j};\qquad i,j=1,....n \tag{S31}$$

The thermodynamic correction factors Γ_{ij} can be calculated by differentiation of the model describing mixture adsorption equilibrium. Generally speaking, the Ideal Adsorbed Solution Theory (IAST) of Myers and Prausnitz[16] is the preferred method for estimation of mixture adsorption equilibrium. In the special case in which the unary isotherms for every component is described by the 1-site Langmuir model with equal saturation capacities, the mixed-gas Langmuir model

$$\frac{q_i}{q_{sat}}=\theta_i=\frac{b_i f_i}{1+\sum_{i=1}^{n}b_i f_i};\quad i=1,2,...n \tag{S32}$$

is derivable from the IAST. Analytic differentiation of equation (S32) yields

$$\Gamma_{ij}=\delta_{ij}+\left(\frac{\theta_i}{\theta_V}\right);\qquad i,j=1,2\ldots n \tag{S33}$$

where the fractional vacancy θ_V is defined as

$$\theta_V=1-\theta_t=1-\sum_{i=1}^{n}\theta_i \tag{S34}$$

The elements of the matrix of thermodynamic factors Γ_{ij} can be calculated explicitly from information on the component loadings q_i in the adsorbed phase; this is the persuasive advantage of the use of the mixed-gas Langmuir model. By contrast, the IAST does not allow the calculation of Γ_{ij} explicitly from knowledge on the component loadings q_i in the adsorbed phase; a numerical procedure is required.

4.2 Explicit expression for the fluxes as function of loading gradients

By defining an n-dimensional square matrix $[B]$ with elements

$$B_{ii} = \frac{1}{Đ_i} + \sum_{\substack{j=1 \\ j \neq i}}^{n} \frac{x_j}{Đ_{ij}}; \quad B_{ij} = -\frac{x_i}{Đ_{ij}}; \quad i, j = 1,2....n \tag{S35}$$

we can recast equation (S28) into the following form

$$-\rho \frac{q_i}{RT} \nabla \mu_i = \sum_{j=1}^{n} B_{ij} N_j; \qquad i = 1,2,..n \tag{S36}$$

Equation (S36) can be re-written in n-dimensional matrix notation as

$$(N) = -\rho [B]^{-1} [\Gamma] \frac{d(q)}{dz} = -\rho [\Lambda][\Gamma] \frac{d(q)}{dz} \tag{S37}$$

We denote the inverse of $[B]$ as $[\Lambda]$:

$$[B]^{-1} \equiv [\Lambda] \tag{S38}$$

The elements of $[\Lambda]$ cannot be determined from experimental measurements. However, Λ_{ij} are directly accessible from MD simulations[10, 22, 25, 26] by monitoring the individual molecular displacements

$$\Lambda_{ij} = \frac{1}{2} \lim_{\Delta t \to \infty} \frac{1}{n_j} \frac{1}{\Delta t} \left\langle \left(\sum_{l=1}^{n_i} \left(\mathbf{r}_{l,i}(t+\Delta t) - \mathbf{r}_{l,i}(t) \right) \right) \bullet \left(\sum_{k=1}^{n_j} \left(\mathbf{r}_{k,j}(t+\Delta t) - \mathbf{r}_{k,j}(t) \right) \right) \right\rangle \tag{S39}$$

In this expression n_i and n_j represent the number of molecules of species i and j respectively, and $\mathbf{r}_{l,i}(t)$ is the position of molecule l of species i at any time t. In this context we note a typographical error in equation (S39) as printed in earlier publications[27-29] wherein the denominator in the right member had n_i instead of n_j. The simulation results presented in these publications are, however, correct as the proper formula given in equation (S39) was used.

Compliance with the Onsager Reciprocal Relations demands

$$n_j \Lambda_{ij} = n_i \Lambda_{ji}; \quad i, j = 1, 2, ...n \tag{S40}$$

5 Unary Diffusion in Microporous Materials

5.1 Unary self-diffusivity, $Đ_{i,self}$, and M-S diffusivity, $Đ_i$

For unary diffusion, equation (S28) simplifies to yield

$$-\rho \frac{q_i}{RT}\frac{d\mu_i}{dz} = \frac{N_i}{Đ_i} \tag{S41}$$

The pure component $Đ_i$ is obtained from MD simulations of molecular displacements using the formula in each of the coordinate direction

$$Đ_i = \frac{1}{2}\lim_{\Delta t \to \infty} \frac{1}{n_i}\frac{1}{\Delta t}\left\langle \left(\sum_{l=1}^{n_i} \left(\mathbf{r}_{l,i}(t+\Delta t) - \mathbf{r}_{l,i}(t) \right) \right)^2 \right\rangle \tag{S42}$$

In this expression n_i represents the number of molecules of species *i*, and $\mathbf{r}_{l,i}(t)$ is the position of molecule *l* of species *i* at any time *t*.

There is no experimental procedure for direct determination of the $Đ_i$. Transient uptake and chromatographic experiments yield the Fick diffusivity D_i, also termed “transport” diffusivity, that relates the flux N_i of species *i* to the gradient of the molar loadings, q_i

$$N_i = -\rho D_i \frac{dq_i}{dz} \tag{S43}$$

The Fick diffusivity D_i are related to the M-S diffusivities by the thermodynamic factor Γ

$$D_i = Đ_i \Gamma; \quad \Gamma \equiv \frac{q_i}{f_i}\frac{\partial f_i}{\partial q_i}; \quad \text{unary diffusion} \tag{S44}$$

The M-S diffusivity $Đ_i$ is often termed the “corrected” diffusivity because the formula (S44) suggests that adsorption thermodynamic effects have been “factored out”. The values of Γ can be determined by analytic differentiation of fits to the adsorption isotherms. For a proper understanding of the concentration dependence of the diffusivities, we need the isotherm fits to be good representations over the entire range of concentrations, and not just in the Henry regime ($q_i \to 0$).

The self-exchange diffusivity, $Đ_{ii}$, is defined by applying the M-S equations (S28) to a binary mixture, that consists of identical species, tagged and un-tagged and assuming, furthermore, that we have equimolar diffusion $N_1 + N_2 = 0$. In this special case, the following relation between the self-diffusivity, $D_{i,self}$, and the M-S diffusivity, $Đ_i$, for *unary* diffusion [25]

$$-\rho \frac{q_1}{RT}\frac{d\mu_1}{dz} = \frac{(x_1 + x_2)N_1}{Đ_{11}} + \frac{N_1}{Đ_1} = \left(\frac{1}{Đ_{11}} + \frac{1}{Đ_1}\right)N_1 \tag{S45}$$

Equation (S44) defines the self-diffusivity within a pore for this special situation describing “tracer” diffusion

$$-\rho \frac{q_i}{RT}\frac{d\mu_i}{dz} = \frac{N_i}{D_{i.self}} \tag{S46}$$

and so we derive the expression

$$\frac{1}{D_{i,self}} = \frac{1}{Đ_i} + \frac{1}{Đ_{ii}} \tag{S47}$$

The self-diffusivities $D_{i,self}$ are computed from MD simulations by analyzing the mean square displacement of each species *i* for each coordinate direction

$$D_{i,self} = \frac{1}{2n_i}\lim_{\Delta t \to \infty}\frac{1}{\Delta t}\left\langle \left(\sum_{l=1}^{n_i} \left(\mathbf{r}_{l,i}(t+\Delta t) - \mathbf{r}_{l,i}(t)\right)^2 \right) \right\rangle \tag{S48}$$

Equation (S47) may used to determine the self-exchange diffusivities $Đ_{ii}$ from MD simulated $D_{i,self}$ and $Đ_i$ for unary diffusion. The self-exchange diffusivity, $Đ_{ii}$, quantifies the extent of correlations for unary diffusion. The $Đ_i$, reflecting *collective* motion of molecules (cf. equation (S42)) is free from such correlation effects; it is for this reason that the $Đ_i$ are amenable to simpler interpretation, and modeling, than the $D_{i,self}$. The Fick diffusivity, determined from say uptake or chromatographic experiments,[2] is *directly* influenced by adsorption thermodynamics and is therefore much more difficult to interpret from a fundamental viewpoint than the M-S $Đ_i$.

MD simulations of the unary self-diffusivities, $D_{i,self}$, and Maxwell-Stefan diffusivities, $Đ_i$, for a variety of guest molecules in a variety of host structures at 300 K were performed; these are reported in our earlier publications.[8, 10, 11, 14, 15, 22, 25-27, 30-34] A small set of representative data are presented in the following set of Figures:

Figure S7: MFI zeolite

Figure S8: all-silica FAU zeolite

Figure S9 NaY zeolite

Figure S10: NaX zeolite

Figure S11: AFI zeolite

Figure S12: BEA zeolite

Figure S13: ISV zeolite

Figure S14: all-silica LTA zeolite

Figure S15: all-silica CHA zeolite

Figure S16: DDR zeolite

Figure S17: IRMOF-1

Figure S18: CuBTC

Figure S19: MgMOF-74

Broadly speaking, for all guest/host combinations, both self-diffusivities, $D_{i,self}$, and Maxwell-Stefan diffusivities, $Đ_i$, are strongly dependent on the molar loadings. The diffusivities tend to decrease as the saturation loadings are approached. The loading dependence is often strongly influenced by the adsorption isotherms, and the spreading pressures. Configurational-Bias Monte Carlo (CBMC) simulations of the unary adsorption isotherms were also determined, and are plotted in the afore-listed Figures. These CBMC simulated isotherms were fitted with the dual-site Langmuir-Freundlich model; the fit parameters for each guest molecule (with sites A, and B) are tabulated for each host material as follows:

Table S5, Table S6, and Table S7: MFI zeolite

Table S8: FAU all-silica zeolite

Table S9: NaY zeolite (48 Al)

Table S10: NaX zeolite (86 Al)

Table S11: AFI all-silica zeolite

Table S12: LTA all-silica zeolite

Table S13: CHA all-silica zeolite

Table S14: DDR all-silica zeolite

Table S15: ISV zeolite

Table S16: BEA zeolite

Table S17: IRMOF-1

Table S18: MgMOF-74

Table S19: CuBTC

Using the dual-site Langmuir-Freundlich isotherm fit parameters, the spreading pressures and occupancy can be determined using Equation (S14). The diffusivities as function of the occupancy, θ, used as proxy for the spreading pressure, are also plotted in the afore-listed Figures. Generally, the diffusivities tend to reduce significantly, virtually to zero, as the occupancy approaches saturation conditions, $\theta \rightarrow 1$.

5.2 Degree of correlations for unary diffusion, $Đ_i / Đ_{ii}$

For the analysis of binary mixture diffusion, to be discussed in the subsequent chapter, it is convenient to define the degree of correlations for unary diffusion in microporous materials, as $\frac{Đ_i}{Đ_{ii}}$. In view Equation (S47) we get

$$\frac{Đ_i}{Đ_{ii}} = \frac{Đ_i}{D_{i,self}} - 1; \quad D_{i,self} = \frac{Đ_i}{1 + \frac{Đ_i}{Đ_{ii}}} \tag{S49}$$

Equation (S49) shows that the degree of correlations can be determined from MD simulations of $D_{i,self}$ and $Đ_i$. From Equation (S49) it can also be concluded that the self-diffusivity is always lower than the

M-S diffusivity due to correlation effects. The larger the degree of correlations, , the lower is the value of $D_{\mathrm{i,self}}$ compared to $Đ_i$.

For any given host material, the degree of correlations, $\frac{Đ_i}{Đ_{ii}}$, for different guest molecules need to be compared at the same fractional occupancy, θ, determined from Equation (S14). Figure S20 shows the data for $\frac{Đ_i}{Đ_{ii}}$, determined from MD simulations for a variety of guest molecules in (a) MFI, (b) all-silica FAU, (c) IRMOF-1, and (d) CuBTC. The relationship between $\frac{Đ_i}{Đ_{ii}}$ and is practically linear as a function of the fractional occupancy, determined from Equation (S14), where the saturation capacity is determined from the unary isotherm fits.. The important advantage of the linear dependence of $\frac{Đ_i}{Đ_{ii}}$ on the occupancy θ is that the data can be simply extrapolated to saturation conditions: $\theta \to 1$. We will exploit the linear dependence of $\frac{Đ_i}{Đ_{ii}}$ on θ for estimating the degrees of correlations for binary mixture diffusion in Chapter 8.3.

A further advantage of using the defining the degree of correlations $\frac{Đ_i}{Đ_{ii}}$ is that there is no need to further model the occupancy dependence of the exchange coefficient, $Đ_{ii}$, because this dependence has been related to that of the M-S diffusivity for which we need to use the appropriate models (e.g. Reed-Ehrlich, to be discussed in the next Chapter) to quantify the occupancy dependence.

5.3 Inverse thermodynamic factor

Also shown in panels (b) of Figure S7 to Figure S19 are the calculations of the inverse thermodynamic factor

$$\frac{1}{\Gamma_i} = \frac{f_i}{q_i}\frac{\partial q_i}{\partial f_i} \tag{S50}$$

where the derivative is obtained by analytic differential of the dual-site Langmuir-Freundlich isotherm fits. For most guest/host combinations in Figure S7 to Figure S19, the inverse thermodynamic factor $\frac{1}{\Gamma_i} = \frac{f_i}{q_i}\frac{\partial q_i}{\partial f_i}$ is seen to linearly decrease with the occupancy determined from

$$\theta = 1 - \exp\left(-\frac{\pi A}{q_{sat} RT}\right); \quad q_{sat} = q_{sat,A} + q_{sat,B} \tag{S51}$$

where the saturation capacity is the sum of the saturation capacities of site A and site B; see data in Table S5 to Table S19. Indeed, in the special case of the single-site Langmuir isotherm, we obtain the simple result

$$\frac{1}{\Gamma_i} = \frac{1}{1-\theta_i}; \quad \theta_i = \frac{b_i f_i}{1+b_i f_i} \tag{S52}$$

5.4 Isotherm inflections

MFI zeolite (also called silicalite-1) has a topology consisting of a set of intersecting straight channels, and zig-zag (or sinusoidal) channels of approximately 5.5 Å size. Preferential location of molecules within the MFI structural framework can cause strong isotherm inflections. For example, branched alkanes, benzene, alkyl benzenes, and cyclohexane prefer to locate at the channel intersections of MFI zeolite due to extra "leg-room" and other configurational considerations.[35] There are only 4 intersection sites available per unit cell of MFI. This implies that to obtain loadings higher than $\Theta_i = 4$ molecules per unit cell, an extra "push" will be required to locate the molecules elsewhere within the channels; this leads to isotherm inflection; see Figure S21(a). Due to strong isotherm inflections, the $1/\Gamma$ exhibits a cusp-like inflection at a loading of $\Theta_i = 4$ molecules/uc, when all the preferred adsorption sites are occupied; is demonstrated in the data on $1/\Gamma$ for iso-butane/MFI in Figure S21(b, c). In the range $0 < \Theta_i < 4$, $1/\Gamma$decreases nearly linearly with Θ_i signifying the fact that the vacancy *decreases* almost linearly with loading. For $\Theta_i > 4$, $1/\Gamma$ increases with Θ_i because additional sites *within* the MFI channels are created to accommodate more than 4 molecules per unit cell, i.e. the number of available sites *increases* within this loading range. These additional sites must be accommodated within the channels, requiring the additional "push" that caused the inflection. Also plotted in Figure S21(b, c) are the adsorption potential, $\pi A/RT$, and the occupancy $\theta = 1 - \exp\left(-\frac{\pi A}{q_{sat} RT}\right)$, as a function of the iso-butane loading. We note that there is a significant increase in $\pi A/RT$, and θ, at $\Theta_i \approx 4$ molecules per unit cell.

The cusp-like dependence of $1/\Gamma$ on the loading Θ_i causes the Maxwell-Stefan diffusivity, $Đ_i$, measured by Chmelik et al.[36], to also exhibit a corresponding cusp-like dependence; see Figure S21(d, e). Plotted as a function of the adsorption potential $\pi A/RT$ or occupancy $\theta = 1 - \exp\left(-\frac{\pi A}{q_{sat} RT}\right)$ leads to a reduction in the sharpness of the "valley" in the M-S diffusivity.

The length of an n-hexane molecule is commensurate with the distance between intersections of MFI zeolite (cf. snapshot in Figure S22). The n-heptane molecule, on the other hand, has a length that is slightly longer than the distance between channel intersections (cf. snapshot in Figure S22). CBMC simulations of the isotherms for nC7 in MFI show a distinct inflection at a loading at a loading of $\Theta_i = 4$ molecules/uc; see Figure S22(a). The isotherm inflections become increasing sharper for adsorption of nC8, nC9, and nC10. The isotherm inflections get reflected in cusp-like dependence of $1/\Gamma$ on the component loading; see Figure S22(b). It is interesting to note that the variation of $1/\Gamma$ with the corresponding occupancy $\theta = 1 - \exp\left(-\frac{\pi A}{q_{sat} RT}\right)$ is practically linear for nC6, nC7, nC8, mC9, and nC10; see Figure S22(c).

There are important consequences of plots in Figure S22(b,c) on the loading dependence of the M-S diffusivities of nC6 and nC7 in MFI zeolite; see plots of the experimental data of Jobic et al.[37] on the M-S diffusivity, $Đ_i$, of n-hexane (nC6) in MFI at 298 K presented in Figure S23. Plotted as a function of the loading Θ_i, expressed in molecules uc^{-1}, there is a slight inflection in the loading dependence at Θ_i = 4 molecules/uc. However, when the M-S diffusivity $Đ_i$ is plotted as a function of θ, the $Đ_i$ versus θ is practically linear, corresponding approximately with $Đ_i = Đ_i(0)(1-\theta)$.

The experimental data of Jobic et al.[37] on the M-S diffusivity, $Đ_i$, of n-heptane (nC7) in MFI at 298 K are presented in Figure S24. Due to the strong isotherm inflection for nC7, the plot of $Đ_i$ versus Θ_i, expressed in molecules uc^{-1}, shows a cusp-like inflection at Θ_i = 4 molecules/uc, analogous to that observed for iso-butane in Figure S21. However, when the M-S diffusivity $Đ_i$ is plotted as a function of θ, the cusp-like dependence on θ is far less prominent.

5.5 List of Tables for Unary Diffusion in Microporous Materials

Table S5. Dual-site Langmuir-Freundlich parameters for guest molecules in MFI at 300 K. To convert from molecules uc^{-1} to mol kg^{-1}, multiply by 0.173367.

	Site A			Site B		
	$\Theta_{A,sat}$ molecules uc^{-1}	b_A $\mathrm{Pa}^{-\nu_A}$	ν_A dimensionless	$\Theta_{B,sat}$ molecules uc^{-1}	b_B $\mathrm{Pa}^{-\nu_A}$	ν_B dimensionless
Ne	57	6.69E-11	1	42	1.70E-08	1
Ar	19	2.61E-07	1	15	6.75E-08	0.8
H2	30	3.57E-08	1	42	1.39E-09	1
N2	16	6.37E-07	1	16	3.82E-07	0.7
CO2	19	6.12E-06	1	11	1.73E-08	1
CH4	7	5.00E-09	1	16	3.10E-06	1
C2H6	3.3	4.08E-07	1	13	7.74E-05	1
C3H8	1.4	3.35E-04	0.67	10.7	6.34E-04	1.06
nC4H10	1.5	2.24E-03	0.57	8.7	9.75E-03	1.12
iso-C4H10	4	2.29E-02	1	6	2.87E-05	1
nC5H12	4	5.35E-02	1.537320948	4	2.28E-01	1
nC6H14	6.6	7.08E-01	0.83	1.4	1.66E+01	1.5
2MP	4	4.513	1.05	4	7.92E-05	1.13
3MP	4	1.59	1.08	4	1.36E-02	0.53
22DMB	4	3.55E-01	1			
nC7H16	4	1.14E+02	1.15	3	1.35E-02	1
nC8H18	4	7.05E+02	1.0	1.9	1.66E-02	0.36

nC9H20	4	1.03E+04	1	1	2.69E-02	0.36
nC10H22	4	1.61E+05	1	0.43	5.99E-02	0.36

Table S6. Dual-site Langmuir-Freundlich parameters for guest molecules in MFI at 363 K. To convert from molecules uc^{-1} to mol kg^{-1}, multiply by 0.173367.

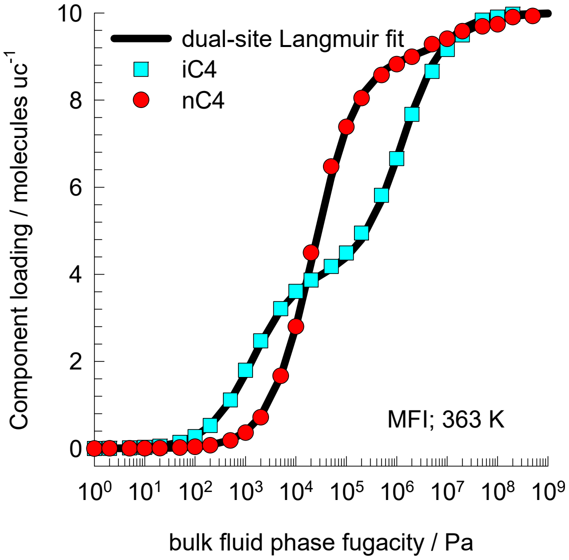

	Site A			Site B		
	$\Theta_{A,sat}$ molecules uc^{-1}	b_A $\mathrm{Pa}^{-\nu_A}$	ν_A dimensionless	$\Theta_{B,sat}$ molecules uc^{-1}	b_B $\mathrm{Pa}^{-\nu_B}$	ν_B dimensionless
nC4H10	1	6.2E-08	1	9	4.48E-05	1
isoC4H10	4	7.54E-04	1	6	8.02E-07	1

Table S7. Dual-site Langmuir-Freundlich parameters for guest molecules in MFI at 433 K. To convert from molecules uc^{-1} to mol kg^{-1}, multiply by 0.173367.

	Site A			Site B		
	$\Theta_{A,sat}$ molecules uc^{-1}	b_A $\mathrm{Pa}^{-\nu_A}$	ν_A dimensionless	$\Theta_{B,sat}$ molecules uc^{-1}	b_B $\mathrm{Pa}^{-\nu_B}$	ν_B dimensionless
nC5	4	6.26×10^{-6}	1.12	4	1.94×10^{-4}	1
2MB	4	1.69×10^{-4}	1	2	4.93×10^{-7}	1
Neo-pentane	4	1.24×10^{-4}	1			
nC6	3.2	2.21×10^{-8}	1.6	4.3	7.42×10^{-4}	1
2MP	4	7.85×10^{-4}	1.03			
3MP	4	4.22×10^{-4}	1.02	1	9.88×10^{-7}	1
22DMB	4	2.55×10^{-4}	1.02			
23DMB	4	4.59×10^{-4}	1.02			

Table S8. Dual-site Langmuir-Freundlich parameters for guest molecules in FAU (all-silica) at 300 K. To convert from molecules uc^{-1} to mol kg^{-1}, multiply by 0.086683044.

	Site A			Site B		
	$\Theta_{A,sat}$ molecules uc^{-1}	b_A $\mathrm{Pa}^{-\nu_A}$	ν_A dimensionless	$\Theta_{B,sat}$ molecules uc^{-1}	b_B $\mathrm{Pa}^{-\nu_A}$	ν_B dimensionless
Ne	158	4.39E-11	1	197	9.12E-09	1
Ar	40	1.00E-09	1	100	6.12E-08	1
Kr	53	2.67E-07	0.7	74	2.12E-07	1
H2	85	2.75E-08	1	100	1.03E-08	1
N2	60	1.53E-09	1	67	1.32E-07	1
CO2	32	2.55E-13	2.2	75	6.86E-07	1
CH4	56	2.78E-08	0.8	70	2.90E-07	1
C2H6	60	2.87E-06	1	60	1.00E-09	1
C3H8	40	1.34E-05	0.6	40	1.72E-06	1.27
isoC4H10	32	6.11E-07	1.7	14	2.23E-03	0.36
nC4H10	30	9.00E-07	1.7	15	2.36E-04	0.56
nC5H12	25	4.69E-07	2.4	20	7.26E-04	0.54

Table S9. Dual-site Langmuir-Freundlich parameters for guest molecules in NaY zeolite at 300 K. Per unit cell of NaY zeolite we have 144 Si, 48 Al, 48 Na+, with Si/Al=3. To convert from molecules uc^{-1} to mol kg^{-1}, multiply by 0.079448462.

	Site A			Site B		
	$\Theta_{A,sat}$ molecules uc^{-1}	b_A $\mathrm{Pa}^{-\nu_A}$	ν_A dimensionless	$\Theta_{B,sat}$ molecules uc^{-1}	b_B $\mathrm{Pa}^{-\nu_A}$	ν_B dimensionless
H2	140	6.32E-05	1	44	2.80E-08	1
CO2	76	4.04E-05	1	24	2.71E-05	0.66
CH4	66	3.77E-07	1.09	58	3.01E-06	0.68
C2H6	18	6.76E-09	1.8	41	1.08E-05	1
C3H8	13	5.68E-09	2.48	35	1.20E-04	1

Table S10. Dual-site Langmuir-Freundlich parameters for guest molecules in NaX zeolite at 300 K. Per unit cell of NaX zeolite we have 106 Si, 86 Al, 86 Na$^+$ with Si/Al=1.23. To convert from molecules uc^{-1} to mol kg^{-1}, multiply by 0.074524437.

	Site A			Site B		
	$\Theta_{A,sat}$ molecules uc^{-1}	b_A $\mathrm{Pa}^{-\nu_A}$	ν_A dimensionless	$\Theta_{B,sat}$ molecules uc^{-1}	b_B $\mathrm{Pa}^{-\nu_A}$	ν_B dimensionless
H2	140	6.32E-09	1	44	2.80E-08	1
N2	28	3.25E-09	1	59	9.98E-08	1
CO2	28	1.57E-04	0.7	59	4.26E-04	1
CH4	73	2.25E-06	1	29	1.56E-08	1
C2H6	64	1.88E-05	1	20	7.63E-07	0.65
C3H8	42	8.25E-05	1.3	17	1.09E-03	0.46

Table S11. Dual-site Langmuir-Freundlich parameters for guest molecules in AFI zeolite at 300 K. To convert from molecules uc^{-1} to mol kg^{-1}, multiply by 0.346732174.

	Site A			Site B		
	$\Theta_{A,sat}$ molecules uc^{-1}	b_A $\mathrm{Pa}^{-\nu_A}$	ν_A dimensionless	$\Theta_{B,sat}$ molecules uc^{-1}	b_B $\mathrm{Pa}^{-\nu_A}$	ν_B dimensionless
Ne	15	1.76E-08	1	19	8.1E-09	0.87
CH4	7	1.29E-06	0.97	5	1.91E-08	0.91
Ar	8	1.53E-07	1	4.5	1.99E-08	1

Table S12. Dual-site Langmuir-Freundlich parameters for guest molecules in LTA (all-silica) at 300 K. To convert from molecules uc^{-1} to mol kg^{-1}, multiply by 0.086683044.

	Site A			Site B		
	$\Theta_{A,sat}$ molecules uc^{-1}	b_A $\text{Pa}^{-\nu_A}$	ν_A dimensionless	$\Theta_{B,sat}$ molecules uc^{-1}	b_B $\text{Pa}^{-\nu_A}$	ν_B dimensionless
Ne	176	4.57E-11	1	180	1.20E-08	1
Ar	88	8.10E-08	1	60	1.57E-09	1
Kr	60	3.72E-07	0.77	60	1.55E-07	1.07
H2	88	2.55E-08	1	88	1.51E-08	1
N2	70	1.36E-07	1	60	5.03E-10	1
CO2	36	1.51E-05	0.54	85	2.06E-07	1.15
CH4	52	6.63E-08	0.82	65	3.77E-07	1

Table S13. Dual-site Langmuir-Freundlich parameters for guest molecules in CHA (all-silica) at 300 K. To convert from molecules uc^{-1} to mol kg^{-1}, multiply by 0.231154783.

	Site A			Site B		
	$\Theta_{A,sat}$ molecules uc^{-1}	b_A $\mathrm{Pa}^{-\nu_A}$	ν_A dimensionless	$\Theta_{B,sat}$ molecules uc^{-1}	b_B $\mathrm{Pa}^{-\nu_A}$	ν_B dimensionless
Ne	62	1.06E-08	1	53	4.73E-11	1
Ar	26	1.22E-07	1	14	4.62E-09	1
H2	63	2.58E-08	0.73	68	1.57E-08	1
N2	28	8.71E-08	0.6	32	4.87E-07	0.88
CO2	28	1.71E-06	1.1	12	8.74E-06	0.7
CH4	12	1.36E-06	1	24	4.59E-07	0.8

Table S14. Dual-site Langmuir-Freundlich parameters for guest molecules in DDR (all-silica) at 300 K. To convert from molecules uc^{-1} to mol kg^{-1}, multiply by 0.069346435.

	Site A			Site B		
	$\Theta_{A,sat}$ molecules uc^{-1}	b_A $\mathrm{Pa}^{-\nu_A}$	ν_A dimensionless	$\Theta_{B,sat}$ molecules uc^{-1}	b_B $\mathrm{Pa}^{-\nu_A}$	ν_B dimensionless
Ne	98	1.56E-08	1	90	6.79E-11	1
Ar	38	2.57E-07	1	40	2.09E-09	1
CO2	21.630528	2.32E-06	0.74	43.261056	5.89E-06	1
CH4	23.0725632	3.46E-06	1	34.6088448	3.41E-06	0.65

Table S15. Dual-site Langmuir-Freundlich parameters for guest molecules in ISV (all-silica) at 300 K. To convert from molecules uc^{-1} to mol kg^{-1}, multiply by 0.260049131.

	Site A			Site B		
	$\Theta_{A,sat}$ molecules uc^{-1}	b_A $\mathrm{Pa}^{-\nu_A}$	ν_A dimensionless	$\Theta_{B,sat}$ molecules uc^{-1}	b_B $\mathrm{Pa}^{-\nu_A}$	ν_B dimensionless
CH4	17	9.31E-07	1	21	1.93E-07	0.61
C2H6	16	1.46E-03	0.21	13	1.59E-05	1

Table S16. Dual-site Langmuir-Freundlich parameters for guest molecules in BEA (all-silica) at 300 K. To convert from molecules uc^{-1} to mol kg^{-1}, multiply by 0.260049131.

	Site A			Site B		
	$\Theta_{A,sat}$ molecules uc^{-1}	b_A $\mathrm{Pa}^{-\nu_A}$	ν_A dimensionless	$\Theta_{B,sat}$ molecules uc^{-1}	b_B $\mathrm{Pa}^{-\nu_A}$	ν_B dimensionless
Ar	15	1.58E-07	1	15	2.98E-08	1
CH4	17	2.12E-08	1	14	1.14E-06	1
C3H8	3.3	4.08E-07	1	13	7.74E-05	1

Table S17. Dual-site Langmuir-Freundlich parameters for guest molecules in IRMOF-1 at 300 K. To convert from molecules uc^{-1} to mol kg^{-1}, multiply by 0.162395981.

	Site A			Site B		
	$\Theta_{A,sat}$ molecules uc^{-1}	b_A $\mathrm{Pa}^{-\nu_A}$	ν_A dimensionless	$\Theta_{B,sat}$ molecules uc^{-1}	b_B $\mathrm{Pa}^{-\nu_A}$	ν_B dimensionless
Ne	342	1.31E-08	1	270	9.66E-11	1
Ar	236	5.56E-08	1	115	5.25E-08	0.75
H2	211	5.00E-10	1	303	1.44E-08	1
N2	160	6.82E-09	0.85	160	7.52E-08	1
CO2	200	1.01E-06	0.66	177	5.82E-10	1.5
CH4	60	1.69E-16	1.8	177	1.26E-07	1.03
C2H6	78	1.66E-06	1	54	2.32E-16	2.9
C3H8	60	1.86E-12	2.6	42	1.17E-05	1
nC4H10	32	6.66E-05	1	50	2.23E-27	7.5
nC5H12	19	4.69E-04	1	50	5.13E-29	10.7
nC6H14	12	3.35E-03	1	46	2.27E-36	19.7

Table S18. Dual-site Langmuir-Freundlich parameters for guest molecules in MgMOF-74 at 300 K. To convert from molecules uc^{-1} to mol kg^{-1}, multiply by 0.457959224.

	Site A			Site B		
	$\Theta_{A,sat}$ molecules uc^{-1}	b_A $\mathrm{Pa}^{-\nu_A}$	ν_A dimensionless	$\Theta_{B,sat}$ molecules uc^{-1}	b_B $\mathrm{Pa}^{-\nu_A}$	ν_B dimensionless
H2	31	7.73E-09	1	31	3.05E-08	1
CO2	28	2.05E-05	1	12	3.03E-07	1
N2	25	2.93E-07	1	20	6.06E-09	1
CH4	32	6.24E-07	1	8	2.71E-17	2

Table S19. Dual-site Langmuir-Freundlich parameters for guest molecules in CuBTC at 300 K. To convert from molecules uc^{-1} to mol kg^{-1}, multiply by 0.103360722.

	Site A			Site B		
	$\Theta_{A,sat}$ molecules uc^{-1}	b_A $\mathrm{Pa}^{-\nu_A}$	ν_A dimensionless	$\Theta_{B,sat}$ molecules uc^{-1}	b_B $\mathrm{Pa}^{-\nu_A}$	ν_B dimensionless
Ne	300	8.45E-09	0.8	300	1.57E-08	1
Ar	202	2.51E-07	0.96	95	3.87E-08	0.76
H2	282	5.86E-09	0.78	346	1.25E-08	1
CO2	38	3.68E-06	0.71	167	1.97E-06	1
CH4	171	1.29E-06	0.91	58	4.87E-07	0.66
C2H6	43	4E-06	0.64	118	5.46E-05	0.82
C3H8	27	3.87E-04	0.4	86	1.14E-06	1.5
nC4H10	14	2.59E-19	6.3	69	2.23E-03	0.86

5.6 List of Figures for Unary Diffusion in Microporous Materials

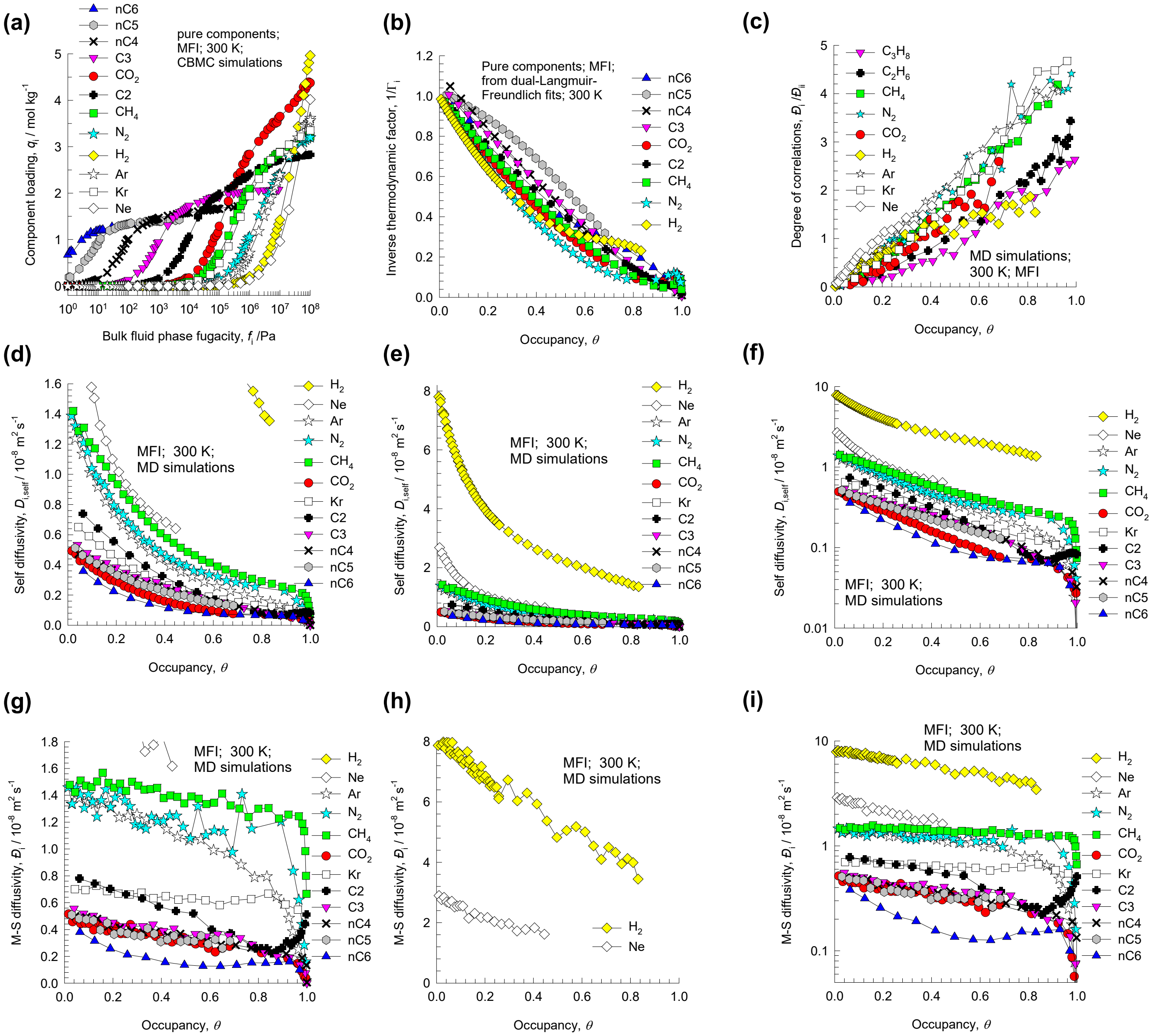

Figure S7. (a-i) CBMC simulations of unary adsorption isotherms, along with MD simulations of unary self-diffusivities, $D_{i,self}$, and Maxwell-Stefan diffusivities, $Đ_i$, for a variety of guest molecules in MFI zeolite at 300 K. The M-S diffusivity data is plotted as function of the occupancy, determined from Equation (S14), where the saturation capacity is determined from the unary isotherm fits.

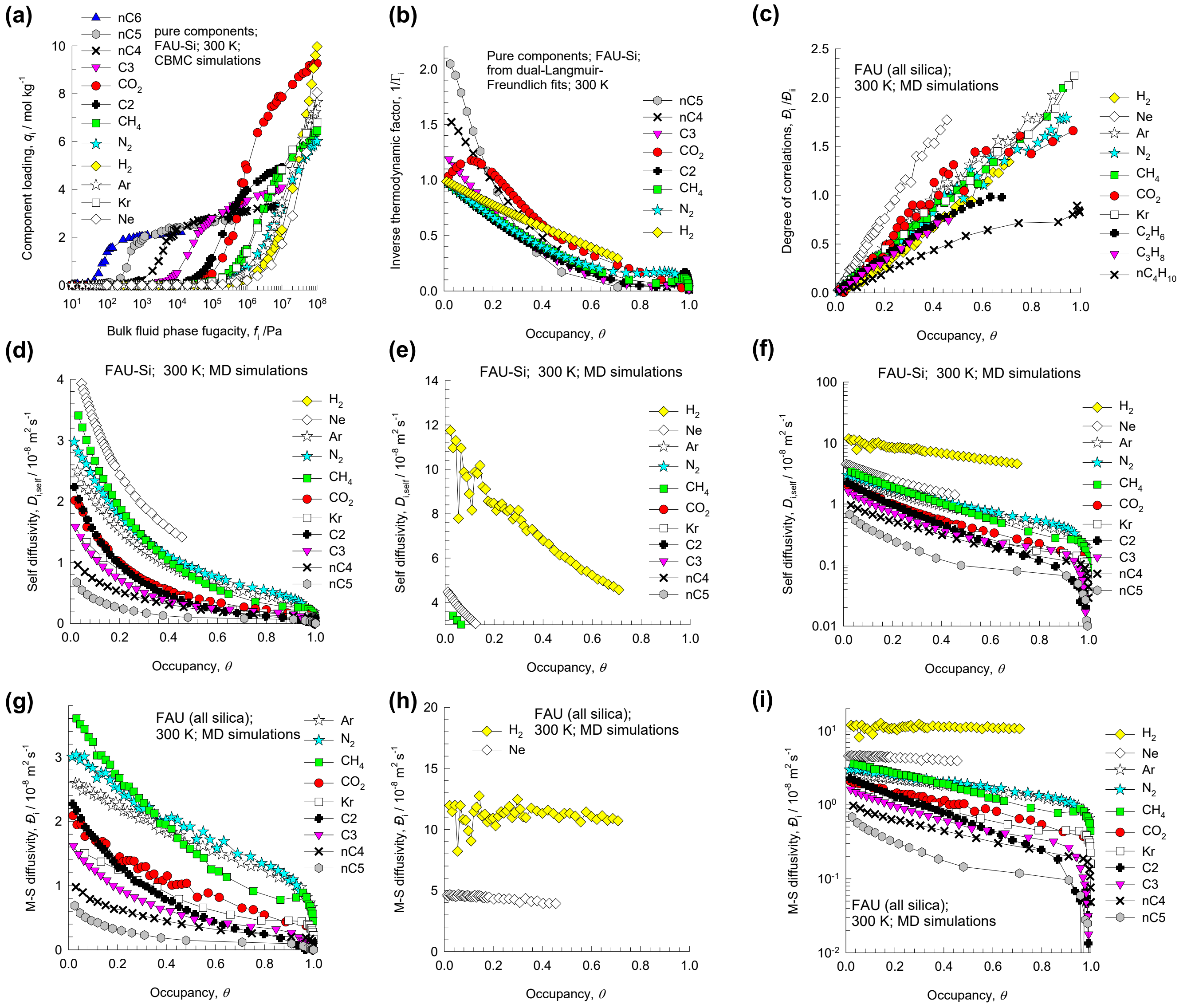

Figure S8. (a-i) CBMC simulations of unary adsorption isotherms, along with MD simulations of unary self-diffusivities, $D_{i,self}$, and Maxwell-Stefan diffusivities, $Đ_i$, for a variety of guest molecules in FAU all-silica zeolite at 300 K. The M-S diffusivity data is plotted as function of the occupancy, determined from Equation (S14), where the saturation capacity is determined from the unary isotherm fits.

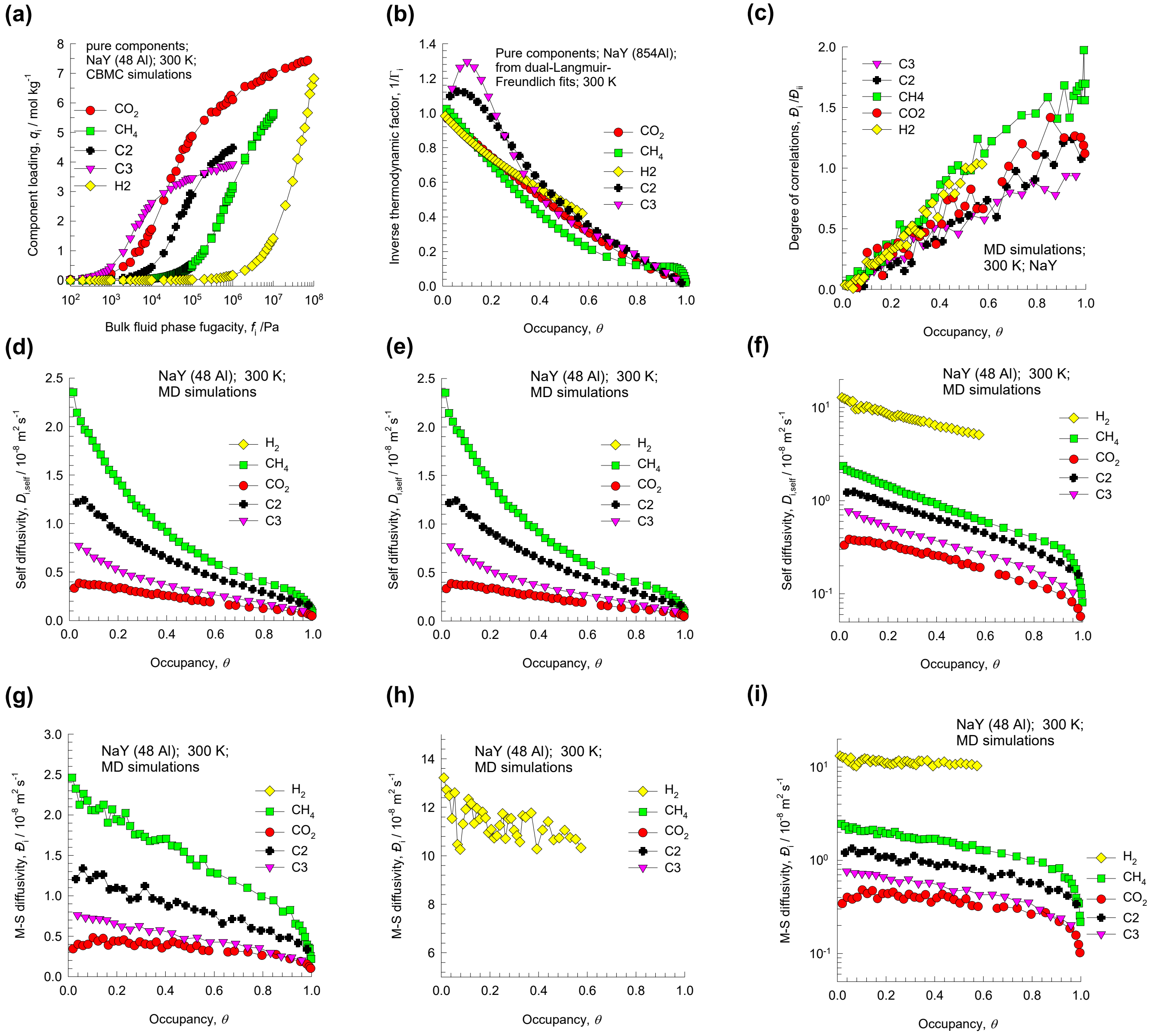

Figure S9. (a-i) CBMC simulations of unary adsorption isotherms, along with MD simulations of unary self-diffusivities, $D_{i,self}$, and Maxwell-Stefan diffusivities, $Đ_i$, for a variety of guest molecules in NaY zeolite with 48 Al atoms per unit cell at 300 K. The M-S diffusivity data is plotted as function of the occupancy, determined from Equation (S14), where the saturation capacity is determined from the unary isotherm fits.

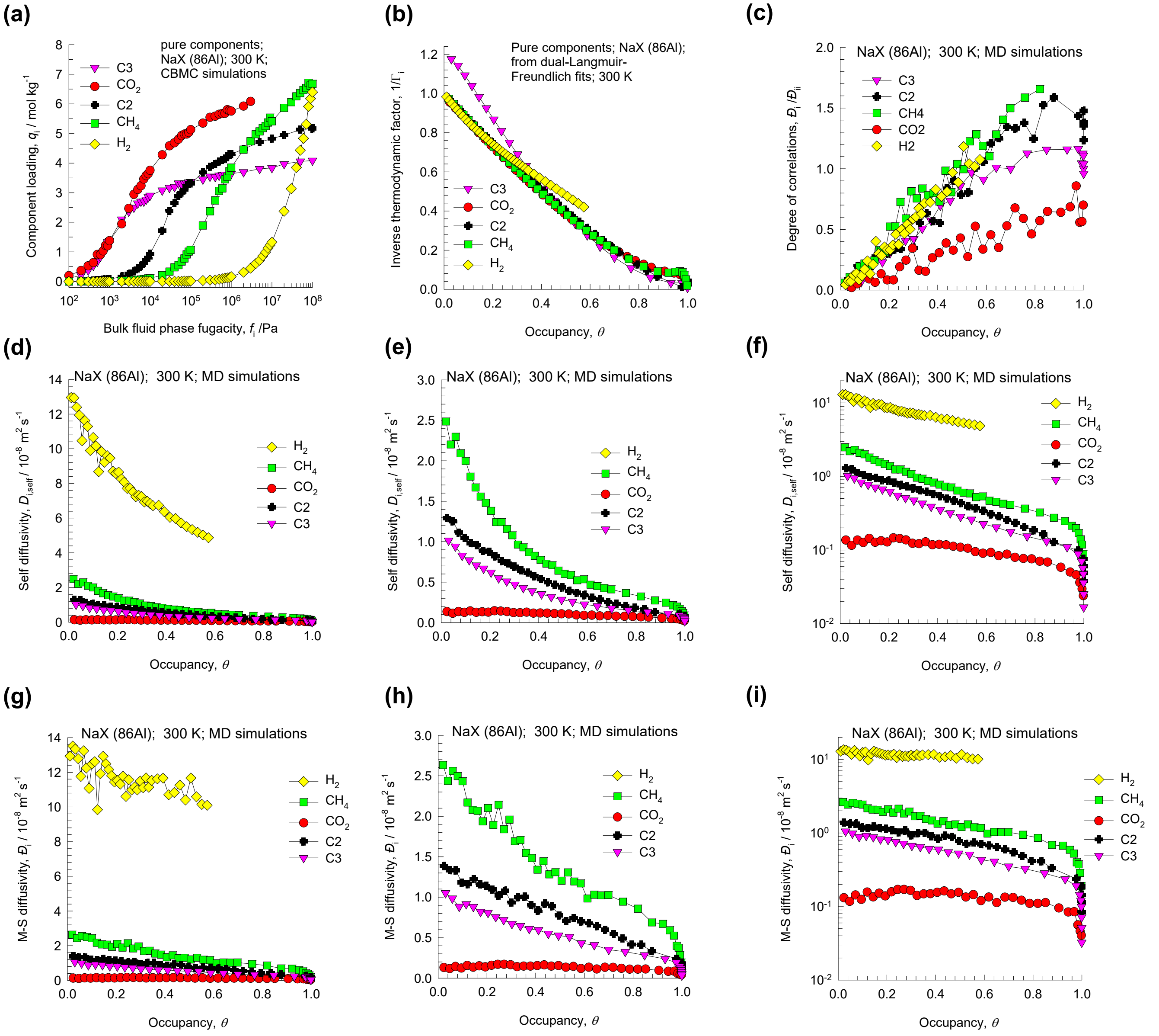

Figure S10. (a-i) CBMC simulations of unary adsorption isotherms, along with MD simulations of unary self-diffusivities, $D_{i,self}$, and Maxwell-Stefan diffusivities, $Đ_i$, for a variety of guest molecules in NaX zeolite with 86 Al atoms per unit cell at 300 K. The M-S diffusivity data is plotted as function of the occupancy, determined from Equation (S14), where the saturation capacity is determined from the unary isotherm fits.

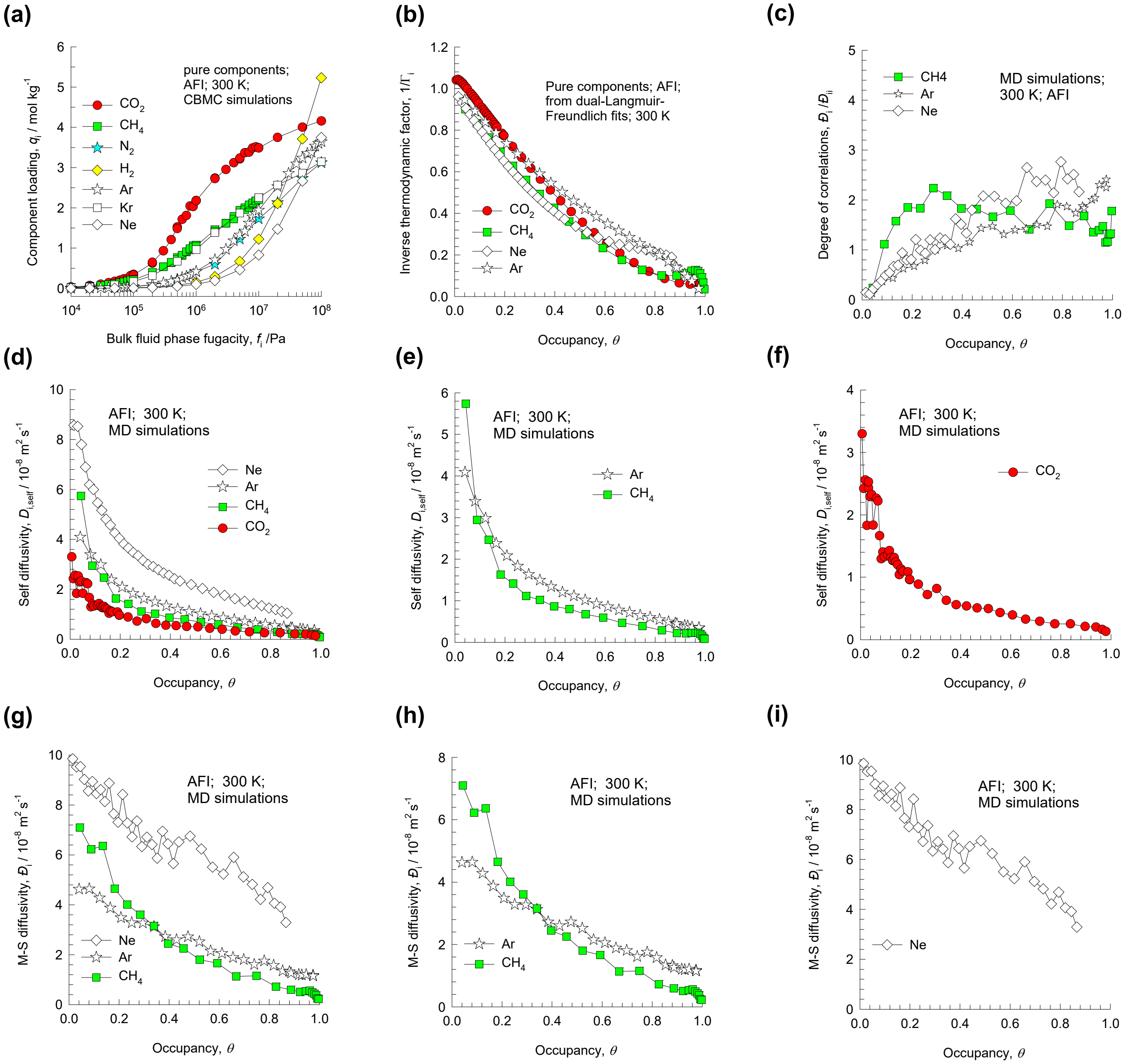

Figure S11. (a-i) CBMC simulations of unary adsorption isotherms, along with MD simulations of unary self-diffusivities, $D_{i,self}$, and Maxwell-Stefan diffusivities, $Đ_i$, for a variety of guest molecules in AFI all-silica zeolite at 300 K. The M-S diffusivity data is plotted as function of the occupancy, determined from Equation (S14), where the saturation capacity is determined from the unary isotherm fits.

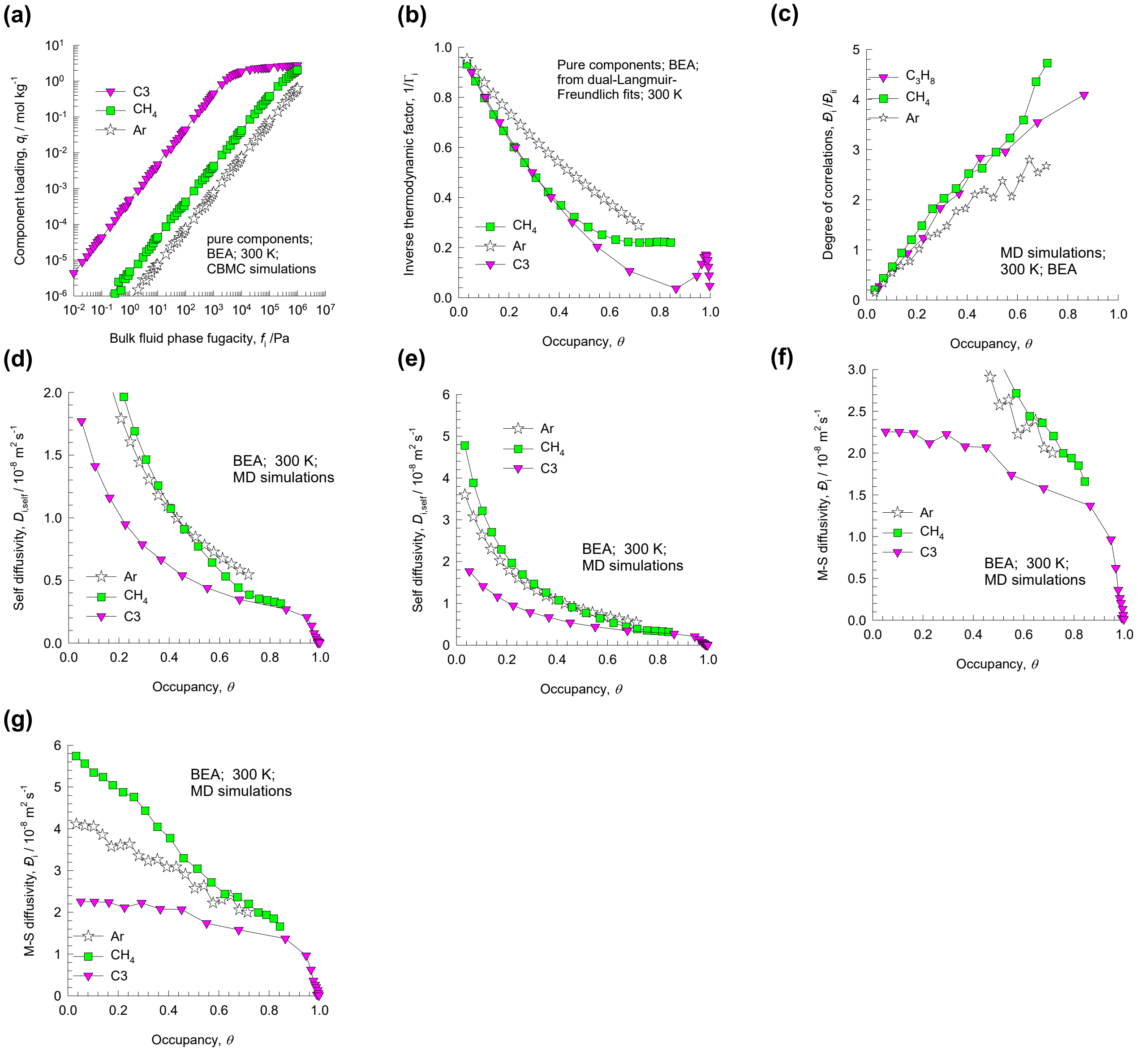

Figure S12. (a-g) CBMC simulations of unary adsorption isotherms, along with MD simulations of unary self-diffusivities, $D_{i,self}$, and Maxwell-Stefan diffusivities, $Đ_i$, for a variety of guest molecules in BEA all-silica zeolite at 300 K. The M-S diffusivity data is plotted as function of the occupancy, determined from Equation (S14), where the saturation capacity is determined from the unary isotherm fits.

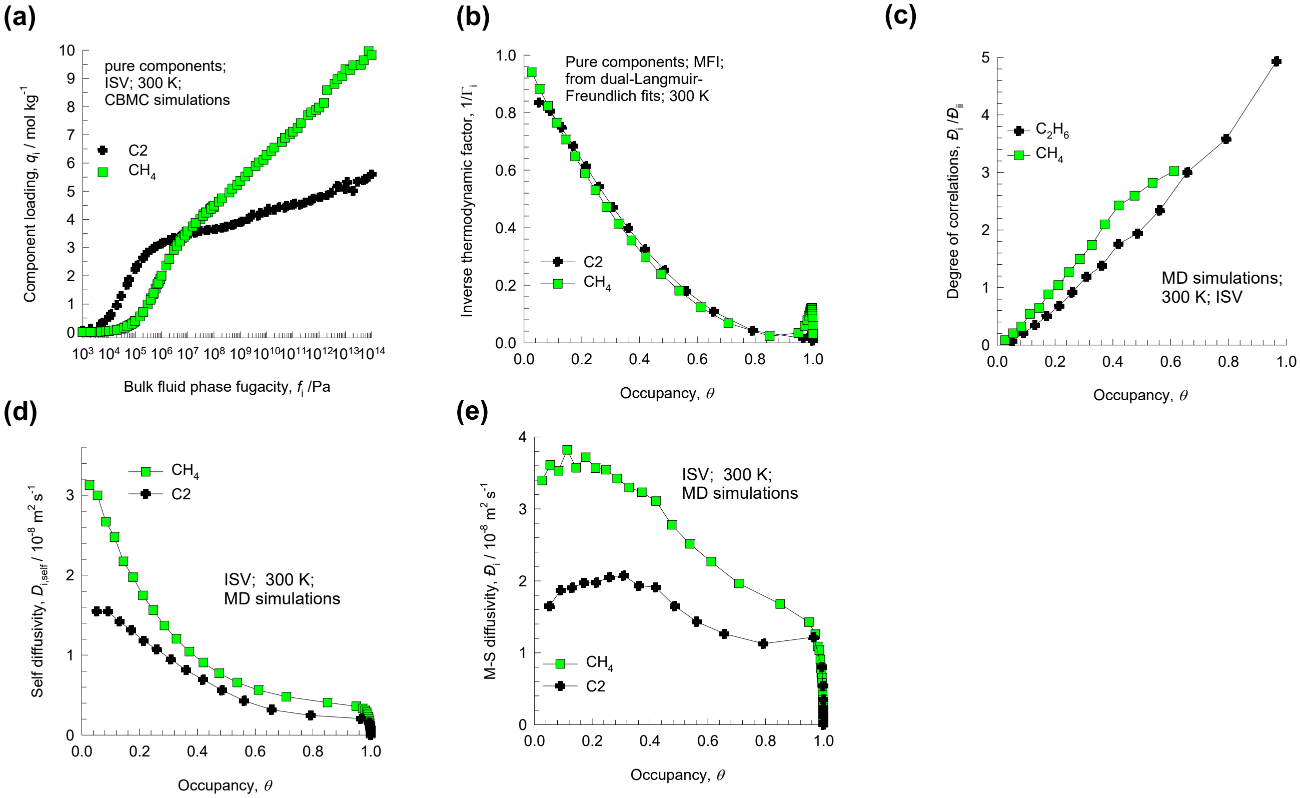

Figure S13. (a-e) CBMC simulations of unary adsorption isotherms, along with MD simulations of unary self-diffusivities, $D_{i,self}$, and Maxwell-Stefan diffusivities, $Đ_i$, for a variety of guest molecules in ISV all-silica zeolite at 300 K. The M-S diffusivity data is plotted as function of the occupancy, determined from Equation (S14), where the saturation capacity is determined from the unary isotherm fits.

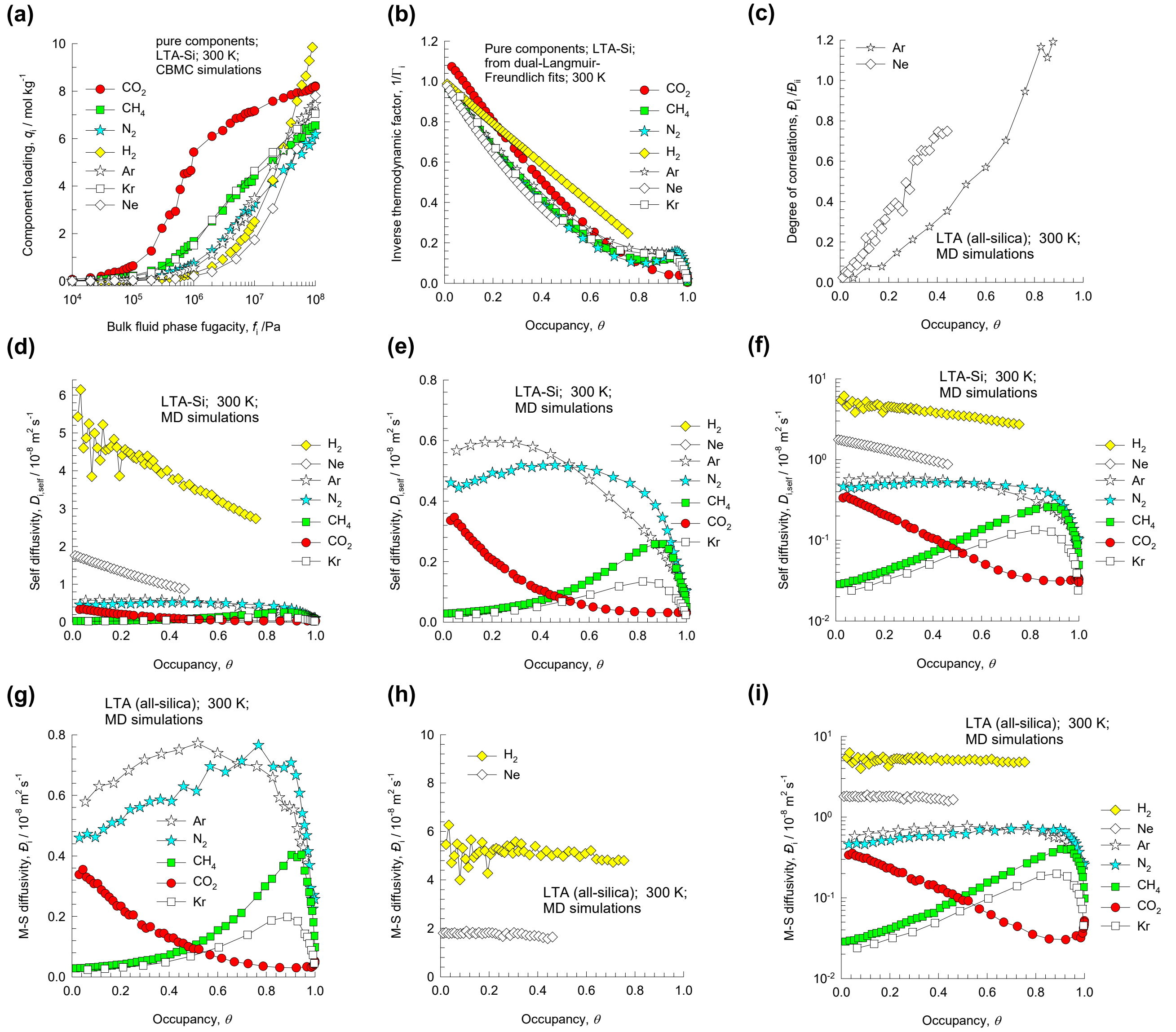

Figure S14. (a-i) CBMC simulations of unary adsorption isotherms, along with MD simulations of unary self-diffusivities, $D_{i,self}$, and Maxwell-Stefan diffusivities, $Đ_i$, for a variety of guest molecules in LTA all-silica zeolite at 300 K. The M-S diffusivity data is plotted as function of the occupancy, determined from Equation (S14), where the saturation capacity is determined from the unary isotherm fits.

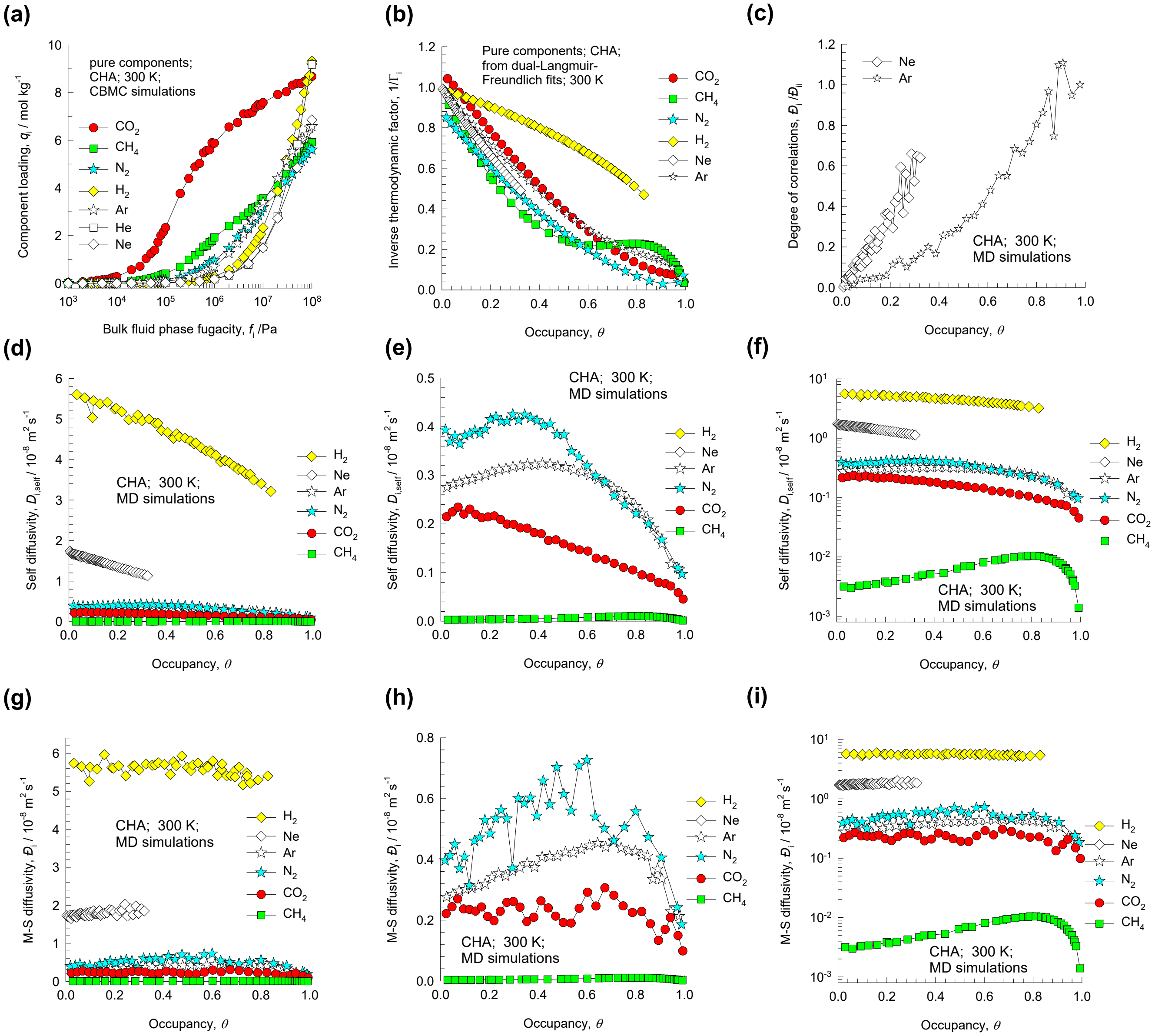

Figure S15. (a-i) CBMC simulations of unary adsorption isotherms, along with MD simulations of unary self-diffusivities, $D_{i,self}$, and Maxwell-Stefan diffusivities, $Đ_i$, for a variety of guest molecules in CHA all-silica zeolite at 300 K. The M-S diffusivity data is plotted as function of the occupancy, determined from Equation (S14), where the saturation capacity is determined from the unary isotherm fits.

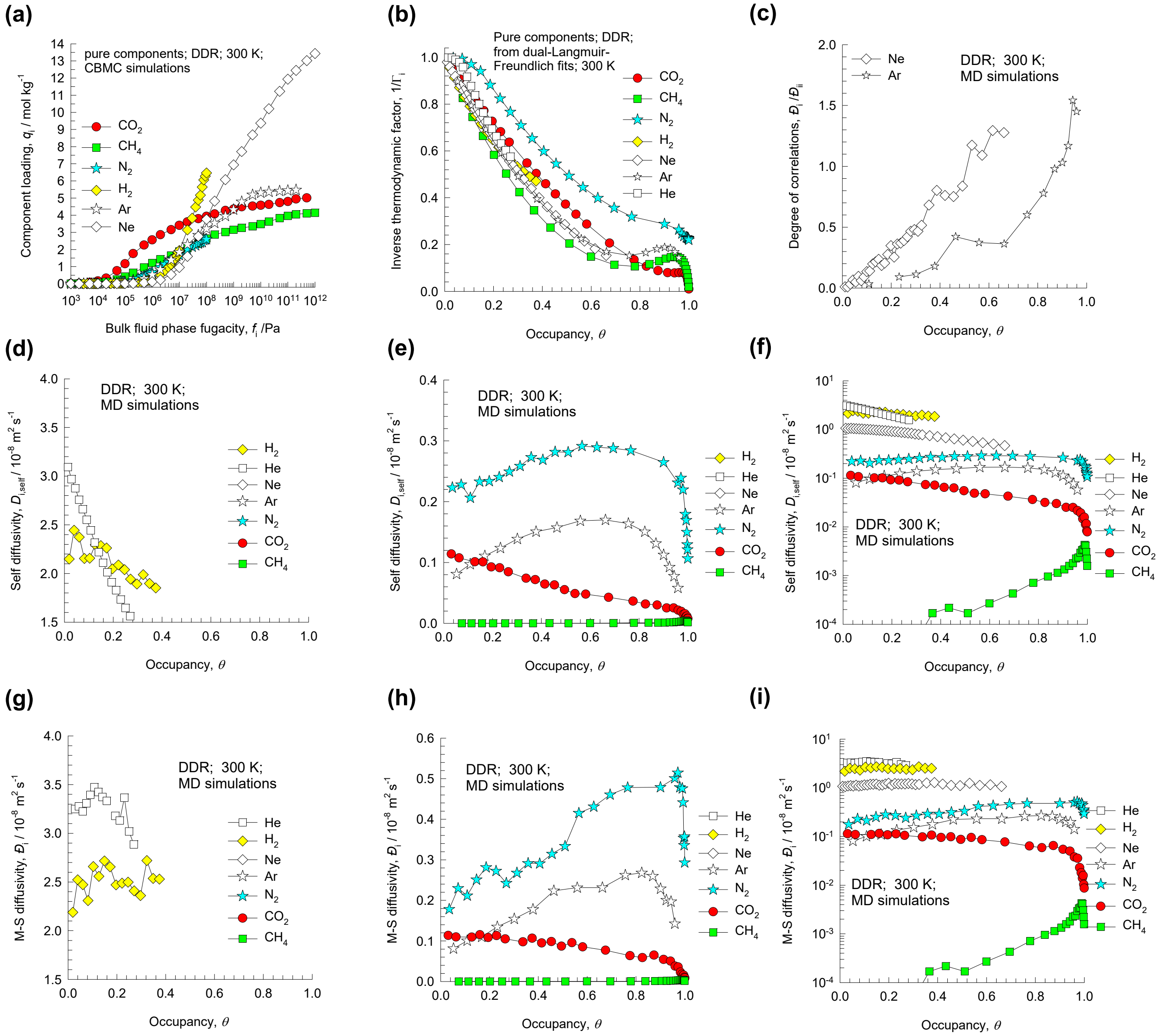

Figure S16. (a-i) CBMC simulations of unary adsorption isotherms, along with MD simulations of unary self-diffusivities, $D_{i,self}$, and Maxwell-Stefan diffusivities, $Đ_i$, for a variety of guest molecules in DDR all-silica zeolite at 300 K. The M-S diffusivity data is plotted as function of the occupancy, determined from Equation (S14), where the saturation capacity is determined from the unary isotherm fits.

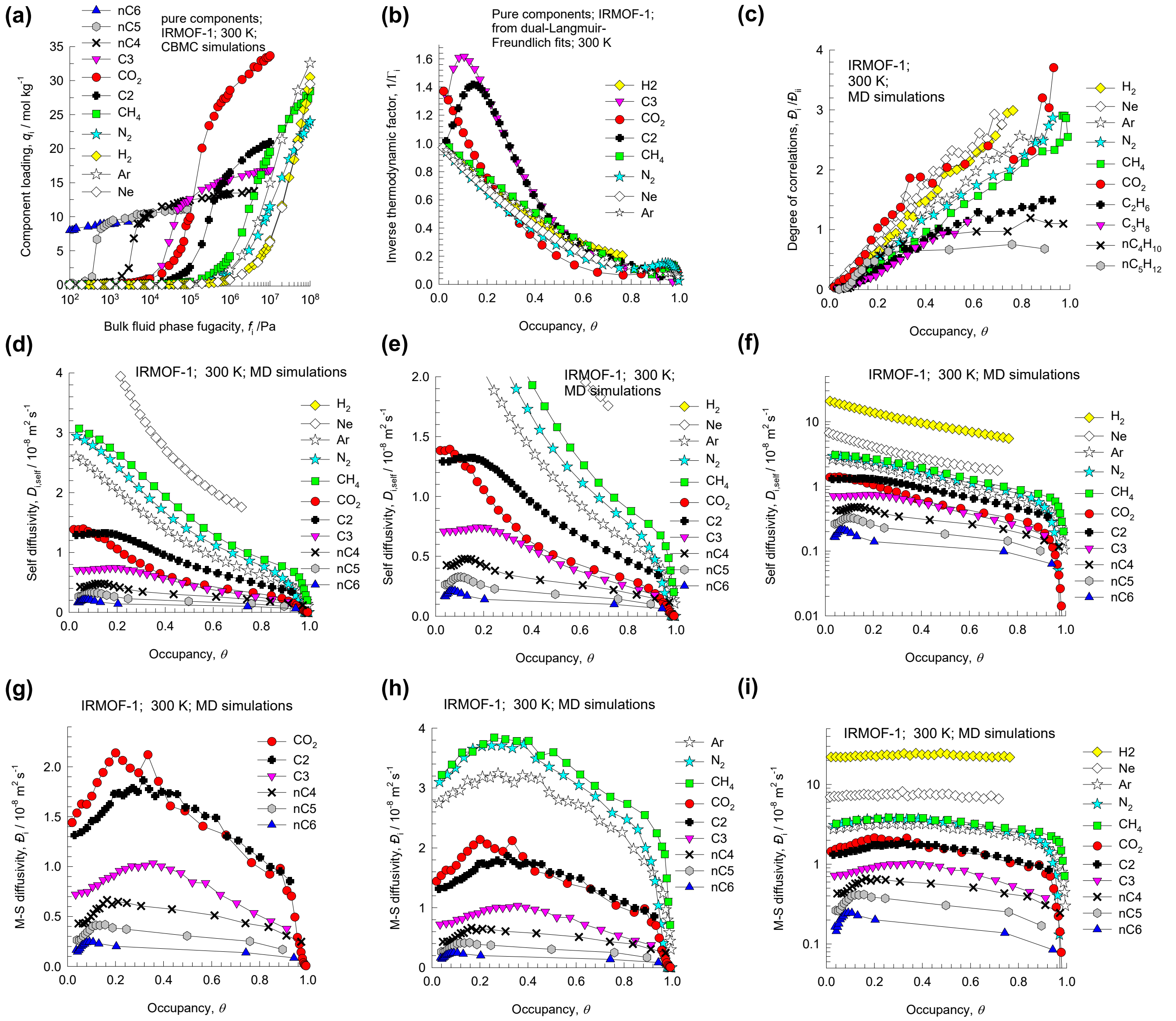

Figure S17. (a-i) CBMC simulations of unary adsorption isotherms, along with MD simulations of unary self-diffusivities, $D_{i,self}$, and Maxwell-Stefan diffusivities, $Đ_i$, for a variety of guest molecules in IRMOF-1 at 300 K. The M-S diffusivity data is plotted as function of the occupancy, determined from Equation (S14), where the saturation capacity is determined from the unary isotherm fits.

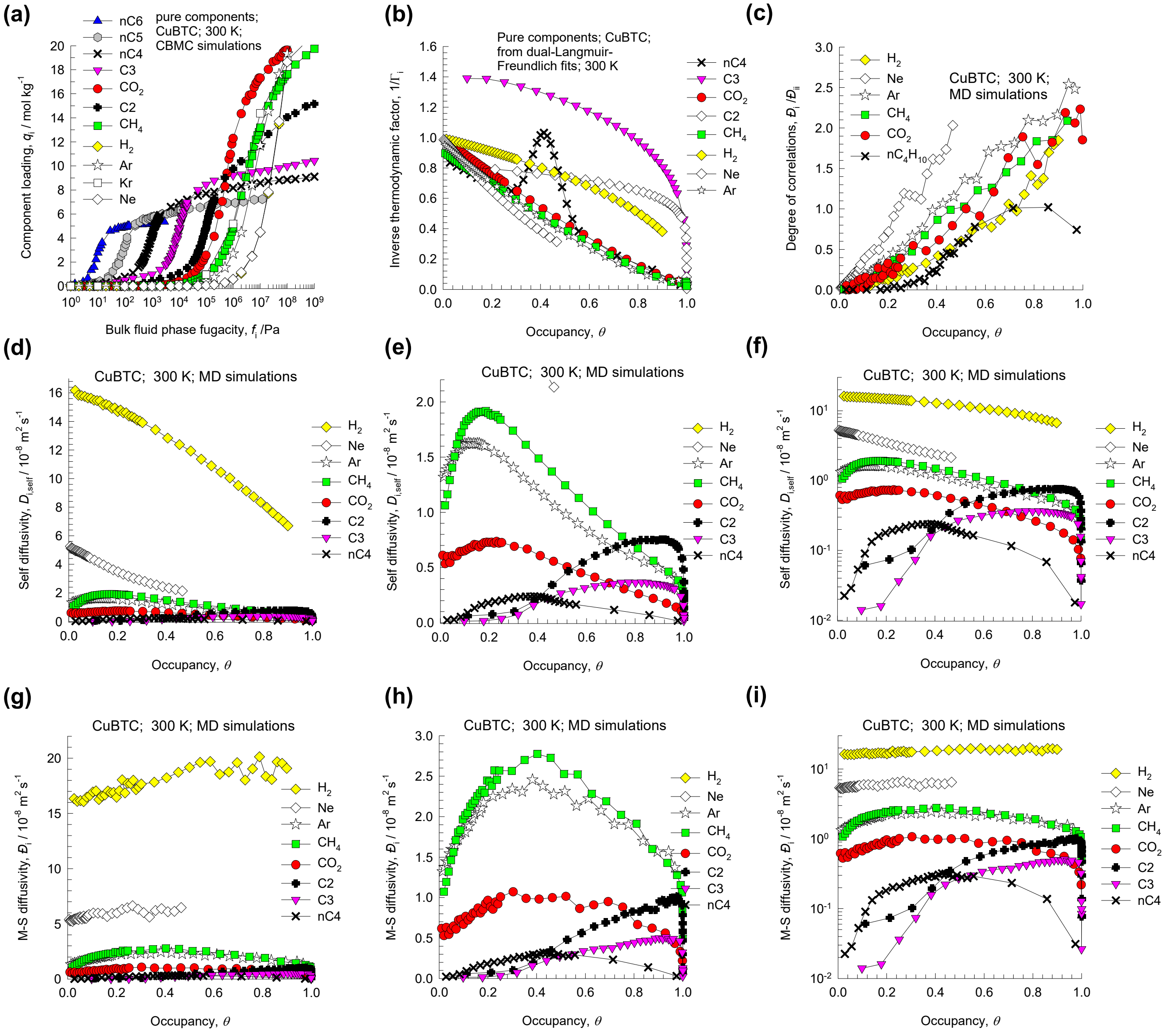

Figure S18. (a-i) CBMC simulations of unary adsorption isotherms, along with MD simulations of unary self-diffusivities, $D_{i,self}$, and Maxwell-Stefan diffusivities, $Đ_i$, for a variety of guest molecules in CuBTC at 300 K. The M-S diffusivity data is plotted as function of the occupancy, determined from Equation (S14), where the saturation capacity is determined from the unary isotherm fits.

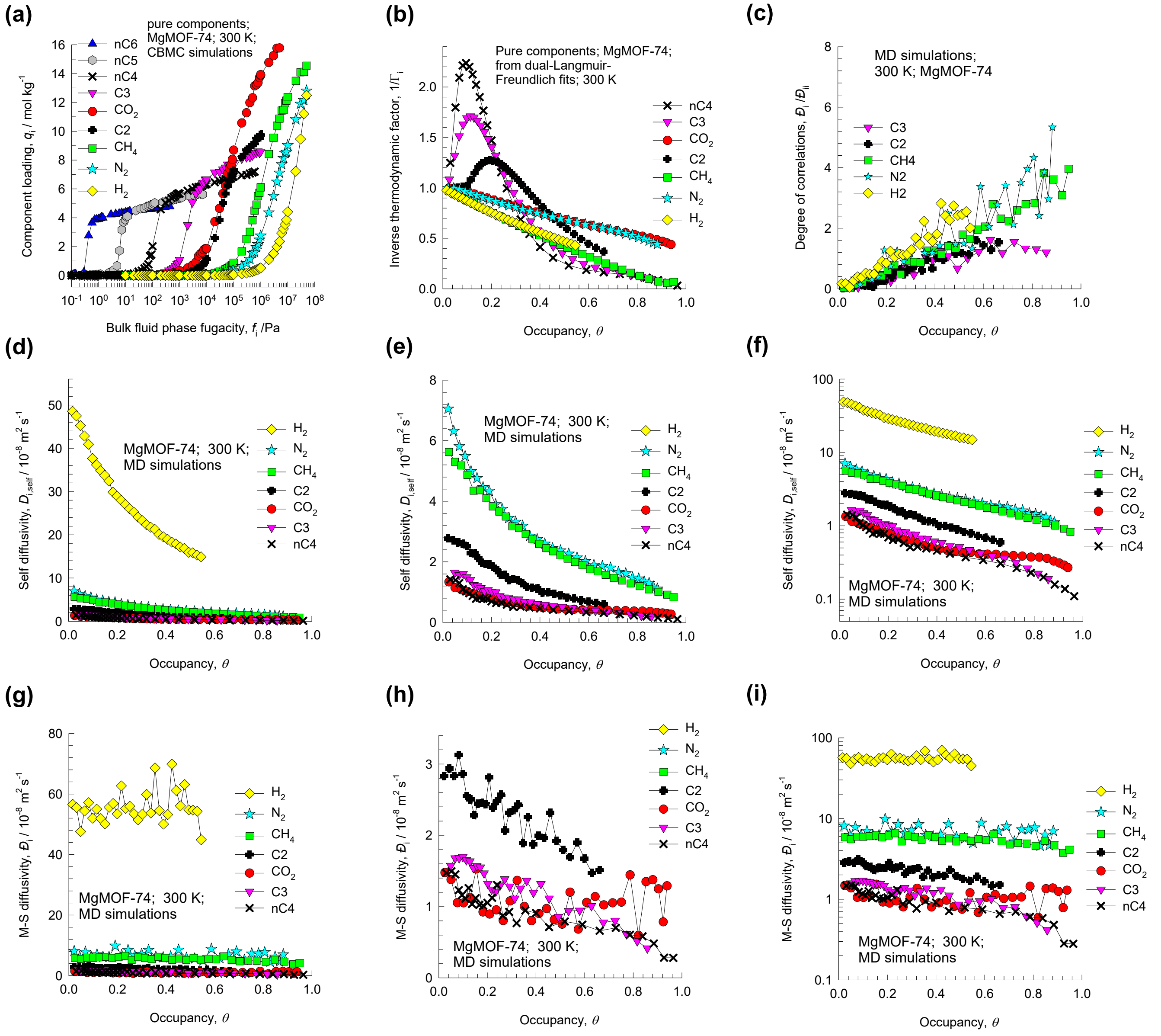

Figure S19. (a-i) CBMC simulations of unary adsorption isotherms, along with MD simulations of unary self-diffusivities, $D_{i,self}$, and Maxwell-Stefan diffusivities, $Đ_i$, for a variety of guest molecules in MgMOF-74 at 300 K. The M-S diffusivity data is plotted as function of the occupancy, determined from Equation (S14), where the saturation capacity is determined from the unary isotherm fits.

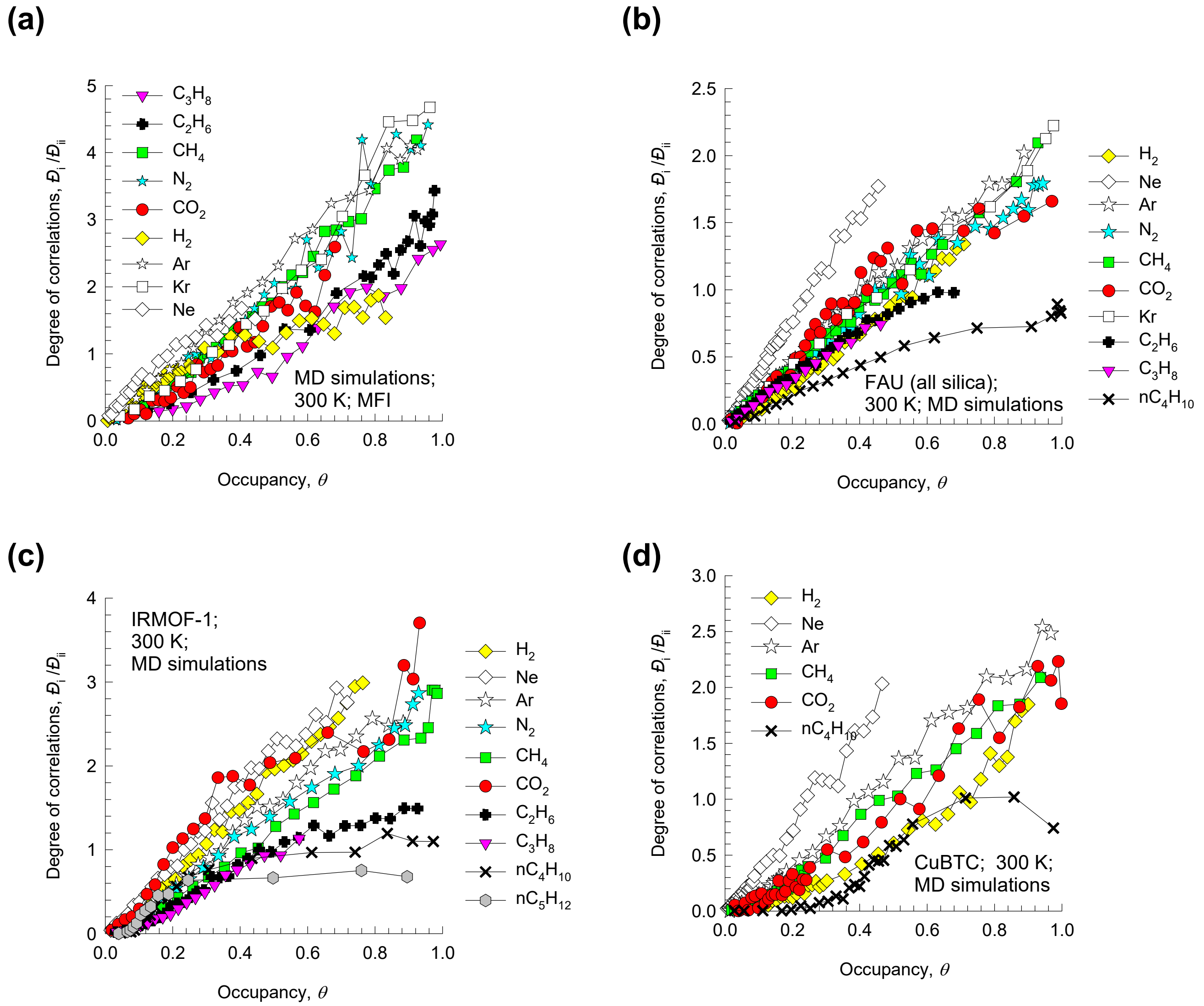

Figure S20. (a-d) The degree of correlations, $Đ_i/Đ_{ii}$, for unary diffusion of a variety of guest molecules in (a) MFI, (b) all-silica FAU, (c) IRMOF-1, and (d) CuBTC as a function of the occupancy, determined from Equation (S14), where the saturation capacity is determined from the unary isotherm fits.

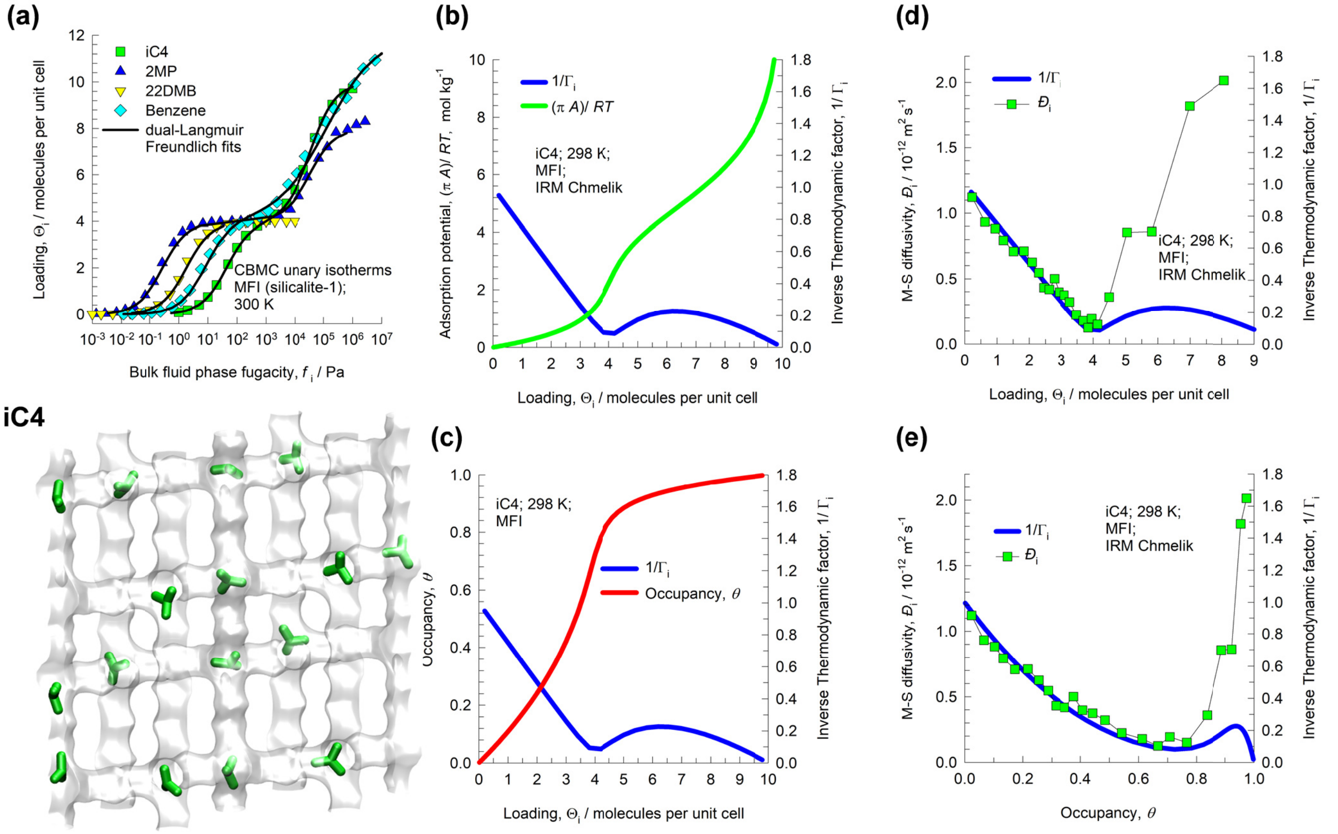

Figure S21. (a) CBMC simulations of unary adsorption isotherms for branched alkanes, and benzene in MFI zeolite at 300 K. (b, c) adsorption potential, $\pi A/RT$, and occupancy, θ, plotted as a function of the loading in molecules per unit cell. (d, e) Experimental data[36] on the M-S diffusivity, $Đ_i$, of iso-butane in MFI at 298 K as a function of (d) loading Θ_i, expressed in molecules uc^{-1}, and (e) occupancy, determined from Equation (S14), where the saturation capacity is determined from the unary isotherm fits. The right hand side of the Figures (b, c, d, e) are the calculations of the inverse thermodynamic factors, using the dual-site Langmuir-Freundlich isotherm fits.

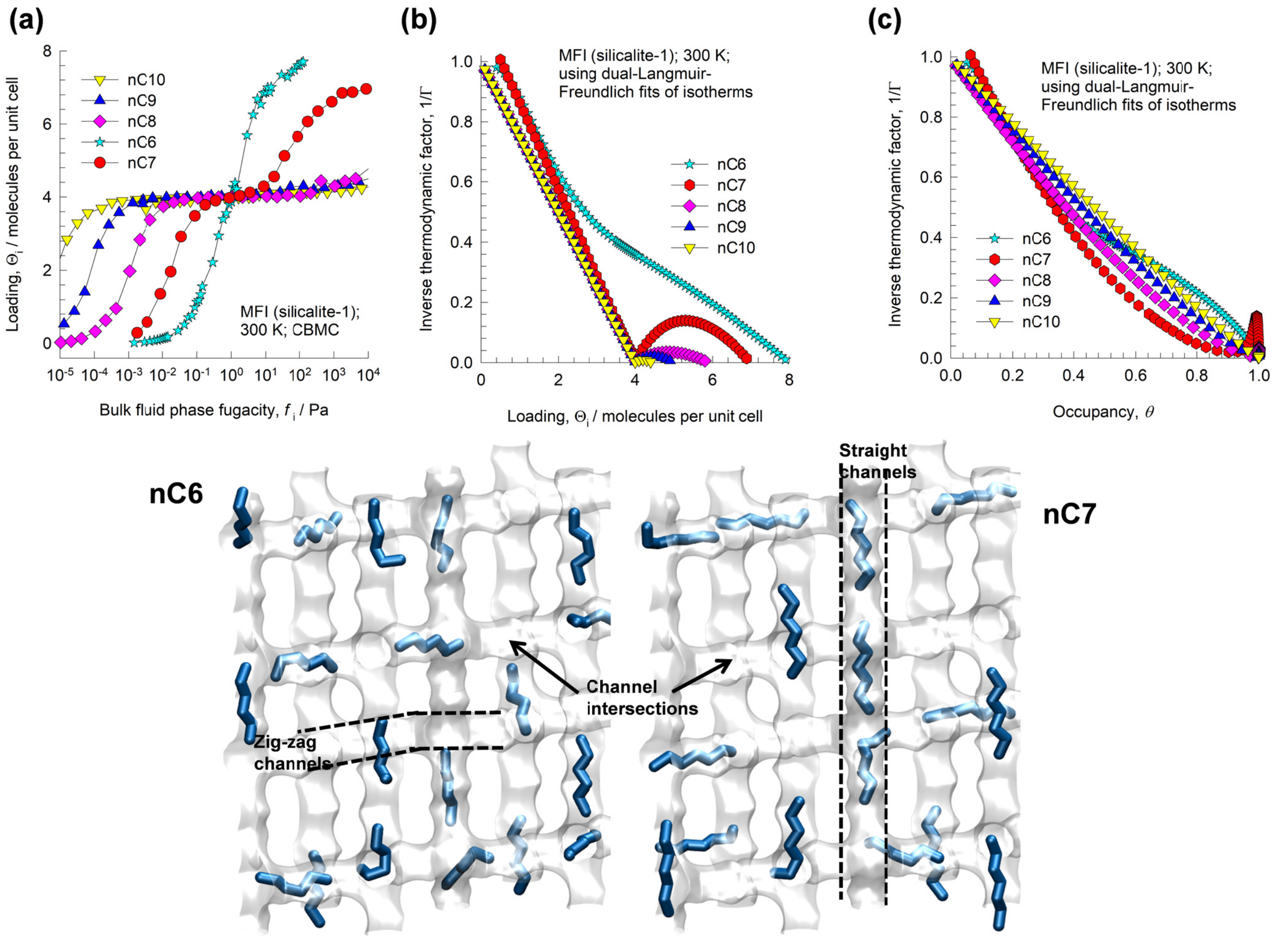

Figure S22. (a) CBMC simulations of unary adsorption isotherms for linear alkanes, nC6, nC7, nC8, nC9, and nC10 in MFI zeolite at 300 K. (b, c) Calculations of the inverse thermodynamic factors, using the dual-site Langmuir-Freundlich isotherm fits, plotted as a function of (b) loading Θ_i, expressed in molecules uc^{-1}, and (c) occupancy, θ, determined from Equation (S14), where the saturation capacity is determined from the unary isotherm fits.

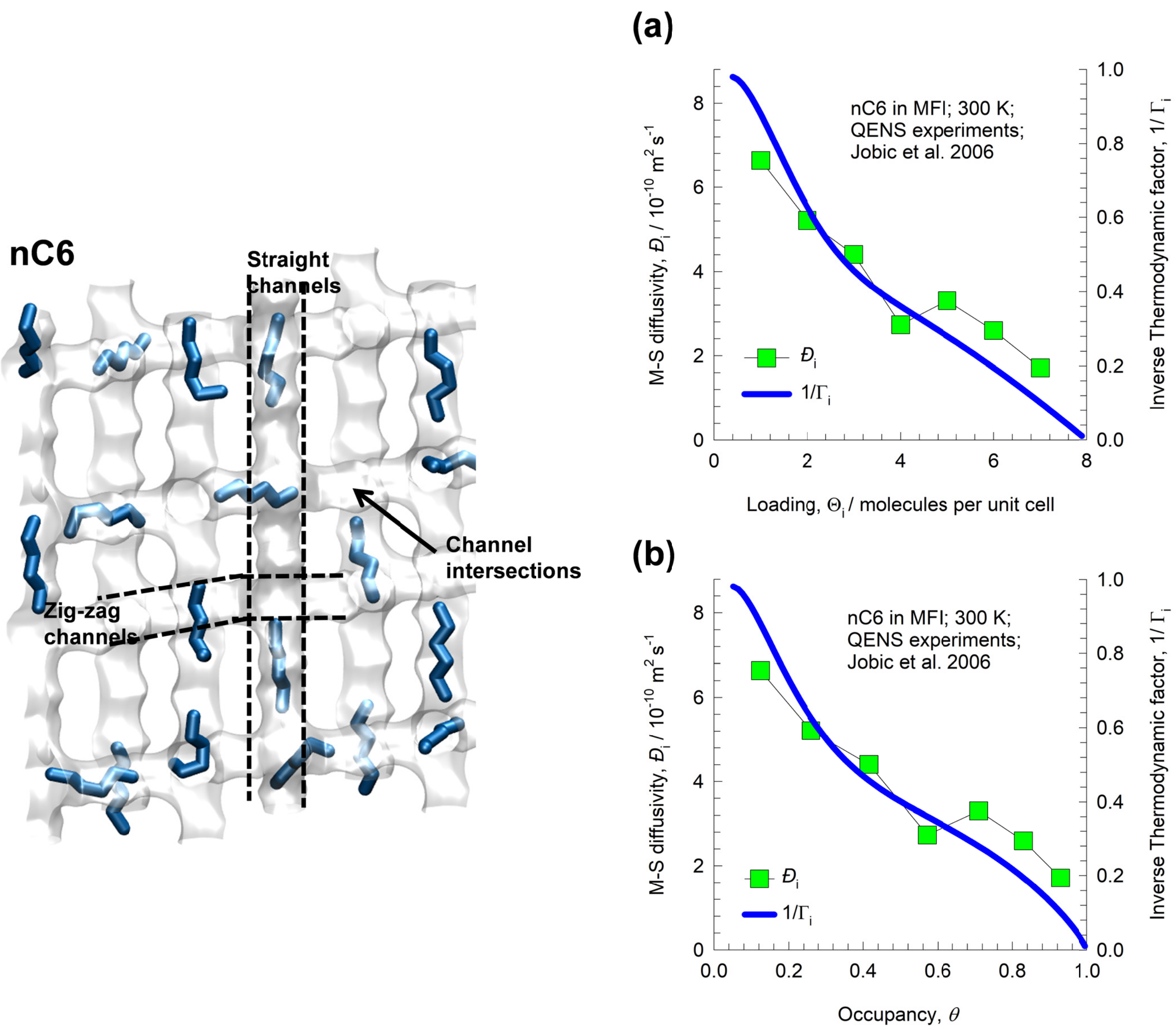

Figure S23. (a, b) Experimental data of Jobic et al.[37] on the M-S diffusivity, $Đ_\mathrm{i}$, of n-hexane (nC6) in MFI at 298 K as a function of (a) loading Θ_i, expressed in molecules uc^{-1}, and (b) occupancy, θ, determined from Equation (S14), where the saturation capacity is determined from the unary isotherm fits. The right hand side of the Figures (a, b) are the calculations of the inverse thermodynamic factors, using the dual-site Langmuir-Freundlich isotherm fits.

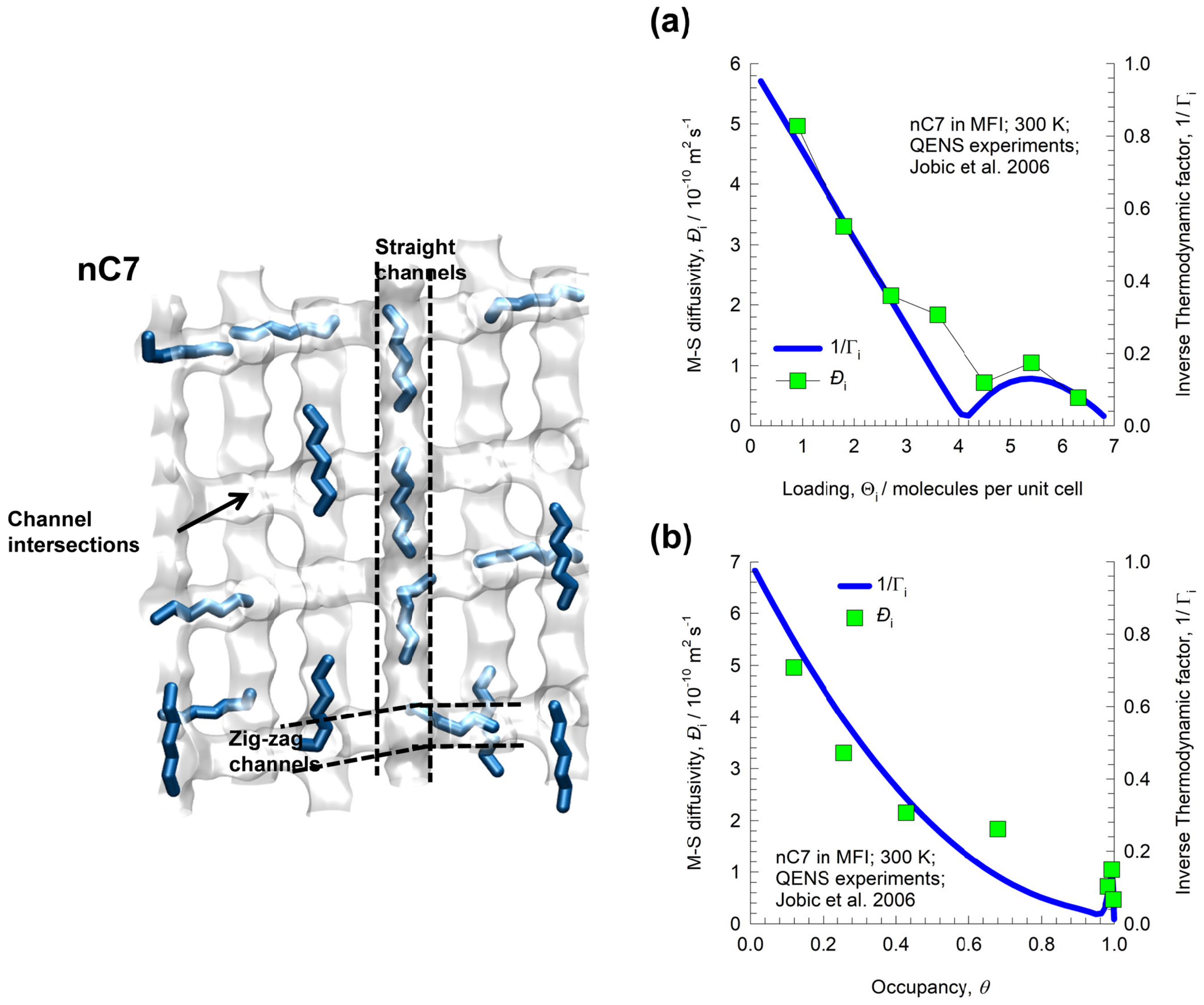

Figure S24. (a, b) Experimental data of Jobic et al.[37] on the M-S diffusivity, $Đ_i$, of n-heptane (nC7) in MFI at 298 K as a function of (a) loading Θ_i, expressed in molecules uc^{-1}, and (b) occupancy, θ, determined from Equation (S14), where the saturation capacity is determined from the unary isotherm fits. The right hand side of the Figures (a, b) are the calculations of the inverse thermodynamic factors, using the dual-site Langmuir-Freundlich isotherm fits.

6 Quasi-Chemical Theory for Occupancy Dependence of Unary Diffusivity

The simplest model to describe this occupancy dependence is

$$Đ_i = Đ_i(0)\left(1-\theta\right) = Đ_i(0)\theta_V \tag{S53}$$

where $Đ_i(0)$ is the M-S diffusivity at "zero-loading", and $\theta_V = \left(1-\theta\right)$ is the fractional vacancy, determined from Equation (S14), where the saturation capacity is determined from the unary isotherm fits. Equation (S53) is essentially based on a simple hopping model in which a molecule can jump from one adsorption site to an adjacent one, provided it is not already occupied. The loading dependence portrayed in equation (S53) has been termed the "strong confinement" scenario by Krishna and Baur.[38]

For the specific case of a binary mixture, the hopping of molecules from one site to another on a 2D lattice is depicted in Figure S25. Using a simple lattice model, the M-S diffusivity in the limit of vanishingly small occupancies, $Đ_i(0) = \frac{1}{\zeta}\nu_i(0)\lambda^2$, where $\zeta = 4$ is the coordination number of the 2D array of lattice sites, λ is the jump distance on the square lattice, and $\nu_i(0)$ is the jump frequency at vanishingly small occupancy.[39]

More generally, molecule-molecule interactions serve to influence the jump frequencies by a factor that depends on the energy of interaction, *w*. For repulsive interactions, $w > 0$, whereas for attractive interactions, $w < 0$. Using the quasi-chemical approach of Reed and Ehrlich[40] to quantify such interactions, the following expression is obtained for the occupancy dependence of the M-S diffusivities [39, 41, 42]

$$Đ_i = Đ_i(0)\left(\frac{1+\beta_i}{2\,(1-\theta_i)}\right)^{-\zeta}\left(1+\frac{(\beta_i-1+2\theta_i)\phi}{2\,(1-\theta_i)}\right)^{\zeta-1} \tag{S54}$$

In equation (S54) the following dimensionless parameters are defined

$$\beta_i = \sqrt{1-4\,\theta_i(1-\theta_i)(1-1/\phi)}; \quad \phi = \exp(w/RT) \tag{S55}$$

In the limiting case of negligible molecule-molecule interactions, $w = 0$, $\phi = 1$, $\beta_i = 1$ equation (S54) degenerates to yield Equation (S53).

A careful examination of the MD simulations of the diffusivities show that the assumption of loading-independent diffusivities, termed the "weak confinement" scenario by Krishna and Baur:[38]

$$Đ_i = Đ_i(0) \tag{S56}$$

can only be applied for small guest molecules such as H_2, and Ne for occupancies below about 0.5.

For any guest molecule, the loading dependence is strongly influenced also by the pore topology and connectivity, and molecule-molecule interactions. To illustrate this, Figure S26(a,b) compares the dependence of the M-S diffusivity of CH_4 in a wide variety of host structures, as a function of the fractional occupancy, determined using Equation (S14). Broadly speaking, the $Đ_i$ versus θ dependence is amenable to easier interpretation and analysis. The continuous solid lines in Figure S26(a,b) are the fits of the occupancy dependence using the quasi-chemical approach of Reed and Ehrlich[40] with fitted parameters: (a) zero-loading diffusivities $Đ_1(0)$, energy parameter $\phi = \phi_0 \exp(-a\theta)$. For three-dimensional structures such as FAU, NaX, LTA, CHA, IRMOF-1, CuBTC, the value of the coordination number ζ is chosen as 5. For intersecting channels of MFI, BEA, and ISV, the coordination number is chosen as 2.5. The rationale for this choice is discussed in our earlier publication.[41] The degree of correlations $\frac{Đ_i}{Đ_{ii}} = \frac{Đ_i}{D_{i,self}} - 1 = b\theta$ is a linear function of the fractional occupancy, θ, determined using Equation (S14); see Figure S26(c). The solid continuous lines in Figure S26(c) are the linear fits of $\frac{Đ_i}{Đ_{ii}}$. The Figure S26(d) presents a comparison of MD simulated data on the self-diffusivities $D_{i,self}$ with the predictions using

$$D_{i,self} = \frac{Đ_i}{\left(1+\frac{Đ_i}{Đ_{ii}}\right)} = \frac{Đ_i(0)\left(\frac{1+\beta_i}{2\,(1-\theta_i)}\right)^{-\zeta}\left(1+\frac{(\beta_i-1+2\theta_i)\phi}{2\,(1-\theta_i)}\right)^{\zeta-1}}{\left(1+\frac{Đ_i}{Đ_{ii}}\right)}.$$

The unary diffusivities $Đ_i$, $D_{i,self}$, along with the degree of correlations $\frac{Đ_i}{Đ_{ii}} = \frac{Đ_i}{D_{i,self}} - 1$ for every guest/host combination were analyzed in the manner to those illustrated in Figure S26 for CH_4. As further illustration, Figure S27, and Figure S28 show the analyses for Ar and CO_2 in a variety of host structures.

6.1 List of Figures for Quasi-Chemical Theory for Occupancy Dependence of Unary Diffusivity

$$-\frac{d\mu_1}{dz} = -RT\frac{d\ln p_1}{dz} = \frac{RT}{Đ_{12}}\theta_2\left(u_1 - u_2\right) + \frac{RT}{Đ_{1V}}\theta_V\left(u_1 - u_V\right)$$

$$-\frac{d\mu_2}{dz} = -RT\frac{d\ln p_2}{dz} = \frac{RT}{Đ_{12}}\theta_1\left(u_2 - u_1\right) + \frac{RT}{Đ_{2V}}\theta_V\left(u_2 - u_V\right)$$

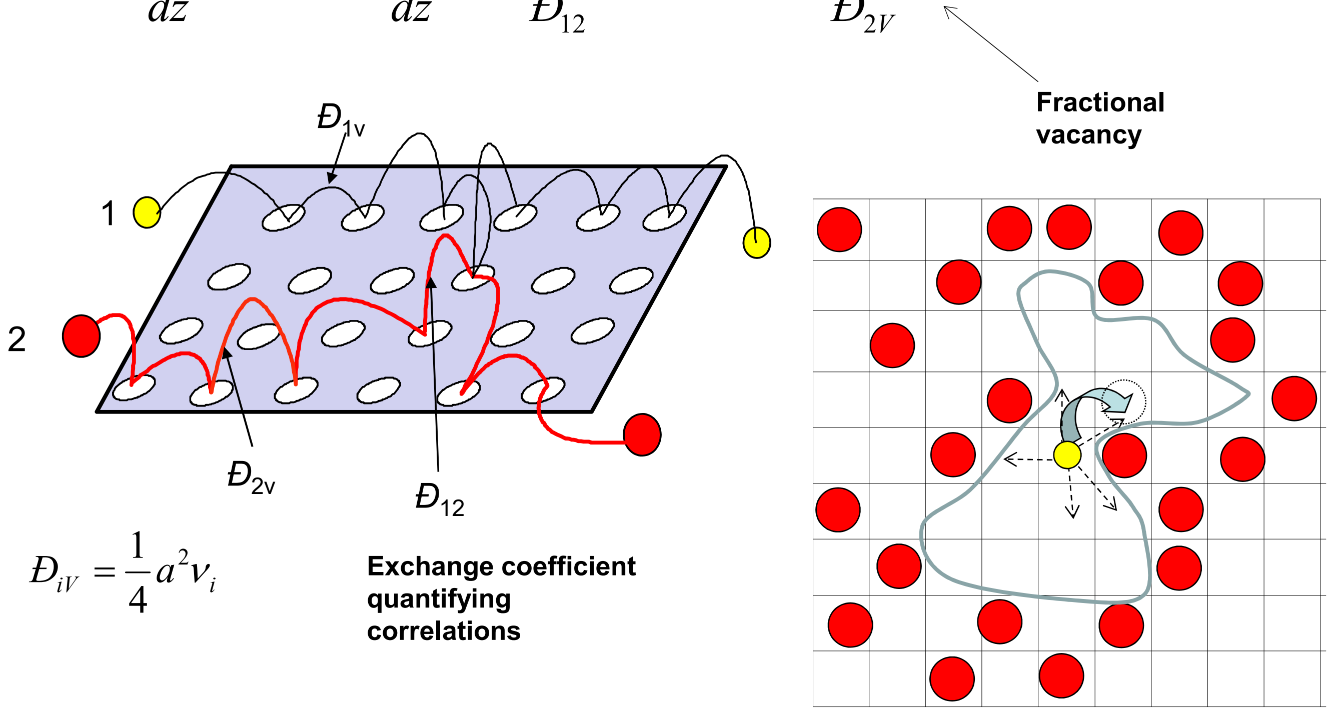

Figure S25. The Maxwell- Stefan description of hopping of molecules on a 2D surface.

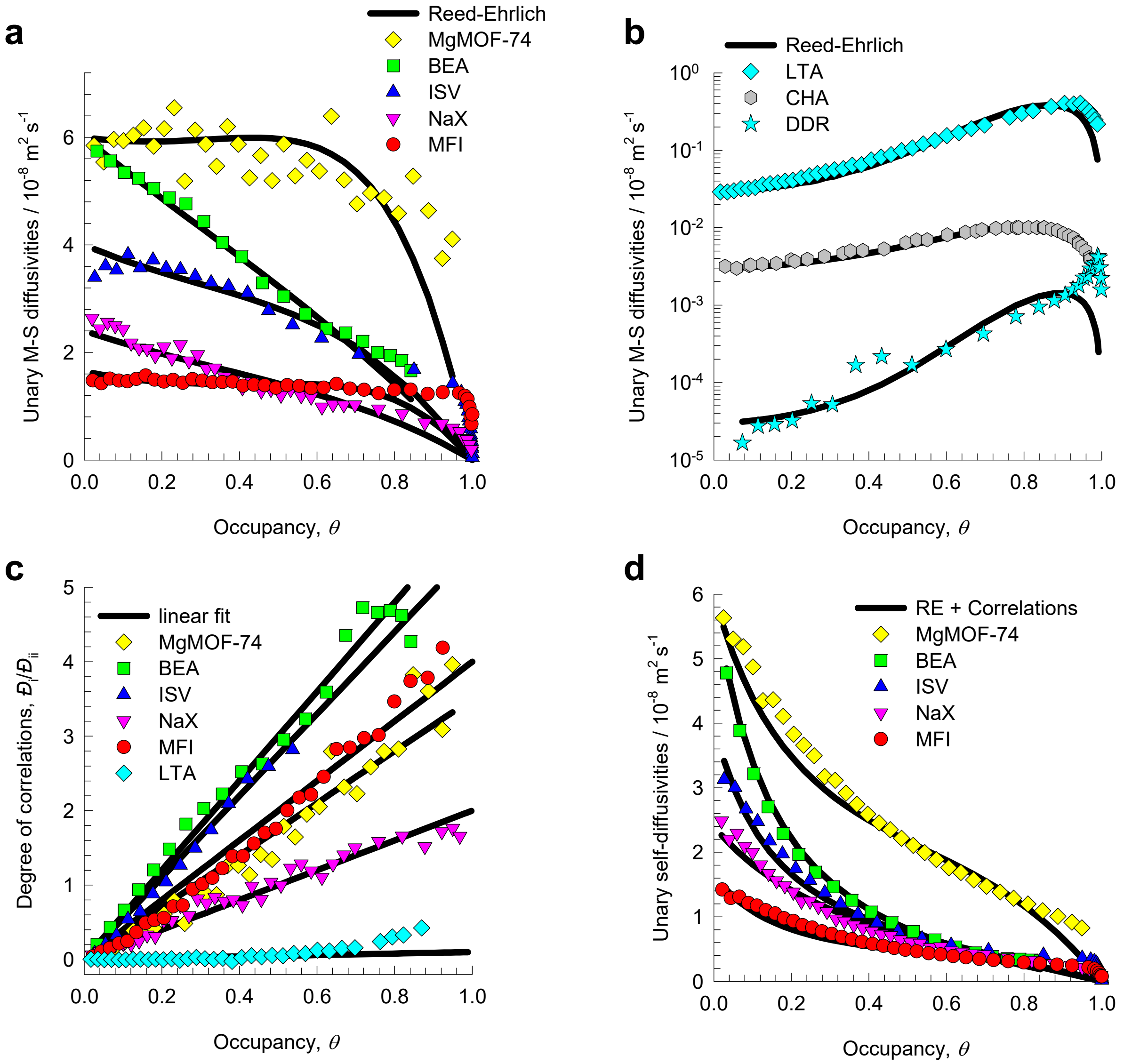

Figure S26. MD simulations of (a, b) Maxwell-Stefan diffusivity, $Đ_i$, (c) degree of correlations, $\frac{Đ_i}{Đ_{ii}}$, and (d) self-diffusivities $D_{i,self}$ of CH_4 in a variety of host structures plotted as a function of the occupancy, determined from Equation (S14), where the saturation capacity is determined from the unary isotherm fits.

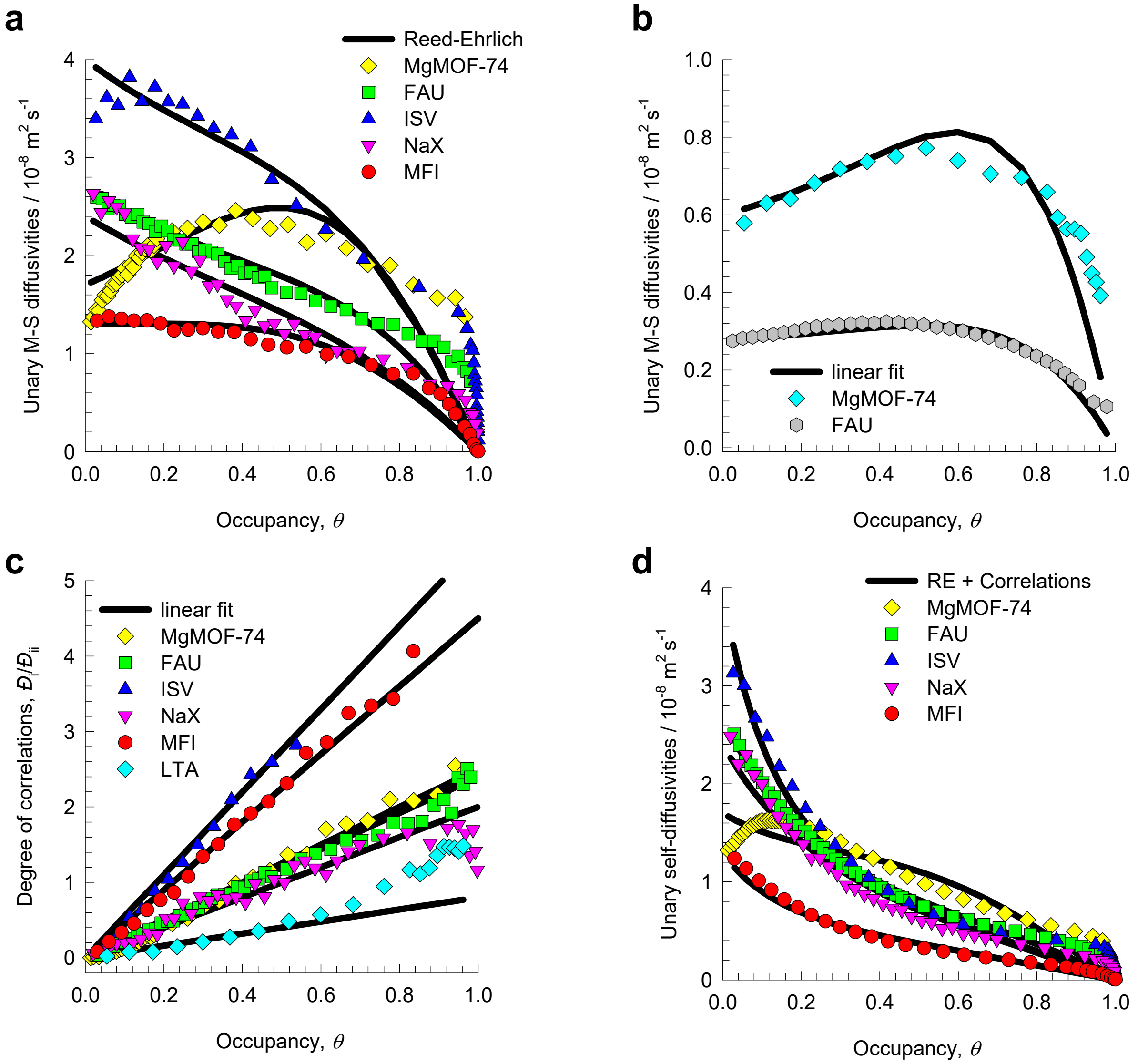

Figure S27. MD simulations of (a, b) Maxwell-Stefan diffusivity, Đ_i, (c) degree of correlations, $\frac{\text{Đ}_i}{\text{Đ}_{ii}}$, and (d) self-diffusivities $D_{i,self}$ of Ar in a variety of host structures plotted as a function of the occupancy, determined from Equation (S14), where the saturation capacity is determined from the unary isotherm fits.

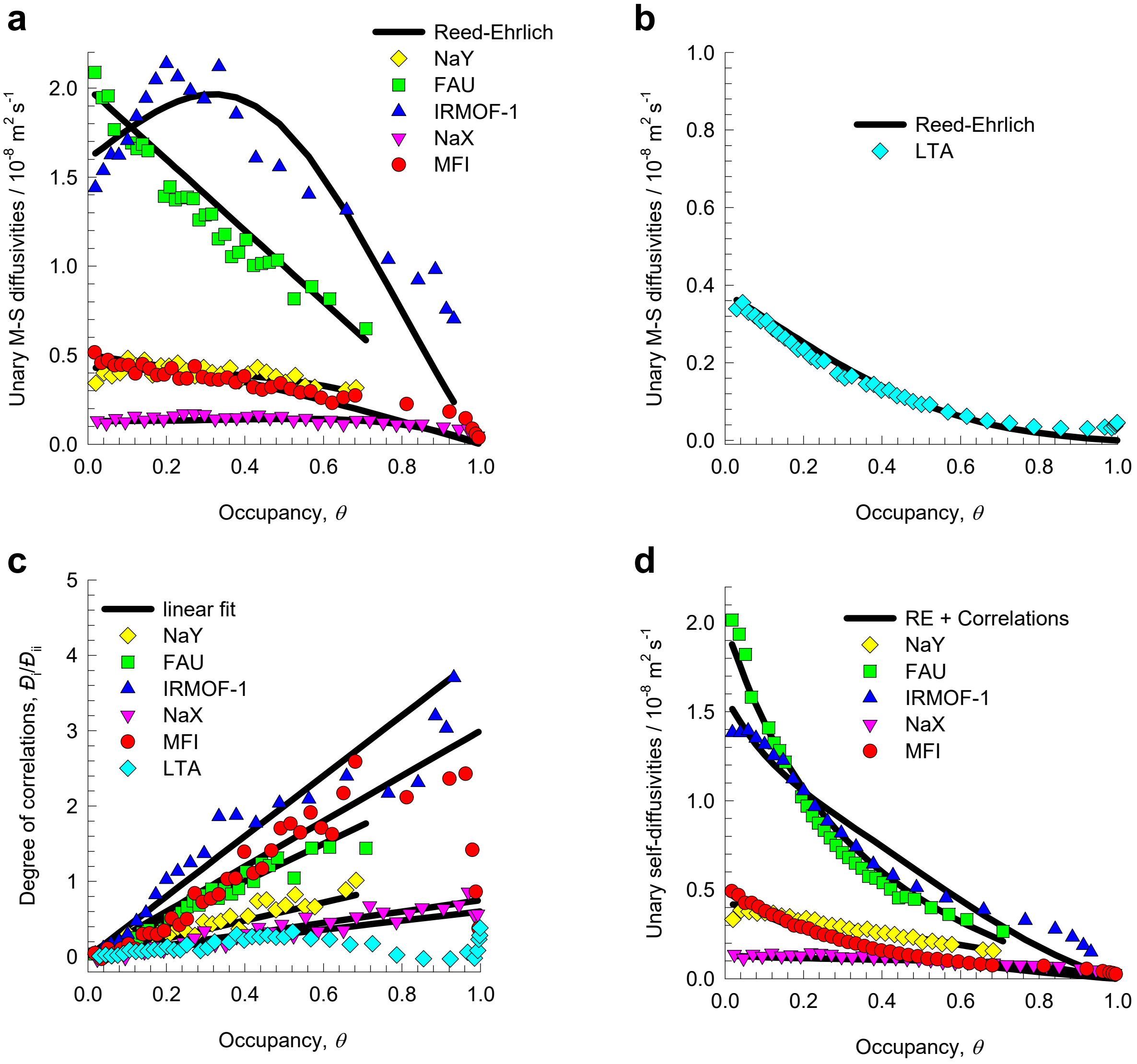

Figure S28. MD simulations of (a, b) Maxwell-Stefan diffusivity, $Đ_i$, (c) degree of correlations, $\frac{Đ_i}{Đ_{ii}}$, and (d) self-diffusivities $D_{i,self}$ of CO_2 in a variety of host structures plotted as a function of the occupancy, determined from Equation (S14), where the saturation capacity is determined from the unary isotherm fits.

7 Diffusion of Binary & Ternary Mixtures in Microporous Materials

7.1 M-S formulation for binary mixture diffusion

For binary mixture diffusion inside microporous crystalline materials the Maxwell-Stefan equations (S28) are written

$$\begin{aligned}-\rho\frac{q_1}{RT}\frac{d\mu_1}{dz}&=\frac{x_2N_1-x_1N_2}{Đ_{12}}+\frac{N_1}{Đ_1}\\-\rho\frac{q_2}{RT}\frac{d\mu_2}{dz}&=\frac{x_1N_2-x_2N_1}{Đ_{12}}+\frac{N_2}{Đ_2}\end{aligned}\tag{S57}$$

The first members on the right hand side of Equation (S57) are required to quantify slowing-down effects that characterize binary mixture diffusion.[8, 10, 12] There is no experimental technique for direct determination of the exchange coefficients $Đ_{12}$, that quantify molecule-molecule interactions.

In two-dimensional matrix notation, equation (S31) take the form

$$-\begin{pmatrix}\frac{q_1}{RT}\frac{d\mu_1}{dz}\\\frac{q_2}{RT}\frac{d\mu_2}{dz}\end{pmatrix}=[\Gamma]\begin{pmatrix}\frac{dq_1}{dz}\\\frac{dq_2}{dz}\end{pmatrix}\tag{S58}$$

For the mixed-gas Langmuir model, equation (S32), we can derive simple analytic expressions for the four elements of the matrix of thermodynamic factors:[38]

$$\begin{bmatrix}\Gamma_{11}&\Gamma_{12}\\\Gamma_{21}&\Gamma_{22}\end{bmatrix}=\frac{1}{1-\theta_1-\theta_2}\begin{bmatrix}1-\theta_2&\theta_1\\\theta_2&1-\theta_1\end{bmatrix}\tag{S59}$$

where the fractional occupancies, θ_i, are defined by equation (S32).

Let us define the square matrix $[B]$

$$[B]=\begin{bmatrix}\frac{1}{Đ_1}+\frac{x_2}{Đ_{12}}&-\frac{x_1}{Đ_{12}}\\-\frac{x_2}{Đ_{12}}&\frac{1}{Đ_2}+\frac{x_1}{Đ_{12}}\end{bmatrix};\quad [B]^{-1}=\frac{1}{1+\frac{x_1Đ_2}{Đ_{12}}+\frac{x_2Đ_1}{Đ_{12}}}\begin{bmatrix}Đ_1\left(1+\frac{x_1Đ_2}{Đ_{12}}\right)&\frac{x_1Đ_1Đ_2}{Đ_{12}}\\\frac{x_2Đ_1Đ_2}{Đ_{12}}&Đ_2\left(1+\frac{x_2Đ_1}{Đ_{12}}\right)\end{bmatrix}\tag{S60}$$

In proceeding further, it is convenient to define a 2×2 dimensional square matrix $\left[\Lambda\right]\equiv\left[B\right]^{-1}$:

$$\left[\Lambda\right]=\begin{bmatrix}\frac{1}{Đ_1}+\frac{x_2}{Đ_{12}} & -\frac{x_1}{Đ_{12}}\\ -\frac{x_2}{Đ_{12}} & \frac{1}{Đ_2}+\frac{x_1}{Đ_{12}}\end{bmatrix}^{-1}=\frac{1}{1+\frac{x_1Đ_2}{Đ_{12}}+\frac{x_2Đ_1}{Đ_{12}}}\begin{bmatrix}Đ_1\left(1+\frac{x_1Đ_2}{Đ_{12}}\right) & \frac{x_1Đ_1Đ_2}{Đ_{12}}\\ \frac{x_2Đ_1Đ_2}{Đ_{12}} & Đ_2\left(1+\frac{x_2Đ_1}{Đ_{12}}\right)\end{bmatrix} \tag{S61}$$

Equation (S57) can be re-cast into 2-dimensional matrix notation

$$\left(N\right)=-\rho\left[\Lambda\right]\left[\Gamma\right]\frac{d\left(q\right)}{dz};$$
$$\begin{pmatrix}N_1\\ N_2\end{pmatrix}=-\frac{\rho}{1+\frac{x_1Đ_2}{Đ_{12}}+\frac{x_2Đ_1}{Đ_{12}}}\begin{bmatrix}Đ_1\left(1+\frac{x_1Đ_2}{Đ_{12}}\right) & \frac{x_1Đ_1Đ_2}{Đ_{12}}\\ \frac{x_2Đ_1Đ_2}{Đ_{12}} & Đ_2\left(1+\frac{x_2Đ_1}{Đ_{12}}\right)\end{bmatrix}\begin{bmatrix}\Gamma_{11} & \Gamma_{12}\\ \Gamma_{21} & \Gamma_{22}\end{bmatrix}\begin{pmatrix}\frac{dq_1}{dz}\\ \frac{dq_2}{dz}\end{pmatrix} \tag{S62}$$

The elements of $\left[B\right]$ can be obtained by inverting the matrix $\left[\Lambda\right]$ determined using MD simulations using equation (S39): $\begin{bmatrix}B_{11} & B_{12}\\ B_{21} & B_{22}\end{bmatrix}=\begin{bmatrix}\frac{1}{Đ_1}+\frac{x_2}{Đ_{12}} & -\frac{x_1}{Đ_{12}}\\ -\frac{x_2}{Đ_{12}} & \frac{1}{Đ_2}+\frac{x_1}{Đ_{12}}\end{bmatrix}=[\Lambda]^{-1}$. The three M-S diffusivities can be backed-out from the four elements $\begin{bmatrix}B_{11} & B_{12}\\ B_{21} & B_{22}\end{bmatrix}$ using;

$$Đ_{12}=-\frac{x_1}{B_{12}}=-\frac{x_2}{B_{21}};\quad Đ_1=\frac{1}{B_{11}-\frac{x_2}{Đ_{12}}};\quad Đ_2=\frac{1}{B_{22}-\frac{x_1}{Đ_{12}}} \tag{S63}$$

For a wide variety of guest/host combinations we used MD simulations to determine the four elements $\Lambda_{11},\Lambda_{12},\Lambda_{21},\Lambda_{22}$ for binary mixtures for a range of total mixture loadings, $q_t= q_1+q_2$, using equation (S39). These simulations are reported in our earlier publications.[8, 10, 11, 14, 15, 22, 25-27, 30-34] In most, but not all cases, the MD simulations are for equimolar ($q_1=q_2$; $c_1=c_2$) binary mixtures.

The M-S diffusivities $Đ_1,Đ_2$ that are backed-out for mixture simulations using equation (S63), for a total of 70 different mixture/host combinations, are in good agreement with the corresponding values of the *unary* M-S diffusivities $Đ_1,Đ_2$; the evidence for this is provided in our earlier publication.[1] The comparison of the unary M-S diffusivities with those backed-out from mixture MD simulations need to be done at the same occupancy. For all of the MD mixture simulations reported in this article, the fractional occupancy for mixture adsorption, θ, were calculated using equations (S11), (S12), and (S13).

The agreement of the unary diffusivities $Đ_1, Đ_2$ with the values characterizing the mixture, underscores the persuasive advantage of the use of the Maxwell-Stefan equations to describing diffusion in microporous crystalline materials.

The M-S diffusivity of any species in a mixture is also not influenced by the choice of the partner molecules. To illustrate this, Figure S29 provides data on the M-S diffusivity of CO_2, $Đ_i$, determined MD simulation data for diffusion of a variety of equimolar ($c_1 = c_2$) binary mixtures of CO_2 and different partner species in seven different host materials (MFI, FAU, LTA, CHA, IRMOF-1, CuBTC, MgMOF-74). For any host material, we note that the diffusivity of CO_2 in a binary mixture is practically independent of the partner species. Furthermore, when compared at the same occupancy, θ, the values of $Đ_i$ are nearly the same in the mixture as those determined for *unary* diffusion, indicated by the open symbols in Figure S29. For all of the MD mixture simulations reported in this article, the fractional occupancy for mixture adsorption, θ, were calculated using equations (S11), (S12), and (S13).

Similar conclusions hold for the diffusivity of CH_4 in binary mixtures, containing different partner species, in nine different host materials (MFI, FAU, NaY, NaX, LTA, CHA, BEA, IRMOF-1, CuBTC); see Figure S30. The M-S diffusivity of CH_4 is the same whether it diffuses on its own, or in the presence of *any other* partner molecule. For MFI, and FAU zeolite, it is noteworthy that the MD data for diffusion in equimolar ternary $CH_4/C_2H_6/C_3H_8$ mixtures are also included.

Figure S31 presents the data on the Maxwell-Stefan diffusivity, $Đ_i$, of Ar determined from MD simulations for diffusion of a variety of equimolar ($q_1 = q_2$) binary mixtures of Ar and different partner species in MFI, FAU, AFI, and IRMOF-1. The M-S diffusivity of Ar is the same whether it diffuses on its own, or in the presence of *any other* partner molecule.

Figure S32(a, b) presents the data on the Maxwell-Stefan diffusivity, $Đ_i$, of C_2H_6 determined MD simulation data for diffusion of binary and ternary mixtures of C_2H_6 in (a) MFI, and (b) FAU at 300 K. The M-S diffusivity of C_2H_6 is the same whether it diffuses on its own, or in the presence of *any other* partner molecule. The same conclusions hold for Maxwell-Stefan diffusivity, $Đ_i$, of C_3H_8 in binary and ternary mixtures in MFI and FAU, as evidenced Figure S32(c,d).

7.2 Degree of correlations for binary mixtures

In order to appreciate the relative importance of correlations on the calculations of the fluxes for binary mixture diffusion, we define the *degrees of correlation*, $Đ_1/Đ_{12}$, and $Đ_2/Đ_{12}$; the values can be determined from those backed-out from mixture MD simulations; from equation (S63) we derive

$$\frac{Đ_1}{Đ_{12}} = -\left(\frac{B_{21}}{x_2}\right)\frac{1}{B_{11}+B_{21}}; \quad \frac{Đ_2}{Đ_{12}} = -\left(\frac{B_{21}}{x_2}\right)\frac{1}{B_{22}+\frac{x_1}{x_2}B_{21}} \tag{S64}$$

The magnitude of $Đ_1$, relative to that of $Đ_{12}$, determines the extent to which the flux of species 1 is influenced by the chemical potential gradient of species 2. The larger the degree of correlation, $Đ_1/Đ_{12}$, the stronger is the influence of coupling. Generally speaking, the more-strongly-adsorbed-tardier partner species will have the effect of slowing down the less-strongly-adsorbed-more-mobile partner in the mixture.

Figure S33 shows MD simulation data for the degree of correlations, $Đ_1/Đ_{12}$, for diffusion of equimolar ($q_1 = q_2$) binary mixtures (a) CO_2/CH_4, (b) H_2/CO_2, (c) N_2/CO_2, (d) Ne/CO_2, (e) CH_4/Ar (f) H_2/CH_4, (g) Ne/Ar, (h) CH_4/C_2H_6, and (i) CH_4/C_3H_8 at 300 K in a variety of host materials. The *x*- axes represent the fractional occupancy θ. For all of the MD mixture simulations reported in this article, the fractional occupancy for mixture adsorption, θ, were calculated using equations (S11), (S12), and (S13). For any guest/host combination, $Đ_1/Đ_{12}$ is seen to increase as the pore occupancy increases; this implies that correlation effects are expected to be stronger for high occupancies.

The degree of correlations is weakest in cage-type structures such as CHA, DDR and LTA; the reason is that the molecules jump one-at-a-time across the narrow windows separating adjacent cages; CO_2 molecules jump length-wise across the windows. At the other end of the spectrum, correlations are strongest in one-dimensional (1D) channel structures (e.g. BTP-COF, MgMOF-74, NiMOF-74), intersecting channels (e.g. MFI), and "open" structures (e.g. IRMOF-1, FAU, NaY, NaX) consisting of large cages separated by wide windows.

7.3 M-S formulation for ternary mixture diffusion

For ternary mixture diffusion inside microporous crystalline materials the Maxwell-Stefan equations (S28) are written

$$
\begin{aligned}
-\rho \frac{q_1}{RT}\frac{d\mu_1}{dz} &= \left(\frac{1}{Đ_1}+\frac{x_2}{Đ_{12}}+\frac{x_3}{Đ_{13}}\right)N_1 - \frac{x_1 N_2}{Đ_{12}} - \frac{x_1 N_3}{Đ_{13}} \\
-\rho \frac{q_2}{RT}\frac{d\mu_2}{dz} &= \left(\frac{1}{Đ_2}+\frac{x_1}{Đ_{21}}+\frac{x_3}{Đ_{23}}\right)N_2 - \frac{x_2 N_1}{Đ_{21}} - \frac{x_2 N_3}{Đ_{23}} \\
-\rho \frac{q_3}{RT}\frac{d\mu_3}{dz} &= \left(\frac{1}{Đ_3}+\frac{x_1}{Đ_{31}}+\frac{x_2}{Đ_{32}}\right)N_3 - \frac{x_3 N_1}{Đ_{31}} - \frac{x_3 N_2}{Đ_{32}}
\end{aligned}
\tag{S65}
$$

By defining an 3-dimensional square matrix $[B]$ with elements

$$
[B] = \begin{bmatrix}
\frac{1}{Đ_1}+\frac{x_2}{Đ_{12}}+\frac{x_3}{Đ_{13}} & -\frac{x_1}{Đ_{12}} & -\frac{x_1}{Đ_{13}} \\
-\frac{x_2 N_1}{Đ_{21}} & \frac{1}{Đ_2}+\frac{x_1}{Đ_{21}}+\frac{x_3}{Đ_{23}} & -\frac{x_2}{Đ_{23}} \\
-\frac{x_3}{Đ_{31}} & -\frac{x_3}{Đ_{32}} & \frac{1}{Đ_3}+\frac{x_1}{Đ_{31}}+\frac{x_2}{Đ_{32}}
\end{bmatrix}
\tag{S66}
$$

The 3-dimensional matrix $[\Lambda]$ is obtained by matrix inversion

$$
[\Lambda] \equiv [B]^{-1} = \begin{bmatrix}
\frac{1}{Đ_1}+\frac{x_2}{Đ_{12}}+\frac{x_3}{Đ_{13}} & -\frac{x_1}{Đ_{12}} & -\frac{x_1}{Đ_{13}} \\
-\frac{x_2}{Đ_{21}} & \frac{1}{Đ_2}+\frac{x_1}{Đ_{21}}+\frac{x_3}{Đ_{23}} & -\frac{x_2}{Đ_{23}} \\
-\frac{x_3}{Đ_{31}} & -\frac{x_3}{Đ_{32}} & \frac{1}{Đ_3}+\frac{x_1}{Đ_{31}}+\frac{x_2}{Đ_{32}}
\end{bmatrix}^{-1}
\tag{S67}
$$

The elements of $[\Lambda]$ are directly accessible from MD simulations [10, 22, 25, 26] by monitoring the individual molecular displacements

$$\Lambda_{ij} = \frac{1}{2} \lim_{\Delta t \to \infty} \frac{1}{n_j} \frac{1}{\Delta t} \left\langle \left(\sum_{l=1}^{n_i} \left(\mathbf{r}_{l,i}(t+\Delta t) - \mathbf{r}_{l,i}(t) \right) \right) \bullet \left(\sum_{k=1}^{n_j} \left(\mathbf{r}_{k,j}(t+\Delta t) - \mathbf{r}_{k,j}(t) \right) \right) \right\rangle \tag{S68}$$

From the MD simulated values of $[\Lambda]$, the 9 elements of the 3-dimensional square matrix $[B]$ can be determined. The M-S diffusivities $Đ_i$ can be backed-out from the 9 elements of $[B]$ using;

$$Đ_{12} = Đ_{21} = -\frac{x_1}{B_{12}} = -\frac{x_2}{B_{21}}; \quad Đ_{13} = Đ_{31} = -\frac{x_1}{B_{13}} = -\frac{x_3}{B_{31}}; \quad Đ_1 = \frac{1}{B_{11} - \frac{x_2}{Đ_{12}} - \frac{x_3}{Đ_{13}}};$$
$$Đ_{23} = Đ_{32} = -\frac{x_2}{B_{23}} = -\frac{x_3}{B_{32}}; \quad Đ_2 = \frac{1}{B_{22} - \frac{x_1}{Đ_{21}} - \frac{x_3}{Đ_{23}}}; \tag{S69}$$
$$Đ_3 = \frac{1}{B_{33} - \frac{x_1}{Đ_{31}} - \frac{x_2}{Đ_{32}}}$$

The MD data on the 3-dimensional matrix $[\Lambda]$ for equimolar ($q_1=q_2=q_3$) CH_4(1)/C_2H_6(2)/C_3H_8(3) ternary mixtures in MFI and FAU zeolites are presented in Figure S59, and Figure S75. The backed-out M-S diffusivities $Đ_i$, using the formula (S14), are included in Figure S30, and. Figure S32.

7.4 List of Figures for Diffusion of Binary & Ternary Mixtures in Microporous Materials

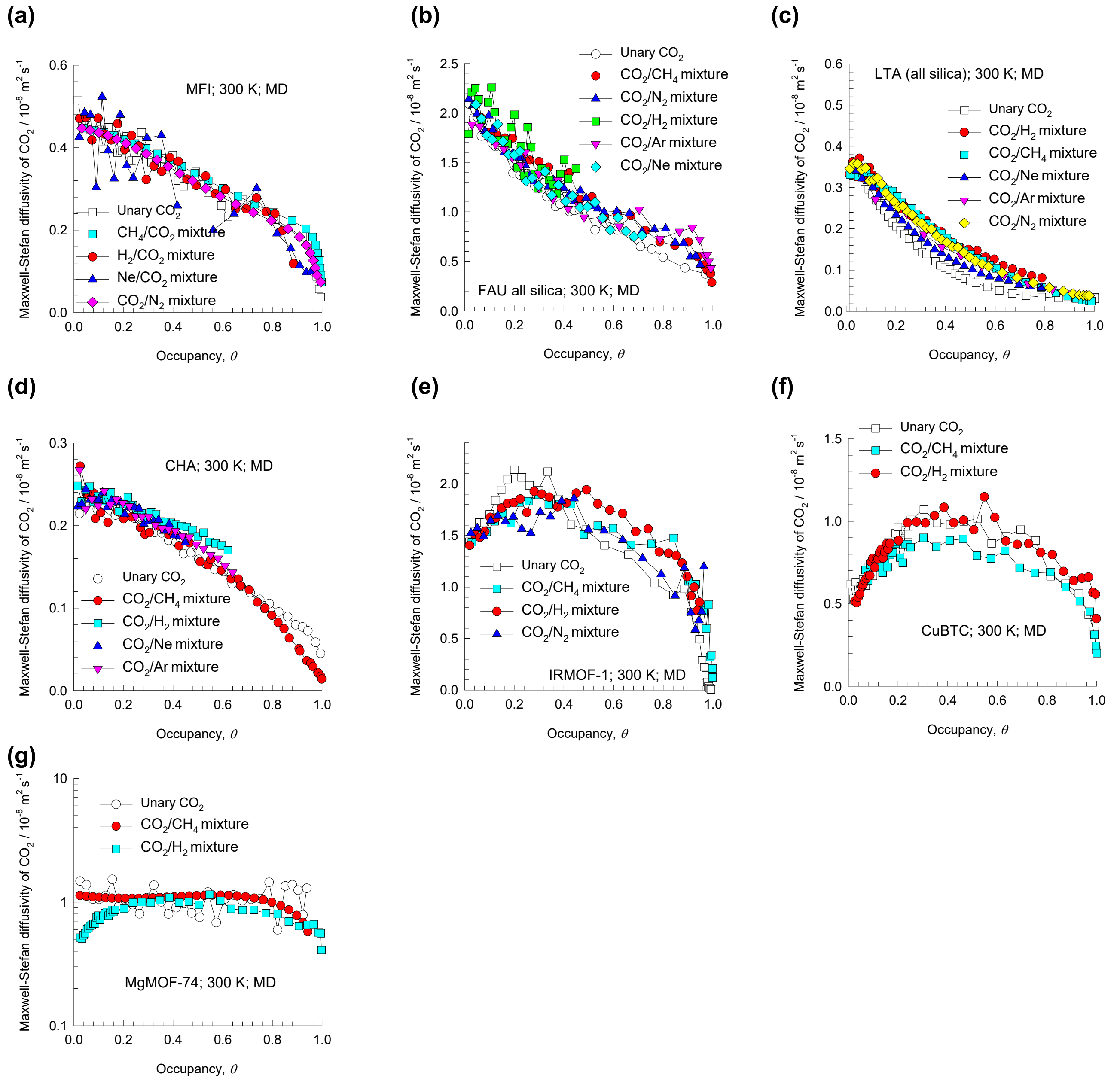

Figure S29. Maxwell-Stefan diffusivity, $Đ_i$, of CO_2 determined MD simulation data for diffusion of a variety of equimolar ($q_1 = q_2$) binary mixtures of CO_2 and different partner species in (a) MFI, (b) FAU (all silica), (c) LTA, (d) CHA, (e) IRMOF-1, (f) CuBTC, and (g) MgMOF-74. The *x*- axes represent the fractional occupancy θ. Also shown in open symbols are the MD simulations of $Đ_i$, for unary CO_2 diffusion.

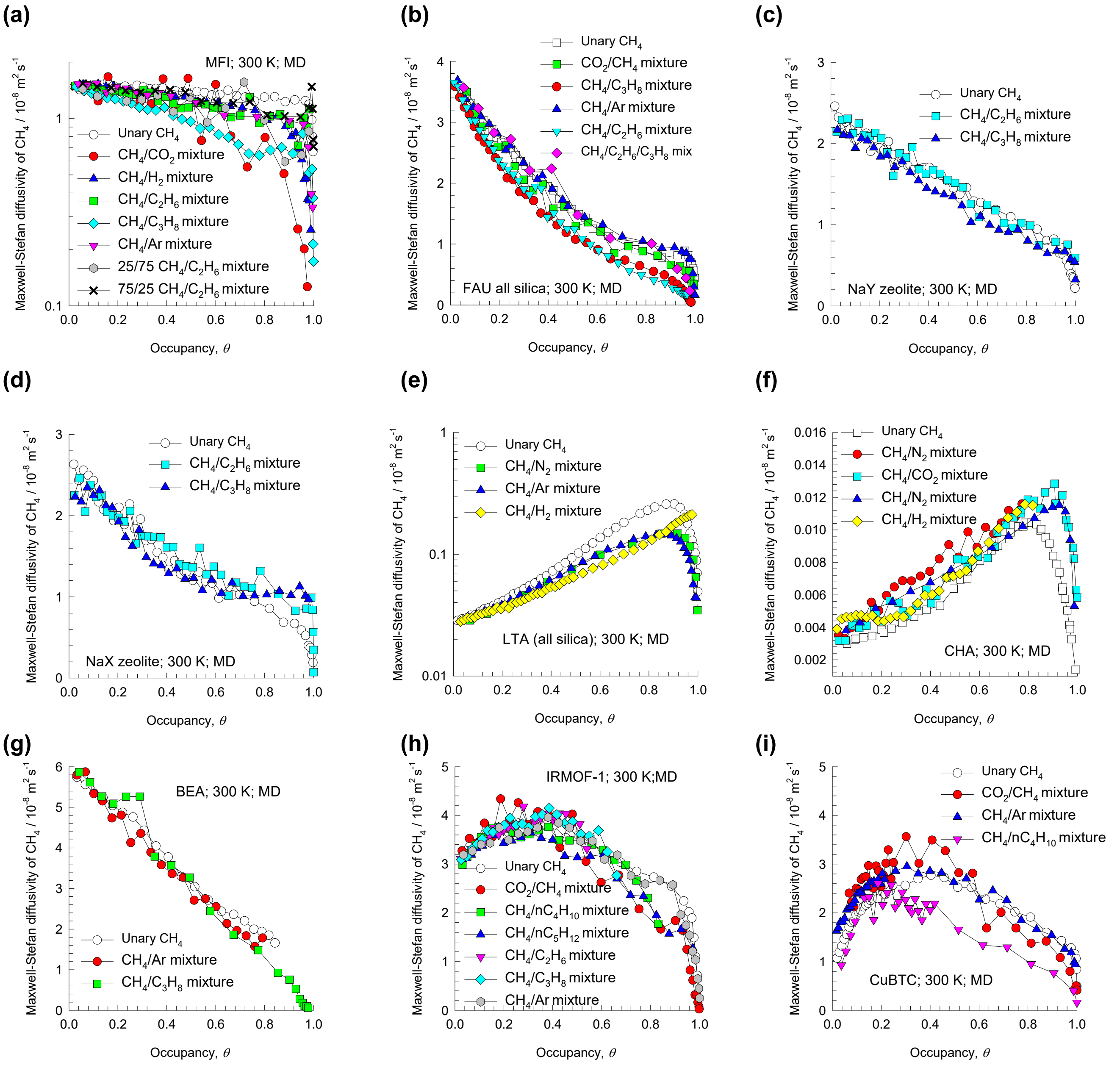

Figure S30. Maxwell-Stefan diffusivity, Đ_{i}, of CH$_4$ determined MD simulation data for diffusion of a variety of equimolar ($q_1 = q_2$) binary mixtures of CH$_4$ and different partner species in (a) MFI, (b) FAU (all silica), (c) NaY (48 Al), (d) NaX (86 Al), (e) LTA, (f) CHA, (g) BEA, (h) IRMOF-1, and (i) CuBTC. The *x*- axes represent the fractional occupancy θ. Also shown in open symbols are the MD simulations of Đ_{i}, for unary CH$_4$ diffusion.

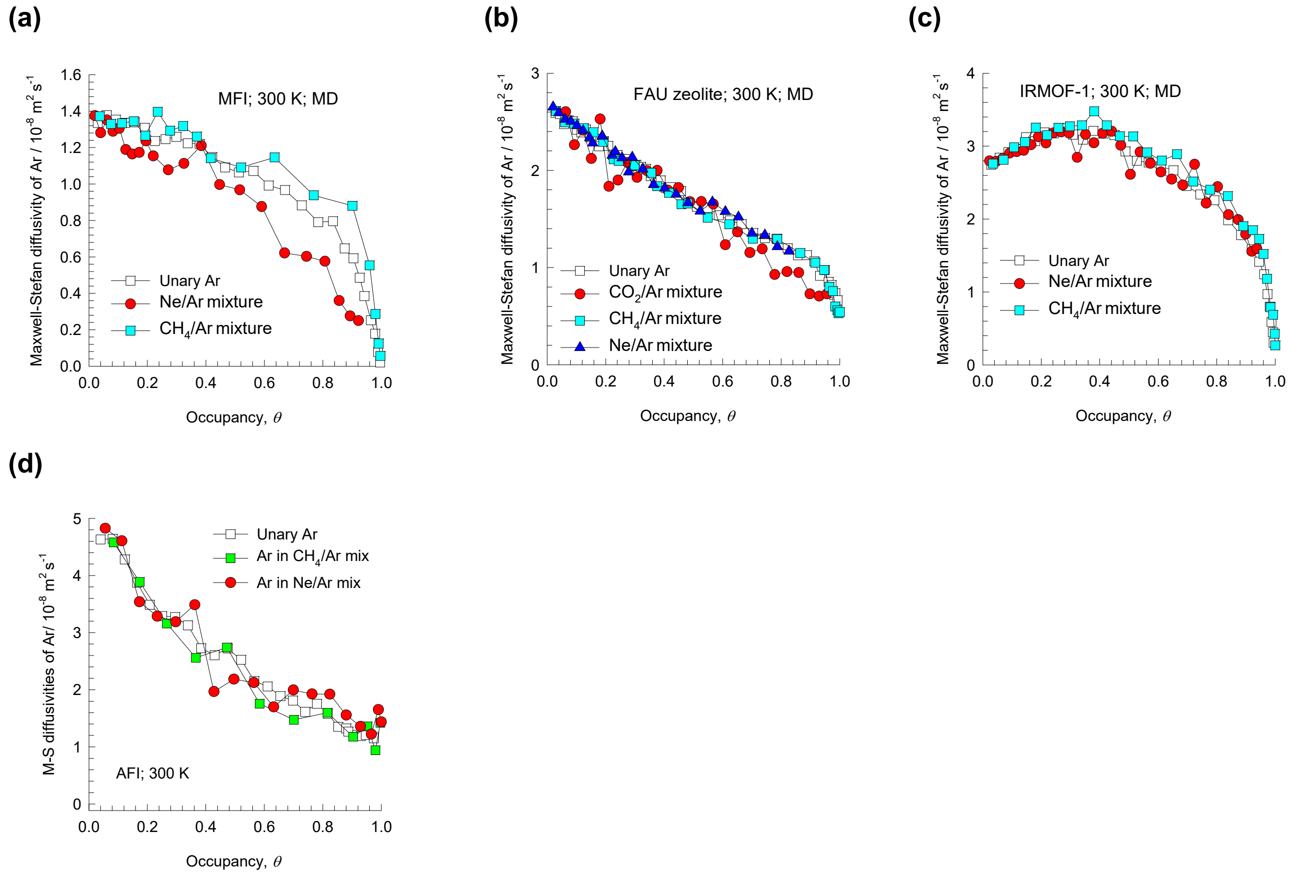

Figure S31. Maxwell-Stefan diffusivity, $Đ_i$, of Ar determined MD simulation data for diffusion of a variety of equimolar ($q_1 = q_2$) binary mixtures of Ar and different partner species in (a) MFI, (b) FAU-Si, (c) IRMOF-1, and (d) AFI. The x- axes represent the fractional occupancy θ. Also shown in open symbols are the MD simulations of $Đ_i$, for unary Ar diffusion.

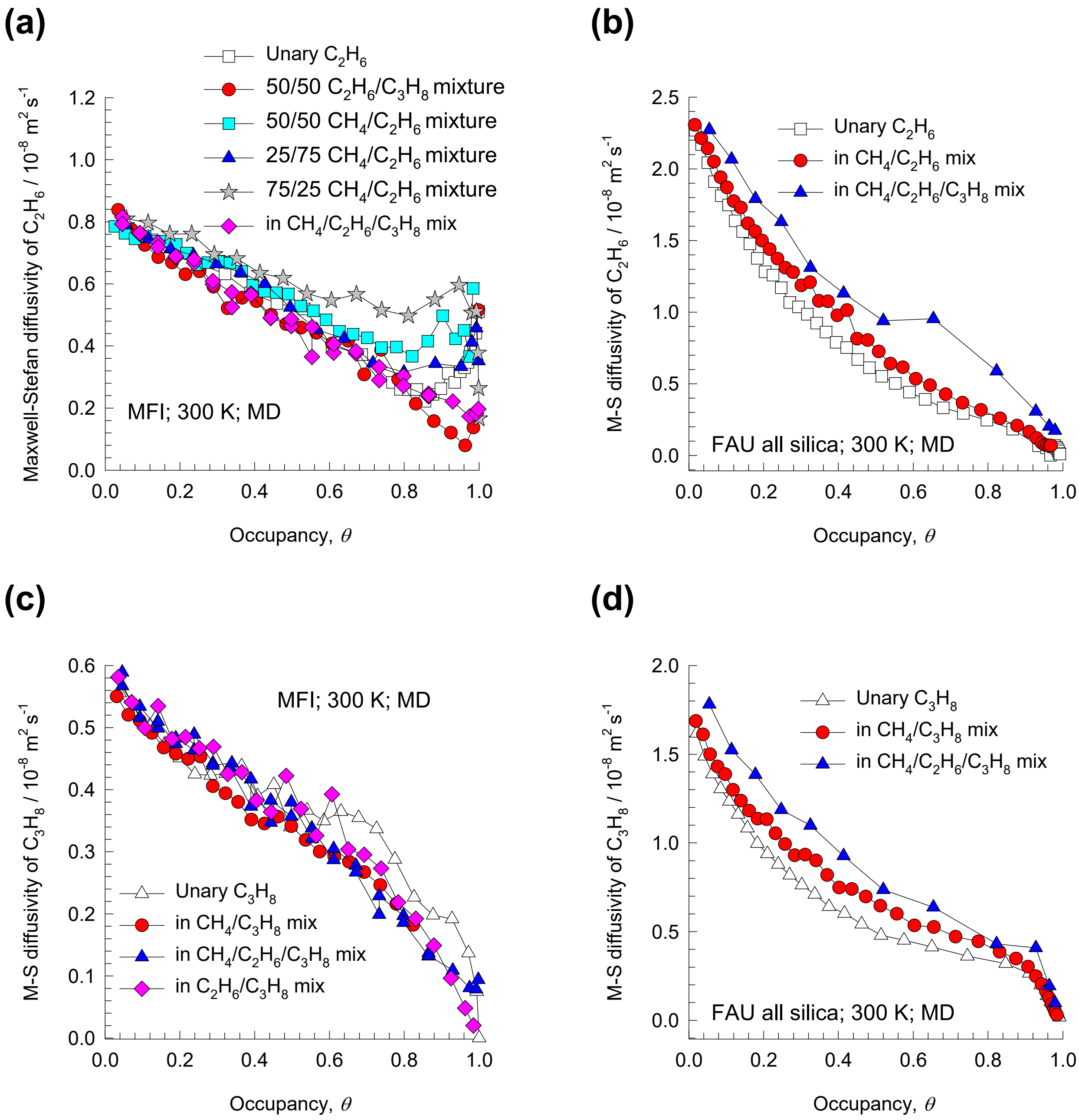

Figure S32. Maxwell-Stefan diffusivity, Đi, of (a, b) C_2H_6, and (c, d) C_3H_8 determined MD simulation data for diffusion of binary and ternary mixtures in (a, c) MFI, and (b, d) all-silica FAU zeolites at 300 K. The *x*- axes represent the fractional occupancy θ. Also shown in open symbols are the MD simulations of Đi, for unary diffusion.

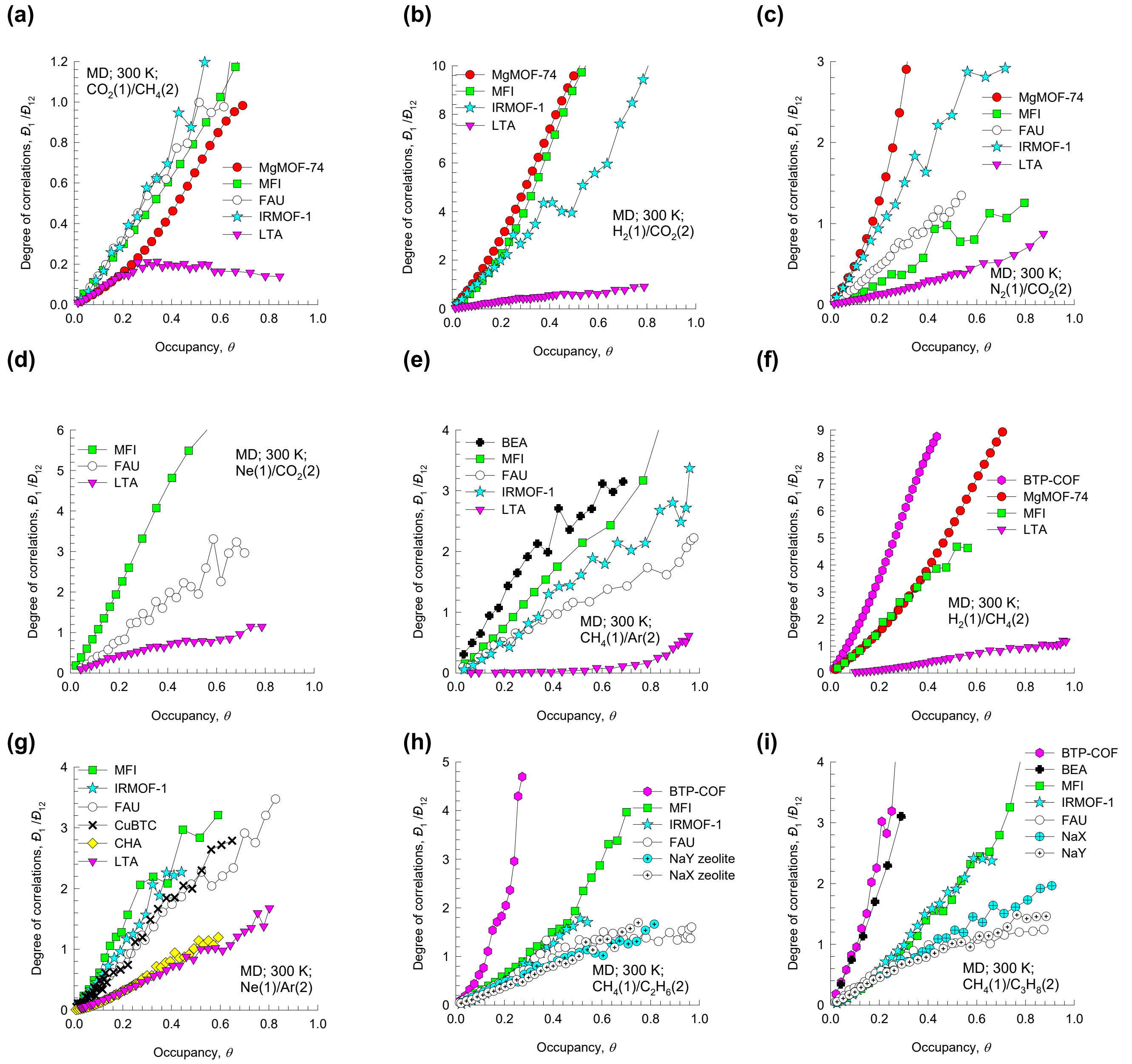

Figure S33. MD simulation data for the degree of correlations, $Đ_1/Đ_{12}$, for diffusion of equimolar ($q_1 = q_2$) binary mixtures (a) CO_2/CH_4, (b) H_2/CO_2, (c) N_2/CO_2, (d) Ne/CO_2, (e) CH_4/Ar (f) H_2/CH_4, (g) Ne/Ar, (h) CH_4/C_2H_6, and (i) CH_4/C_3H_8 at 300 K in a variety of host materials. The *x*- axes represent the fractional occupancy θ.

8 Estimation of the Degree of Correlations for Mixture Diffusion

The objective in this chapter is to develop a procedure for estimation of the degree of correlations for binary mixture diffusion, that are quantified by the metrics $Đ_1/Đ_{12}$, and $Đ_2/Đ_{12}$ using data (MD or experimental) on the data for *unary* diffusivities (both $D_{i,self}$ and M-S $Đ_i$) of each constituent partner. The development of the estimation procedure relies on the estimation procedure for the M-S diffusivity for binary fluid phase mixtures; as is first discussed below.

8.1 M-S diffusivities for diffusion in fluid phase mixtures

The Maxwell-Stefan equation for describing bulk *fluid phase* mixture diffusion are[43]

$$-\frac{c_i}{RT}\frac{d\mu_i}{dz}=\sum_{\substack{j=1\\ j\neq i}}^{n}\frac{x_jN_i-x_iN_j}{Đ_{ij,fl}};\qquad i=1,2,...n;\quad \text{bulk fluid mixture} \tag{S70}$$

where $Đ_{ij,fl}$ represents the M-S diffusivity for the binary pair *i-j* in the *n*-component fluid mixture, and c_i are the molar concentrations in the fluid mixture, with units of mol m^{-3}. For bulk fluid phase mixtures, the chemical potential gradients satisfy the Gibbs-Duhem relationship

$$\sum_{i=1}^{n}x_i d\mu_i=0 \tag{S71}$$

and so only *n*-1 of the equations (S70) are independent. For a binary fluid phase mixture, equations (S70) simplify to yield just one independent equation

$$-\frac{c_1}{RT}\frac{d\mu_1}{dz}=-c_t\left(1+\frac{\partial\ln\gamma_1}{\partial\ln x_1}\right)\frac{dx_1}{dz}=-c_t\Gamma\frac{dx_1}{dz}=\frac{x_2N_1-x_1N_2}{Đ_{12,fl}} \tag{S72}$$

where $c_t=\sum_{i=1}^{n}c_i$ is the total molar concentration of the mixture. Equation (S72) can be recast into the form

$$N_1-x_1\left(N_1+N_2\right)=-\frac{c_1}{RT}Đ_{12,fl}\frac{d\mu_1}{dz}=-c_tĐ_{12,fl}\Gamma\frac{dx_1}{dz} \tag{S73}$$

The Fick diffusivity for binary fluid mixtures is related to the corresponding M-S diffusivity

$$D_{12,fl} = Đ_{12,fl}\Gamma \tag{S74}$$

It is to be noted that for binary fluid mixtures, the Fick and M-S diffusivities are defined in terms of fluxes defined with respect to the molar average velocity of the mixture $u = \sum_{i=1}^{n} x_i u_i$.

For highly non-ideal liquid mixtures, because of the strong composition dependence of the thermodynamic factor $\Gamma = \left(1 + \frac{\partial \ln \gamma_1}{\partial \ln x_1}\right)$, we should expect the Fick diffusivity to also exhibit a corresponding strong composition dependence.

For a fluid phase mixture, the Vignes[44, 45] interpolation formula is commonly used in practice for estimation of the $Đ_{12,\mathrm{fl}}$

$$Đ_{12,fl} = \left(Đ_{11,fl}\right)^{x_1}\left(Đ_{22,fl}\right)^{x_2} \tag{S75}$$

where the $Đ_{\mathrm{ii,fl}}$ represent the self-exchange coefficients, or self-diffusivities, for *unary* fluid phase diffusion. The Vignes relation (S75) implies that the logarithm of $Đ_{12,\mathrm{fl}}$ should be linear in the mole fraction x_1

8.2 Estimating $Đ_{12}$ from information on self-exchange coefficients $Đ_{\mathrm{ii}}$

The Vignes interpolation formula (S75), for binary *flui*d mixtures, can be extended to apply to micro-porous materials in the following manner

$$Đ_{12} = \left(Đ_{11}\right)^{x_1}\left(Đ_{22}\right)^{x_2} \tag{S76}$$

where the $Đ_{\mathrm{ii}}$ represent the self-exchange coefficients determined for unary systems. For estimation of the elements of the 3-dimensional matrix $[\Lambda]$ for equimolar (q_1=q_2=q_3) CH_4(1)/C_2H_6(2)/C_3H_8(3) ternary mixtures in MFI and FAU zeolites, the following extension of the Vignes interpolation formula

$$Đ_{ij} = \left(Đ_{ii}\right)^{x_i/(x_i+x_j)}\left(Đ_{jj}\right)^{x_j/(x_i+x_j)} \tag{S77}$$

has been used in Figure S59, and Figure S75.

8.3 Estimating the degree of correlations for binary mixture diffusion

As noted in Figure S20, the degree of correlations, $\frac{Đ_i}{Đ_{ii}}$, for *unary* diffusion of various guest/host combinations is linearly dependent on fractional occupancy, θ, For all of the MD mixture simulations reported in this article, the fractional occupancy for mixture adsorption, θ, were calculated using equations (S11), (S12), and (S13), using the spreading pressure determined from IAST for mixture adsorption equilibrium.

Therefore for a binary 1-2 mixture, the degree of correlations, $\frac{Đ_1}{Đ_{12}}$ can be estimated from $\frac{Đ_1}{Đ_{11}}$ and $\frac{Đ_2}{Đ_{22}}$ by invoking the Vignes interpolation formula (S76), as follows:

$$\frac{Đ_1}{Đ_{12}} = \left(\frac{Đ_1}{Đ_{11}}\right)^{x_1} \left(\frac{Đ_2}{Đ_{22}}\right)^{x_2} \left(\frac{Đ_1}{Đ_2}\right)^{x_2} \tag{S78}$$

The interpolation formula (S78) is applied using the mixture occupancy calculated using equations (S11) using the spreading pressure determined from IAST for mixture adsorption equilibrium.

As illustration, the validation of Equation (S78) is demonstrated for a selected set of mixture/host combinations in Figure S34, Figure S35, Figure S36, and Figure S37. In the above set of Figures, the MD simulated data for $\frac{Đ_1}{Đ_{12}}$, indicated by the red circles, are to be compared with the estimations of Equation (S78), indicated by the crosses. In these estimations: (a) the ratio of the M-S diffusivities $\left(\frac{Đ_1}{Đ_2}\right)$ is calculated on the basis of the backed-out M-S diffusivities for binary mixture diffusion, and (b) the $\left(\frac{Đ_1}{Đ_{11}}\right)$ and $\left(\frac{Đ_2}{Đ_{22}}\right)$ are determined from the corresponding *unary* diffusion data (on self, and M-S diffusivities) at the same occupancy θ as in the mixture. These comparisons show that Equation (S78) provides good estimates of $\frac{Đ_1}{Đ_{12}}$ in the various guest/host combinations.

8.4 List of Figures for Estimation of the Degree of Correlations for Mixture Diffusion

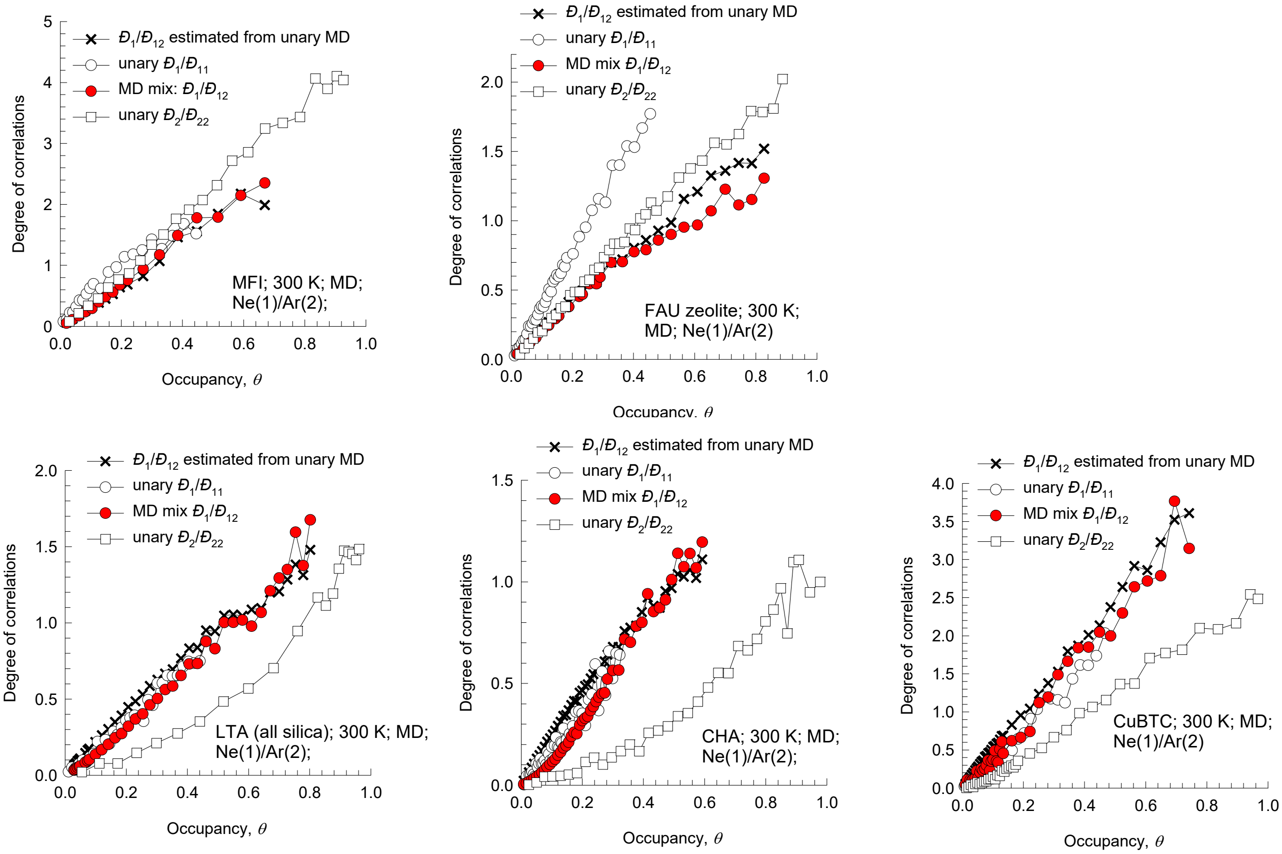

Figure S34. Test of the Vignes interpolation formula interpolation formula (S78) for equimolar (q_1=q_2) binary Ne(1)/Ar(2) mixtures in MFI, all-silica FAU, all-silica LTA, all-silica CHA, and CuBTC at 300 K.

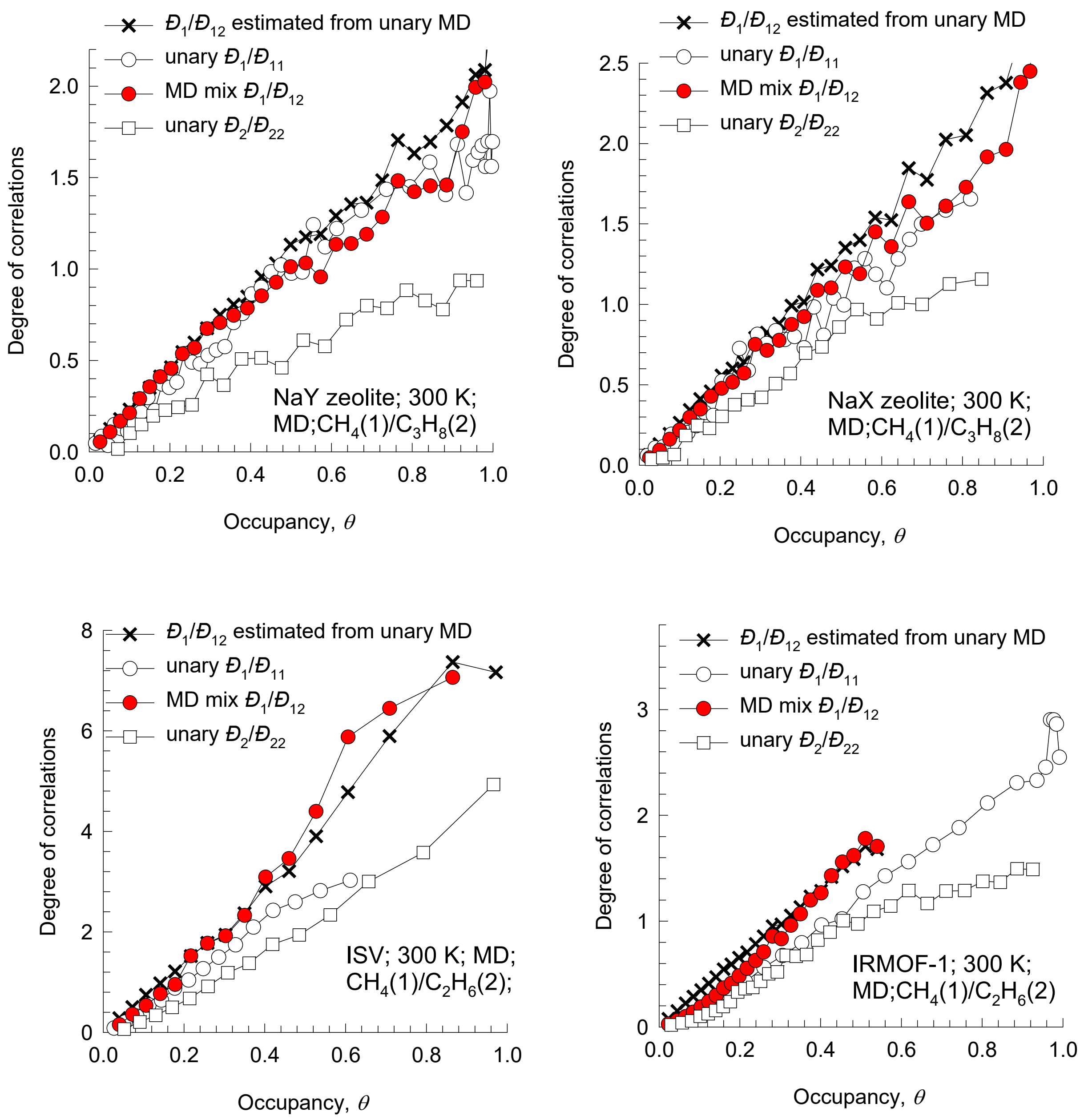

Figure S35. Test of the Vignes interpolation formula interpolation formula (S78) for equimolar (q_1=q_2) binary $CH_4(1)/C_2H_6(2)$, and $CH_4(1)/C_3H_8(2)$ mixtures in NaY, NaX, ISV, and IRMOF-1 at 300 K.

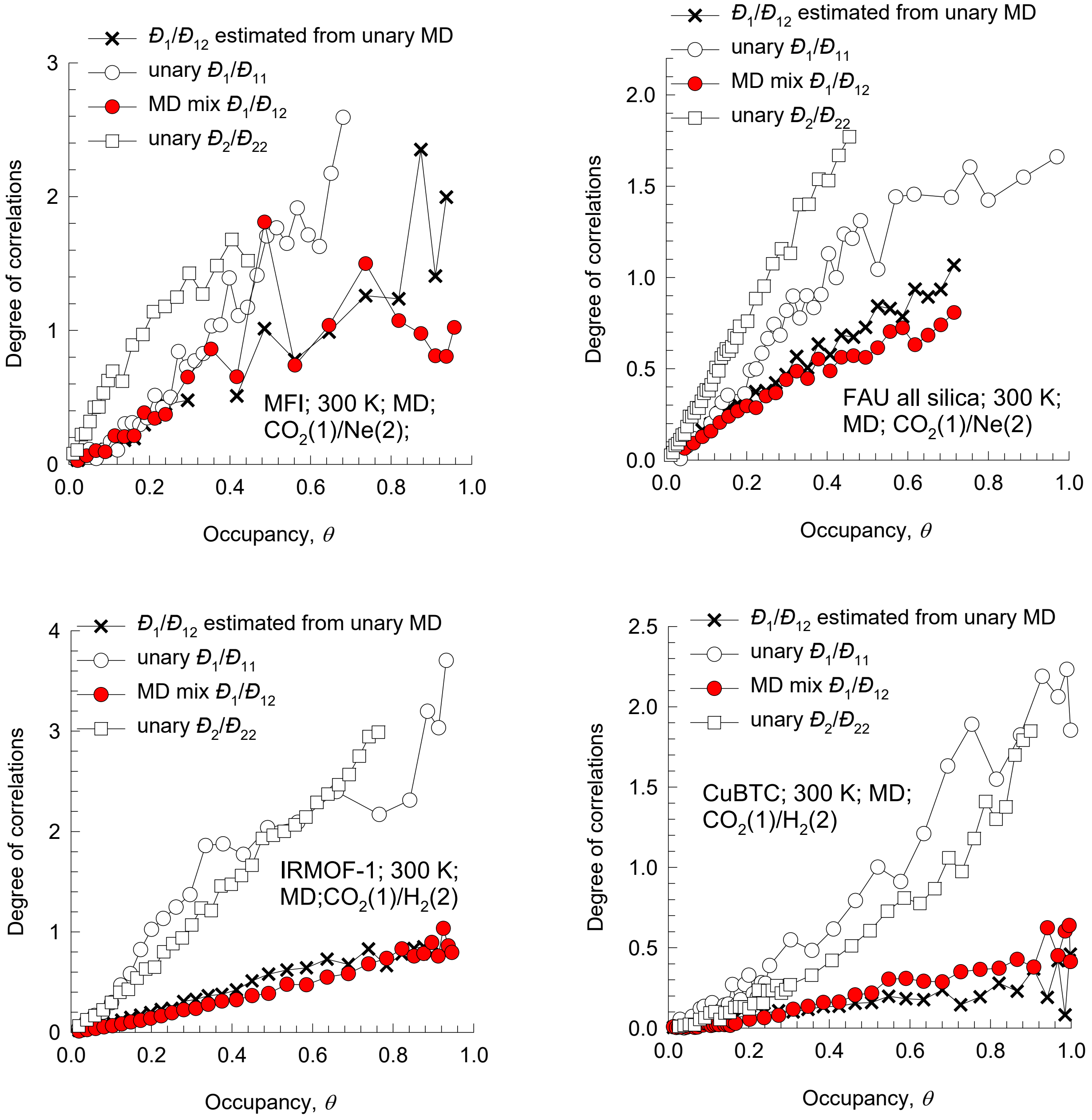

Figure S36. Test of the Vignes interpolation formula interpolation formula (S78) for equimolar (q_1=q_2) binary CO_2(1)/Ne(2), and CO_2(1)/H_2(2) mixtures in MFI, all-silica FAU, IRMOF-1, and CuBTC at 300 K.

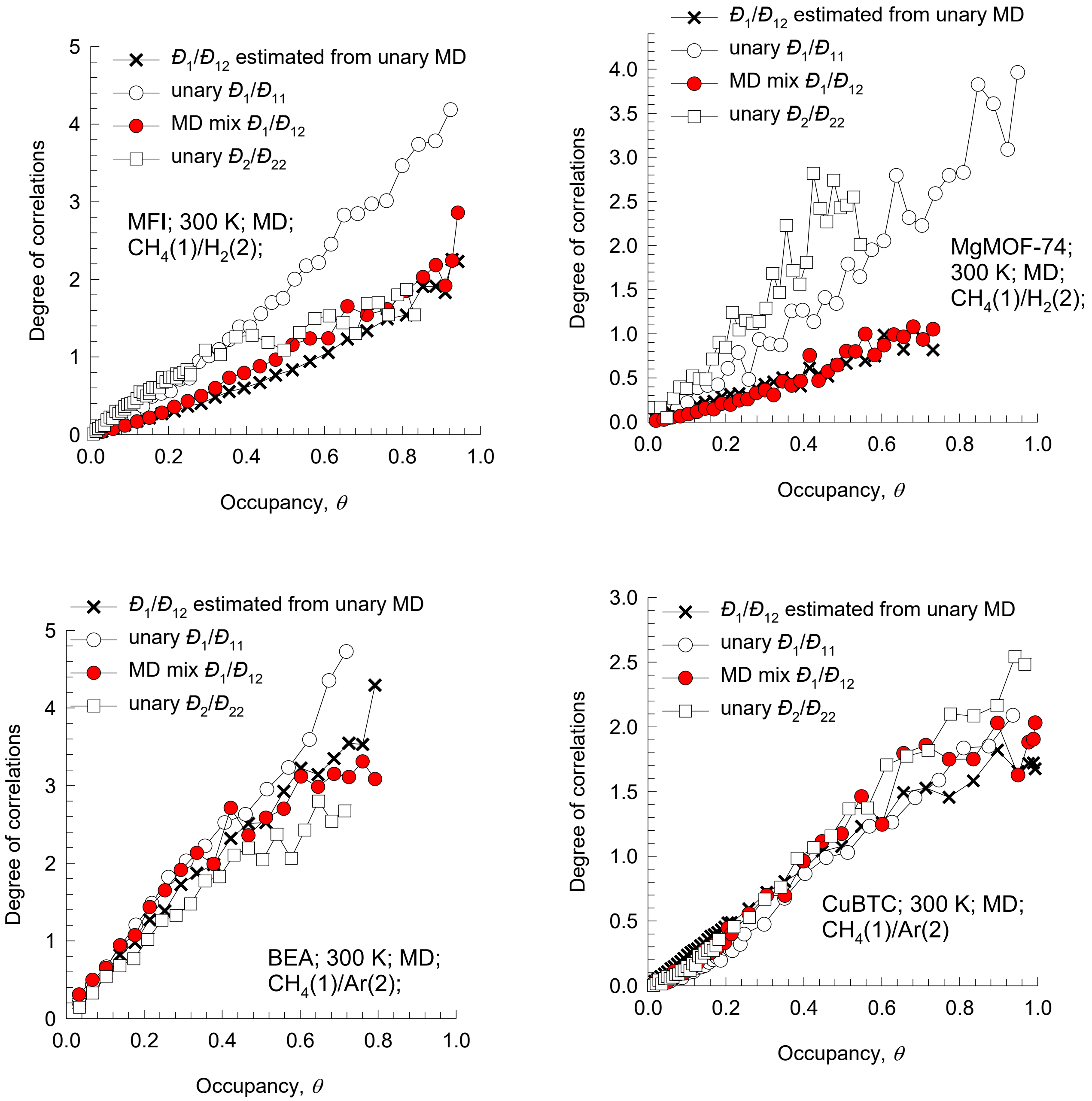

Figure S37. Test of the Vignes interpolation formula interpolation formula (S78) for equimolar $(q_1=q_2)$ binary $CH_4(1)/H_2(2)$, and $CH_4(1)/Ar(2)$ mixtures in MFI, BEA, MgMOF-74, and CuBTC at 300 K.

9 Maxwell-Stefan estimation of mixture diffusion

The major objective of this article is to demonstrate the validity of the Maxwell-Stefan model for prediction of the 2×2 dimensional square matrix $\left[\Lambda\right]$ on the basis of unary diffusivity data. The prediction method is based on the following steps:

Firstly, the loading dependence of the unary M-S diffusivities $Đ_1, Đ_2$ are fitted using the Quasi-Chemical theory of Reed and Ehrlich:[40]

$$
\begin{aligned}
&Đ = Đ(0)\left(\frac{1+\beta}{2\,(1-\theta)}\right)^{-\zeta}\left(1+\frac{(\beta-1+2\theta)\phi}{2\,(1-\theta)}\right)^{\zeta-1} \\
&\beta = \sqrt{1-4\,\theta\left(1-\theta\right)\left(1-1/\phi\right)}; \quad \phi = \phi_0 \exp\left(-a\theta\right)
\end{aligned}
$$

If the unary adsorption isotherm is described by the dual-Langmuir-Freundlich isotherm, equation (S6), the fractional occupancy θ can be determined as follows

$$
\begin{aligned}
&\frac{\pi A}{RT} = \frac{q_{A,sat}}{\nu_A}\ln\left(1+b_A\left(P^0\right)^{\nu_A}\right)+\frac{q_{B,sat}}{\nu_B}\ln\left(1+b_B\left(P^0\right)^{\nu_B}\right); \quad q_{sat} = q_{A,sat}+q_{B,sat} \\
&\theta = 1-\exp\left(-\frac{\pi A}{q_{sat}RT}\right); \quad \text{unary adsorption}
\end{aligned}
$$

For unary diffusion, the occupancy θ is determined from equation (S14); the spreading pressures and saturation capacity values are determined from Configurational-Bias Monte Carlo (CBMC) simulations of the unary adsorption isotherms that are fitted with the dual-site Langmuir-Freundlich model. The required dual-site Langmuir-Freundlich model fit parameters for each guest molecule (with sites A, and B) are tabulated for each host material:

Table S5, Table S6, and Table S7: MFI zeolite

Table S8: FAU all-silica zeolite

Table S9: NaY zeolite (48 Al)

Table S10: NaX zeolite (86 Al)

Table S11: AFI all-silica zeolite

Table S12: LTA all-silica zeolite

Table S13: CHA all-silica zeolite

Table S14: DDR all-silica zeolite

Table S15: ISV zeolite

Table S16: BEA zeolite

Table S17: IRMOF-1

Table S18: MgMOF-74

Table S19: CuBTC

For each guest/host combination, the loading dependence is described by the following fit parameters: $Đ(0)$, ϕ_0, and a. For intersecting channel structures such as MFI, BEA, and ISV, the coordination number $\zeta = 2.5$, following our earlier work.[41] Each guest molecule located within the straight or zig-zag channels "sees" only 2 neighbors. On the other hand each guest molecule located at the intersections, sees 4 neighboring molecules. The weighted-average coordination number for guest diffusion in the MFI topology is taken as $\zeta = 2.5$. For all other topologies such as FAU, AFI, IRMOF-1, LTA, CHA, DDR, CuBTC, and MgMOF-74, we take $\zeta = 5$, signifying that each guest molecule "sees" five neighboring molecules.

The degrees of correlation for unary diffusion of each guest molecule is fitted with the linear model $\frac{Đ_i}{Đ_{ii}} = b\theta$.

For a binary 1-2 mixture, the degree of correlations, $\frac{Đ_1}{Đ_{12}}$ can be estimated from $\frac{Đ_1}{Đ_{11}}$ and $\frac{Đ_2}{Đ_{22}}$ by invoking the Vignes interpolation formula: $\frac{Đ_1}{Đ_{12}} = \left(\frac{Đ_1}{Đ_{11}}\right)^{x_1} \left(\frac{Đ_2}{Đ_{22}}\right)^{x_2} \left(\frac{Đ_1}{Đ_2}\right)^{x_2}$; this interpolation formula is applied by determining the mixture occupancy, θ, from equations (S11), (S12), and (S13), using the spreading pressure determined from IAST for mixture adsorption equilibrium.

The four elements of the matrix $\left[\Lambda\right]$ can be estimated using:

$$\left[\Lambda\right]=\frac{1}{1+\frac{x_1 Đ_2}{Đ_{12}}+\frac{x_2 Đ_1}{Đ_{12}}}\begin{bmatrix} Đ_1\left(1+\frac{x_1 Đ_2}{Đ_{12}}\right) & \frac{x_1 Đ_1 Đ_2}{Đ_{12}} \\ \frac{x_2 Đ_1 Đ_2}{Đ_{12}} & Đ_2\left(1+\frac{x_2 Đ_1}{Đ_{12}}\right) \end{bmatrix} \tag{S79}$$

Each of the elements of the right member of equation (S79) is estimated from the fitted unary diffusivity data, determined at the fractional occupancy in the mixture, θ, from equations (S11), (S12), and (S13), using the spreading pressure determined from IAST for mixture adsorption equilibrium.

The comparisons of the MD simulated values of the four elements of the matrix $\left[\Lambda\right]$ with estimations based on the M-S model using equation (S79), and fitted data on unary diffusivities, are summarized in Panels f and g of Figure S38 to Figure S108 for various host mixtures in MFI, ISV, BEA, all-silica FAU, NaY, NaX, AFI, IRMOF-1, MgMOF-74, CuBTC, all-silica LTA, all-silica CHA, and DDR. The data inputs are specified in each of the individual Figures.

Figure S38: equimolar Ne(1)/Ar(2) mixtures in MFI zeolite

Figure S39: Ne(1)/Ar(2) mixtures of varying composition in MFI zeolite

Figure S40: CH_4(1)/Ar(2) mixtures in MFI zeolite

Figure S41: CH_4(1)/N_2(2) mixtures in MFI zeolite

Figure S42: equimolar (q_1=q_2) binary CH_4(1)/C_2H_6(2) mixtures in MFI zeolite

Figure S43: 25/75 (q_1/q_2=25/75) binary CH_4(1)/C_2H_6(2) mixtures in MFI zeolite

Figure S44: 75/25 (q_1/q_2=75/25) binary CH_4(1)/C_2H_4(2) mixtures in MFI zeolite

Figure S45: binary CH_4(1)/C_2H_6(2) mixtures of varying composition in MFI zeolite

Figure S46: equimolar CH_4(1)/C_3H_8(2) mixtures in MFI zeolite

Figure S47: binary CH_4(1)/C_3H_8(2) mixtures of varying composition in MFI zeolite

Figure S48: binary CH_4(1)/nC_4H_{10}(2) mixtures of varying composition in MFI zeolite

Figure S49: CH_4(1)/CO_2(2) mixtures in MFI zeolite

Figure S75: CH_4(1)/C_2H_6(2)/C_3H_8(3) mixtures in FAU all-silica zeolite

Figure S76: CH_4(1)/CO_2(2) mixtures in NaY zeolite (48 Al)

Figure S77: CH_4(1)/C_2H_6(2) mixtures in NaY zeolite (48 Al)

Figure S78: CH_4(1)/C_3H_8(2) mixtures in NaY zeolite (48 Al)

Figure S79: CO_2(1)/N_2(2) mixtures in NaX zeolite (86 Al)

Figure S80: CH_4(1)/CO_2(2) mixtures in NaX zeolite (86 Al)

Figure S81: CH_4(1)/C_2H_6(2) mixtures in NaX zeolite (86 Al)

Figure S82: CH_4(1)/C_3H_8(2) mixtures in NaX zeolite (86 Al)

Figure S83: CH_4(1)/Ar(2) mixtures in AFI all-silica zeolite

Figure S84: Ne(1)/Ar(2) mixtures in AFI all-silica zeolite

Figure S85: Ne(1)/Ar(2) mixtures of varying composition in AFI all-silica zeolite

Figure S86: Ne(1)/Ar(2) mixtures in IRMOF-1

Figure S87: CH_4(1)/Ar(2) mixtures in IRMOF-1

Figure S88: CH_4(1)/C_2H_6(2) mixtures in IRMOF-1

Figure S89: CH_4(1)/C_3H_8(2) mixtures in IRMOF-1

Figure S90: CO_2(1)/N_2(2) mixtures in IRMOF-1

Figure S91: CO_2(1)/H_2(2) mixtures in IRMOF-1

Figure S92: CH_4(1)/CO_2(2) mixtures in IRMOF-1

Figure S93: CO_2(1)/H_2(2) mixtures in MgMOF-74

Figure S95: Ne(1)/Ar(2) mixtures in CuBTC

Figure S96: CH_4(1)/Ar(2) mixtures in CuBTC

Figure S97: Ne(1)/Ar(2) mixtures in LTA all-silica zeolite

Figure S98: Ne(1)/Ar(2) mixtures of varying composition in LTA all-silica zeolite

Figure S99: CH_4(1)/N_2(2) mixtures in LTA all-silica zeolite

Figure S100: CH_4(1)/H_2(2) mixtures in LTA all-silica zeolite

Figure S101: CH_4(1)/Ar(2) mixtures in LTA all-silica zeolite

Figure S102: Ar(1)/Kr(2) mixtures in LTA all-silica zeolite

Figure S103: Ne(1)/Ar(2) mixtures in CHA all-silica zeolite

Figure S104: Ne(1)/Ar(2) mixtures of varying composition in CHA all-silica zeolite

Figure S105: CH_4(1)/H_2(2) mixtures in CHA all-silica zeolite

Figure S106: CH_4(1)/Ar(2) mixtures in CHA all-silica zeolite

Figure S107: Ne(1)/Ar(2) mixtures in DDR all-silica zeolite

Figure S108: Ne(1)/Ar(2) mixtures of varying composition in DDR all-silica zeolite

Detailed case-by-case examination of panels f and g of Figure S38 to Figure S108 demonstrate that the predictions of the elements of the matrix $\left[\Lambda\right]$ using the M-S model, in combination with the Reed-Ehrlich fits of the occupancy dependence, are in good agreement with the MD simulated values. It is noteworthy, that the predictions are also good for equimolar CH_4(1)/C_2H_6(2)/C_3H_8(3) ternary mixtures in MFI and FAU zeolites; see Figure S59, and Figure S75.

9.1 Negligible correlations scenario for M-S diffusivities

For values of $Đ_1/Đ_{12} \rightarrow 0$, and $Đ_2/Đ_{12} \rightarrow 0$, the contribution of the first right member of M-S Equation (S57) can be ignored and correlations can be considered to be of negligible importance; we derive

$$\frac{Đ_1}{Đ_{12}} \rightarrow 0; \quad \frac{Đ_2}{Đ_{12}} \rightarrow 0; \quad \begin{bmatrix} \Lambda_{11} & \Lambda_{12} \\ \Lambda_{21} & \Lambda_{22} \end{bmatrix} \rightarrow \begin{bmatrix} Đ_1 & 0 \\ 0 & Đ_2 \end{bmatrix} \tag{S80}$$

As validation of equation (S80), the following set of five Figures:

Figure S99: CH_4(1)/N_2(2) mixtures in LTA all-silica zeolite

Figure S100: CH_4(1)/H_2(2) mixtures in LTA all-silica zeolite

Figure S101: CH_4(1)/Ar(2) mixtures in LTA all-silica zeolite

Figure S105: CH_4(1)/H_2(2) mixtures in CHA all-silica zeolite

Figure S106: CH_4(1)/Ar(2) mixtures in CHA all-silica zeolite

present MD simulations of the elements of the matrix $\Lambda_{11},\Lambda_{12},\Lambda_{22}$ for equimolar binary mixtures in LTA, and CHA zeolites. We note that the values of the off-diagonal elements $\Lambda_{12}=\Lambda_{21}$ are about 1 – 3 orders of magnitude lower than the corresponding values of the diagonal elements $\Lambda_{11},\Lambda_{22}$; the diagonal elements are practically the same as the unary M-S diffusivities $Đ_1$, and $Đ_2$; this is consistent with equation (S80).

When correlation effects are negligible, the diffusional coupling effects are solely traceable to mixture adsorption thermodynamics, embodied in the matrix $[\Gamma]$.

9.2 Self-diffusivities in mixture diffusion

The panel h of Figure S38 to Figure S108 compare the MD simulated data on the self-diffusivities in the binary mixture, with the predictions using equation (S81), derived in our earlier publication[1]

$$\begin{aligned}
\frac{1}{D_{1,self}}&=\frac{1}{Đ_1}+\frac{x_2}{Đ_{12}}+\frac{x_1}{Đ_{11}}=\frac{1}{Đ_1}\left(1+\frac{x_2Đ_1}{Đ_{12}}+\frac{x_1Đ_1}{Đ_{11}}\right);\\
\frac{1}{D_{2,self}}&=\frac{1}{Đ_2}+\frac{x_1}{Đ_{12}}+\frac{x_2}{Đ_{22}}=\frac{1}{Đ_2}\left(1+\frac{x_1Đ_2}{Đ_{12}}+\frac{x_2Đ_2}{Đ_{22}}\right)
\end{aligned}\tag{S81}$$

Examination of the Figures demonstrate the potency of the M-S formulation to estimate the self-diffusivities in mixture. It should also be evident from equation (S81) that the self-diffusivities are strongly influenced by both (a) degrees of self correlations, $\frac{Đ_1}{Đ_{11}},\frac{Đ_2}{Đ_{22}}$ along with (b) degrees of 1-2 correlations, $\frac{Đ_1}{Đ_{12}},\frac{Đ_2}{Đ_{12}}$.

The tardier the partner species, the higher the slowing-down of the more mobile partner species in the mixture. As illustration, Figure S109(a) presents MD simulation data on the self-diffusivities of CH_4 in binary mixtures with C_2H_6, C_3H_8, nC_4H_{10}, nC_6H_{14}, nC_7H_{16}, and nC_8H_{18} in MFI zeolite at 300 K at a total loading of 4 molecules per unit cell. The longer the chain length of the partner molecule, the larger is the reduction of the self-diffusivity of the mixture of CH_4. The same set of MD data presented in , Figure S109(a) is presented in Figure S109(b) in which the *x*-axis represents the total mixture occupancy, θ, that are determined using equations (S11), (S12), and (S13). The important conclusion to be drawn from Figure S109(a, b) the reduction in the self-diffusivity of methane in the mixture is largely attributable to the increase in the occupancy; for the same molar loading, mixture with longer alkane chains have higher pore occupancy resulting in increased slowing-down effects.

9.3 List of Figures for Maxwell-Stefan estimation of mixture diffusion

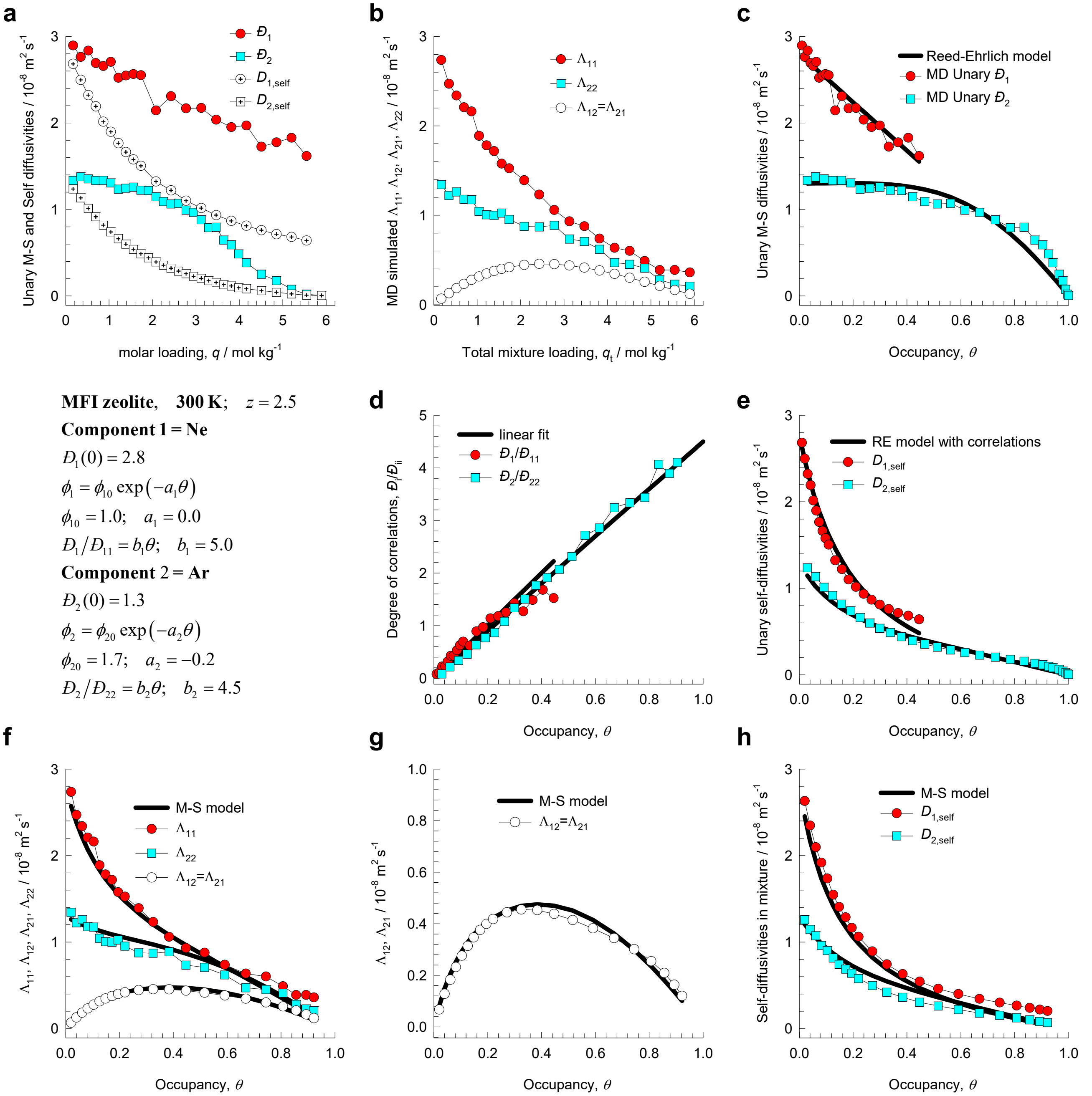

MFI zeolite, 300 K; $z = 2.5$

Component 1 = Ne

$\text{Đ}_1(0) = 2.8$

$\phi_1 = \phi_{10}\exp(-a_1\theta)$

$\phi_{10} = 1.0;\quad a_1 = 0.0$

$\text{Đ}_1/\text{Đ}_{11} = b_1\theta;\quad b_1 = 5.0$

Component 2 = Ar

$\text{Đ}_2(0) = 1.3$

$\phi_2 = \phi_{20}\exp(-a_2\theta)$

$\phi_{20} = 1.7;\quad a_2 = -0.2$

$\text{Đ}_2/\text{Đ}_{22} = b_2\theta;\quad b_2 = 4.5$

Figure S38. (a-h) MD simulated values of $\Lambda_{11},\Lambda_{12},\Lambda_{21},\Lambda_{22}$ for equimolar (q_1=q_2) binary Ne(1)/Ar(2) mixtures in MFI zeolite at 300 K, compared with the estimations (continuous solid lines) using the Maxwell-Stefan model, based on fitted data for unary diffusivities, $\text{Đ}_1,\text{Đ}_2$, and unary degrees of correlations, $\text{Đ}_1/\text{Đ}_{11},\text{Đ}_2/\text{Đ}_{22}$.

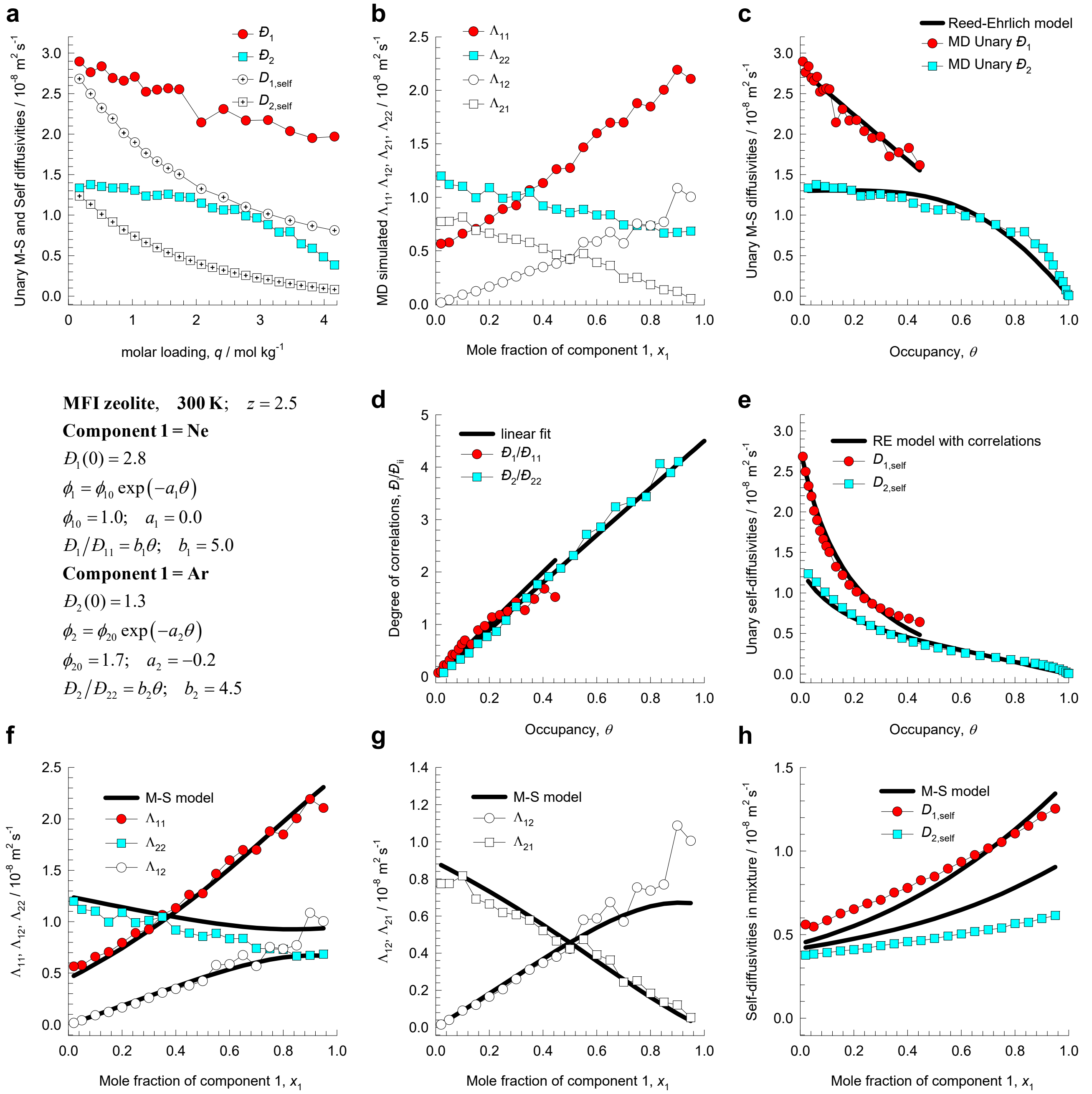

MFI zeolite, 300 K; $z = 2.5$
Component 1 = Ne
$Đ_1(0) = 2.8$
$\phi_1 = \phi_{10}\exp(-a_1\theta)$
$\phi_{10} = 1.0; \quad a_1 = 0.0$
$Đ_1/Đ_{11} = b_1\theta; \quad b_1 = 5.0$
Component 1 = Ar
$Đ_2(0) = 1.3$
$\phi_2 = \phi_{20}\exp(-a_2\theta)$
$\phi_{20} = 1.7; \quad a_2 = -0.2$
$Đ_2/Đ_{22} = b_2\theta; \quad b_2 = 4.5$

Figure S39. (a-h) MD simulated values of $\Lambda_{11},\Lambda_{12},\Lambda_{21},\Lambda_{22}$ for binary Ne(1)/Ar(2) mixtures of varying composition (total loading = 12.5 molecules uc^{-1}) in MFI zeolite at 300 K, compared with the estimations (continuous solid lines) using the Maxwell-Stefan model, based on fitted data for unary diffusivities, $Đ_1, Đ_2$, and unary degrees of correlations, $Đ_1/Đ_{11}, Đ_2/Đ_{22}$.

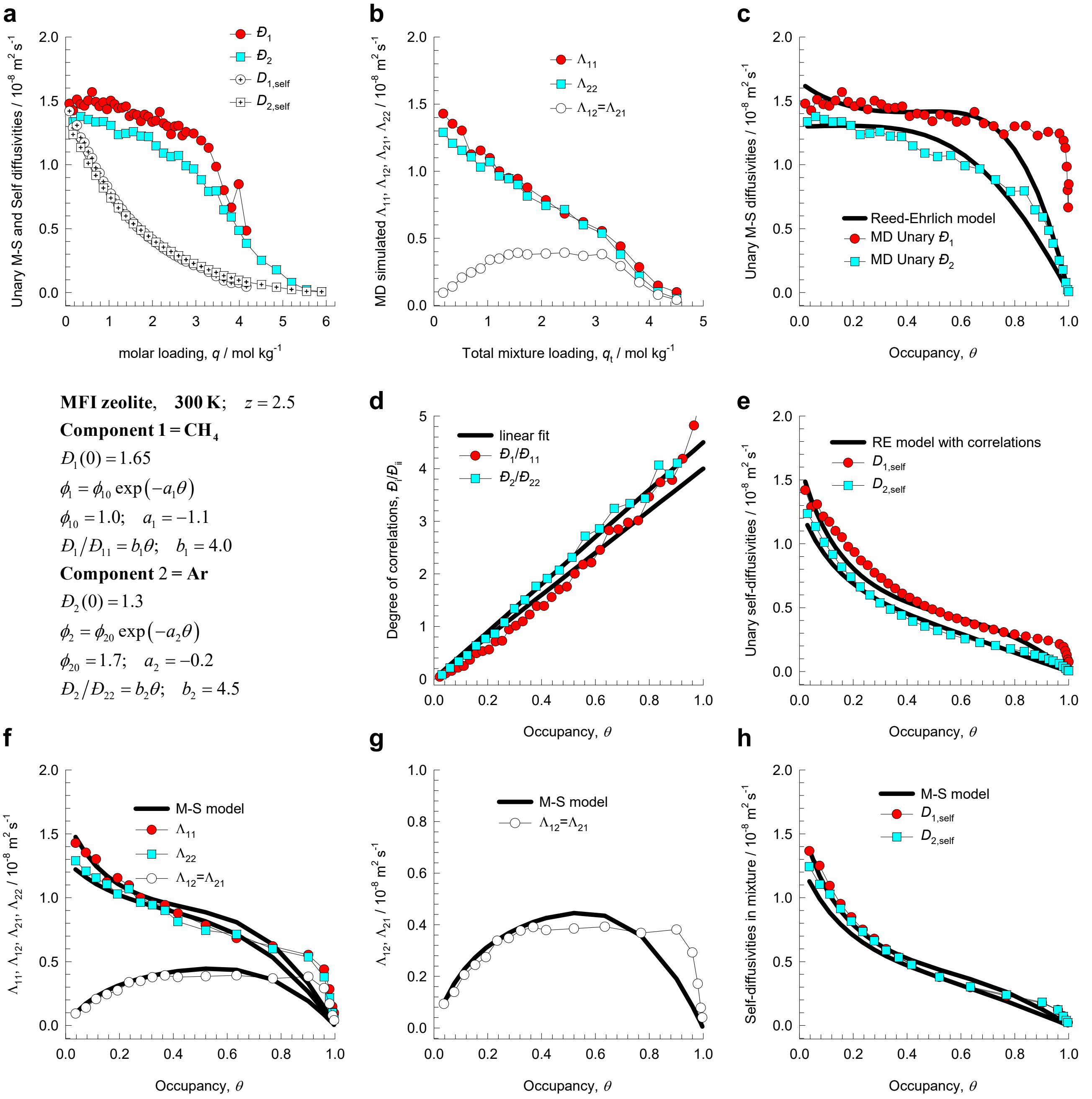

MFI zeolite, 300 K; $z = 2.5$

Component 1 = CH$_4$

$Đ_1(0) = 1.65$

$\phi_1 = \phi_{10}\exp(-a_1\theta)$

$\phi_{10} = 1.0;\quad a_1 = -1.1$

$Đ_1/Đ_{11} = b_1\theta;\quad b_1 = 4.0$

Component 2 = Ar

$Đ_2(0) = 1.3$

$\phi_2 = \phi_{20}\exp(-a_2\theta)$

$\phi_{20} = 1.7;\quad a_2 = -0.2$

$Đ_2/Đ_{22} = b_2\theta;\quad b_2 = 4.5$

Figure S40. (a-h) MD simulated values of $\Lambda_{11},\Lambda_{12},\Lambda_{21},\Lambda_{22}$ for equimolar (q_1=q_2) binary CH$_4$(1)/Ar(2) mixtures in MFI zeolite at 300 K, compared with the estimations (continuous solid lines) using the Maxwell-Stefan model, based on fitted data for unary diffusivities, $Đ_1, Đ_2$, and unary degrees of correlations, $Đ_1/Đ_{11}, Đ_2/Đ_{22}$.

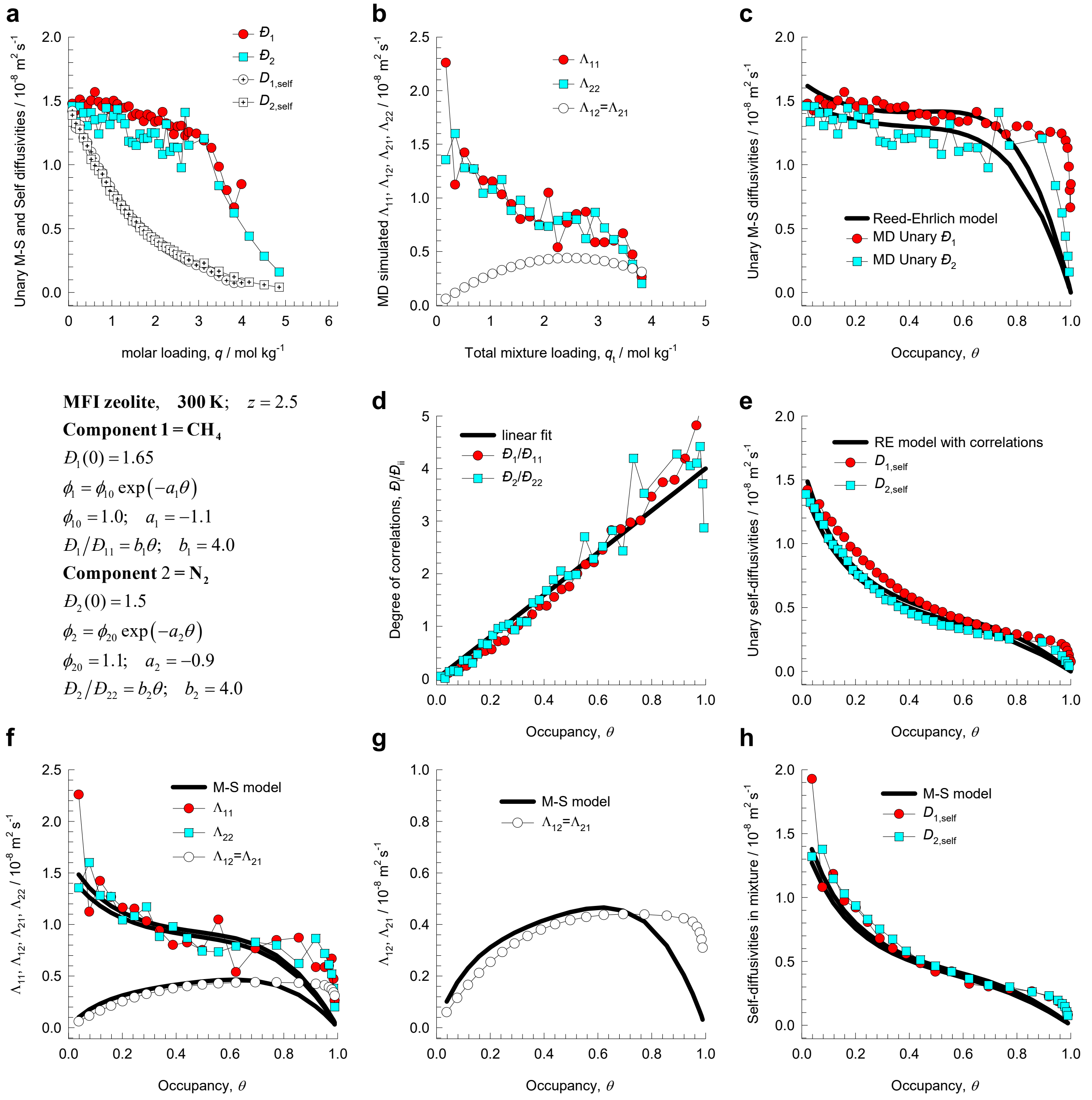

MFI zeolite, 300 K; $z = 2.5$

Component 1 = CH_4

$Đ_1(0) = 1.65$

$\phi_1 = \phi_{10} \exp(-a_1\theta)$

$\phi_{10} = 1.0; \quad a_1 = -1.1$

$Đ_1/Đ_{11} = b_1\theta; \quad b_1 = 4.0$

Component 2 = N_2

$Đ_2(0) = 1.5$

$\phi_2 = \phi_{20} \exp(-a_2\theta)$

$\phi_{20} = 1.1; \quad a_2 = -0.9$

$Đ_2/Đ_{22} = b_2\theta; \quad b_2 = 4.0$

Figure S41. (a-h) MD simulated values of $\Lambda_{11}, \Lambda_{12}, \Lambda_{21}, \Lambda_{22}$ for equimolar (q_1=q_2) binary CH_4(1)/N_2(2) mixtures in MFI zeolite at 300 K, compared with the estimations (continuous solid lines) using the Maxwell-Stefan model, based on fitted data for unary diffusivities, $Đ_1, Đ_2$, and unary degrees of correlations, $Đ_1/Đ_{11}, Đ_2/Đ_{22}$.

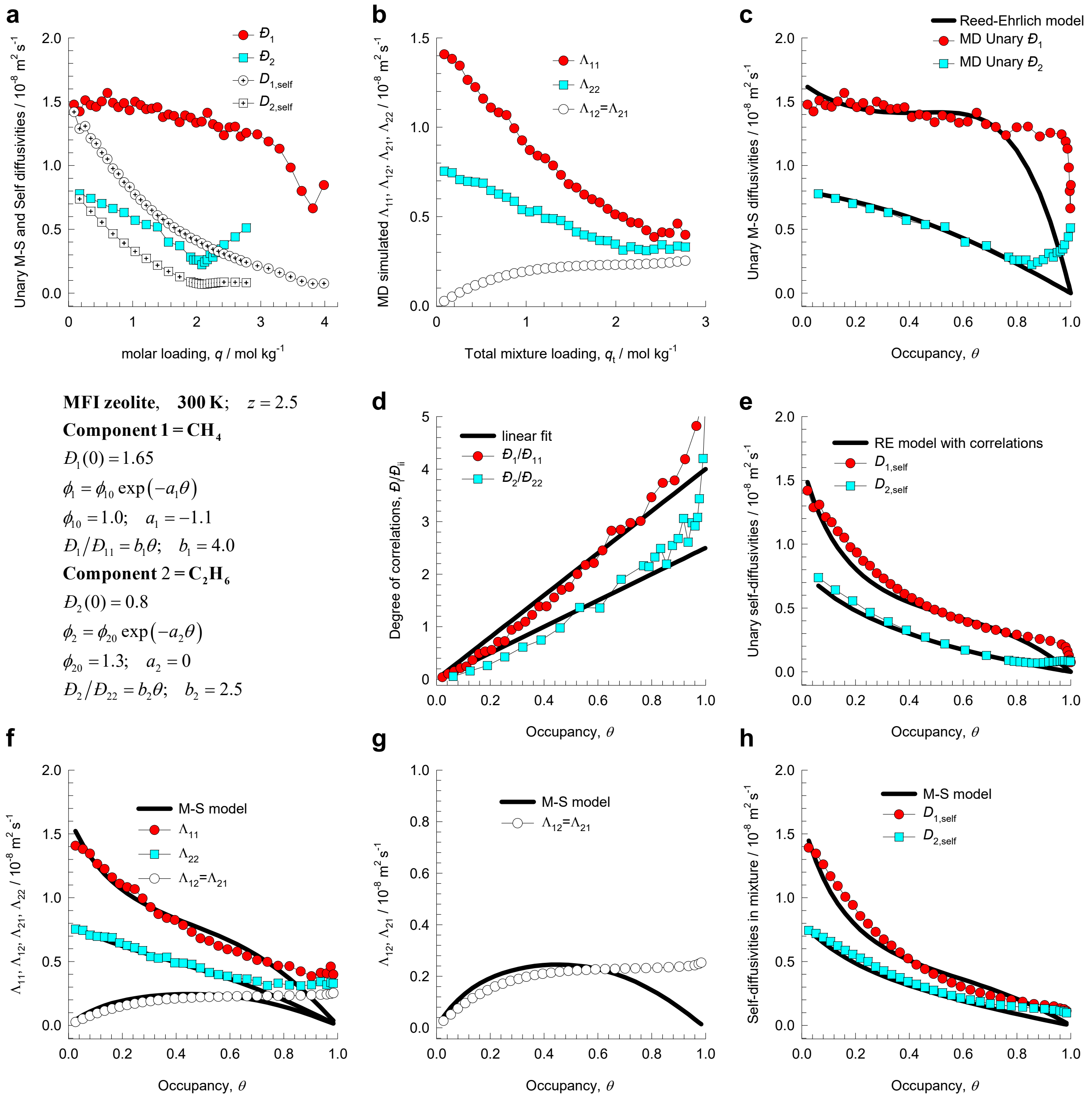

MFI zeolite, 300 K; $z = 2.5$

Component 1 = $\mathbf{CH_4}$

$\text{Đ}_1(0) = 1.65$

$\phi_1 = \phi_{10}\exp(-a_1\theta)$

$\phi_{10} = 1.0; \quad a_1 = -1.1$

$\text{Đ}_1/\text{Đ}_{11} = b_1\theta; \quad b_1 = 4.0$

Component 2 = $\mathbf{C_2H_6}$

$\text{Đ}_2(0) = 0.8$

$\phi_2 = \phi_{20}\exp(-a_2\theta)$

$\phi_{20} = 1.3; \quad a_2 = 0$

$\text{Đ}_2/\text{Đ}_{22} = b_2\theta; \quad b_2 = 2.5$

Figure S42. (a-h) MD simulated values of $\Lambda_{11}, \Lambda_{12}, \Lambda_{21}, \Lambda_{22}$ for equimolar (q_1=q_2) binary CH_4(1)/C_2H_6(2) mixtures in MFI zeolite at 300 K, compared with the estimations (continuous solid lines) using the Maxwell-Stefan model, based on fitted data for unary diffusivities, $\text{Đ}_1, \text{Đ}_2$, and unary degrees of correlations, $\text{Đ}_1/\text{Đ}_{11}, \text{Đ}_2/\text{Đ}_{22}$.

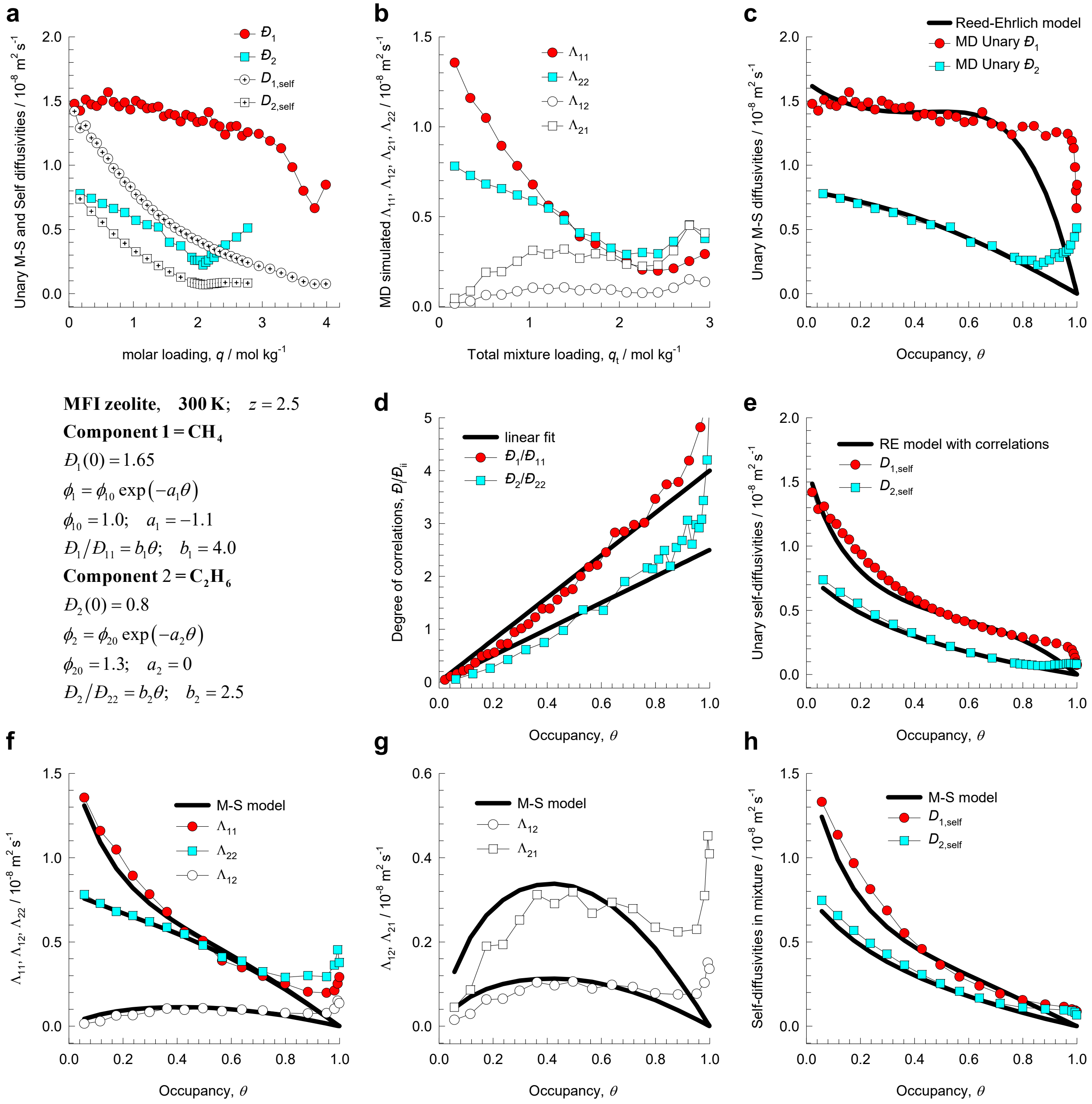

MFI zeolite, 300 K; $z = 2.5$

Component 1 = CH$_4$

$Đ_1(0) = 1.65$

$\phi_1 = \phi_{10} \exp(-a_1\theta)$

$\phi_{10} = 1.0; \quad a_1 = -1.1$

$Đ_1/Đ_{11} = b_1\theta; \quad b_1 = 4.0$

Component 2 = C$_2$H$_6$

$Đ_2(0) = 0.8$

$\phi_2 = \phi_{20} \exp(-a_2\theta)$

$\phi_{20} = 1.3; \quad a_2 = 0$

$Đ_2/Đ_{22} = b_2\theta; \quad b_2 = 2.5$

Figure S43. (a-h) MD simulated values of $\Lambda_{11}, \Lambda_{12}, \Lambda_{21}, \Lambda_{22}$ for 25/75 (q_1/q_2=25/75) binary CH$_4$(1)/C$_2$H$_6$(2) mixtures in MFI zeolite at 300 K, compared with the estimations (continuous solid lines) using the Maxwell-Stefan model, based on fitted data for unary diffusivities, $Đ_1, Đ_2$, and unary degrees of correlations, $Đ_1/Đ_{11}, Đ_2/Đ_{22}$.

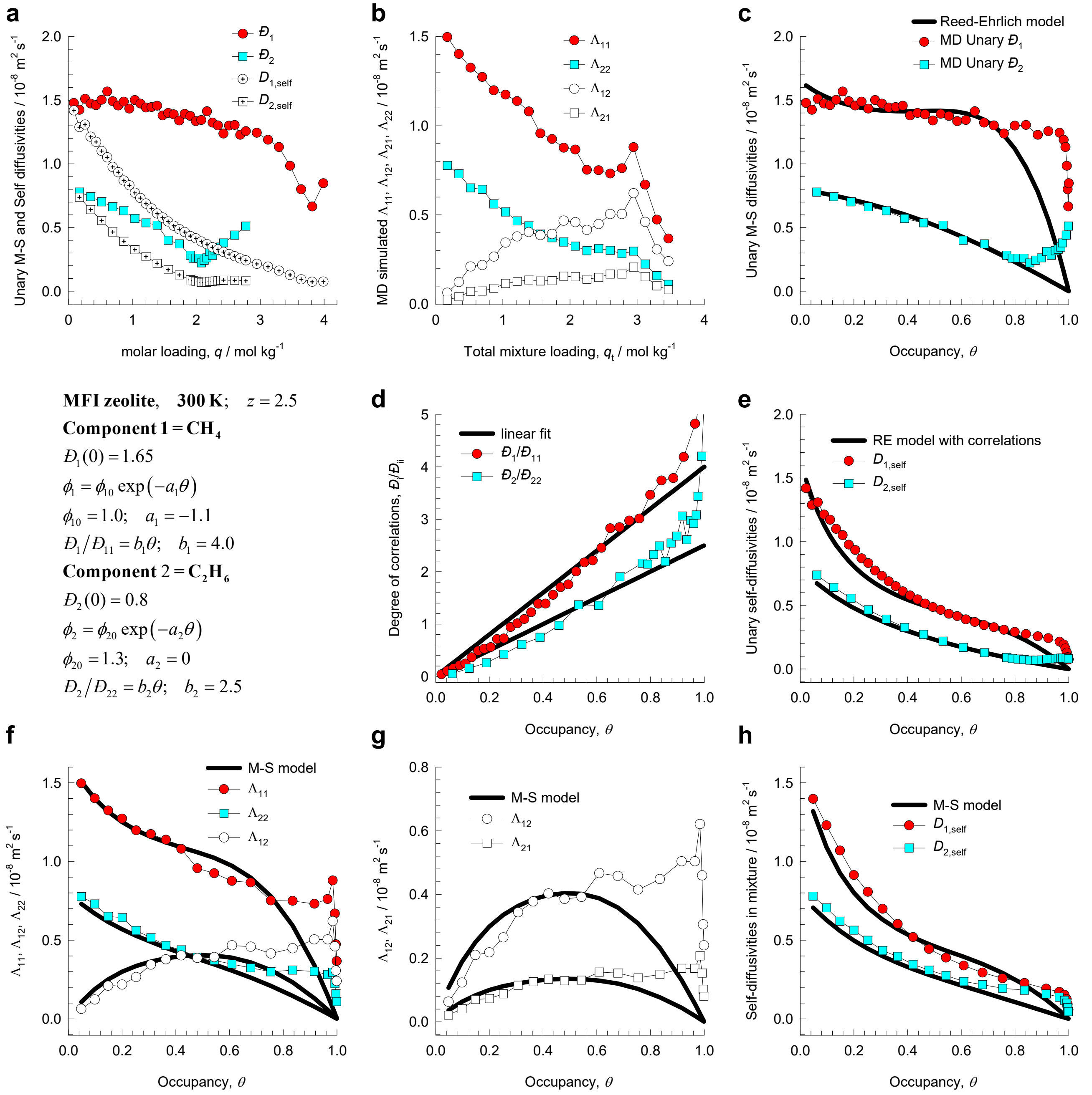

MFI zeolite, 300 K; $z = 2.5$

Component 1 = CH_4

$Đ_1(0) = 1.65$

$\phi_1 = \phi_{10} \exp(-a_1\theta)$

$\phi_{10} = 1.0; \quad a_1 = -1.1$

$Đ_1/Đ_{11} = b_1\theta; \quad b_1 = 4.0$

Component 2 = C_2H_6

$Đ_2(0) = 0.8$

$\phi_2 = \phi_{20} \exp(-a_2\theta)$

$\phi_{20} = 1.3; \quad a_2 = 0$

$Đ_2/Đ_{22} = b_2\theta; \quad b_2 = 2.5$

Figure S44. (a-h) MD simulated values of $\Lambda_{11},\Lambda_{12},\Lambda_{21},\Lambda_{22}$ for 75/25 (q_1/q_2=75/25) binary CH_4(1)/C_2H_4(2) mixtures in MFI zeolite at 300 K, compared with the estimations (continuous solid lines) using the Maxwell-Stefan model, based on fitted data for unary diffusivities, $Đ_1, Đ_2$, and unary degrees of correlations, $Đ_1/Đ_{11}, Đ_2/Đ_{22}$.

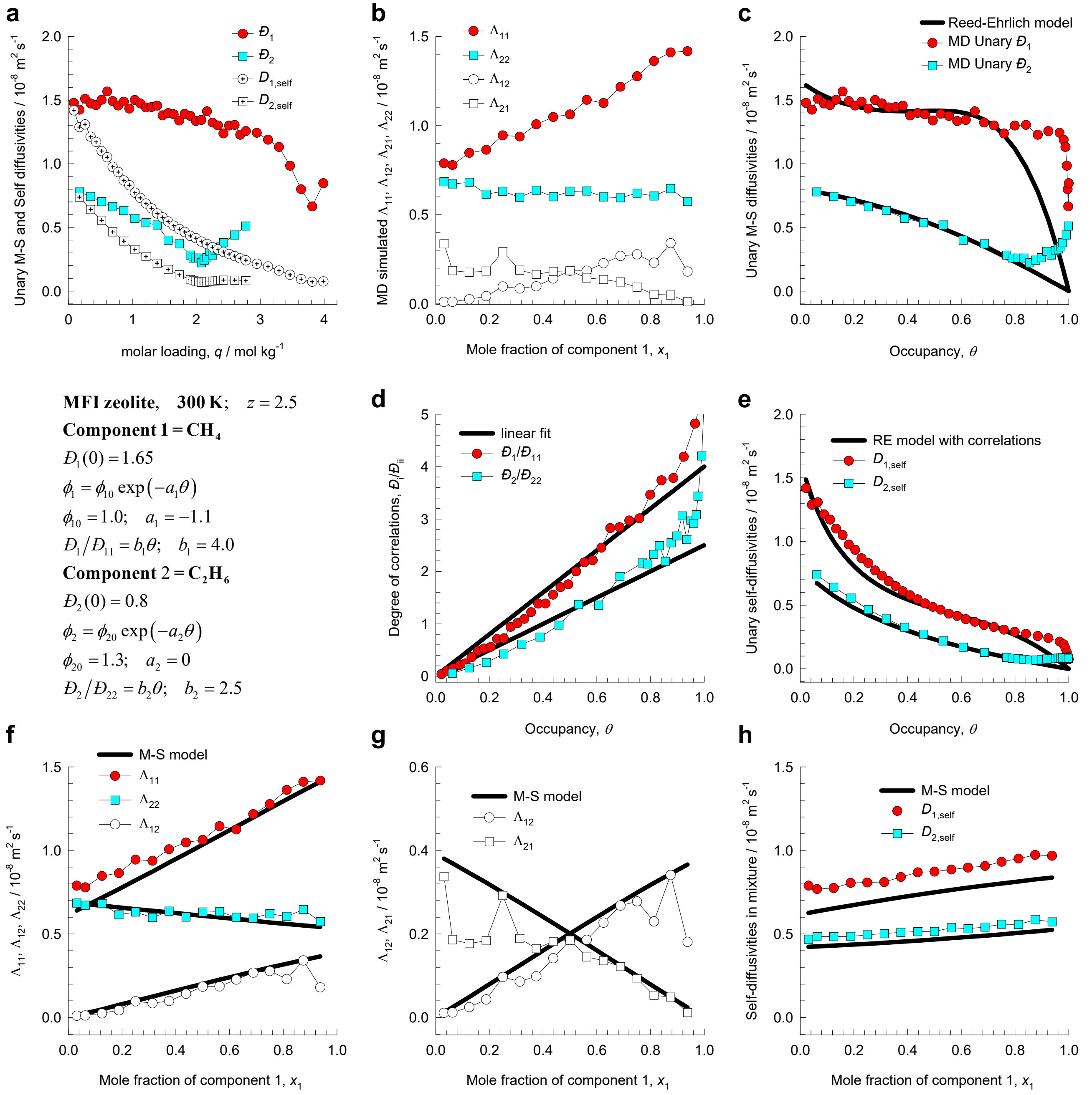

MFI zeolite, 300 K; $z = 2.5$

Component 1 = $\mathbf{CH_4}$

$\text{Đ}_1(0) = 1.65$

$\phi_1 = \phi_{10} \exp(-a_1\theta)$

$\phi_{10} = 1.0; \quad a_1 = -1.1$

$\text{Đ}_1/\text{Đ}_{11} = b_1\theta; \quad b_1 = 4.0$

Component 2 = $\mathbf{C_2H_6}$

$\text{Đ}_2(0) = 0.8$

$\phi_2 = \phi_{20} \exp(-a_2\theta)$

$\phi_{20} = 1.3; \quad a_2 = 0$

$\text{Đ}_2/\text{Đ}_{22} = b_2\theta; \quad b_2 = 2.5$

Figure S45. (a-h) MD simulated values of $\Lambda_{11},\Lambda_{12},\Lambda_{21},\Lambda_{22}$ for binary CH_4(1)/C_2H_4(2) mixtures of varying composition (total loading = 4 molecules uc^{-1}) in MFI zeolite at 300 K, compared with the estimations (continuous solid lines) using the Maxwell-Stefan model, based on fitted data for unary diffusivities, $\text{Đ}_1,\text{Đ}_2$, and unary degrees of correlations, $\text{Đ}_1/\text{Đ}_{11},\text{Đ}_2/\text{Đ}_{22}$.

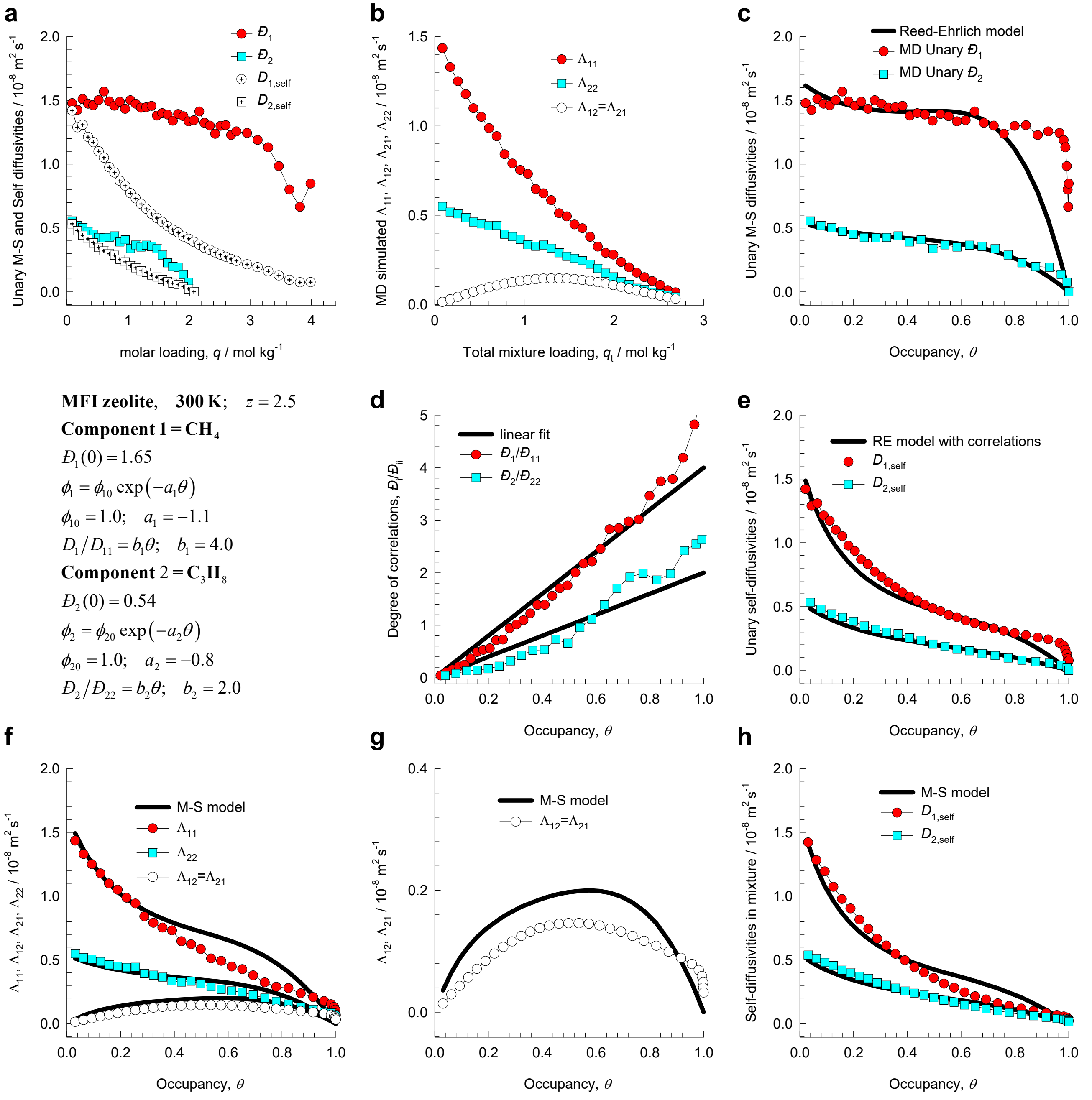

MFI zeolite, 300 K; $z = 2.5$

Component 1 = CH$_4$

$\text{Đ}_1(0) = 1.65$

$\phi_1 = \phi_{10}\exp(-a_1\theta)$

$\phi_{10} = 1.0;\quad a_1 = -1.1$

$\text{Đ}_1/\text{Đ}_{11} = b_1\theta;\quad b_1 = 4.0$

Component 2 = C$_3$H$_8$

$\text{Đ}_2(0) = 0.54$

$\phi_2 = \phi_{20}\exp(-a_2\theta)$

$\phi_{20} = 1.0;\quad a_2 = -0.8$

$\text{Đ}_2/\text{Đ}_{22} = b_2\theta;\quad b_2 = 2.0$

Figure S46. (a-h) MD simulated values of $\Lambda_{11},\Lambda_{12},\Lambda_{21},\Lambda_{22}$ for equimolar (q_1=q_2) binary CH$_4$(1)/C$_3$H$_8$(2) mixtures in MFI zeolite at 300 K, compared with the estimations (continuous solid lines) using the Maxwell-Stefan model, based on fitted data for unary diffusivities, $\text{Đ}_1,\text{Đ}_2$, and unary degrees of correlations, $\text{Đ}_1/\text{Đ}_{11},\text{Đ}_2/\text{Đ}_{22}$.

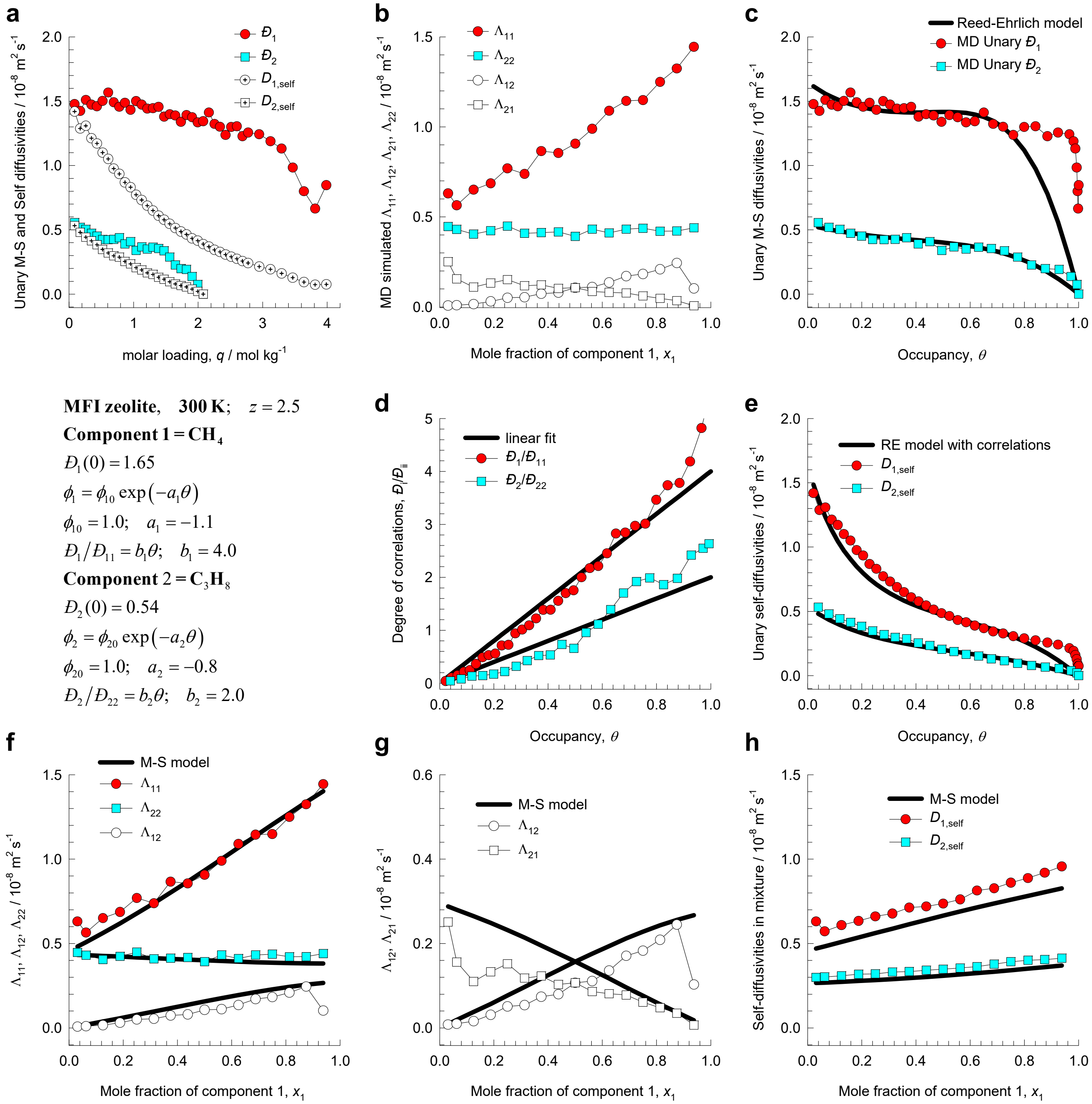

MFI zeolite, 300 K; $z = 2.5$

Component 1 = CH_4

$\text{Đ}_1(0) = 1.65$

$\phi_1 = \phi_{10}\exp(-a_1\theta)$

$\phi_{10} = 1.0; \quad a_1 = -1.1$

$\text{Đ}_1/\text{Đ}_{11} = b_1\theta; \quad b_1 = 4.0$

Component 2 = C_3H_8

$\text{Đ}_2(0) = 0.54$

$\phi_2 = \phi_{20}\exp(-a_2\theta)$

$\phi_{20} = 1.0; \quad a_2 = -0.8$

$\text{Đ}_2/\text{Đ}_{22} = b_2\theta; \quad b_2 = 2.0$

Figure S47. (a-h) MD simulated values of $\Lambda_{11},\Lambda_{12},\Lambda_{21},\Lambda_{22}$ for binary CH_4(1)/C_3H_8(2) mixtures of varying composition (total loading = 4 molecules uc^{-1}) in MFI zeolite at 300 K, compared with the estimations (continuous solid lines) using the Maxwell-Stefan model, based on fitted data for unary diffusivities, $\text{Đ}_1,\text{Đ}_2$, and unary degrees of correlations, $\text{Đ}_1/\text{Đ}_{11},\text{Đ}_2/\text{Đ}_{22}$.

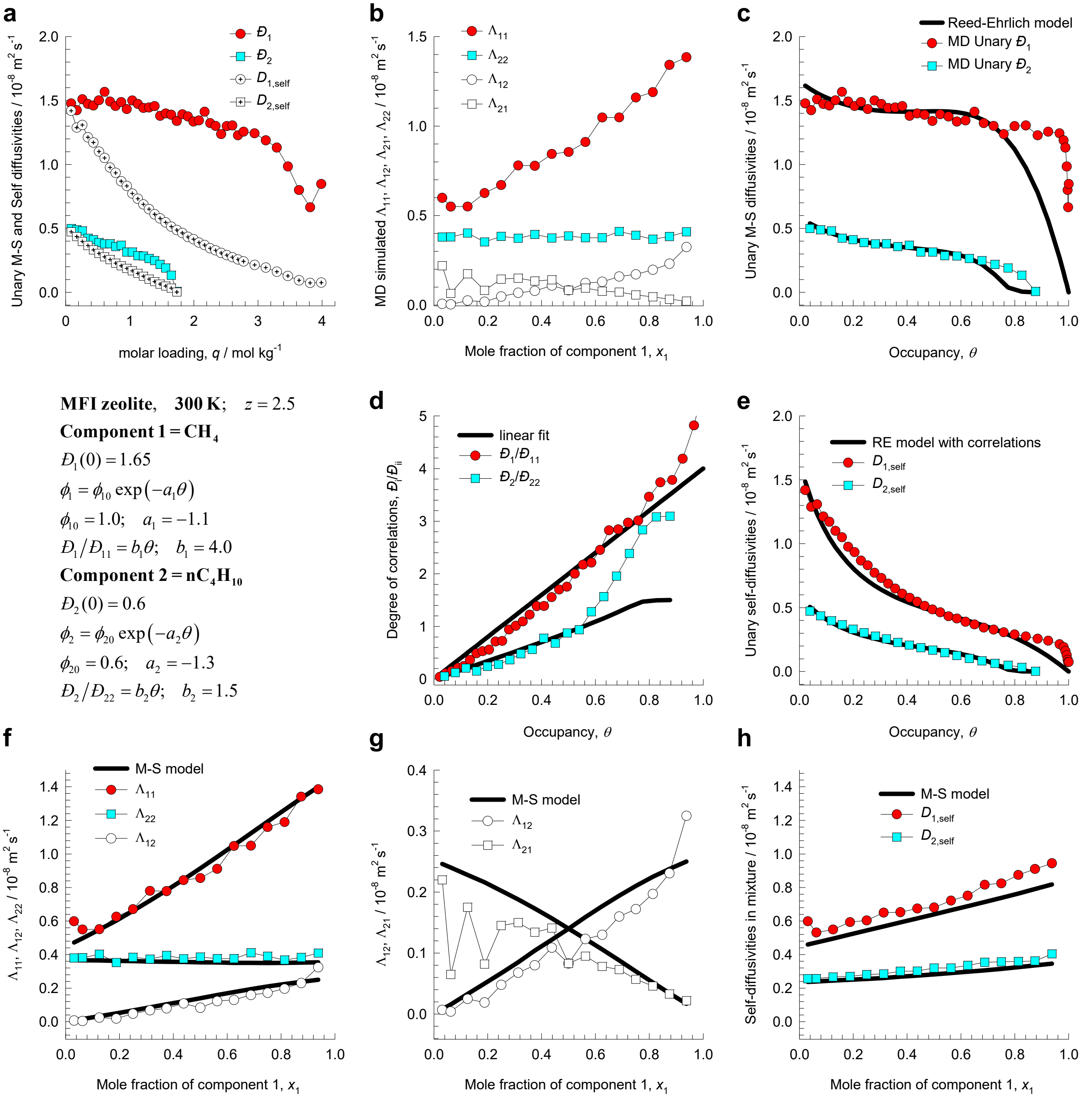

MFI zeolite, 300 K; $z = 2.5$

Component 1 = CH_4

$Đ_1(0) = 1.65$

$\phi_1 = \phi_{10} \exp(-a_1\theta)$

$\phi_{10} = 1.0; \quad a_1 = -1.1$

$Đ_1/Đ_{11} = b_1\theta; \quad b_1 = 4.0$

Component 2 = nC_4H_{10}

$Đ_2(0) = 0.6$

$\phi_2 = \phi_{20} \exp(-a_2\theta)$

$\phi_{20} = 0.6; \quad a_2 = -1.3$

$Đ_2/Đ_{22} = b_2\theta; \quad b_2 = 1.5$

Figure S48. (a-h) MD simulated values of $\Lambda_{11}, \Lambda_{12}, \Lambda_{21}, \Lambda_{22}$ for binary CH_4(1)/nC_4H_{10}(2) mixtures of varying composition (total loading = 4 molecules uc^{-1}) in MFI zeolite at 300 K, compared with the estimations (continuous solid lines) using the Maxwell-Stefan model, based on fitted data for unary diffusivities, $Đ_1, Đ_2$, and unary degrees of correlations, $Đ_1/Đ_{11}, Đ_2/Đ_{22}$.

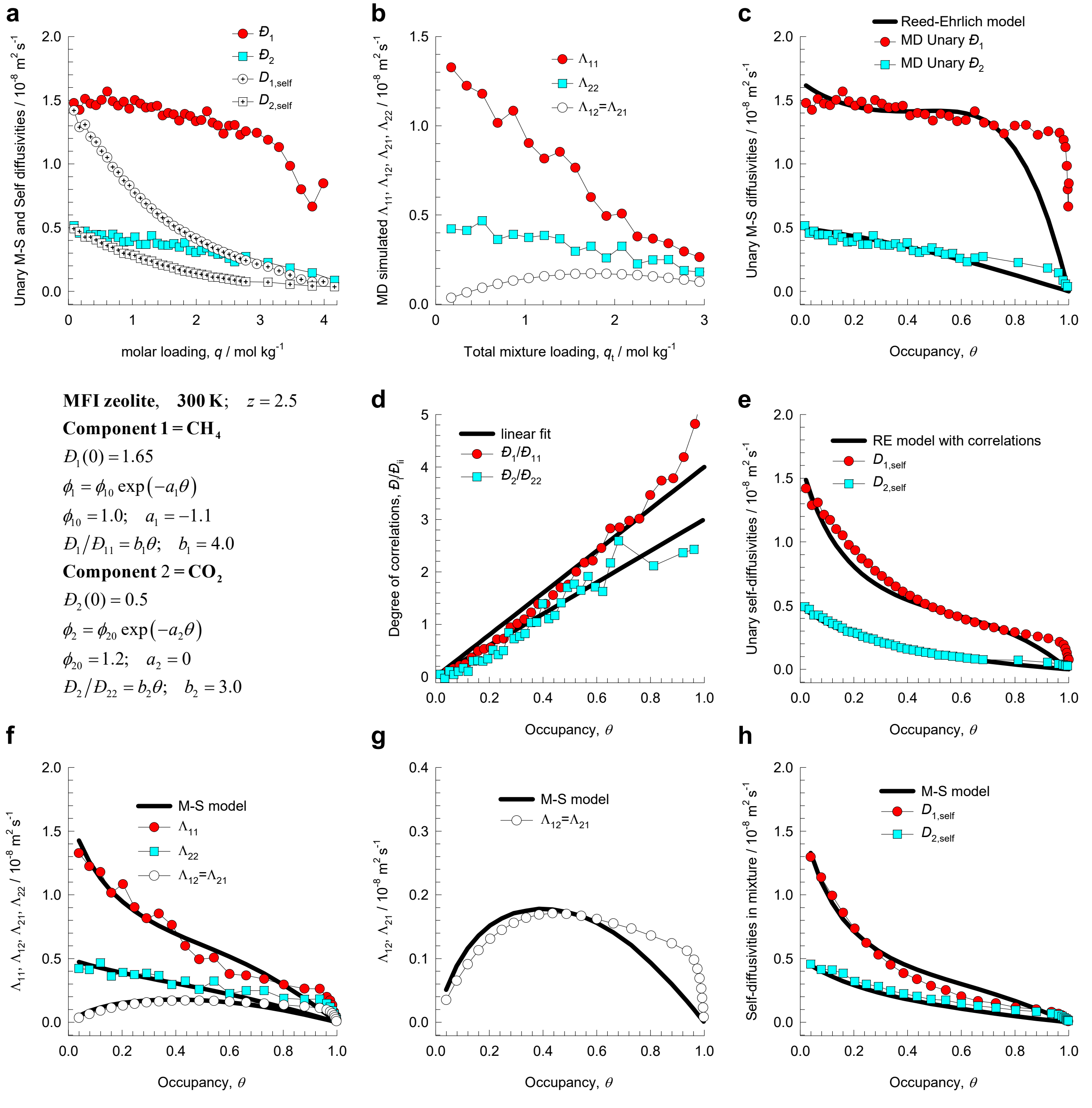

MFI zeolite, 300 K; $z = 2.5$

Component 1 = CH_4

$Đ_1(0) = 1.65$

$\phi_1 = \phi_{10} \exp(-a_1\theta)$

$\phi_{10} = 1.0; \quad a_1 = -1.1$

$Đ_1/Đ_{11} = b_1\theta; \quad b_1 = 4.0$

Component 2 = CO_2

$Đ_2(0) = 0.5$

$\phi_2 = \phi_{20} \exp(-a_2\theta)$

$\phi_{20} = 1.2; \quad a_2 = 0$

$Đ_2/Đ_{22} = b_2\theta; \quad b_2 = 3.0$

Figure S49. (a-h) MD simulated values of $\Lambda_{11},\Lambda_{12},\Lambda_{21},\Lambda_{22}$ for equimolar (q_1=q_2) binary CH_4(1)/CO_2(2) mixtures in MFI zeolite at 300 K, compared with the estimations (continuous solid lines) using the Maxwell-Stefan model, based on fitted data for unary diffusivities, $Đ_1, Đ_2$, and unary degrees of correlations, $Đ_1/Đ_{11}, Đ_2/Đ_{22}$.

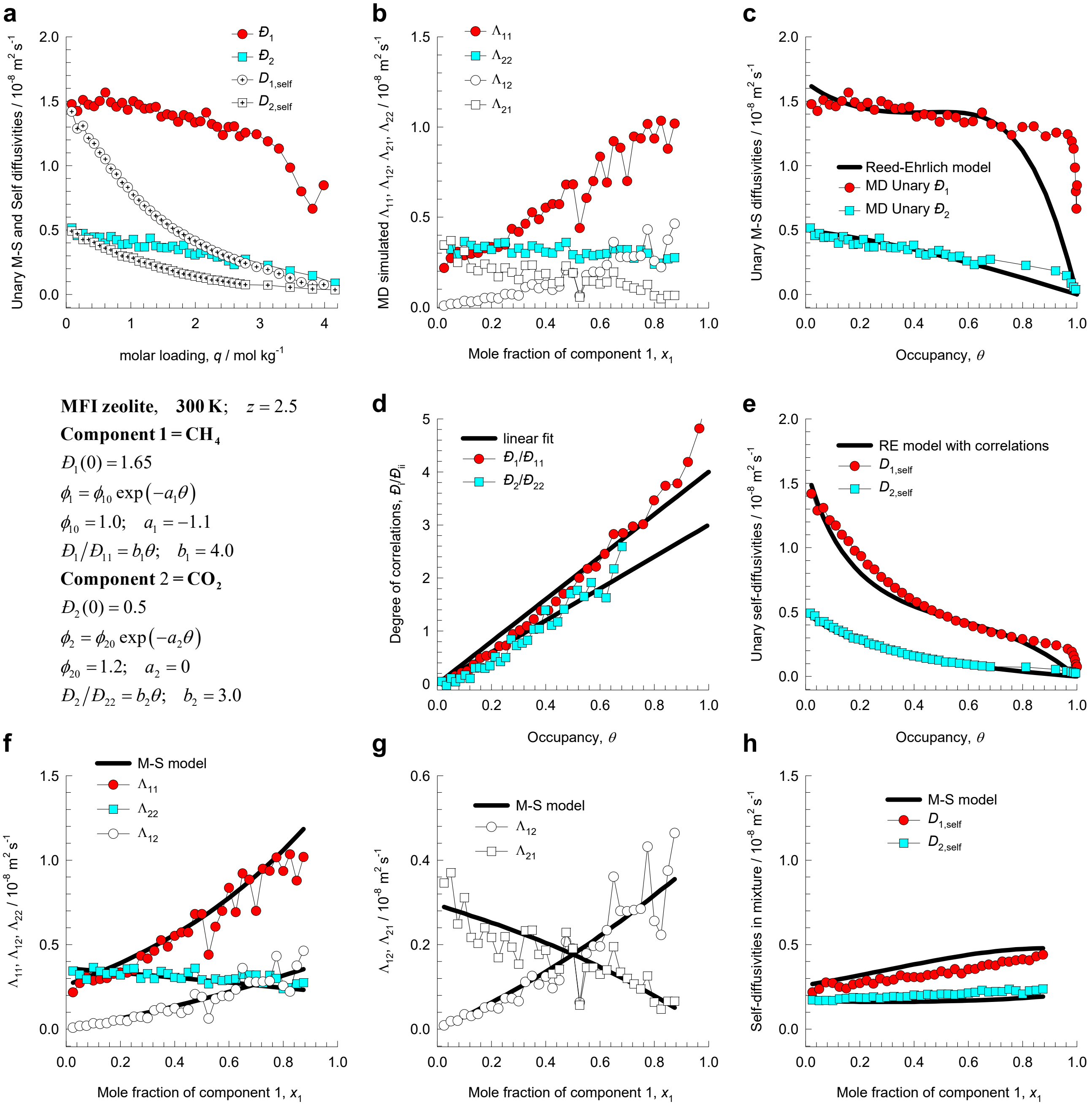

MFI zeolite, 300 K; $z = 2.5$
Component 1 = CH$_4$
$Đ_1(0) = 1.65$
$\phi_1 = \phi_{10}\exp(-a_1\theta)$
$\phi_{10} = 1.0;\quad a_1 = -1.1$
$Đ_1/Đ_{11} = b_1\theta;\quad b_1 = 4.0$
Component 2 = CO$_2$
$Đ_2(0) = 0.5$
$\phi_2 = \phi_{20}\exp(-a_2\theta)$
$\phi_{20} = 1.2;\quad a_2 = 0$
$Đ_2/Đ_{22} = b_2\theta;\quad b_2 = 3.0$

Figure S50. (a-h) MD simulated values of $\Lambda_{11}, \Lambda_{12}, \Lambda_{21}, \Lambda_{22}$ for binary CH$_4$(1)/CO$_2$(2) mixtures of varying composition (keeping total loading constant at 10 molecules uc^{-1}) in MFI zeolite at 300 K, compared with the estimations (continuous solid lines) using the Maxwell-Stefan model, based on fitted data for unary diffusivities, $Đ_1, Đ_2$, and unary degrees of correlations, $Đ_1/Đ_{11}, Đ_2/Đ_{22}$.

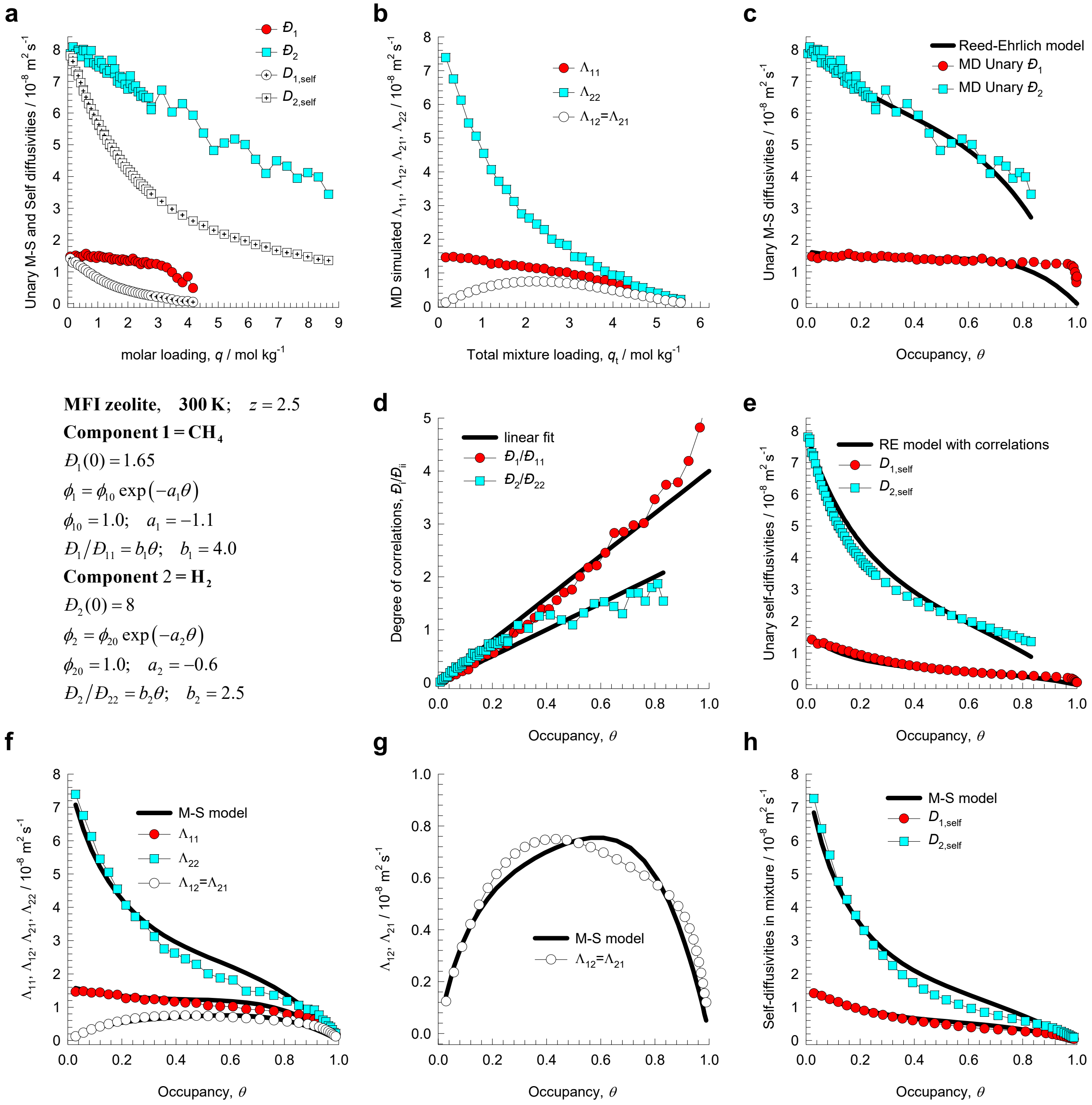

MFI zeolite, 300 K; $z = 2.5$
Component 1 = CH_4
$Đ_1(0) = 1.65$
$\phi_1 = \phi_{10} \exp(-a_1\theta)$
$\phi_{10} = 1.0; \quad a_1 = -1.1$
$Đ_1/Đ_{11} = b_1\theta; \quad b_1 = 4.0$
Component 2 = H_2
$Đ_2(0) = 8$
$\phi_2 = \phi_{20} \exp(-a_2\theta)$
$\phi_{20} = 1.0; \quad a_2 = -0.6$
$Đ_2/Đ_{22} = b_2\theta; \quad b_2 = 2.5$

Figure S51. (a-h) MD simulated values of $\Lambda_{11}, \Lambda_{12}, \Lambda_{21}, \Lambda_{22}$ for equimolar (q_1=q_2) binary CH_4(1)/H_2(2) mixtures in MFI zeolite at 300 K, compared with the estimations (continuous solid lines) using the Maxwell-Stefan model, based on fitted data of unary diffusivities, $Đ_1, Đ_2$, and unary degrees of correlations, $Đ_1/Đ_{11}, Đ_2/Đ_{22}$.

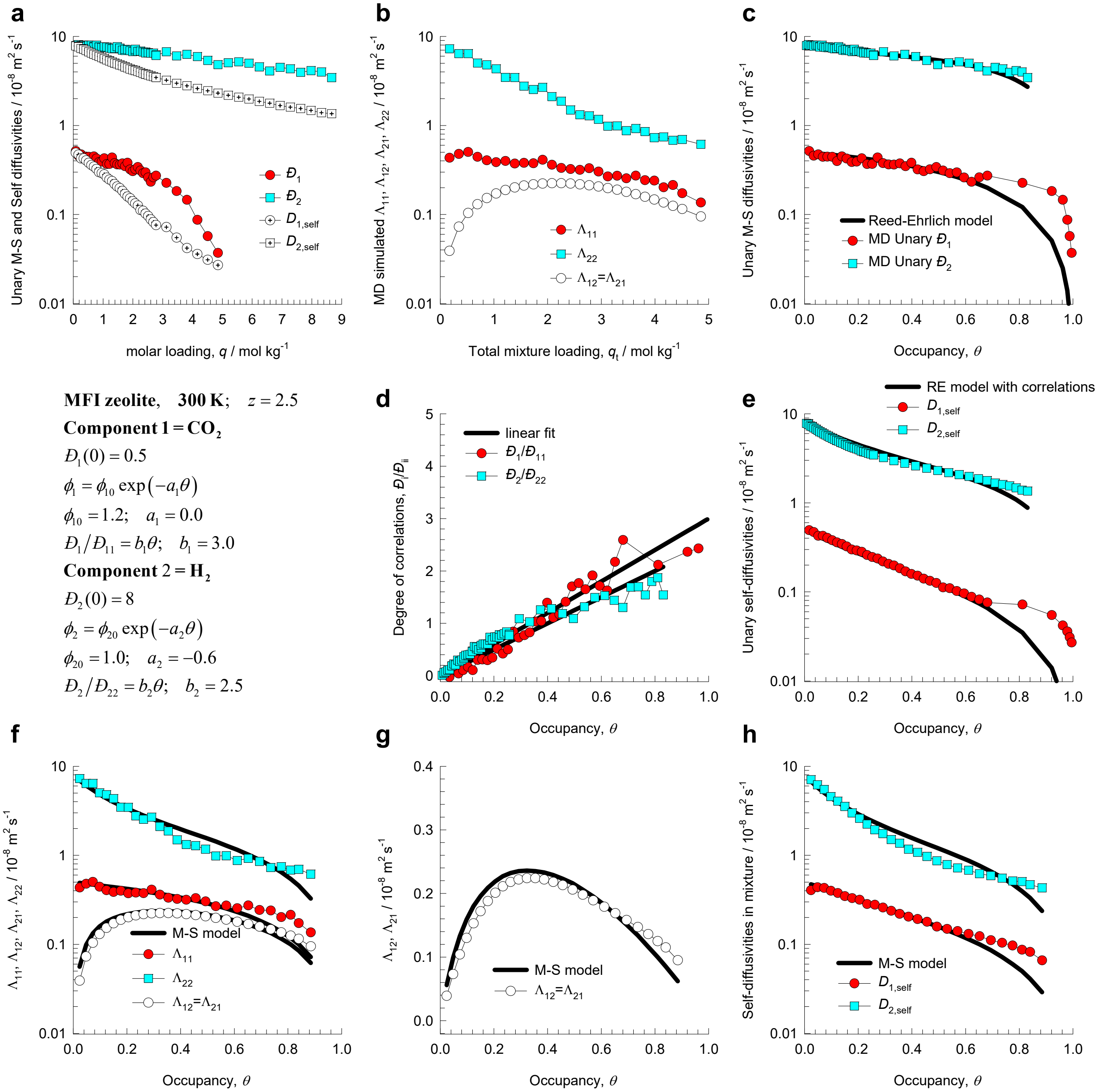

MFI zeolite, 300 K; $z = 2.5$

Component 1 = CO_2

$Đ_1(0) = 0.5$

$\phi_1 = \phi_{10}\exp(-a_1\theta)$

$\phi_{10} = 1.2; \quad a_1 = 0.0$

$Đ_1/Đ_{11} = b_1\theta; \quad b_1 = 3.0$

Component 2 = H_2

$Đ_2(0) = 8$

$\phi_2 = \phi_{20}\exp(-a_2\theta)$

$\phi_{20} = 1.0; \quad a_2 = -0.6$

$Đ_2/Đ_{22} = b_2\theta; \quad b_2 = 2.5$

Figure S52. (a-h) MD simulated values of $\Lambda_{11},\Lambda_{12},\Lambda_{21},\Lambda_{22}$ for equimolar (q_1=q_2) binary CO_2(1)/H_2(2) mixtures in MFI zeolite at 300 K, compared with the estimations (continuous solid lines) using the Maxwell-Stefan model, based on fitted data of unary diffusivities, $Đ_1,Đ_2$, and unary degrees of correlations, $Đ_1/Đ_{11}, Đ_2/Đ_{22}$.

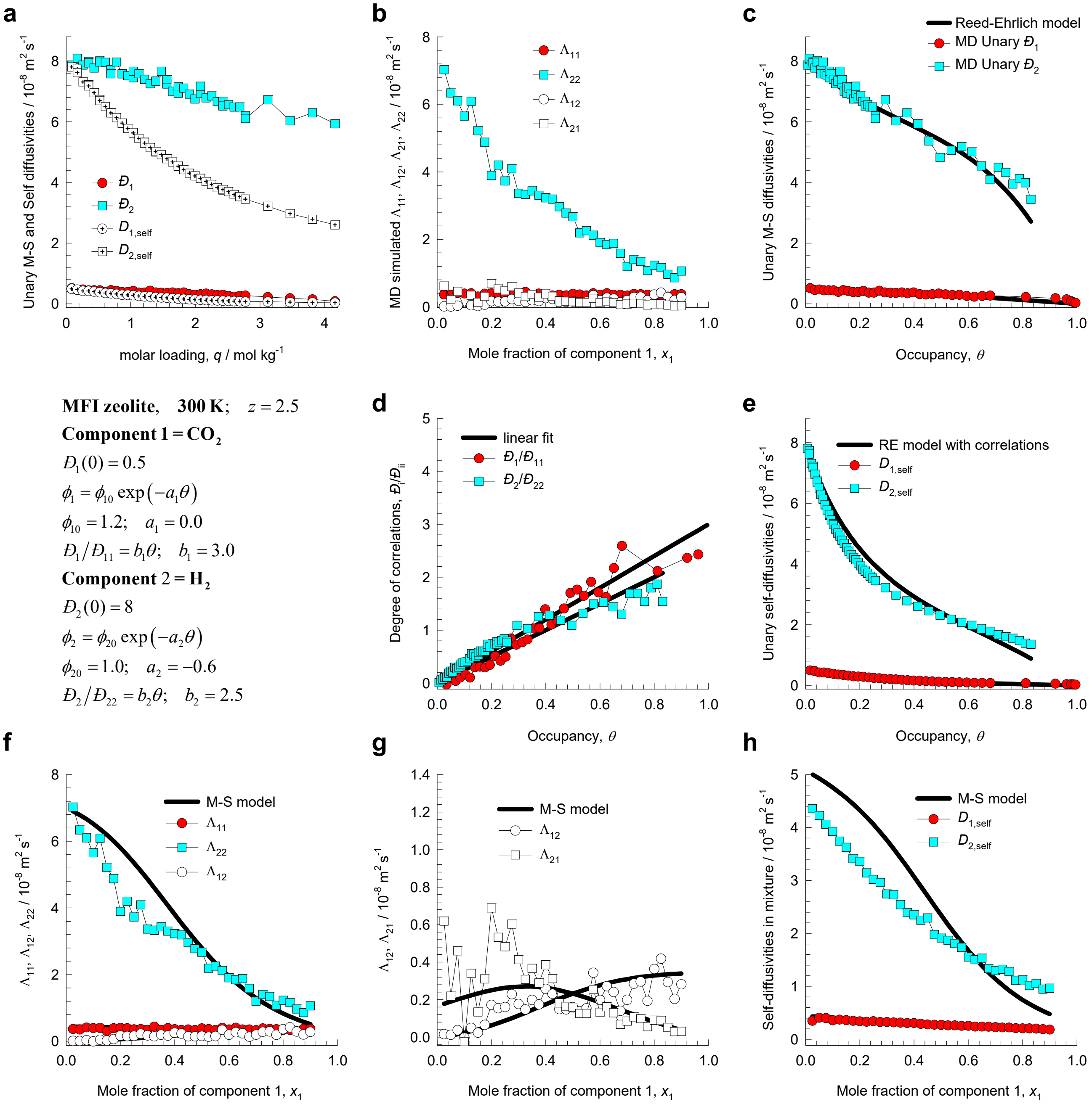

Figure S53. (a-h) MD simulated values of $\Lambda_{11},\Lambda_{12},\Lambda_{21},\Lambda_{22}$ for binary CO_2(1)/H_2(2) mixtures of varying compositions (total loading = 10 molecules uc^{-1}) in MFI zeolite at 300 K, compared with the estimations (continuous solid lines) using the Maxwell-Stefan model, based on fitted data of unary diffusivities, $Đ_1, Đ_2$, and unary degrees of correlations, $Đ_1/Đ_{11}, Đ_2/Đ_{22}$.

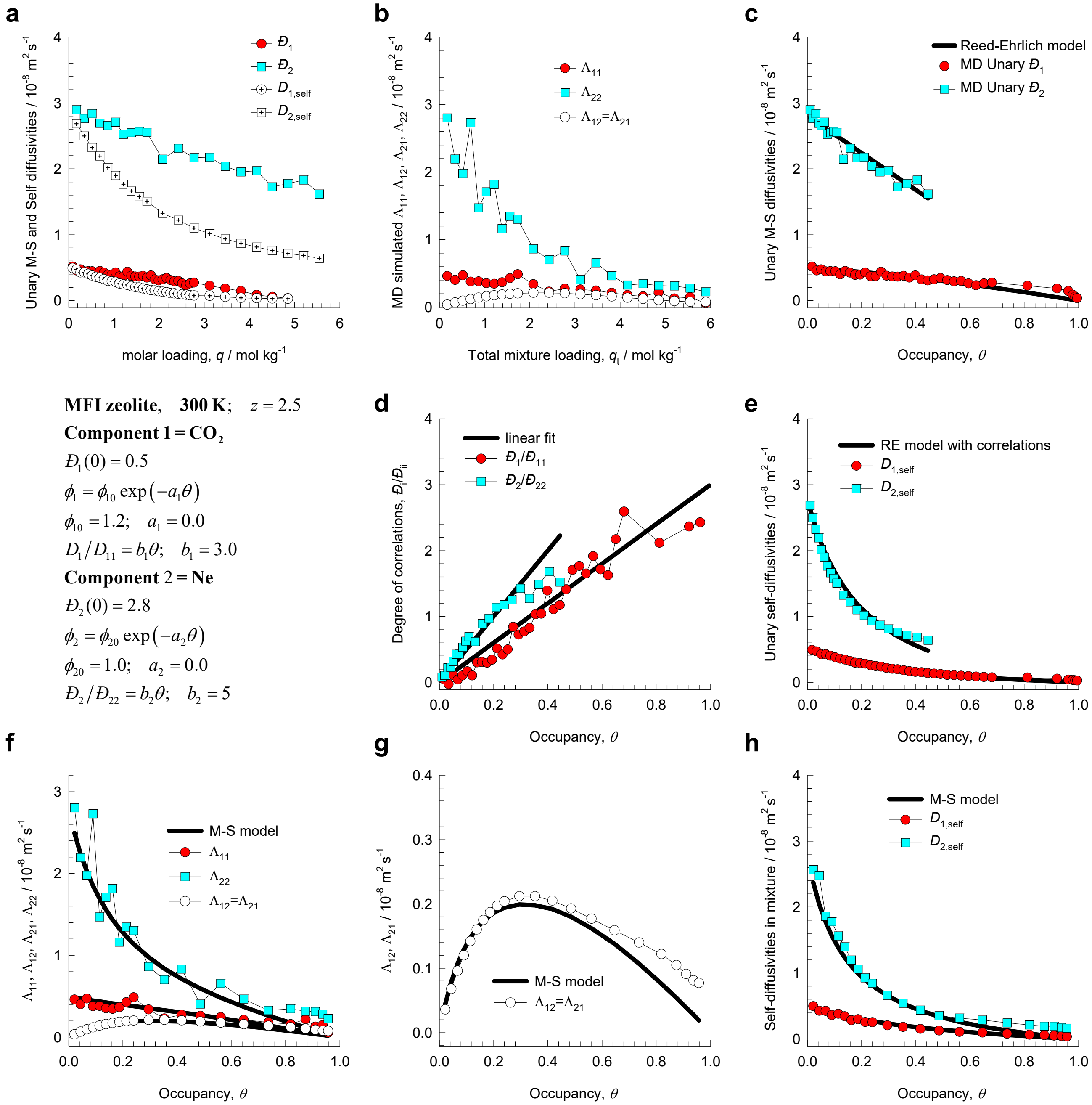

Figure S54. (a-h) MD simulated values of $\Lambda_{11},\Lambda_{12},\Lambda_{21},\Lambda_{22}$ for equimolar (q_1=q_2) binary CO$_2$(1)/Ne(2) mixtures in MFI zeolite at 300 K, compared with the estimations (continuous solid lines) using the Maxwell-Stefan model, based on fitted data of unary diffusivities, $Đ_1,Đ_2$, and unary degrees of correlations, $Đ_1/Đ_{11}, Đ_2/Đ_{22}$.

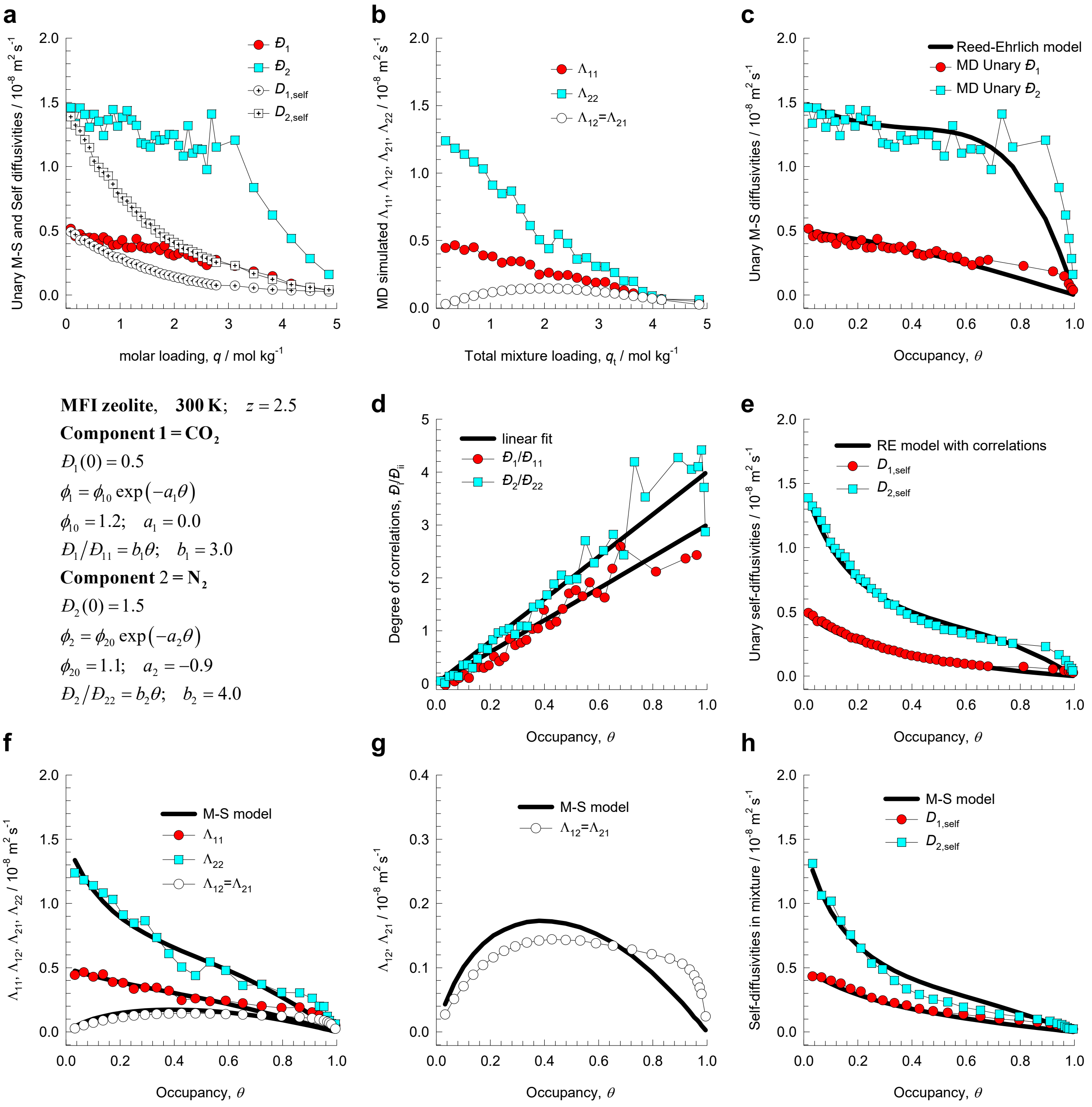

MFI zeolite, 300 K; $z = 2.5$

Component 1 = CO$_2$

$Đ_1(0) = 0.5$

$\phi_1 = \phi_{10} \exp(-a_1\theta)$

$\phi_{10} = 1.2; \quad a_1 = 0.0$

$Đ_1/Đ_{11} = b_1\theta; \quad b_1 = 3.0$

Component 2 = N$_2$

$Đ_2(0) = 1.5$

$\phi_2 = \phi_{20} \exp(-a_2\theta)$

$\phi_{20} = 1.1; \quad a_2 = -0.9$

$Đ_2/Đ_{22} = b_2\theta; \quad b_2 = 4.0$

Figure S55. (a-h) MD simulated values of $\Lambda_{11}, \Lambda_{12}, \Lambda_{21}, \Lambda_{22}$ for equimolar (q_1=q_2) binary CO$_2$(1)/N$_2$(2) mixtures in MFI zeolite at 300 K, compared with the estimations (continuous solid lines) using the Maxwell-Stefan model, based on fitted data of unary diffusivities, $Đ_1, Đ_2$, and unary degrees of correlations, $Đ_1/Đ_{11}, Đ_2/Đ_{22}$.

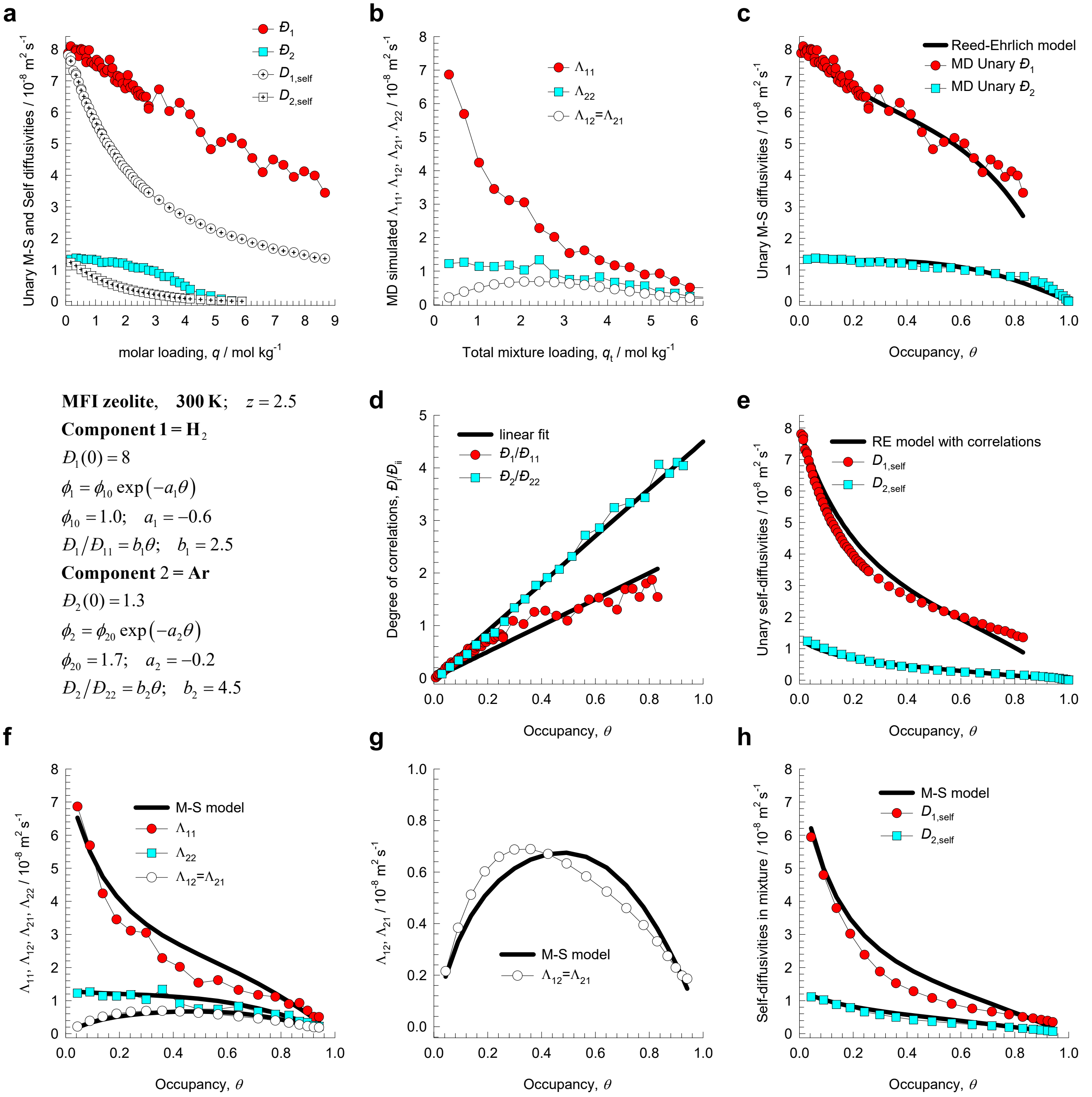

Figure S56. (a-h) MD simulated values of $\Lambda_{11},\Lambda_{12},\Lambda_{21},\Lambda_{22}$ for equimolar (q_1=q_2) binary H_2(1)/Ar(2) mixtures in MFI zeolite at 300 K, compared with the estimations (continuous solid lines) using the Maxwell-Stefan model, based on fitted data of unary diffusivities, $Đ_1, Đ_2$, and unary degrees of correlations, $Đ_1/Đ_{11}, Đ_2/Đ_{22}$.

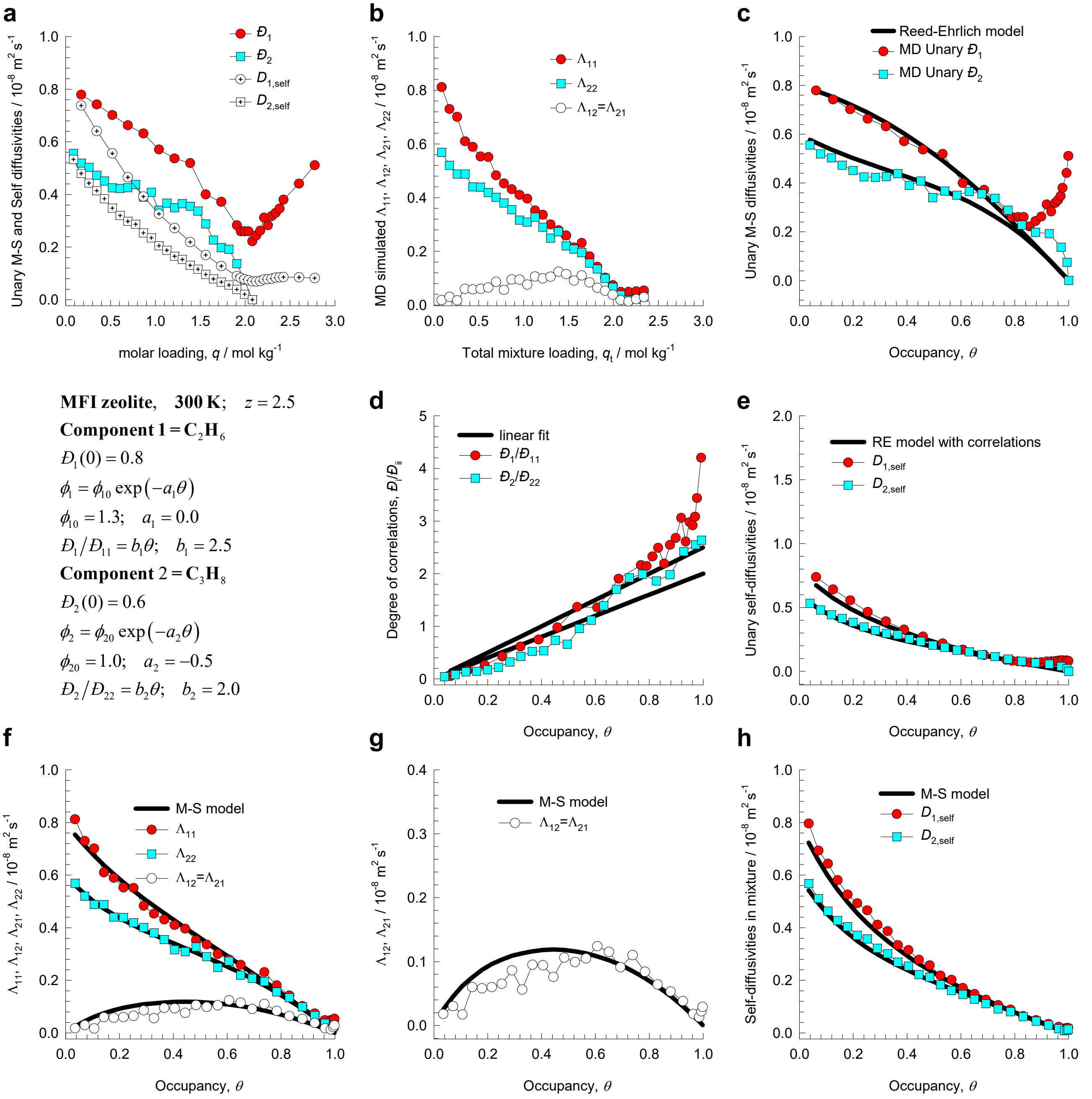

MFI zeolite, 300 K; $z = 2.5$

Component 1 = C_2H_6

$Đ_1(0) = 0.8$

$\phi_1 = \phi_{10}\exp(-a_1\theta)$

$\phi_{10} = 1.3;\quad a_1 = 0.0$

$Đ_1/Đ_{11} = b_1\theta;\quad b_1 = 2.5$

Component 2 = C_3H_8

$Đ_2(0) = 0.6$

$\phi_2 = \phi_{20}\exp(-a_2\theta)$

$\phi_{20} = 1.0;\quad a_2 = -0.5$

$Đ_2/Đ_{22} = b_2\theta;\quad b_2 = 2.0$

Figure S57. (a-h) MD simulated values of $\Lambda_{11},\Lambda_{12},\Lambda_{21},\Lambda_{22}$ for equimolar (q_1=q_2) binary C_2H_6(1)/C_3H_8(2) mixtures in MFI zeolite at 300 K, compared with the estimations (continuous solid lines) using the Maxwell-Stefan model, based on fitted data of unary diffusivities, $Đ_1, Đ_2$, and unary degrees of correlations, $Đ_1/Đ_{11}, Đ_2/Đ_{22}$.

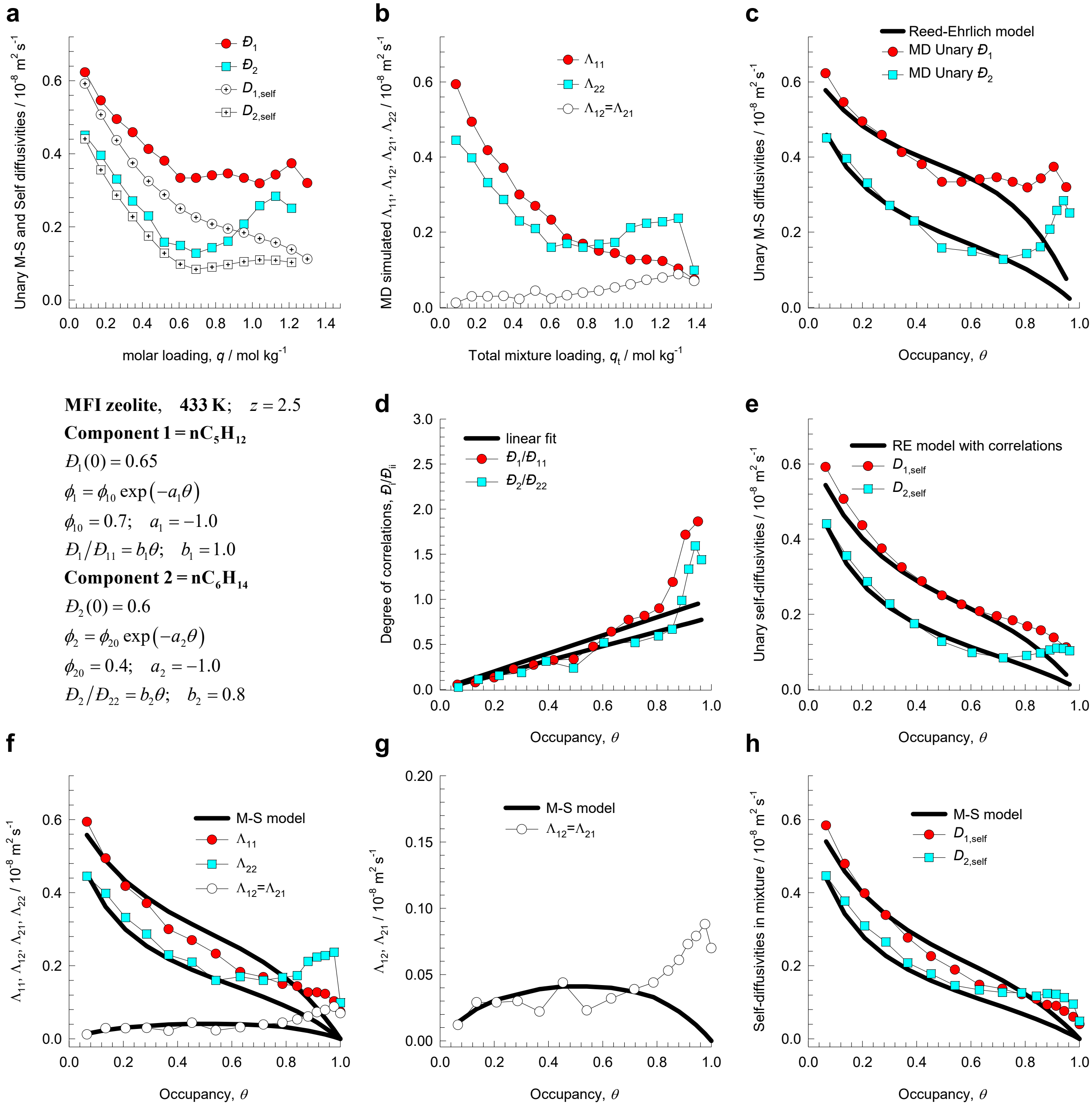

Figure S58. (a-h) MD simulated values of $\Lambda_{11},\Lambda_{12},\Lambda_{21},\Lambda_{22}$ for equimolar (q_1=q_2) binary nC_5H_{12}(1)/nC_6H_{14}(2) mixtures in MFI zeolite at 433 K, compared with the estimations (continuous solid lines) using the Maxwell-Stefan model, based on fitted data of unary diffusivities, $Đ_1,Đ_2$, and unary degrees of correlations, $Đ_1/Đ_{11},Đ_2/Đ_{22}$.

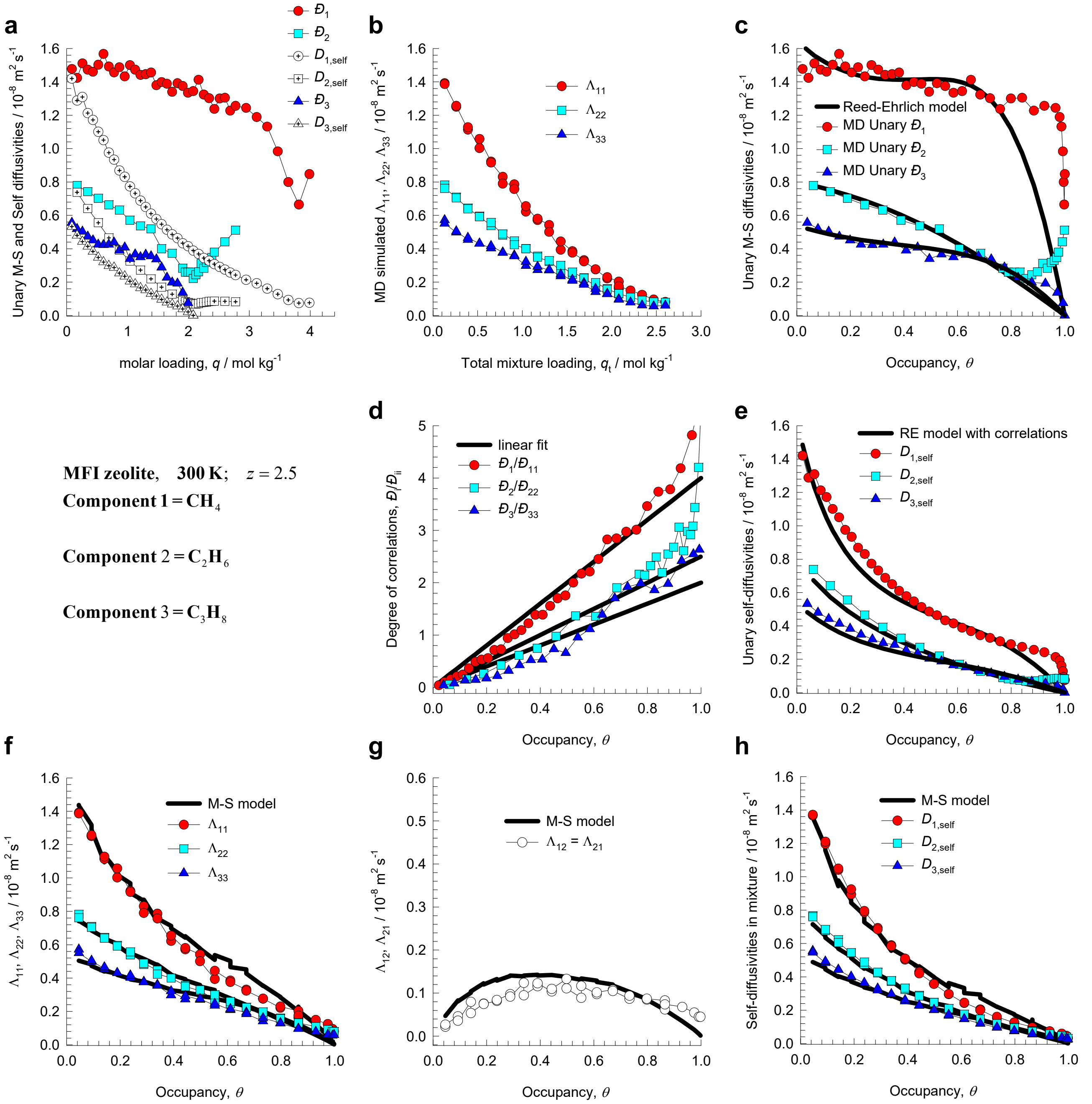

Figure S59. (a-h) MD simulated values of $\Lambda_{11},\Lambda_{12},\Lambda_{21},\Lambda_{22}$ for equimolar ($q_1=q_2=q_3$) ternary $CH_4(1)/C_2H_6(2)/C_3H_8(2)$ mixtures in MFI zeolite at 300 K, compared with the estimations (continuous solid lines) using the Maxwell-Stefan model, based on fitted data of unary diffusivities, $Đ_1, Đ_2$, and unary degrees of correlations, $Đ_1/Đ_{11}, Đ_2/Đ_{22}, Đ_3/Đ_{33}$. The input data fits are the same as in the foregoing Figures for methane, ethane, and propane.

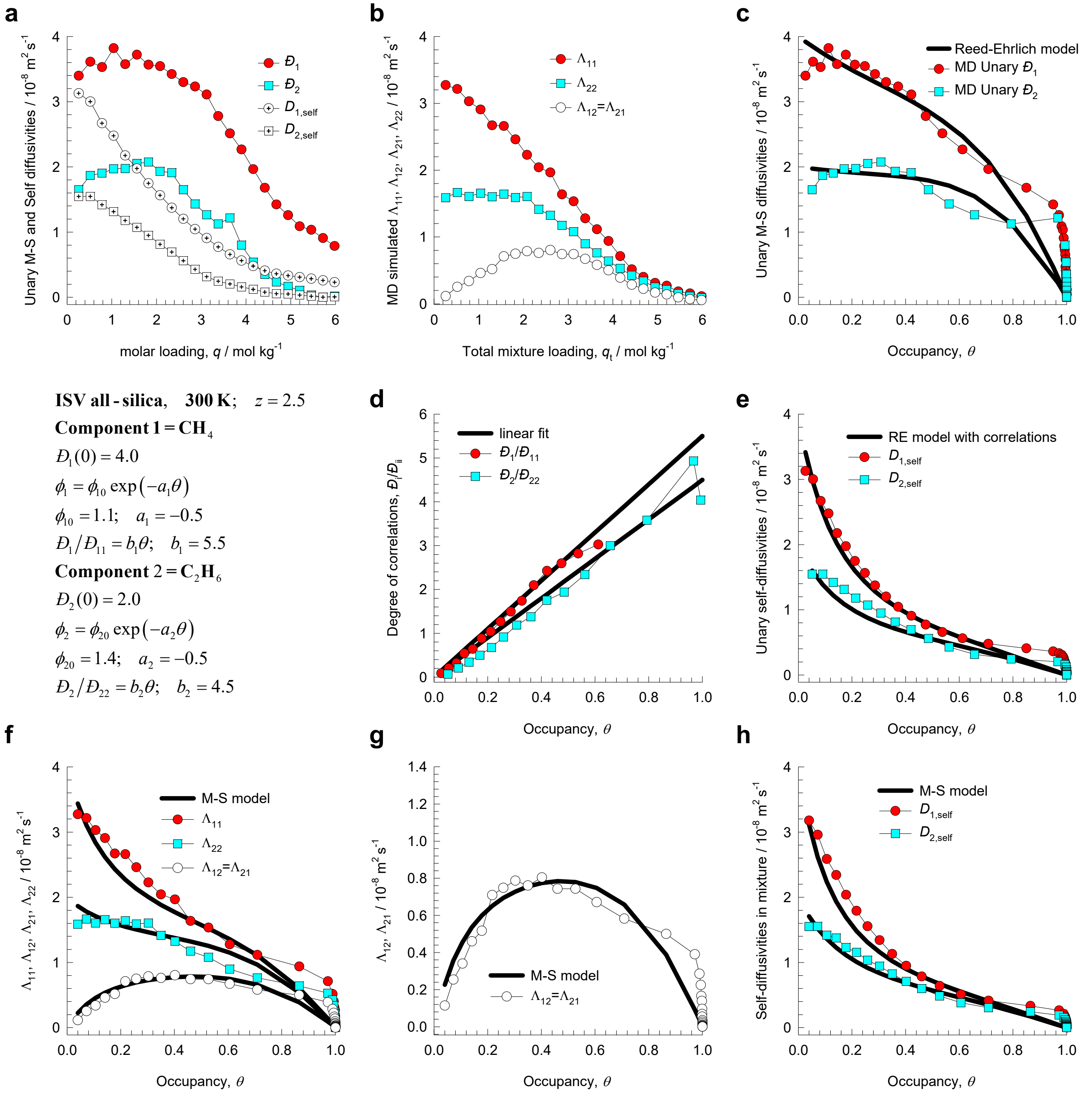

Figure S60. (a-h) MD simulated values of $\Lambda_{11},\Lambda_{12},\Lambda_{21},\Lambda_{22}$ for equimolar (q_1=q_2) binary CH$_4$(1)/C$_2$H$_6$(2) mixtures in ISV zeolite at 300 K, compared with the estimations (continuous solid lines) using the Maxwell-Stefan model, based on fitted data of unary diffusivities, $Đ_1,Đ_2$, and unary degrees of correlations, $Đ_1/Đ_{11},Đ_2/Đ_{22}$.

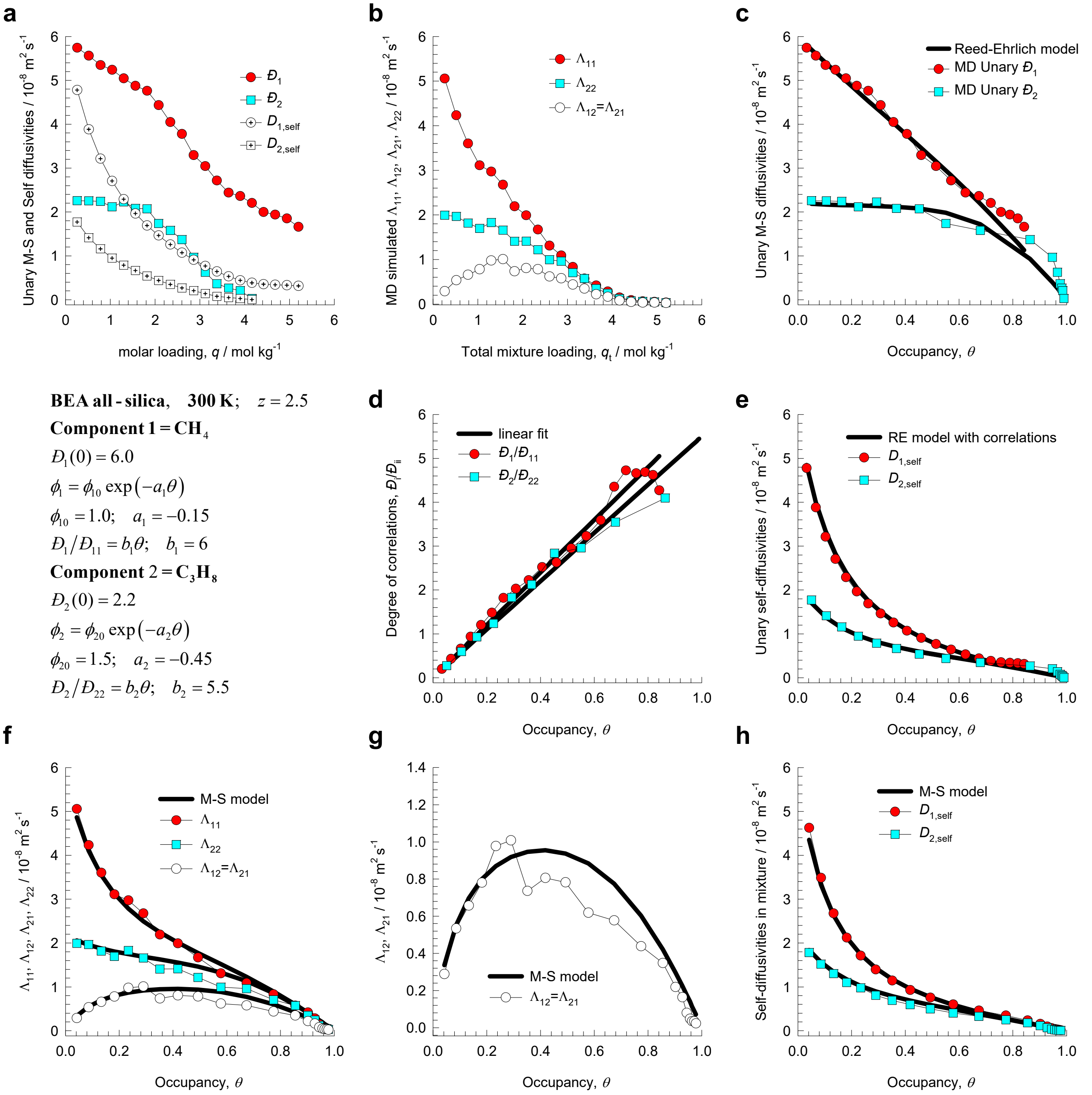

Figure S61. (a-h) MD simulated values of $\Lambda_{11},\Lambda_{12},\Lambda_{21},\Lambda_{22}$ for equimolar (q_1=q_2) binary CH$_4$(1)/C$_3$H$_8$(2) mixtures in BEA zeolite at 300 K, compared with the estimations (continuous solid lines) using the Maxwell-Stefan model, based on fitted data of unary diffusivities, $Đ_1,Đ_2$, and unary degrees of correlations, $Đ_1/Đ_{11}, Đ_2/Đ_{22}$.

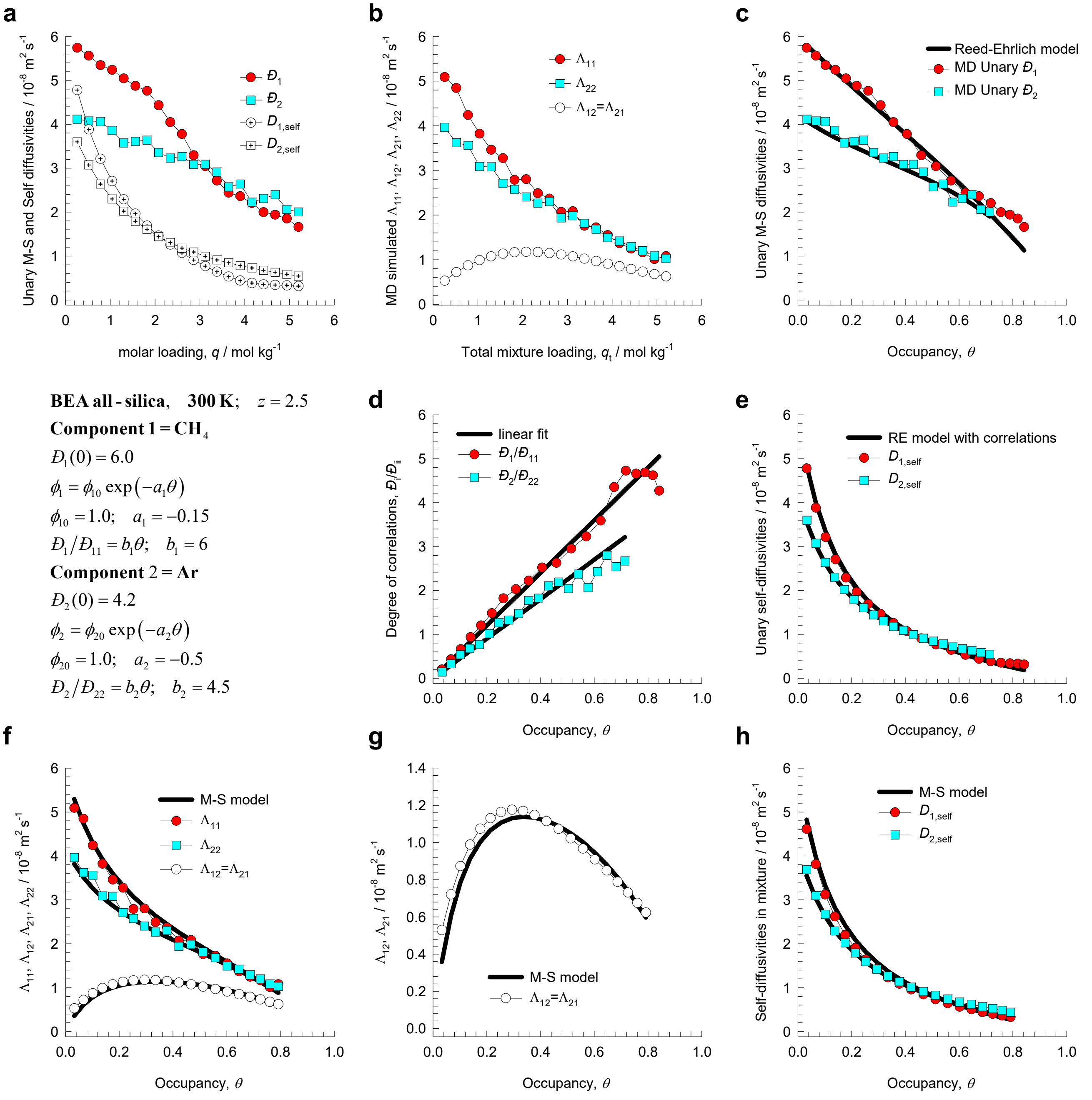

BEA all - silica, 300 K; $z = 2.5$

Component 1 = CH$_4$

$Đ_1(0) = 6.0$

$\phi_1 = \phi_{10} \exp(-a_1\theta)$

$\phi_{10} = 1.0; \quad a_1 = -0.15$

$Đ_1/Đ_{11} = b_1\theta; \quad b_1 = 6$

Component 2 = Ar

$Đ_2(0) = 4.2$

$\phi_2 = \phi_{20} \exp(-a_2\theta)$

$\phi_{20} = 1.0; \quad a_2 = -0.5$

$Đ_2/Đ_{22} = b_2\theta; \quad b_2 = 4.5$

Figure S62. (a-h) MD simulated values of $\Lambda_{11},\Lambda_{12},\Lambda_{21},\Lambda_{22}$ for equimolar (q_1=q_2) binary CH$_4$(1)/Ar(2) mixtures in BEA zeolite at 300 K, compared with the estimations (continuous solid lines) using the Maxwell-Stefan model, based on fitted data of unary diffusivities, $Đ_1,Đ_2$, and unary degrees of correlations, $Đ_1/Đ_{11}, Đ_2/Đ_{22}$.

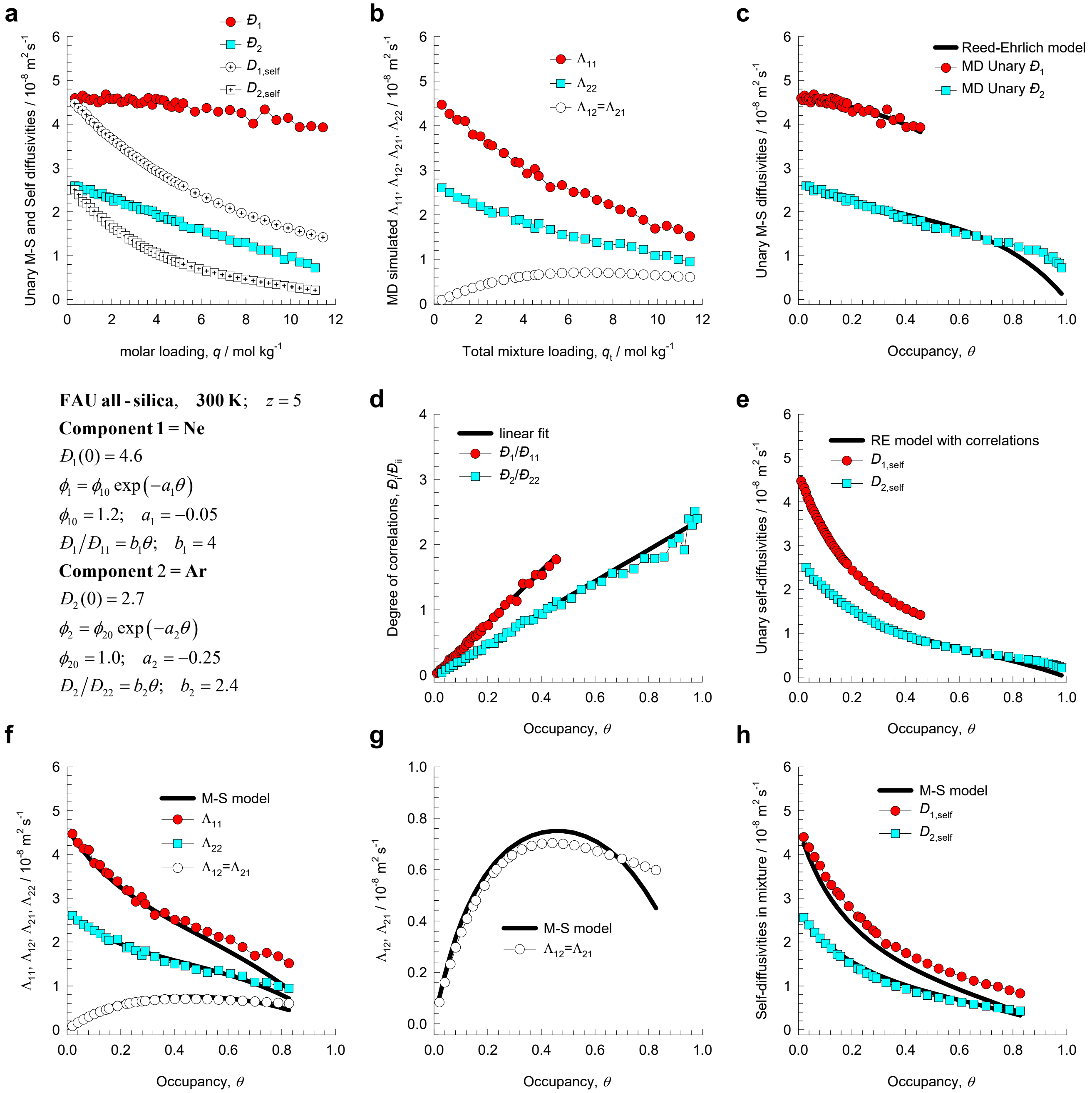

FAU all-silica, 300 K; $z = 5$

Component 1 = Ne

$Đ_1(0) = 4.6$

$\phi_1 = \phi_{10}\exp(-a_1\theta)$

$\phi_{10} = 1.2; \quad a_1 = -0.05$

$Đ_1/Đ_{11} = b_1\theta; \quad b_1 = 4$

Component 2 = Ar

$Đ_2(0) = 2.7$

$\phi_2 = \phi_{20}\exp(-a_2\theta)$

$\phi_{20} = 1.0; \quad a_2 = -0.25$

$Đ_2/Đ_{22} = b_2\theta; \quad b_2 = 2.4$

Figure S63. (a-h) MD simulated values of $\Lambda_{11}, \Lambda_{12}, \Lambda_{21}, \Lambda_{22}$ for equimolar (q_1=q_2) binary Ne(1)/Ar(2) mixtures in FAU all-silica zeolite at 300 K, compared with the estimations (continuous solid lines) using the Maxwell-Stefan model, based on fitted data of unary diffusivities, $Đ_1, Đ_2$, and unary degrees of correlations, $Đ_1/Đ_{11}, Đ_2/Đ_{22}$.

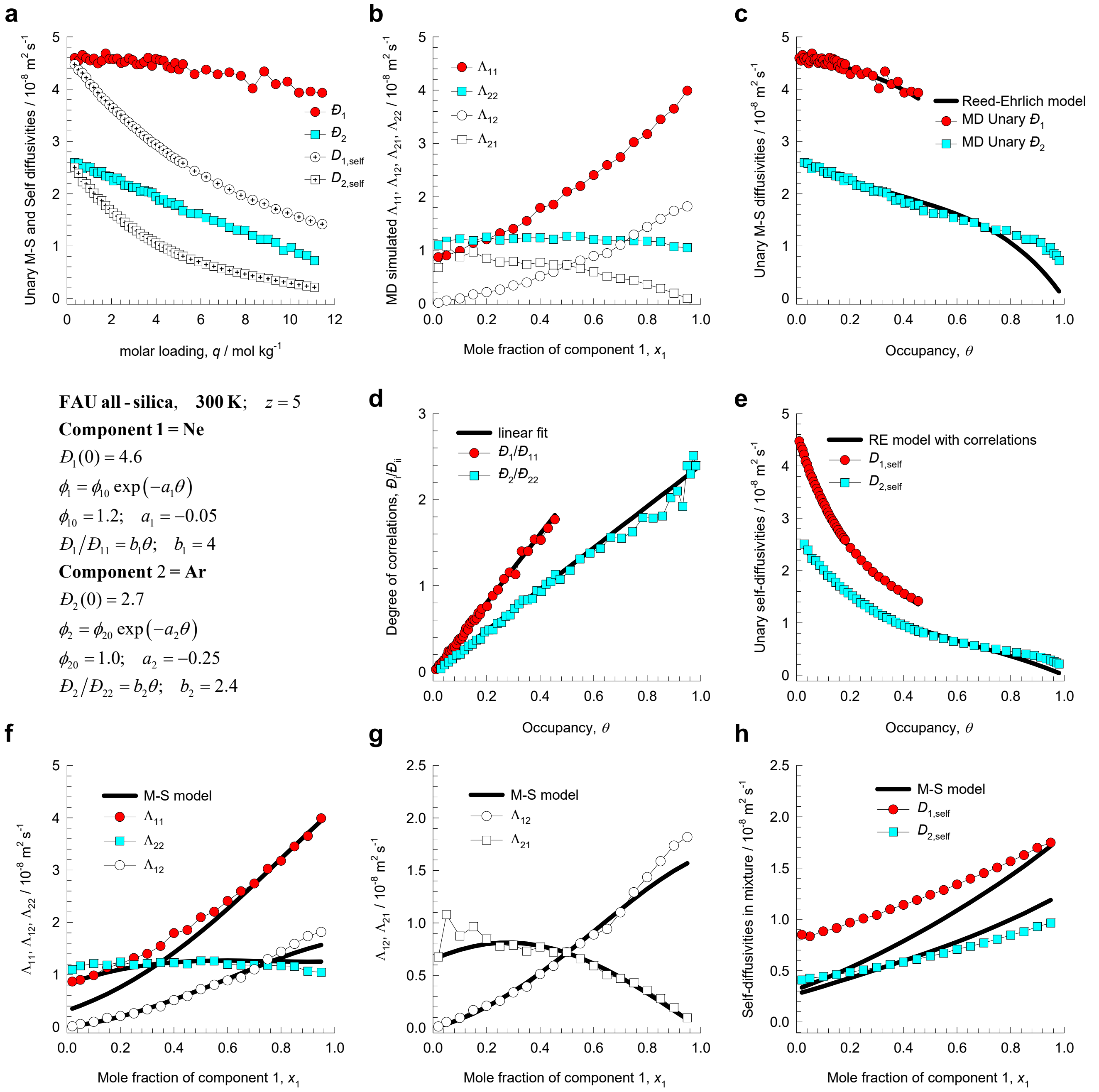

Figure S64. (a-h) MD simulated values of $\Lambda_{11}, \Lambda_{12}, \Lambda_{21}, \Lambda_{22}$ for binary Ne(1)/Ar(2) mixtures of varying composition (total loading = 100 molecules uc^{-1}) in FAU all-silica zeolite at 300 K, compared with the estimations (continuous solid lines) using the Maxwell-Stefan model, based on fitted data of unary diffusivities, $Đ_1, Đ_2$, and unary degrees of correlations, $Đ_1/Đ_{11}, Đ_2/Đ_{22}$.

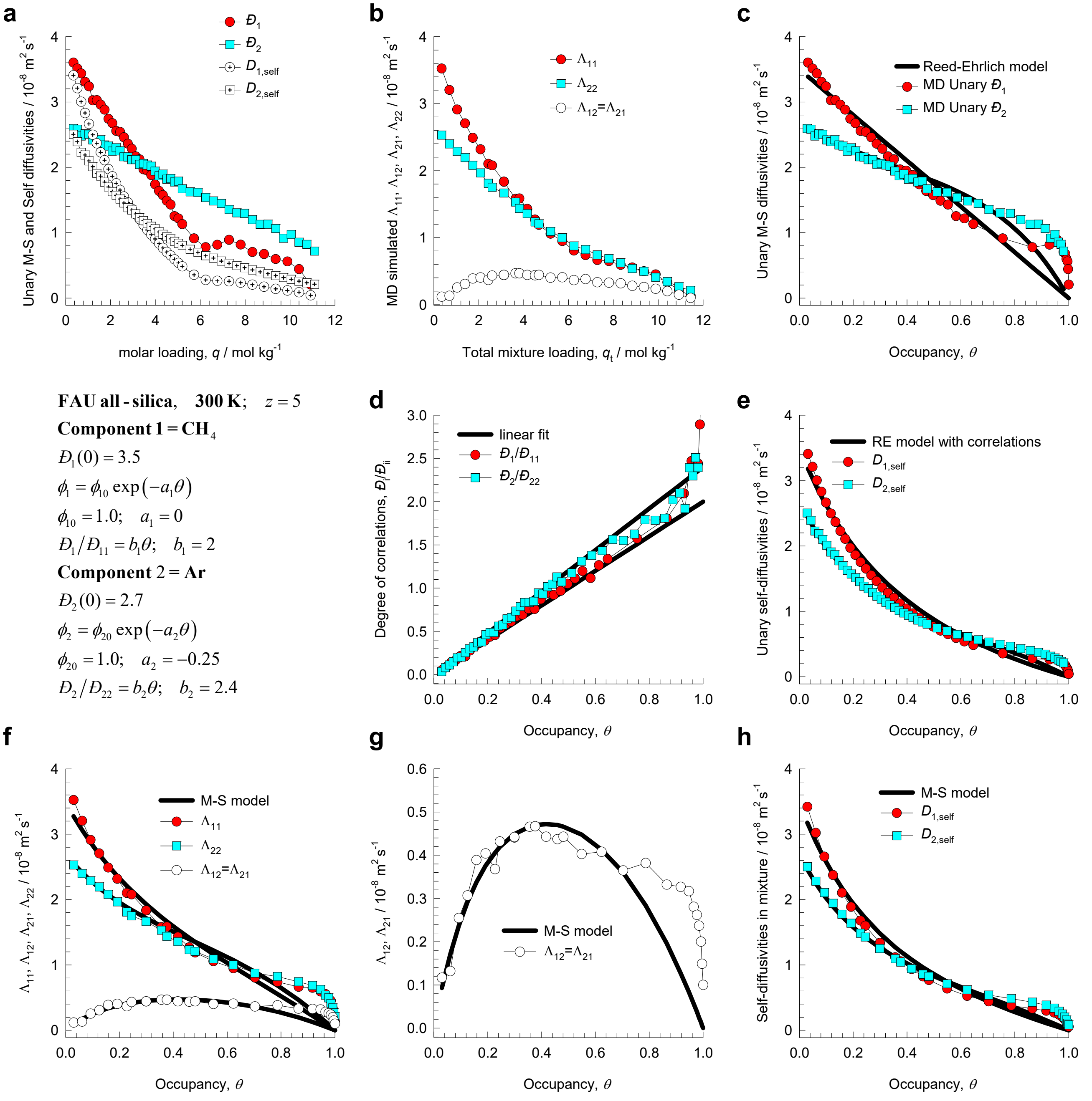

FAU all - silica, 300 K; $z = 5$

Component 1 = CH$_4$

$Đ_1(0) = 3.5$

$\phi_1 = \phi_{10} \exp(-a_1\theta)$

$\phi_{10} = 1.0; \quad a_1 = 0$

$Đ_1/Đ_{11} = b_1\theta; \quad b_1 = 2$

Component 2 = Ar

$Đ_2(0) = 2.7$

$\phi_2 = \phi_{20} \exp(-a_2\theta)$

$\phi_{20} = 1.0; \quad a_2 = -0.25$

$Đ_2/Đ_{22} = b_2\theta; \quad b_2 = 2.4$

Figure S65. (a-h) MD simulated values of $\Lambda_{11},\Lambda_{12},\Lambda_{21},\Lambda_{22}$ for equimolar (q_1=q_2) binary CH$_4$(1)/Ar(2) mixtures in FAU all-silica zeolite at 300 K, compared with the estimations (continuous solid lines) using the Maxwell-Stefan model, based on fitted data of unary diffusivities, $Đ_1,Đ_2$, and unary degrees of correlations, $Đ_1/Đ_{11}, Đ_2/Đ_{22}$.

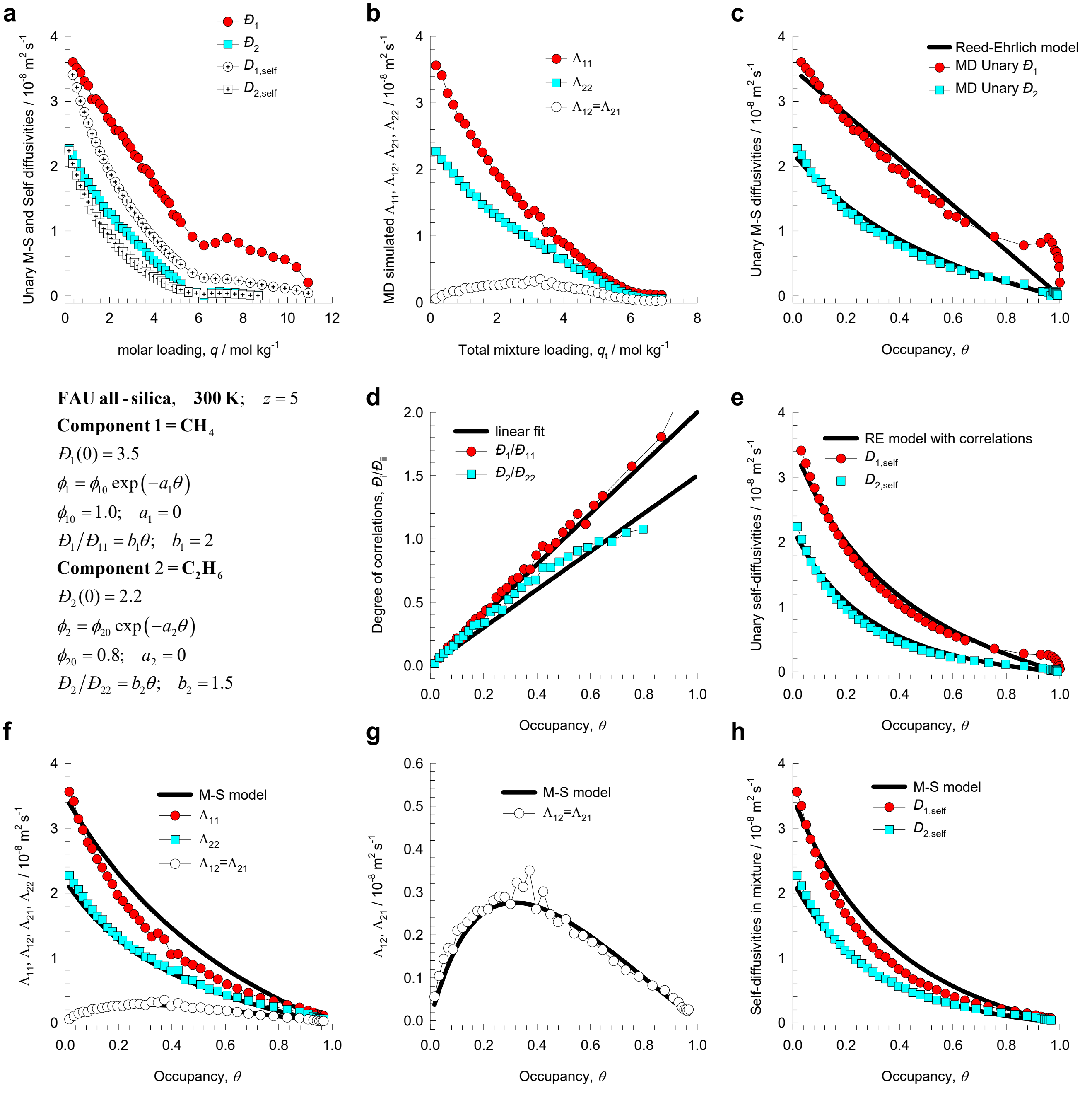

Figure S66. (a-h) MD simulated values of $\Lambda_{11}, \Lambda_{12}, \Lambda_{21}, \Lambda_{22}$ for equimolar (q_1=q_2) binary CH_4(1)/C_2H_6(2) mixtures in FAU all-silica zeolite at 300 K, compared with the estimations (continuous solid lines) using the Maxwell-Stefan model, based on fitted data of unary diffusivities, $Đ_1, Đ_2$, and unary degrees of correlations, $Đ_1/Đ_{11}, Đ_2/Đ_{22}$.

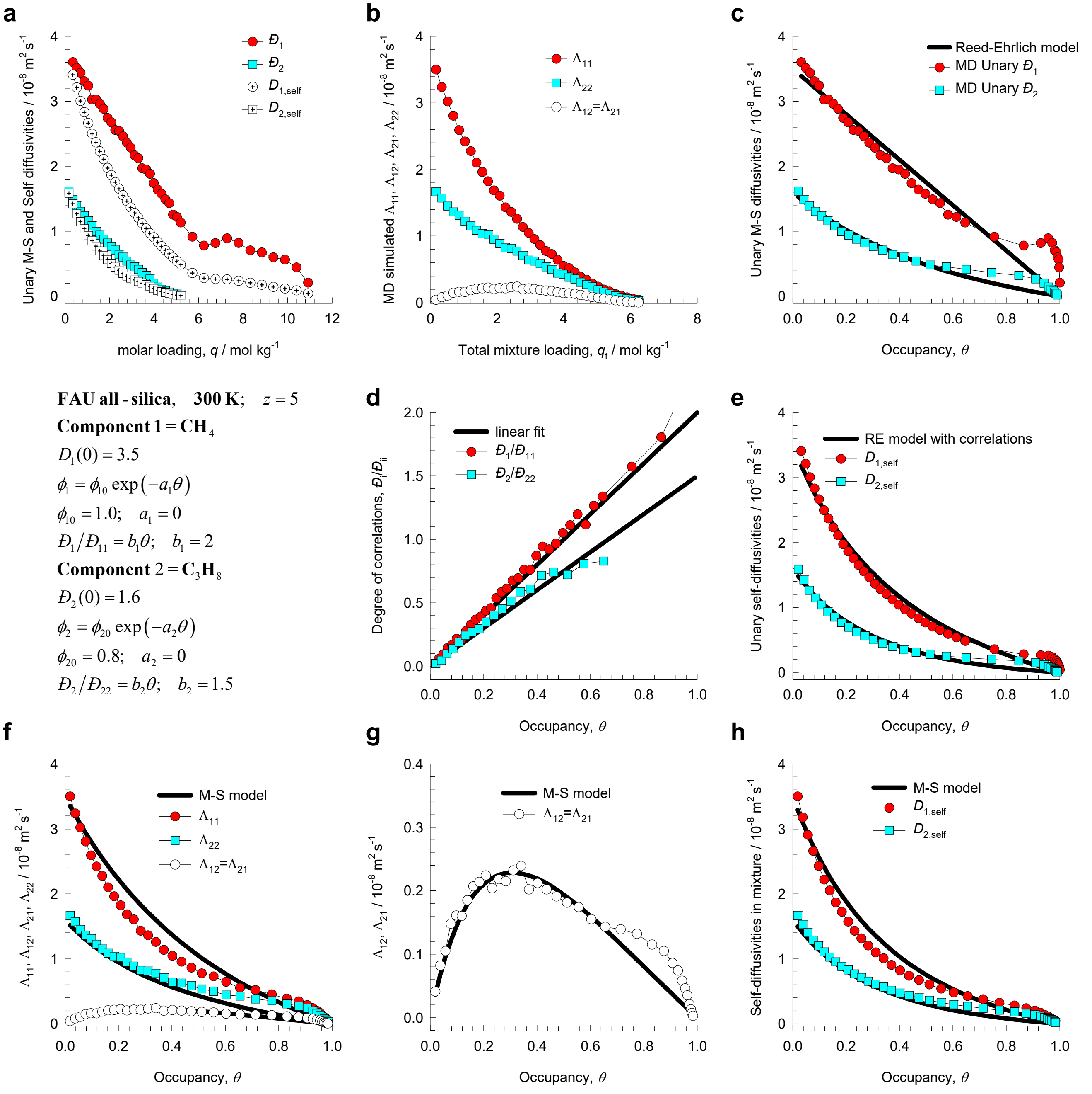

FAU all-silica, 300 K; $z = 5$

Component 1 = CH$_4$

$Đ_1(0) = 3.5$

$\phi_1 = \phi_{10}\exp(-a_1\theta)$

$\phi_{10} = 1.0; \quad a_1 = 0$

$Đ_1/Đ_{11} = b_1\theta; \quad b_1 = 2$

Component 2 = C$_3$H$_8$

$Đ_2(0) = 1.6$

$\phi_2 = \phi_{20}\exp(-a_2\theta)$

$\phi_{20} = 0.8; \quad a_2 = 0$

$Đ_2/Đ_{22} = b_2\theta; \quad b_2 = 1.5$

Figure S67. (a-h) MD simulated values of $\Lambda_{11},\Lambda_{12},\Lambda_{21},\Lambda_{22}$ for equimolar (q_1=q_2) binary CH$_4$(1)/C$_3$H$_8$(2) mixtures in FAU all-silica zeolite at 300 K, compared with the estimations (continuous solid lines) using the Maxwell-Stefan model, based on fitted data of unary diffusivities, $Đ_1,Đ_2$, and unary degrees of correlations, $Đ_1/Đ_{11}, Đ_2/Đ_{22}$.

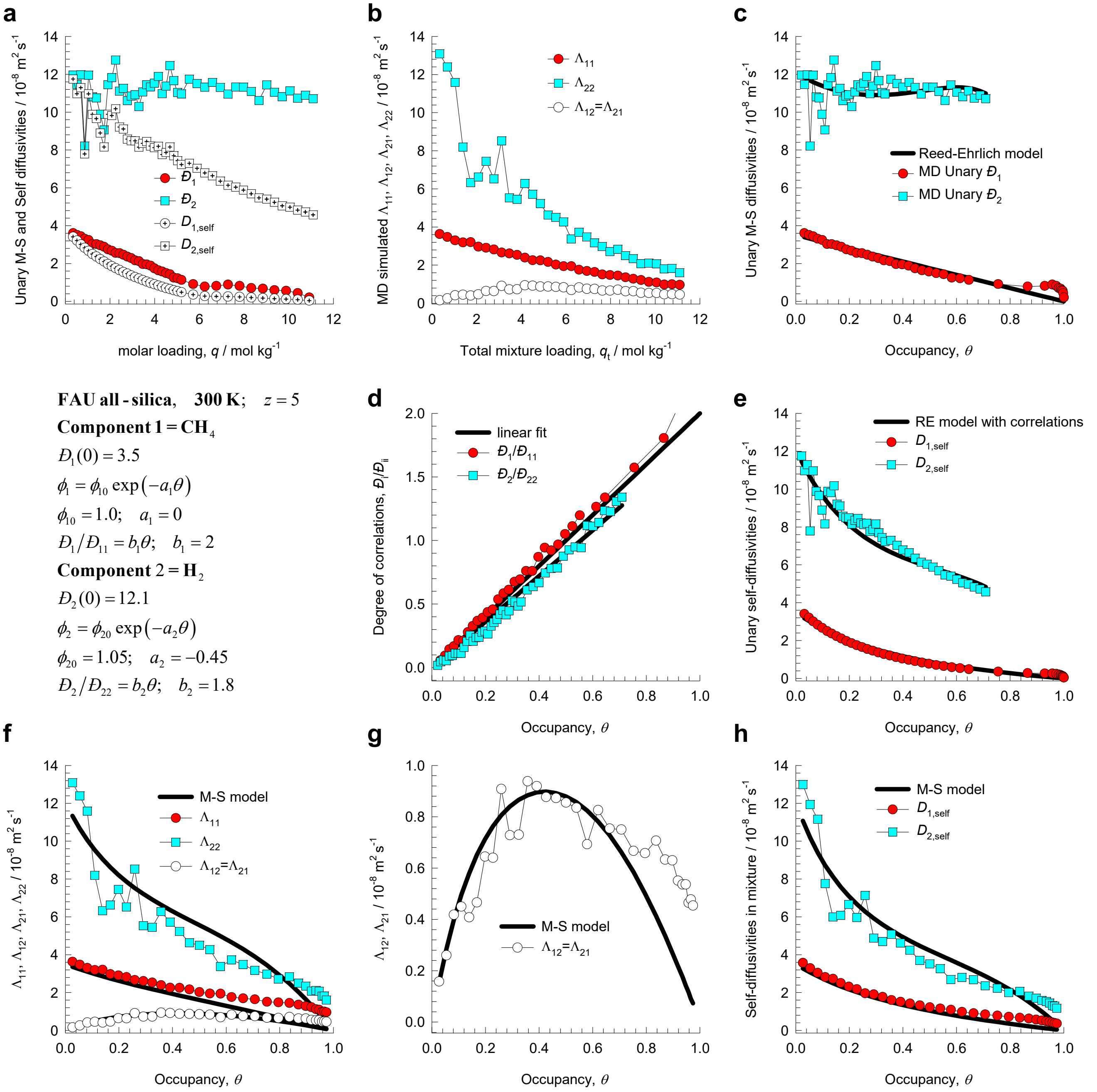

Figure S68. (a-h) MD simulated values of $\Lambda_{11},\Lambda_{12},\Lambda_{21},\Lambda_{22}$ for equimolar (q_1=q_2) binary CH$_4$(1)/H$_2$(2) mixtures in FAU all-silica zeolite at 300 K, compared with the estimations (continuous solid lines) using the Maxwell-Stefan model, based on fitted data of unary diffusivities, $Đ_1,Đ_2$, and unary degrees of correlations, $Đ_1/Đ_{11}, Đ_2/Đ_{22}$.

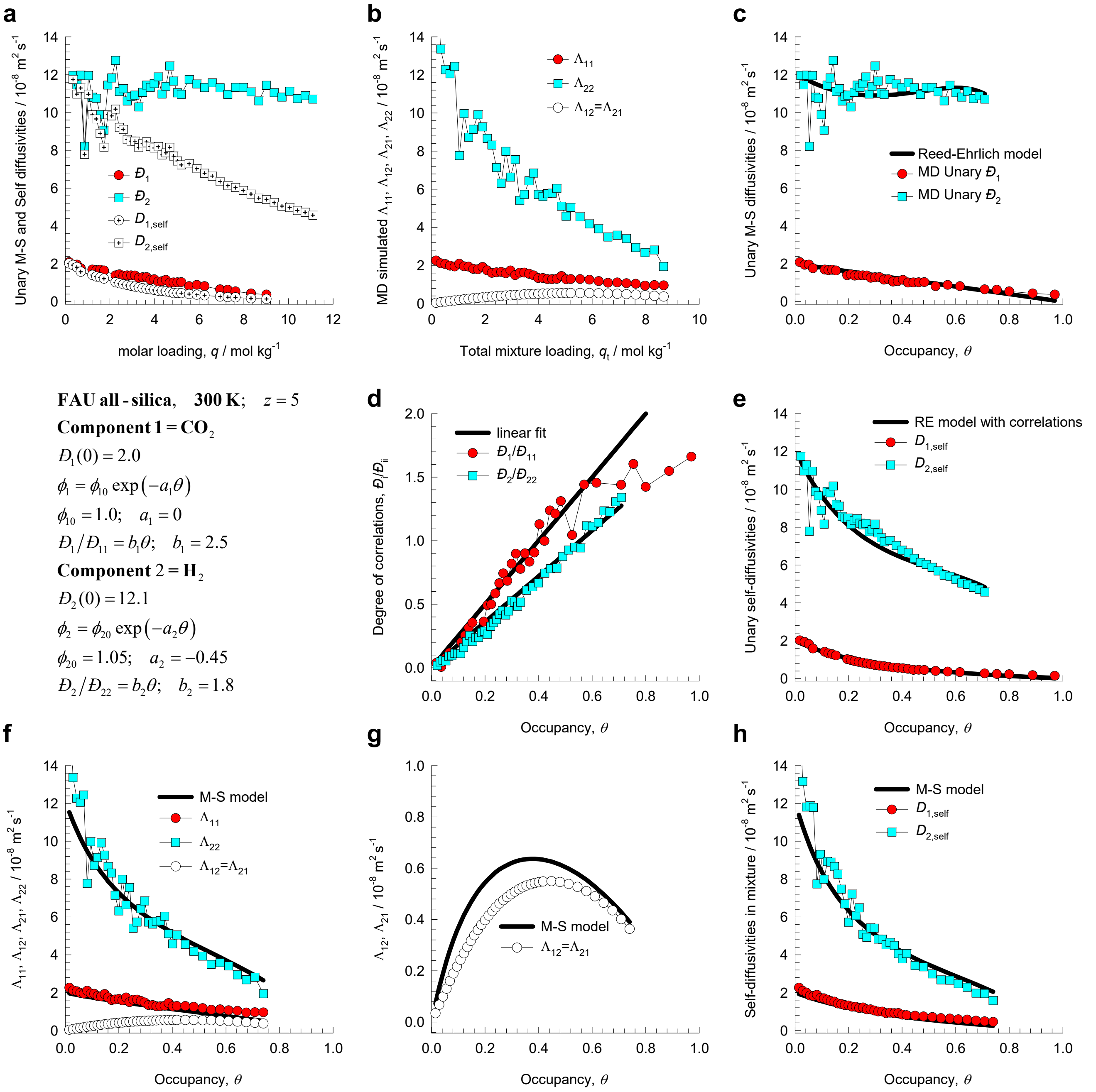

Figure S69. (a-h) MD simulated values of $\Lambda_{11},\Lambda_{12},\Lambda_{21},\Lambda_{22}$ for equimolar (q_1=q_2) binary CO_2(1)/H_2(2) mixtures in FAU all-silica zeolite at 300 K, compared with the estimations (continuous solid lines) using the Maxwell-Stefan model, based on fitted data of unary diffusivities, $Đ_1,Đ_2$, and unary degrees of correlations, $Đ_1/Đ_{11},Đ_2/Đ_{22}$.

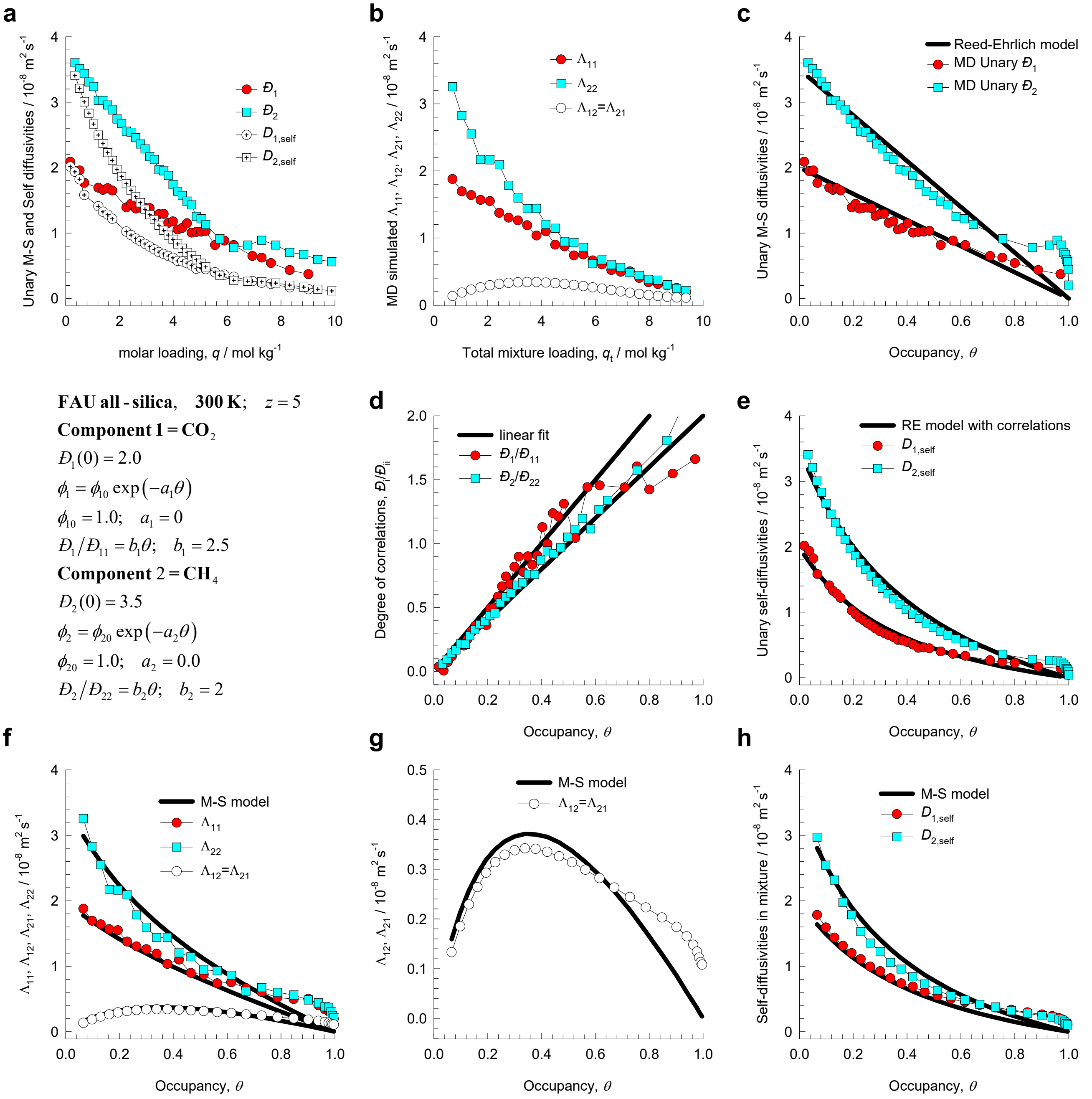

FAU all-silica, 300 K; $z = 5$

Component 1 = CO$_2$

$Đ_1(0) = 2.0$

$\phi_1 = \phi_{10} \exp(-a_1\theta)$

$\phi_{10} = 1.0; \quad a_1 = 0$

$Đ_1/Đ_{11} = b_1\theta; \quad b_1 = 2.5$

Component 2 = CH$_4$

$Đ_2(0) = 3.5$

$\phi_2 = \phi_{20} \exp(-a_2\theta)$

$\phi_{20} = 1.0; \quad a_2 = 0.0$

$Đ_2/Đ_{22} = b_2\theta; \quad b_2 = 2$

Figure S70. (a-h) MD simulated values of $\Lambda_{11}, \Lambda_{12}, \Lambda_{21}, \Lambda_{22}$ for equimolar (q_1=q_2) binary CO_2(1)/CH_4(2) mixtures in FAU all-silica zeolite at 300 K, compared with the estimations (continuous solid lines) using the Maxwell-Stefan model, based on fitted data of unary diffusivities, $Đ_1$,$Đ_2$, and unary degrees of correlations, $Đ_1/Đ_{11}, Đ_2/Đ_{22}$.

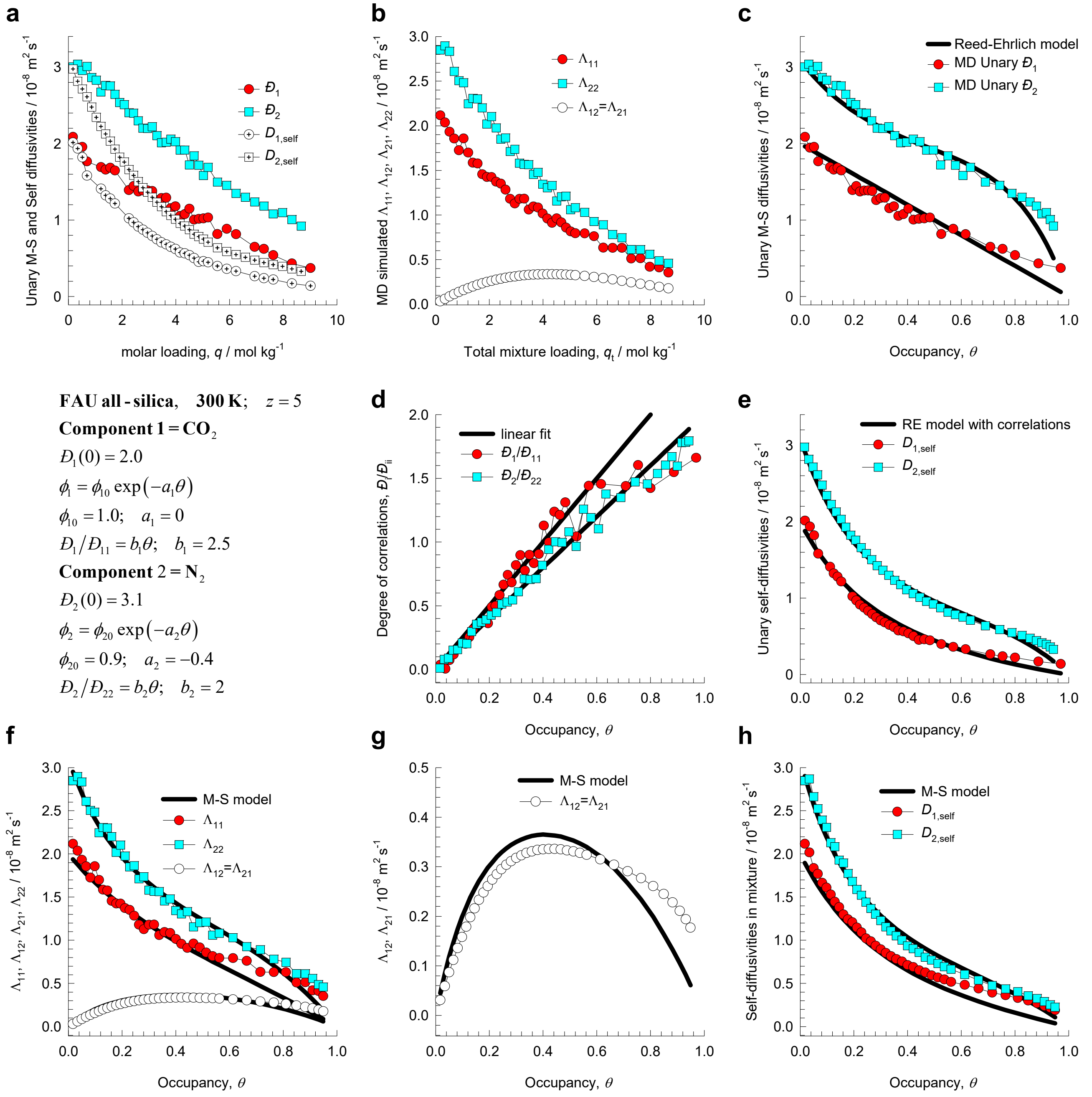

Figure S71. (a-h) MD simulated values of $\Lambda_{11},\Lambda_{12},\Lambda_{21},\Lambda_{22}$ for equimolar (q_1=q_2) binary CO_2(1)/N_2(2) mixtures in FAU all-silica zeolite at 300 K, compared with the estimations (continuous solid lines) using the Maxwell-Stefan model, based on fitted data of unary diffusivities, $Đ_1, Đ_2$, and unary degrees of correlations, $Đ_1/Đ_{11}, Đ_2/Đ_{22}$.

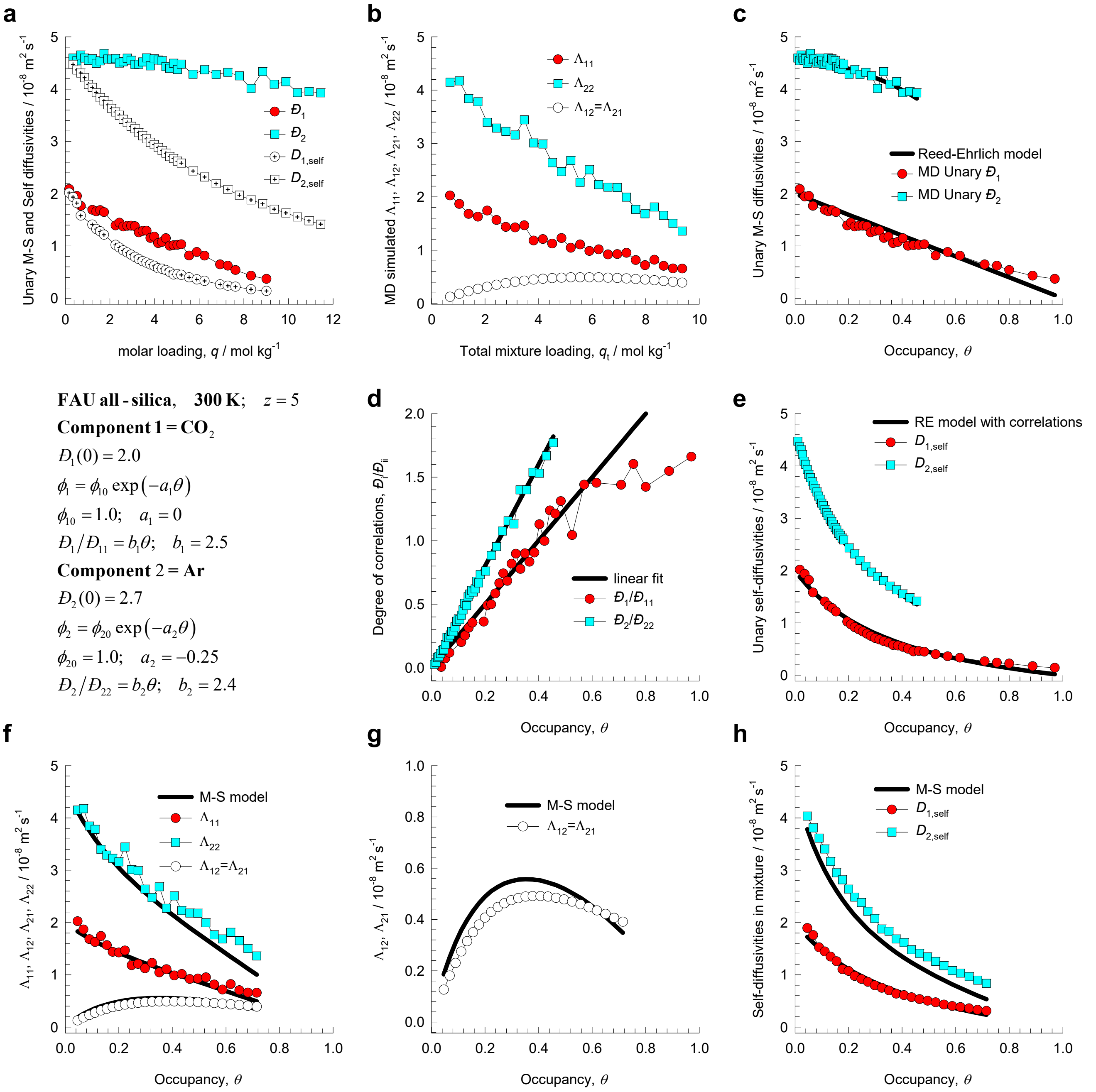

Figure S72. (a-h) MD simulated values of $\Lambda_{11},\Lambda_{12},\Lambda_{21},\Lambda_{22}$ for equimolar (q_1=q_2) binary CO_2(1)/Ar(2) mixtures in FAU all-silica zeolite at 300 K, compared with the estimations (continuous solid lines) using the Maxwell-Stefan model, based on fitted data of unary diffusivities, $Đ_1,Đ_2$, and unary degrees of correlations, $Đ_1/Đ_{11},Đ_2/Đ_{22}$.

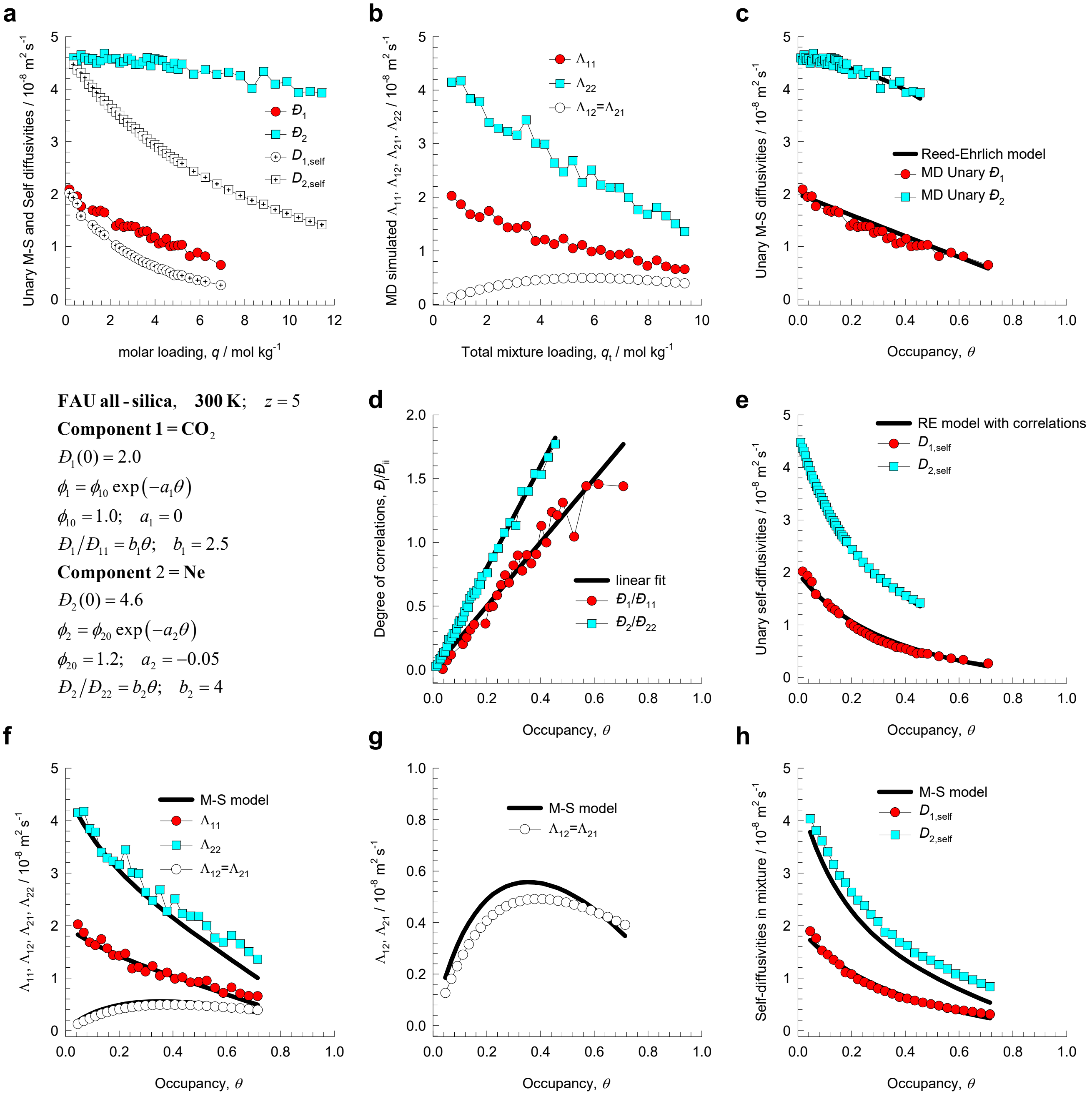

FAU all-silica, 300 K; $z = 5$

Component 1 = CO_2

$Đ_1(0) = 2.0$

$\phi_1 = \phi_{10} \exp(-a_1\theta)$

$\phi_{10} = 1.0; \quad a_1 = 0$

$Đ_1/Đ_{11} = b_1\theta; \quad b_1 = 2.5$

Component 2 = Ne

$Đ_2(0) = 4.6$

$\phi_2 = \phi_{20} \exp(-a_2\theta)$

$\phi_{20} = 1.2; \quad a_2 = -0.05$

$Đ_2/Đ_{22} = b_2\theta; \quad b_2 = 4$

Figure S73. (a-h) MD simulated values of $\Lambda_{11},\Lambda_{12},\Lambda_{21},\Lambda_{22}$ for equimolar (q_1=q_2) binary CO_2(1)/Ne(2) mixtures in FAU all-silica zeolite at 300 K, compared with the estimations (continuous solid lines) using the Maxwell-Stefan model, based on fitted data of unary diffusivities, $Đ_1$,$Đ_2$, and unary degrees of correlations, $Đ_1/Đ_{11}, Đ_2/Đ_{22}$.

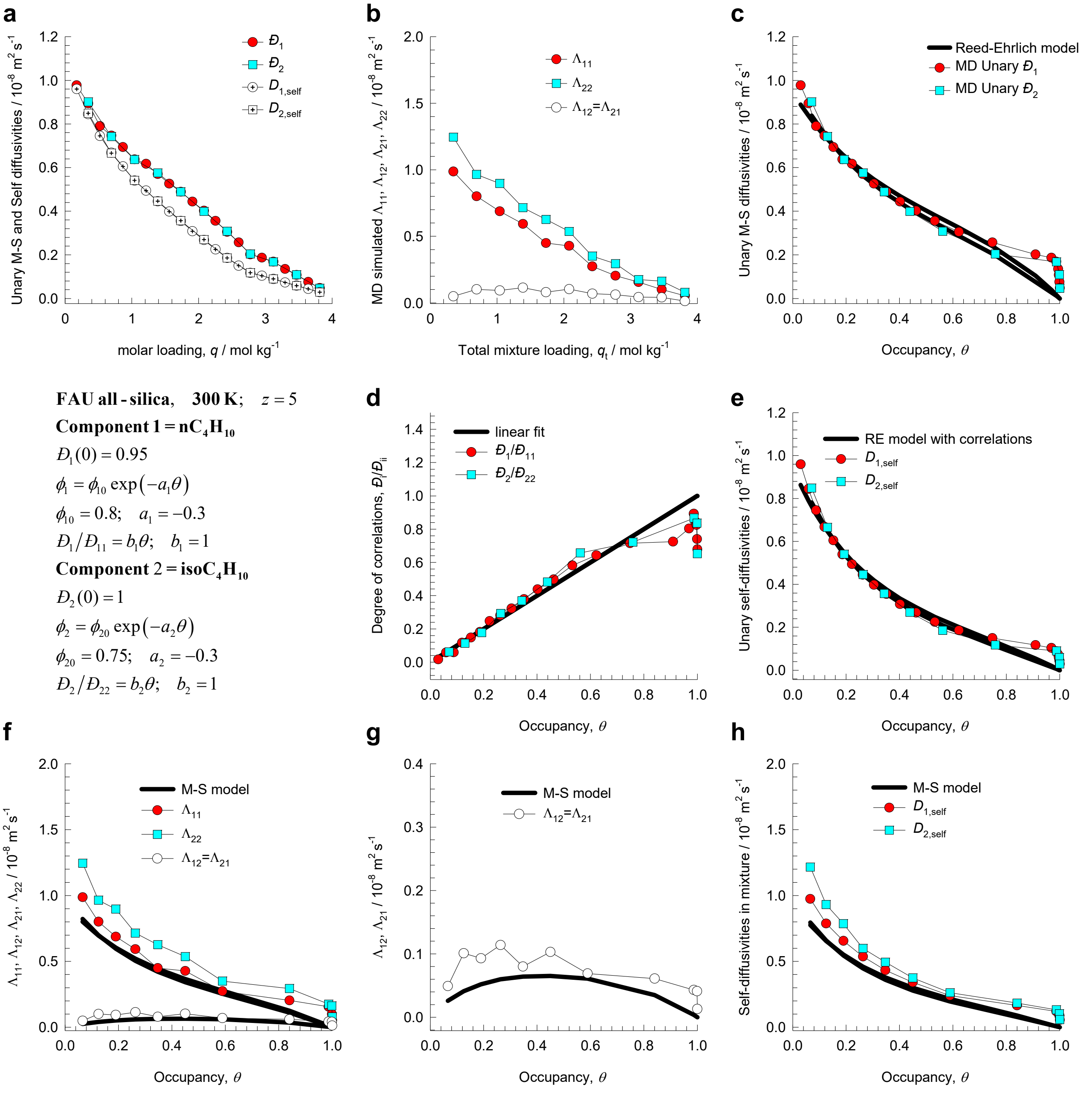

FAU all-silica, 300 K; $z=5$

Component 1 = $\mathbf{nC_4H_{10}}$

$Đ_1(0)=0.95$

$\phi_1=\phi_{10}\exp(-a_1\theta)$

$\phi_{10}=0.8;\quad a_1=-0.3$

$Đ_1/Đ_{11}=b_1\theta;\quad b_1=1$

Component 2 = $\mathbf{isoC_4H_{10}}$

$Đ_2(0)=1$

$\phi_2=\phi_{20}\exp(-a_2\theta)$

$\phi_{20}=0.75;\quad a_2=-0.3$

$Đ_2/Đ_{22}=b_2\theta;\quad b_2=1$

Figure S74. (a-h) MD simulated values of $\Lambda_{11},\Lambda_{12},\Lambda_{21},\Lambda_{22}$ for equimolar ($q_1=q_2$) binary nC_4H_{10}(1)/iso-C_4H_{10}(2) mixtures in FAU all-silica zeolite at 300 K, compared with the estimations (continuous solid lines) using the Maxwell-Stefan model, based on fitted data of unary diffusivities, $Đ_1,Đ_2$, and unary degrees of correlations, $Đ_1/Đ_{11},Đ_2/Đ_{22}$.

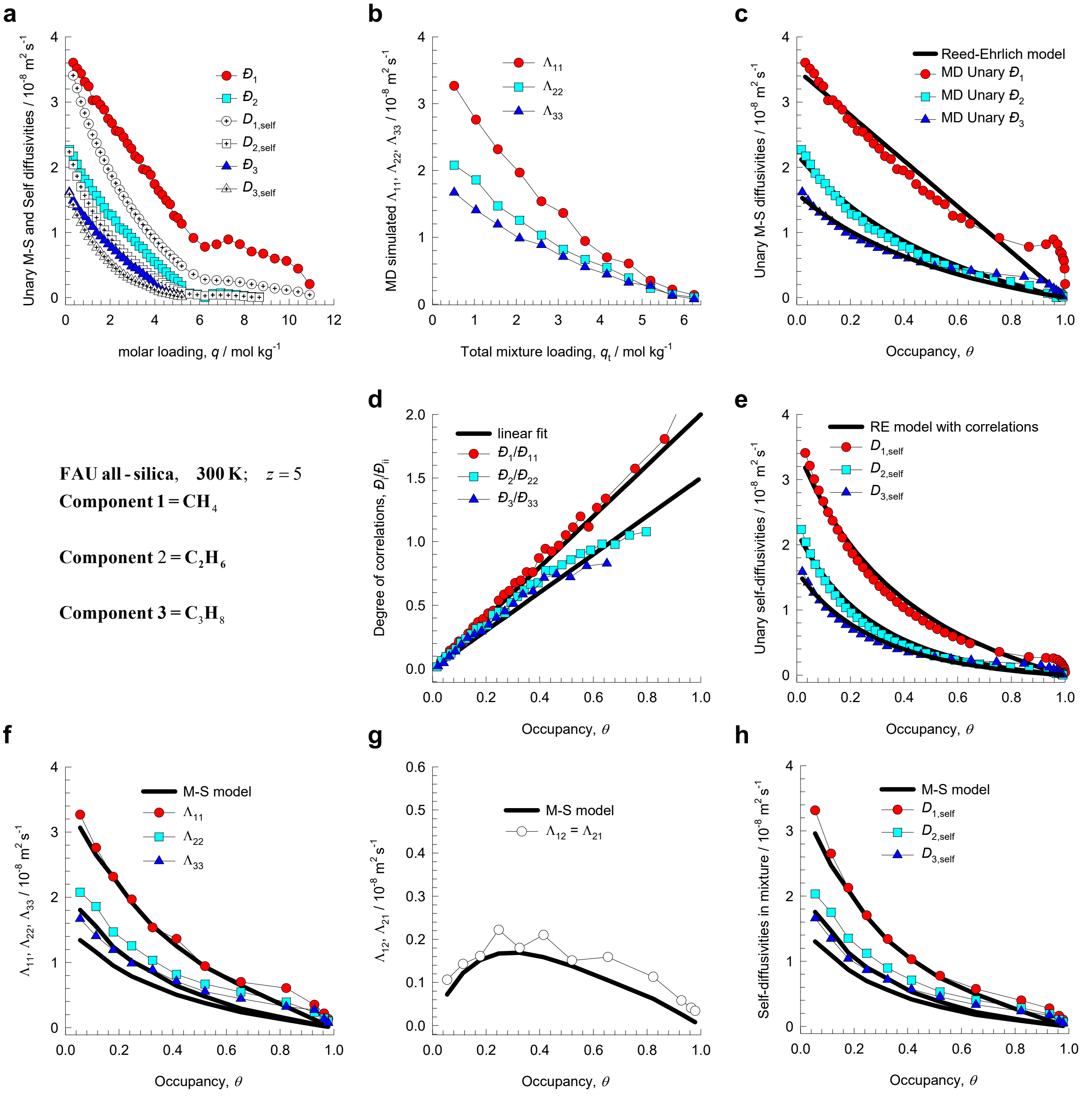

Figure S75. (a-h) MD simulated values of $\Lambda_{11},\Lambda_{12},\Lambda_{21},\Lambda_{22}$ for equimolar (q_1=q_2=q_3) ternary CH_4(1)/C_2H_6(2)/C_3H_8(2) mixtures in FAU all-silica zeolite at 300 K, compared with the estimations (continuous solid lines) using the Maxwell-Stefan model, based on fitted data of unary diffusivities, $Đ_1,Đ_2$, and unary degrees of correlations, $Đ_1/Đ_{11},Đ_2/Đ_{22},Đ_3/Đ_{33}$. The input data fits are the same as in the foregoing Figures for methane, ethane, and propane.

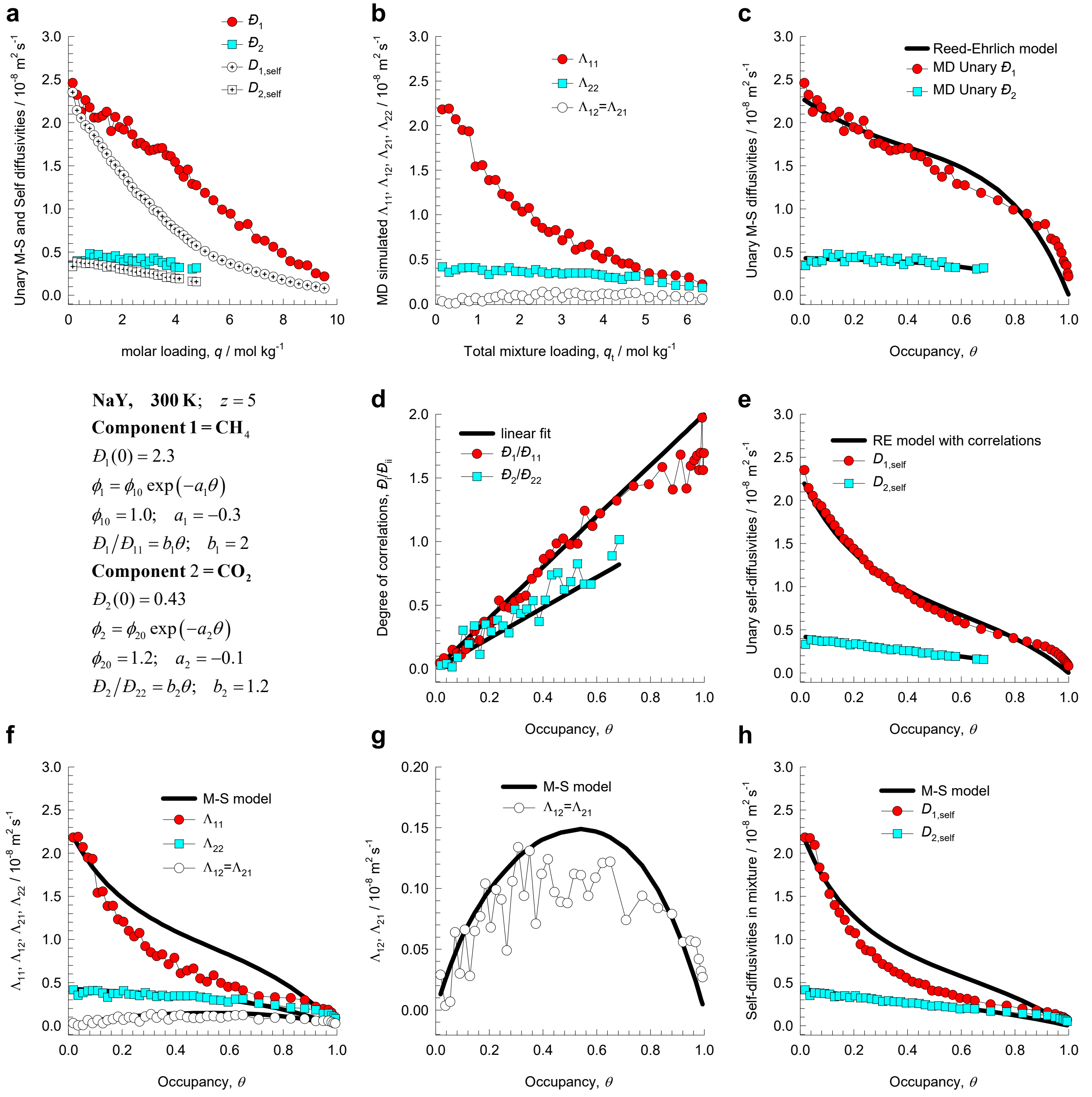

NaY, 300 K; $z = 5$

Component 1 = CH$_4$

$Đ_1(0) = 2.3$

$\phi_1 = \phi_{10}\exp(-a_1\theta)$

$\phi_{10} = 1.0; \quad a_1 = -0.3$

$Đ_1/Đ_{11} = b_1\theta; \quad b_1 = 2$

Component 2 = CO$_2$

$Đ_2(0) = 0.43$

$\phi_2 = \phi_{20}\exp(-a_2\theta)$

$\phi_{20} = 1.2; \quad a_2 = -0.1$

$Đ_2/Đ_{22} = b_2\theta; \quad b_2 = 1.2$

Figure S76. (a-h) MD simulated values of $\Lambda_{11},\Lambda_{12},\Lambda_{21},\Lambda_{22}$ for equimolar (q_1=q_2) binary CH$_4$(1)/CO$_2$(2) mixtures in NaY zeolite (48 Al) at 300 K, compared with the estimations (continuous solid lines) using the Maxwell-Stefan model, based on fitted data of unary diffusivities, $Đ_1$,$Đ_2$, and unary degrees of correlations, $Đ_1/Đ_{11}, Đ_2/Đ_{22}$.

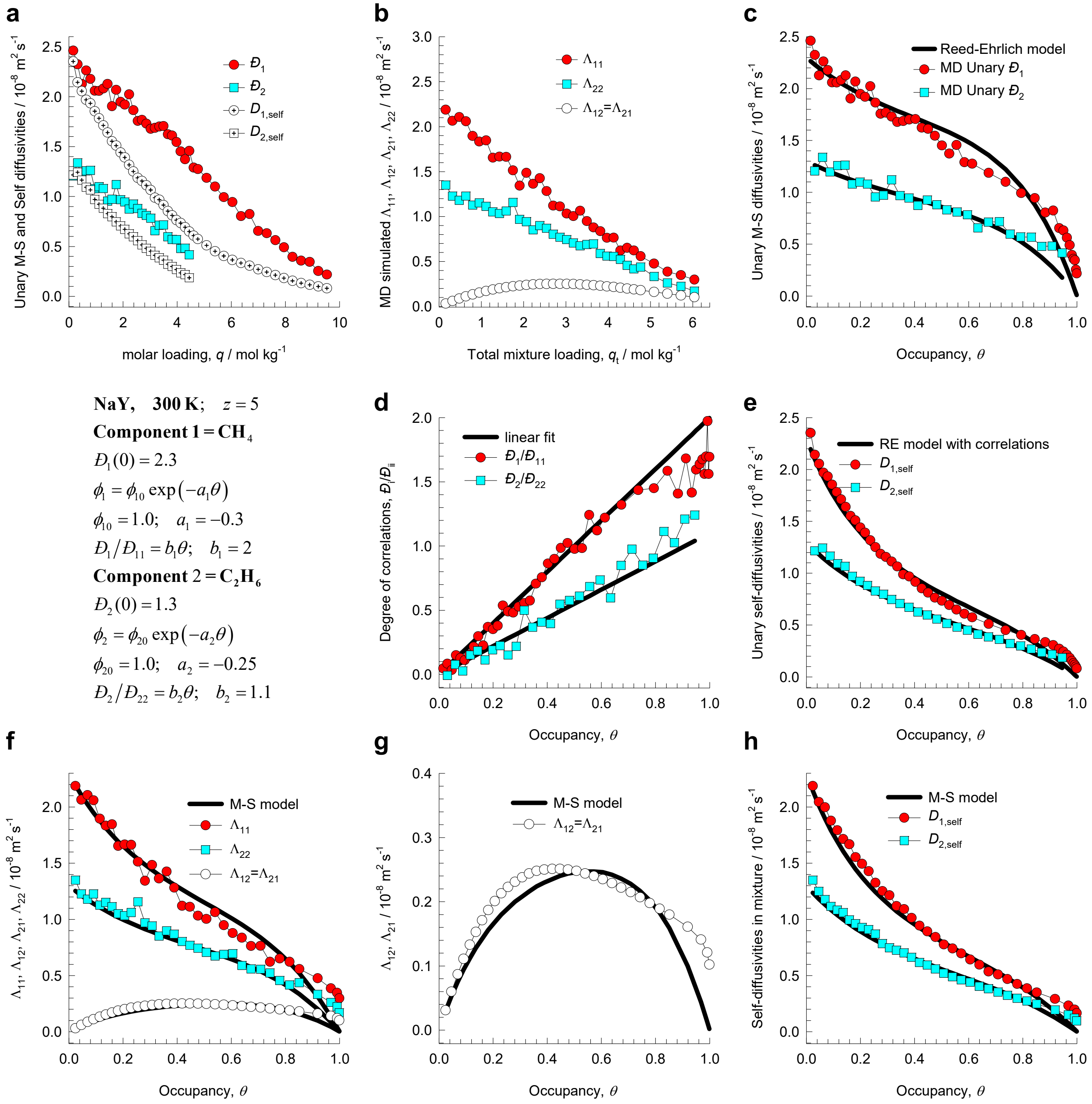

Figure S77. (a-h) MD simulated values of $\Lambda_{11},\Lambda_{12},\Lambda_{21},\Lambda_{22}$ for equimolar (q_1=q_2) binary CH$_4$(1)/C$_2$H$_6$(2) mixtures in NaY zeolite (48 Al) at 300 K, compared with the estimations (continuous solid lines) using the Maxwell-Stefan model, based on fitted data of unary diffusivities, $Đ_1,Đ_2$, and unary degrees of correlations, $Đ_1/Đ_{11},Đ_2/Đ_{22}$.

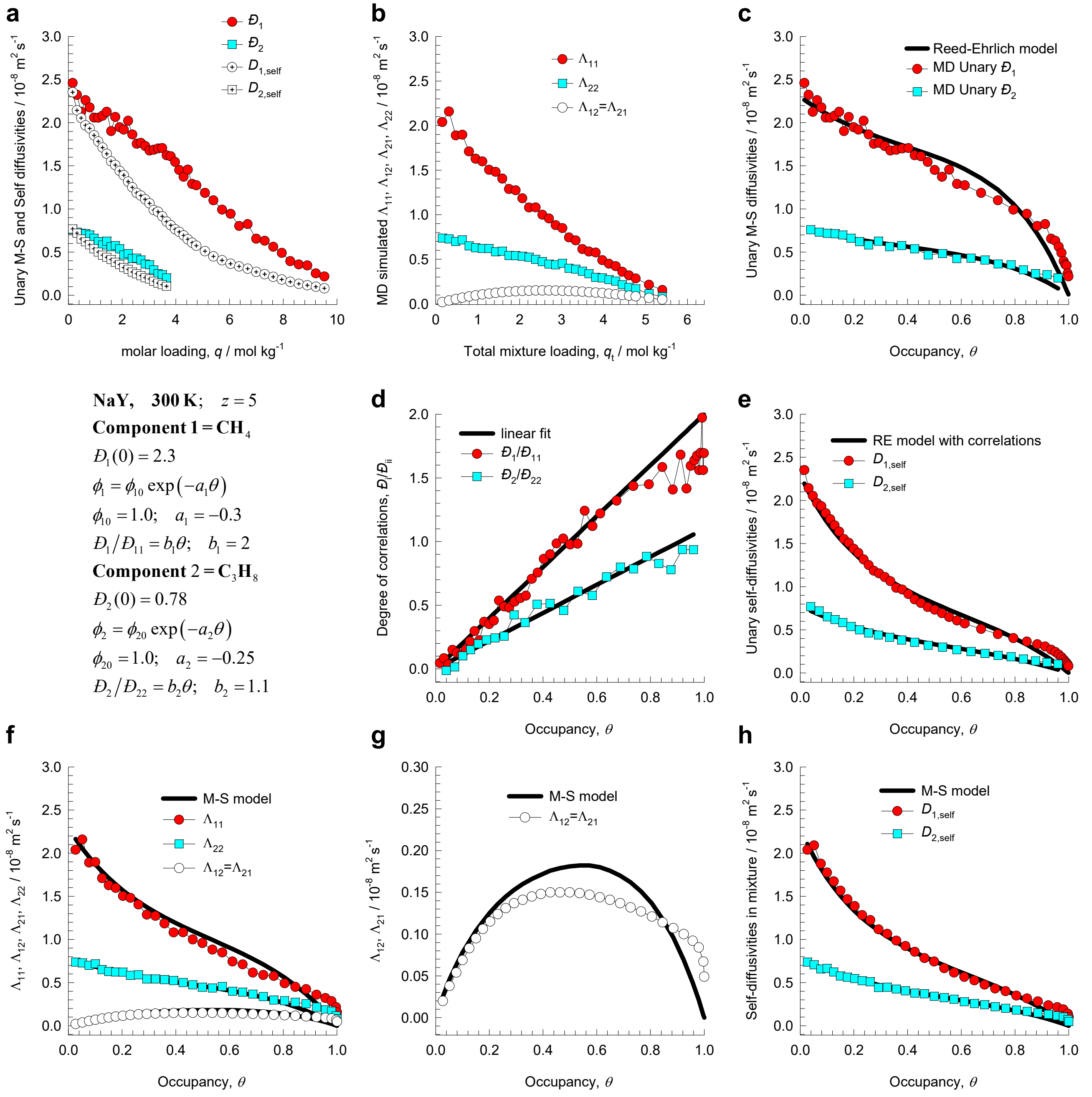

Figure S78. (a-h) MD simulated values of $\Lambda_{11},\Lambda_{12},\Lambda_{21},\Lambda_{22}$ for equimolar (q_1=q_2) binary CH_4(1)/C_3H_8(2) mixtures in NaY zeolite (48 Al) at 300 K, compared with the estimations (continuous solid lines) using the Maxwell-Stefan model, based on fitted data of unary diffusivities, $Đ_1,Đ_2$, and unary degrees of correlations, $Đ_1/Đ_{11}, Đ_2/Đ_{22}$.

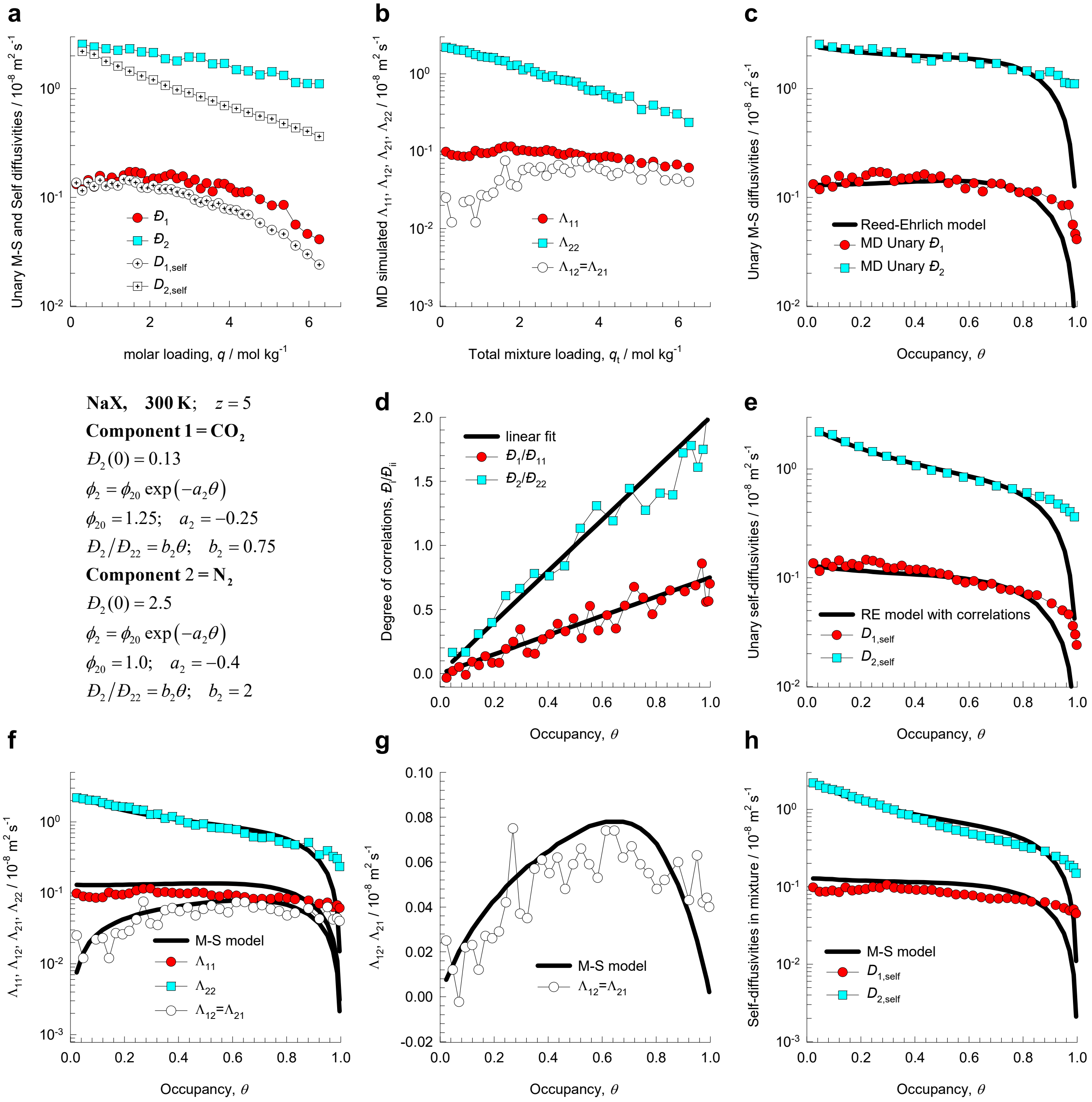

Figure S79. (a-h) MD simulated values of $\Lambda_{11},\Lambda_{12},\Lambda_{21},\Lambda_{22}$ for equimolar ($q_1=q_2$) binary CO_2(1)/N_2(2) mixtures in NaX zeolite (86 Al) at 300 K, compared with the estimations (continuous solid lines) using the Maxwell-Stefan model, based on fitted data of unary diffusivities, $Đ_1,Đ_2$, and unary degrees of correlations, $Đ_1/Đ_{11}, Đ_2/Đ_{22}$.

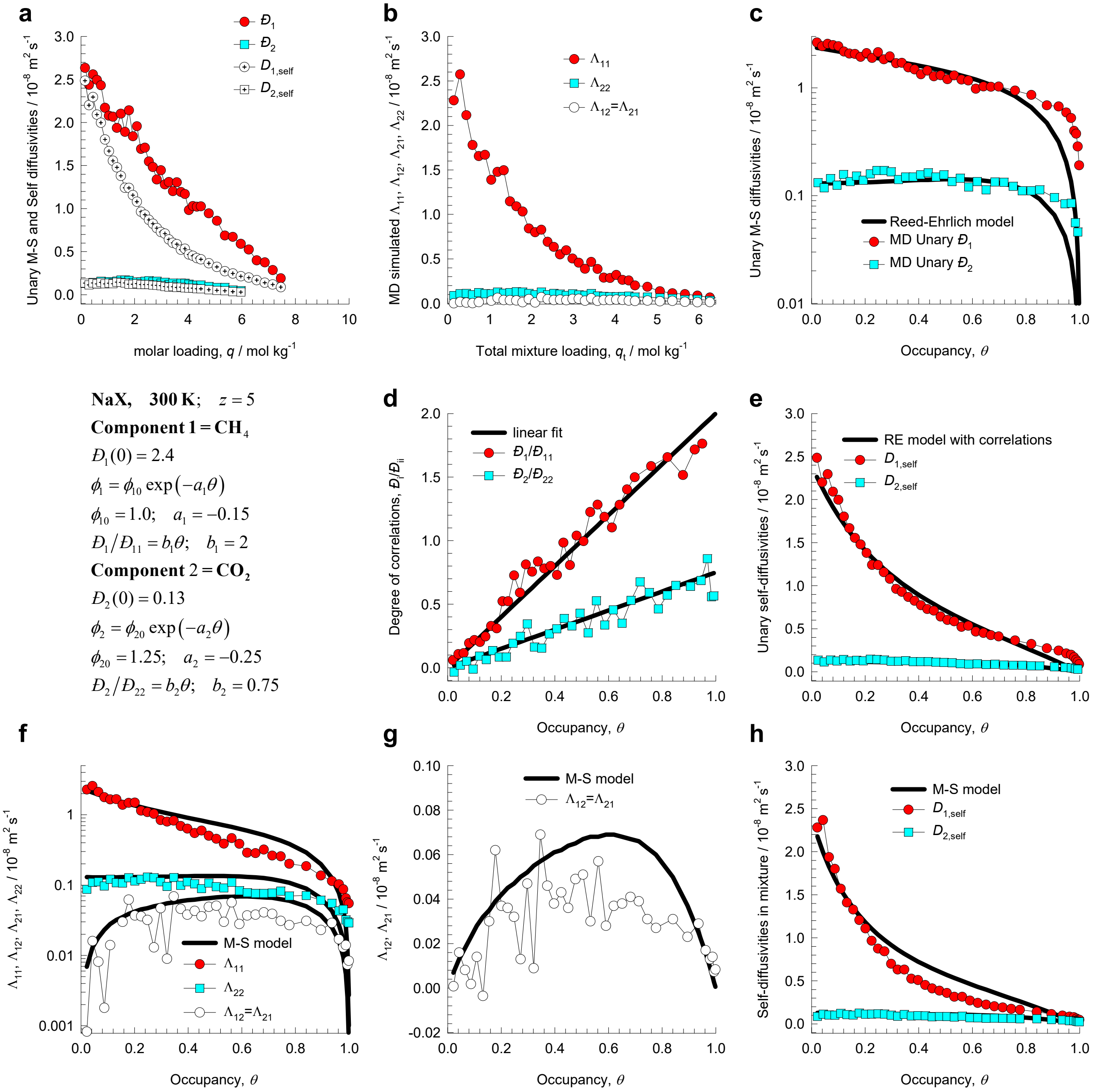

NaX, 300 K; $z = 5$

Component 1 = CH_4

$Đ_1(0) = 2.4$

$\phi_1 = \phi_{10}\exp(-a_1\theta)$

$\phi_{10} = 1.0; \quad a_1 = -0.15$

$Đ_1/Đ_{11} = b_1\theta; \quad b_1 = 2$

Component 2 = CO_2

$Đ_2(0) = 0.13$

$\phi_2 = \phi_{20}\exp(-a_2\theta)$

$\phi_{20} = 1.25; \quad a_2 = -0.25$

$Đ_2/Đ_{22} = b_2\theta; \quad b_2 = 0.75$

Figure S80. (a-h) MD simulated values of $\Lambda_{11}, \Lambda_{12}, \Lambda_{21}, \Lambda_{22}$ for equimolar (q_1=q_2) binary CH_4(1)/CO_2(2) mixtures in NaX zeolite (86 Al) at 300 K, compared with the estimations (continuous solid lines) using the Maxwell-Stefan model, based on fitted data of unary diffusivities, $Đ_1, Đ_2$, and unary degrees of correlations, $Đ_1/Đ_{11}, Đ_2/Đ_{22}$.

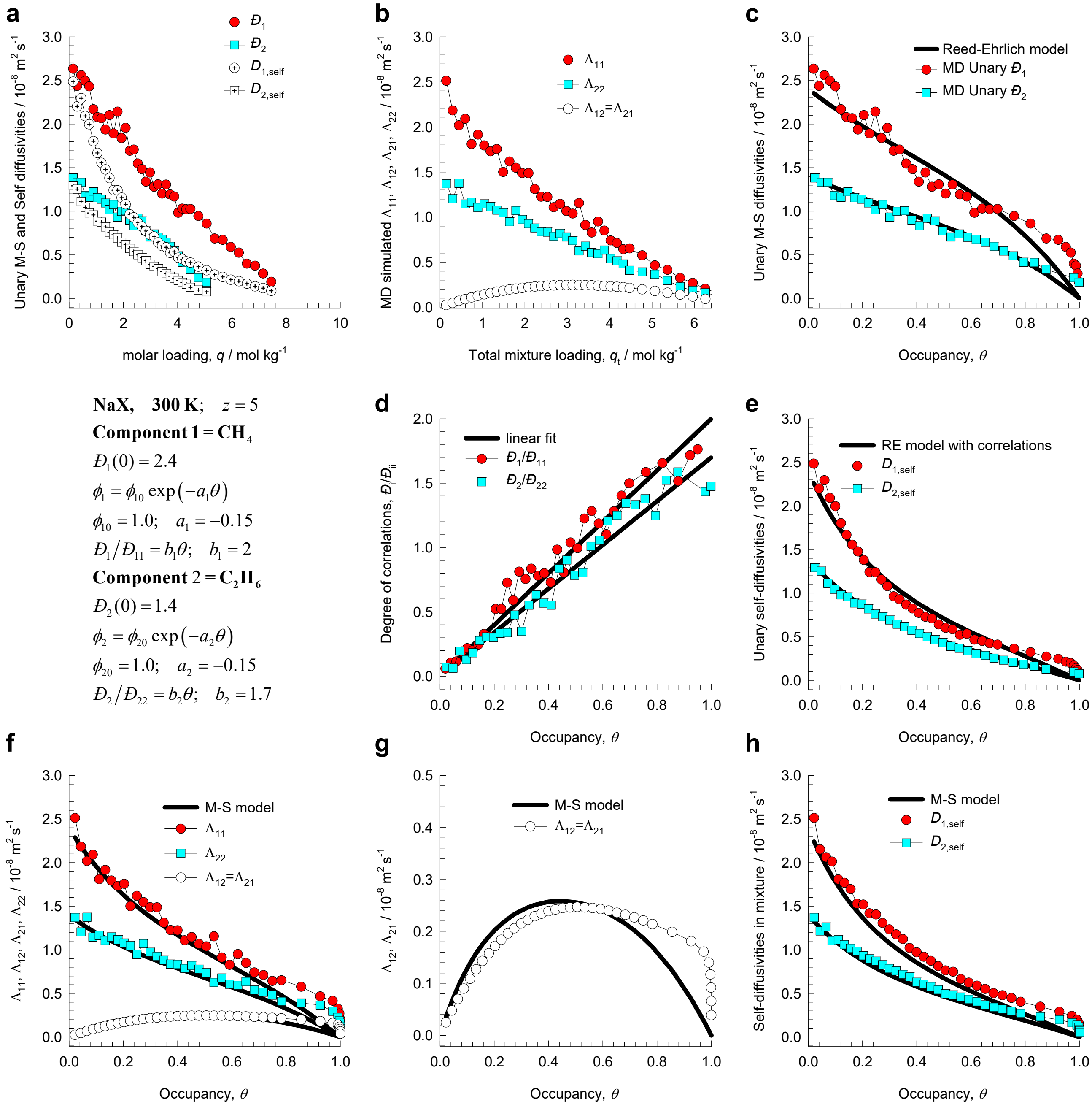

NaX, 300 K; $z = 5$

Component 1 = $\mathbf{CH_4}$

$Đ_1(0) = 2.4$

$\phi_1 = \phi_{10}\exp(-a_1\theta)$

$\phi_{10} = 1.0;\quad a_1 = -0.15$

$Đ_1/Đ_{11} = b_1\theta;\quad b_1 = 2$

Component 2 = $\mathbf{C_2H_6}$

$Đ_2(0) = 1.4$

$\phi_2 = \phi_{20}\exp(-a_2\theta)$

$\phi_{20} = 1.0;\quad a_2 = -0.15$

$Đ_2/Đ_{22} = b_2\theta;\quad b_2 = 1.7$

Figure S81. (a-h) MD simulated values of $\Lambda_{11},\Lambda_{12},\Lambda_{21},\Lambda_{22}$ for equimolar (q_1=q_2) binary CH_4(1)/C_2H_6(2) mixtures in NaX zeolite (86 Al) at 300 K, compared with the estimations (continuous solid lines) using the Maxwell-Stefan model, based on fitted data of unary diffusivities, $Đ_1$,$Đ_2$, and unary degrees of correlations, $Đ_1/Đ_{11}, Đ_2/Đ_{22}$.

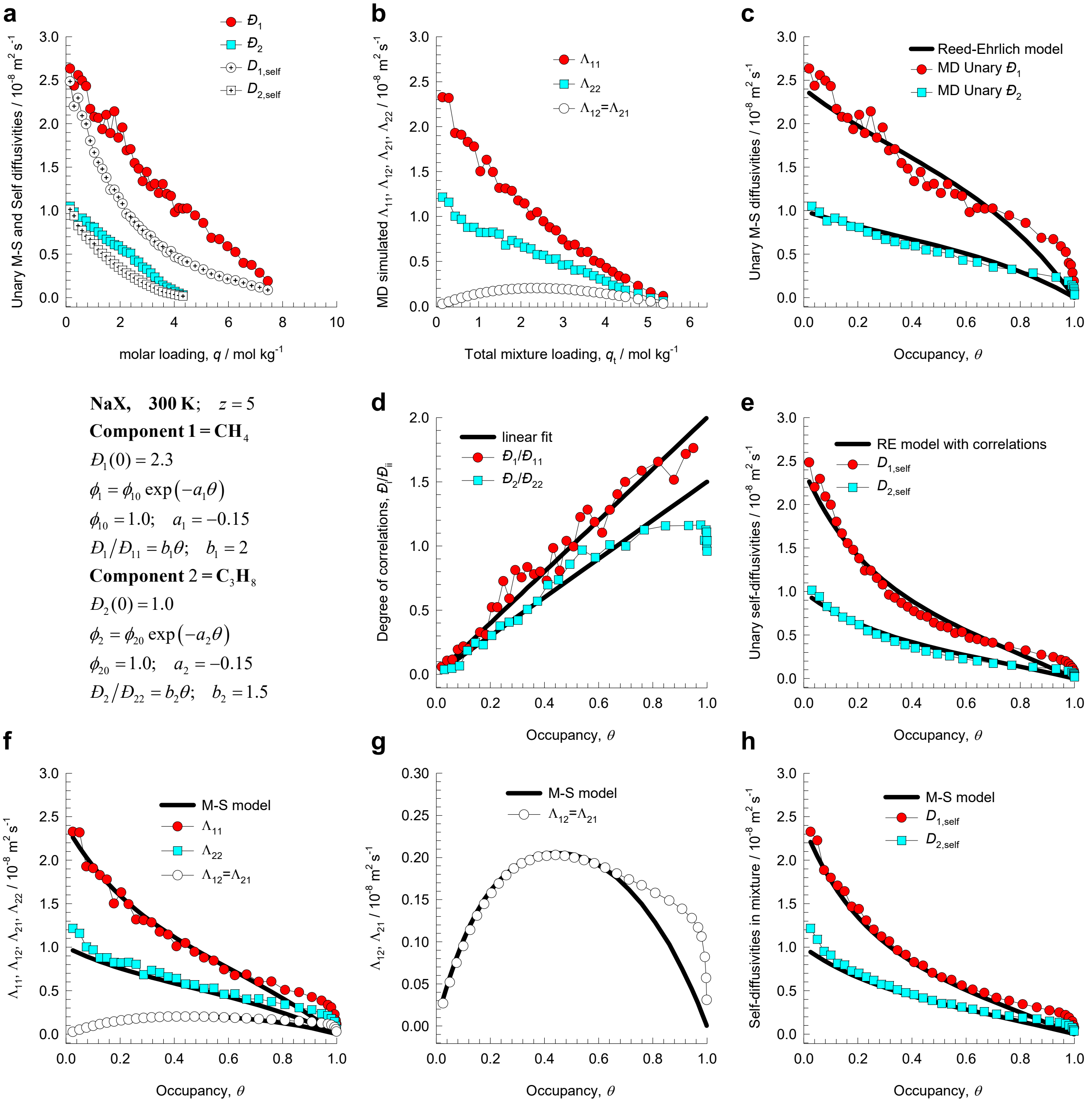

NaX, 300 K; $z = 5$

Component $1 = \mathbf{CH_4}$

$Đ_1(0) = 2.3$

$\phi_1 = \phi_{10} \exp(-a_1\theta)$

$\phi_{10} = 1.0; \quad a_1 = -0.15$

$Đ_1/Đ_{11} = b_1\theta; \quad b_1 = 2$

Component $2 = \mathbf{C_3H_8}$

$Đ_2(0) = 1.0$

$\phi_2 = \phi_{20} \exp(-a_2\theta)$

$\phi_{20} = 1.0; \quad a_2 = -0.15$

$Đ_2/Đ_{22} = b_2\theta; \quad b_2 = 1.5$

Figure S82. (a-h) MD simulated values of $\Lambda_{11}, \Lambda_{12}, \Lambda_{21}, \Lambda_{22}$ for equimolar (q_1=q_2) binary CH_4(1)/C_3H_8(2) mixtures in NaX zeolite (86 Al) at 300 K, compared with the estimations (continuous solid lines) using the Maxwell-Stefan model, based on fitted data of unary diffusivities, $Đ_1, Đ_2$, and unary degrees of correlations, $Đ_1/Đ_{11}, Đ_2/Đ_{22}$.

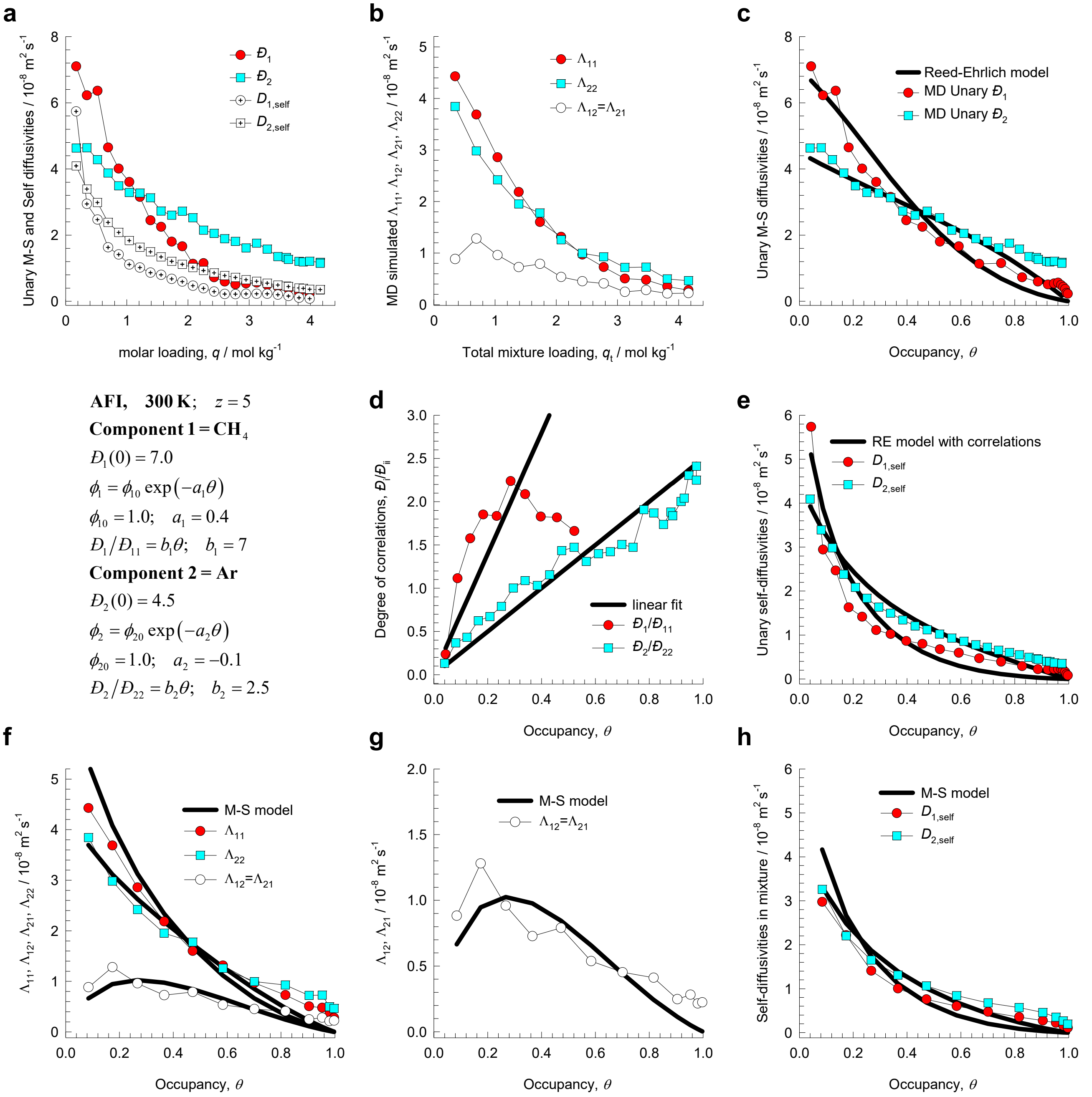

AFI, 300 K; $z = 5$

Component 1 = $\mathbf{CH_4}$

$\text{Đ}_1(0) = 7.0$

$\phi_1 = \phi_{10}\exp(-a_1\theta)$

$\phi_{10} = 1.0; \quad a_1 = 0.4$

$\text{Đ}_1/\text{Đ}_{11} = b_1\theta; \quad b_1 = 7$

Component 2 = Ar

$\text{Đ}_2(0) = 4.5$

$\phi_2 = \phi_{20}\exp(-a_2\theta)$

$\phi_{20} = 1.0; \quad a_2 = -0.1$

$\text{Đ}_2/\text{Đ}_{22} = b_2\theta; \quad b_2 = 2.5$

Figure S83. (a-h) MD simulated values of $\Lambda_{11},\Lambda_{12},\Lambda_{21},\Lambda_{22}$ for equimolar (q_1=q_2) binary CH_4(1)/Ar(2) mixtures in AFI all-silica zeolite at 300 K, compared with the estimations (continuous solid lines) using the Maxwell-Stefan model, based on fitted data of unary diffusivities, $\text{Đ}_1,\text{Đ}_2$, and unary degrees of correlations, $\text{Đ}_1/\text{Đ}_{11},\text{Đ}_2/\text{Đ}_{22}$.

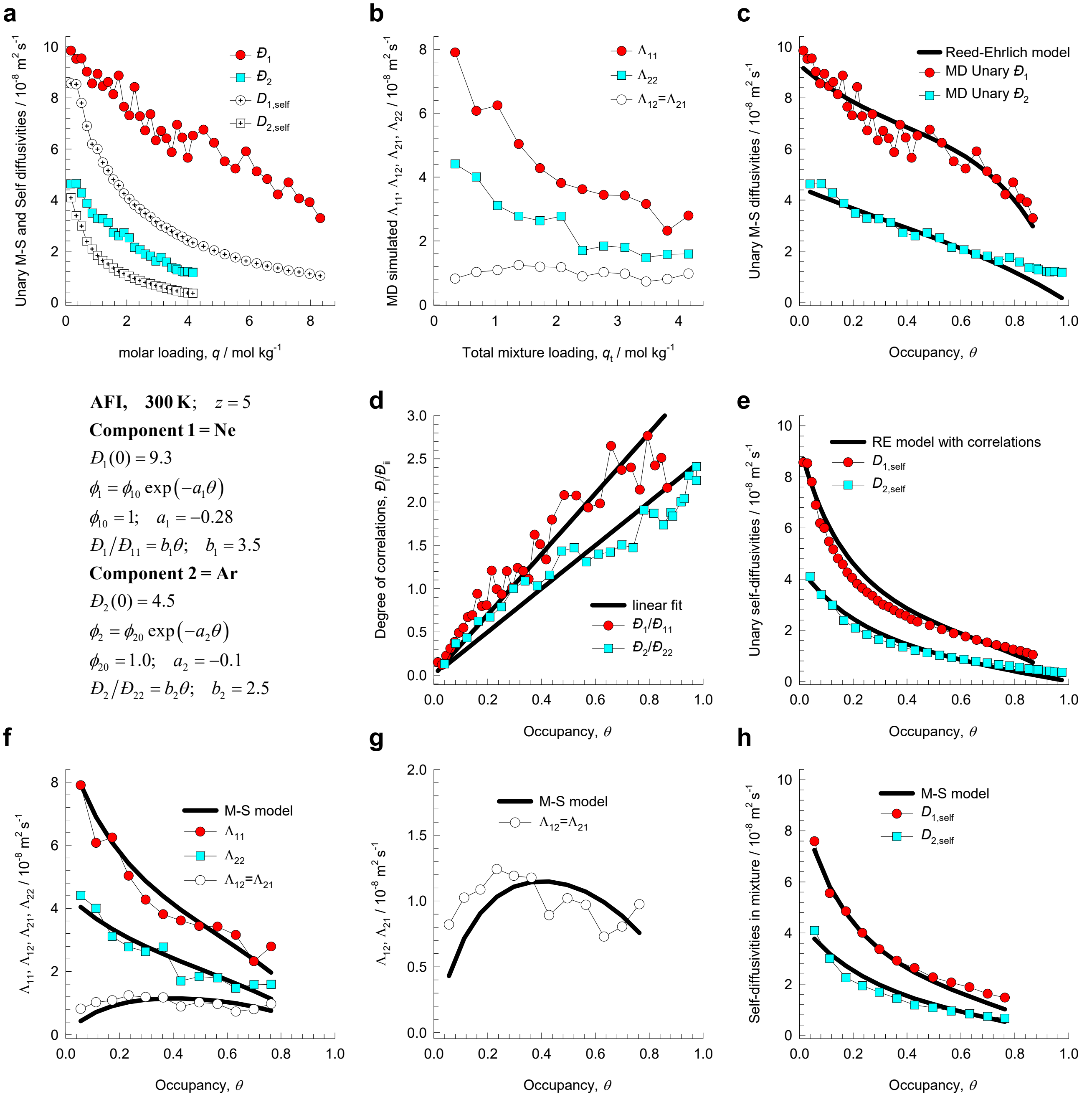

Figure S84. (a-h) MD simulated values of $\Lambda_{11},\Lambda_{12},\Lambda_{21},\Lambda_{22}$ for equimolar (q_1=q_2) binary Ne(1)/Ar(2) mixtures in AFI all-silica zeolite at 300 K, compared with the estimations (continuous solid lines) using the Maxwell-Stefan model, based on fitted data of unary diffusivities, $Đ_1,Đ_2$, and unary degrees of correlations, $Đ_1/Đ_{11},Đ_2/Đ_{22}$.

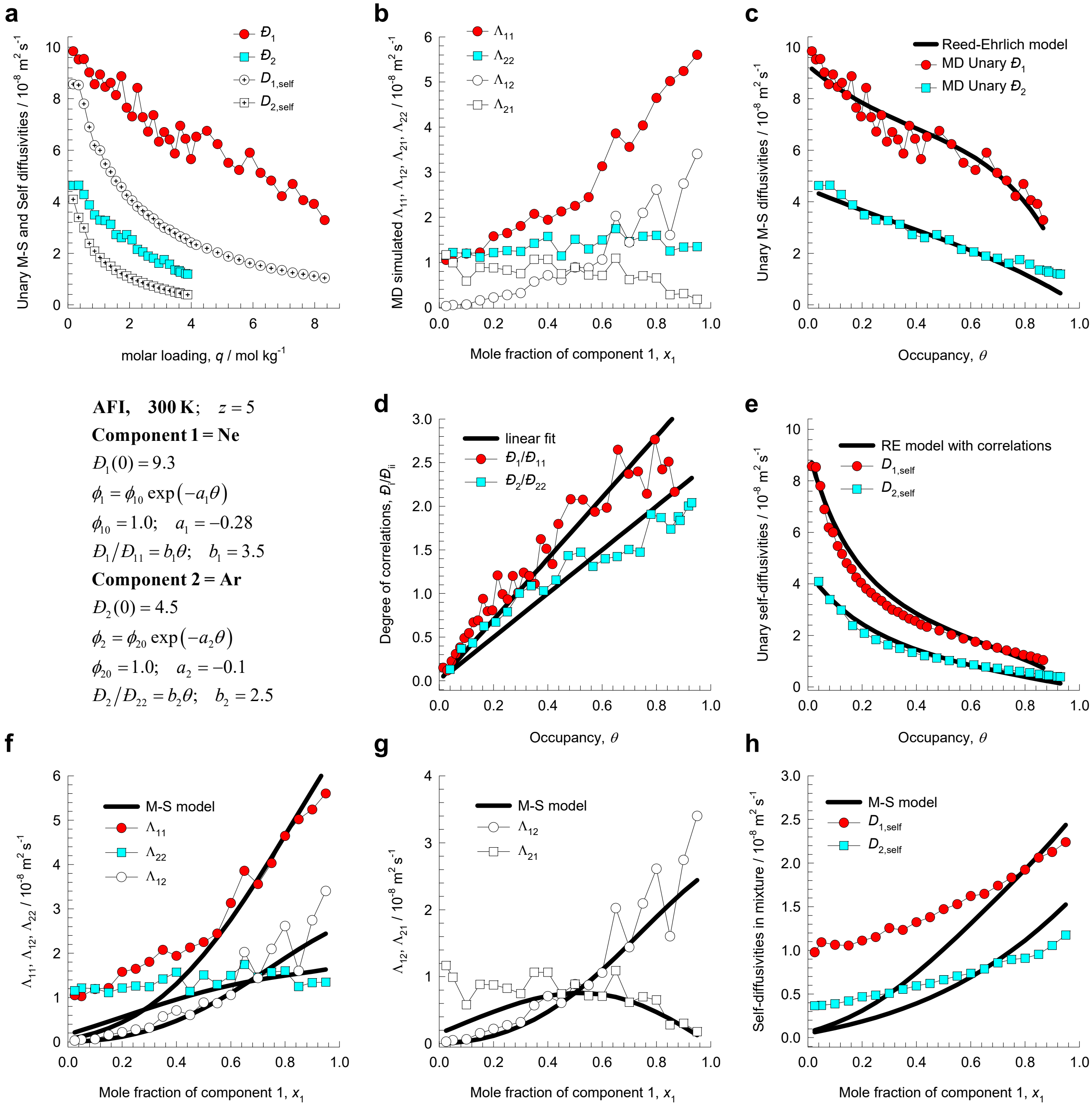

AFI, 300 K; $z = 5$

Component 1 = Ne

$Đ_1(0) = 9.3$

$\phi_1 = \phi_{10}\exp(-a_1\theta)$

$\phi_{10} = 1.0; \quad a_1 = -0.28$

$Đ_1/Đ_{11} = b_1\theta; \quad b_1 = 3.5$

Component 2 = Ar

$Đ_2(0) = 4.5$

$\phi_2 = \phi_{20}\exp(-a_2\theta)$

$\phi_{20} = 1.0; \quad a_2 = -0.1$

$Đ_2/Đ_{22} = b_2\theta; \quad b_2 = 2.5$

Figure S85. (a-h) MD simulated values of $\Lambda_{11},\Lambda_{12},\Lambda_{21},\Lambda_{22}$ for binary Ne(1)/Ar(2) mixtures of varying composition (total loading = 12 molecules uc^{-1}) in AFI all-silica zeolite at 300 K, compared with the estimations (continuous solid lines) using the Maxwell-Stefan model, based on fitted data of unary diffusivities, $Đ_1, Đ_2$, and unary degrees of correlations, $Đ_1/Đ_{11}, Đ_2/Đ_{22}$.

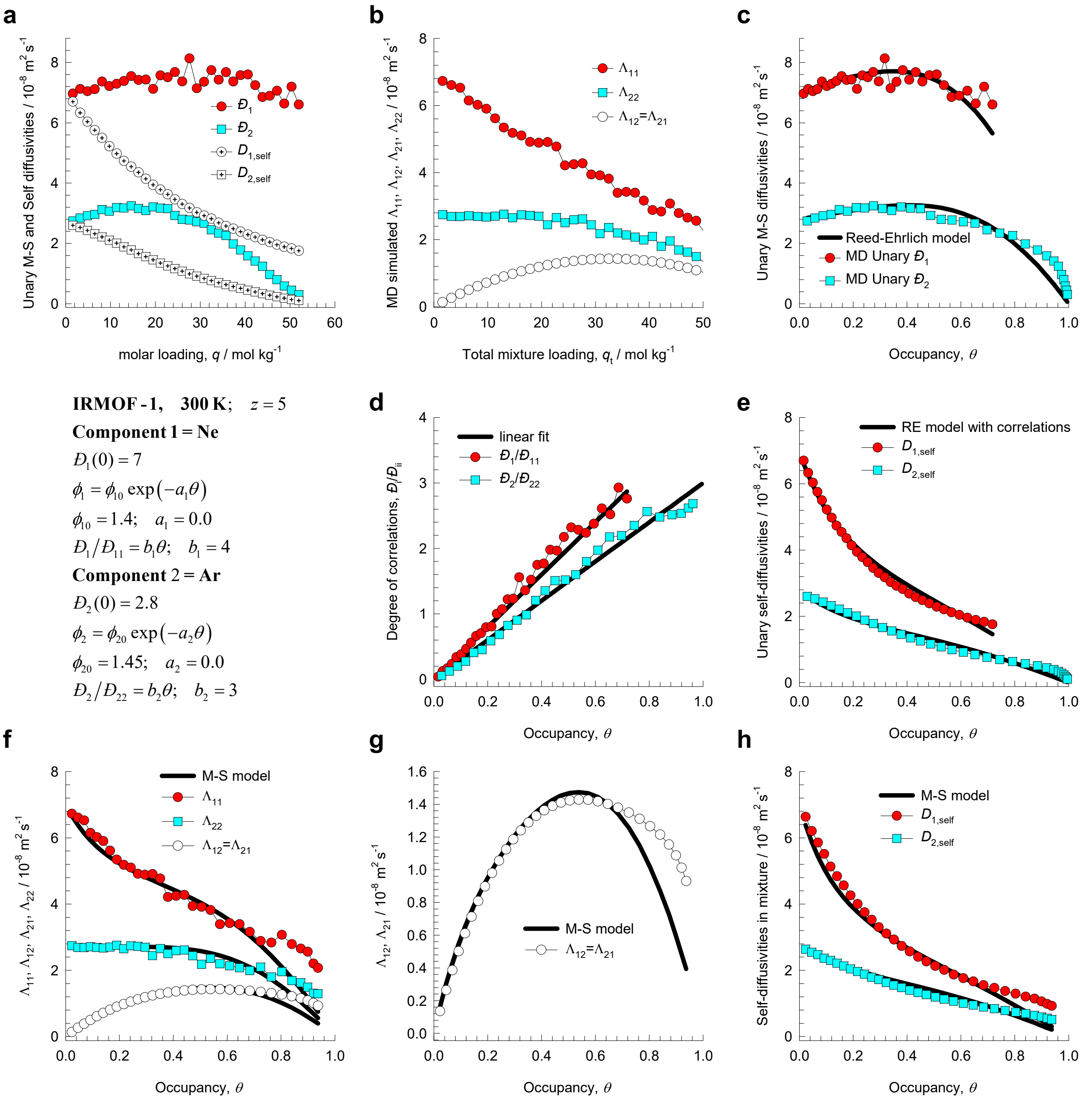

IRMOF-1, 300 K; $z = 5$

Component 1 = Ne

$Đ_1(0) = 7$

$\phi_1 = \phi_{10}\exp(-a_1\theta)$

$\phi_{10} = 1.4; \quad a_1 = 0.0$

$Đ_1/Đ_{11} = b_1\theta; \quad b_1 = 4$

Component 2 = Ar

$Đ_2(0) = 2.8$

$\phi_2 = \phi_{20}\exp(-a_2\theta)$

$\phi_{20} = 1.45; \quad a_2 = 0.0$

$Đ_2/Đ_{22} = b_2\theta; \quad b_2 = 3$

Figure S86. (a-h) MD simulated values of $\Lambda_{11},\Lambda_{12},\Lambda_{21},\Lambda_{22}$ for equimolar (q_1=q_2) binary Ne(1)/Ar(2) mixtures in IRMOF-1 at 300 K, compared with the estimations (continuous solid lines) using the Maxwell-Stefan model, based on fitted data of unary diffusivities, $Đ_1, Đ_2$, and unary degrees of correlations, $Đ_1/Đ_{11}, Đ_2/Đ_{22}$.

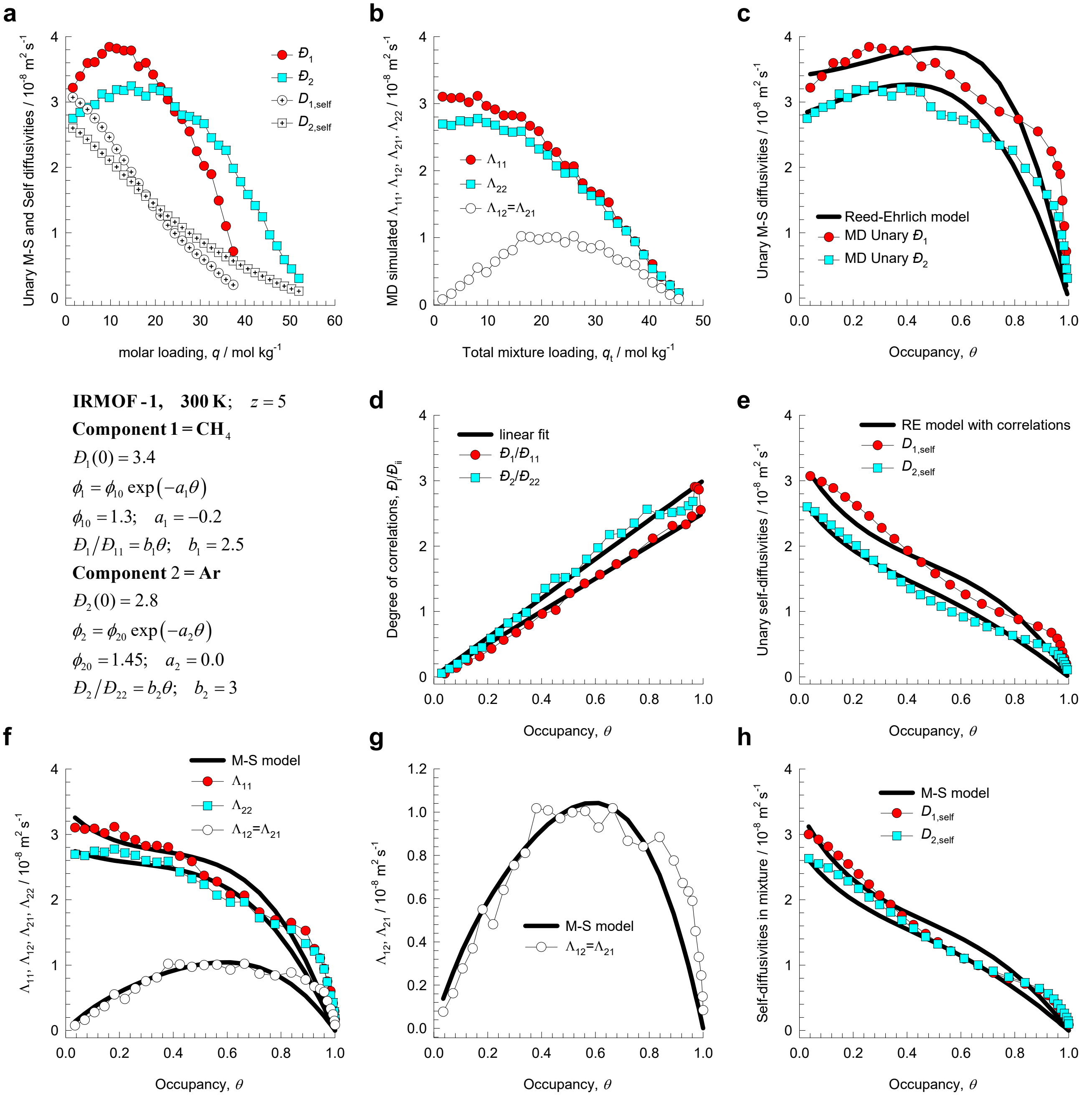

Figure S87. (a-h) MD simulated values of $\Lambda_{11},\Lambda_{12},\Lambda_{21},\Lambda_{22}$ for equimolar (q_1=q_2) binary CH_4(1)/Ar(2) mixtures in IRMOF-1 at 300 K, compared with the estimations (continuous solid lines) using the Maxwell-Stefan model, based on fitted data of unary diffusivities, $Đ_1,Đ_2$, and unary degrees of correlations, $Đ_1/Đ_{11}, Đ_2/Đ_{22}$.

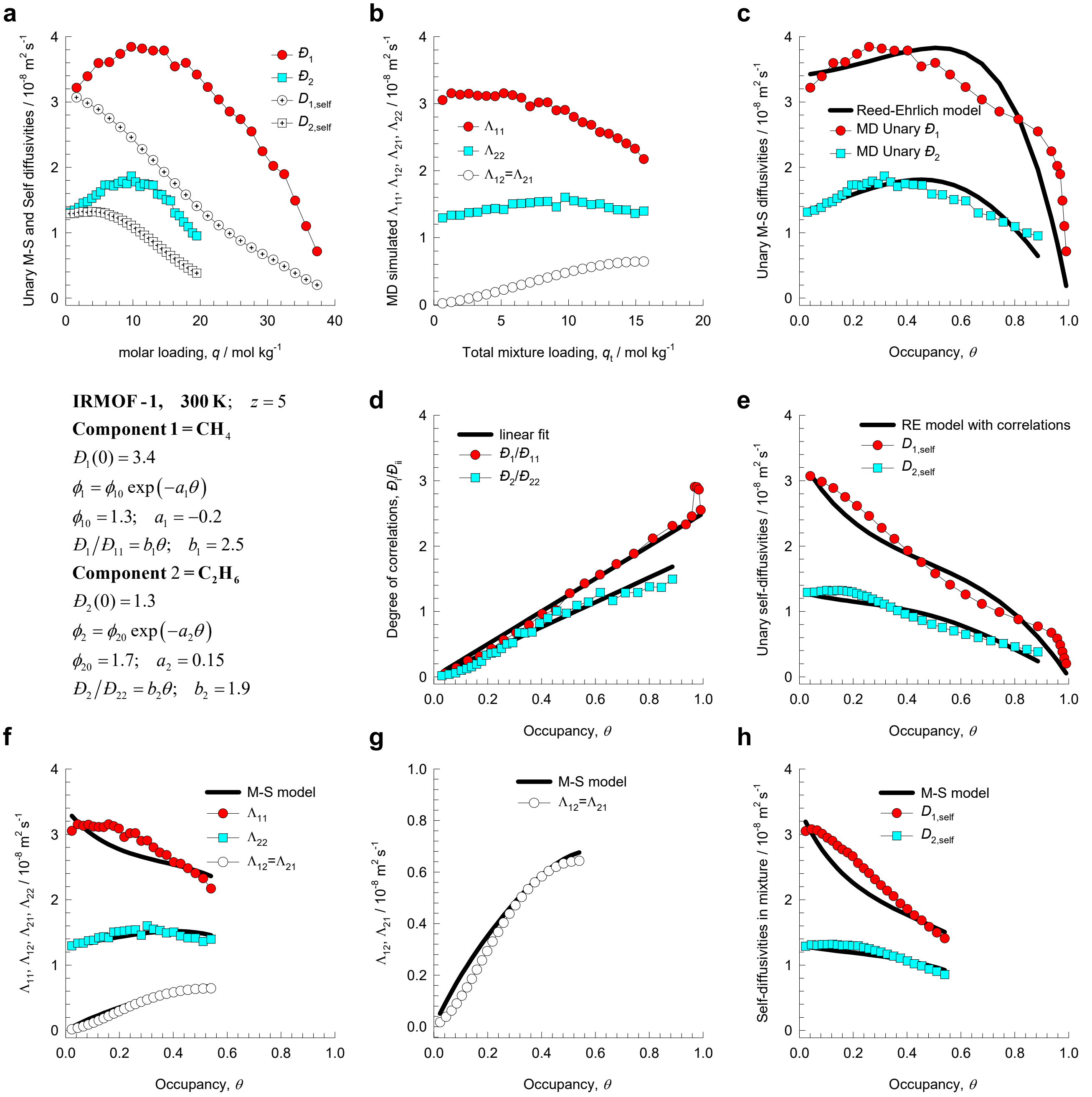

Figure S88. (a-h) MD simulated values of $\Lambda_{11},\Lambda_{12},\Lambda_{21},\Lambda_{22}$ for equimolar (q_1=q_2) binary CH_4(1)/C_2H_6(2) mixtures in IRMOF-1 at 300 K, compared with the estimations (continuous solid lines) using the Maxwell-Stefan model, based on fitted data of unary diffusivities, $Đ_1,Đ_2$, and unary degrees of correlations, $Đ_1/Đ_{11},Đ_2/Đ_{22}$.

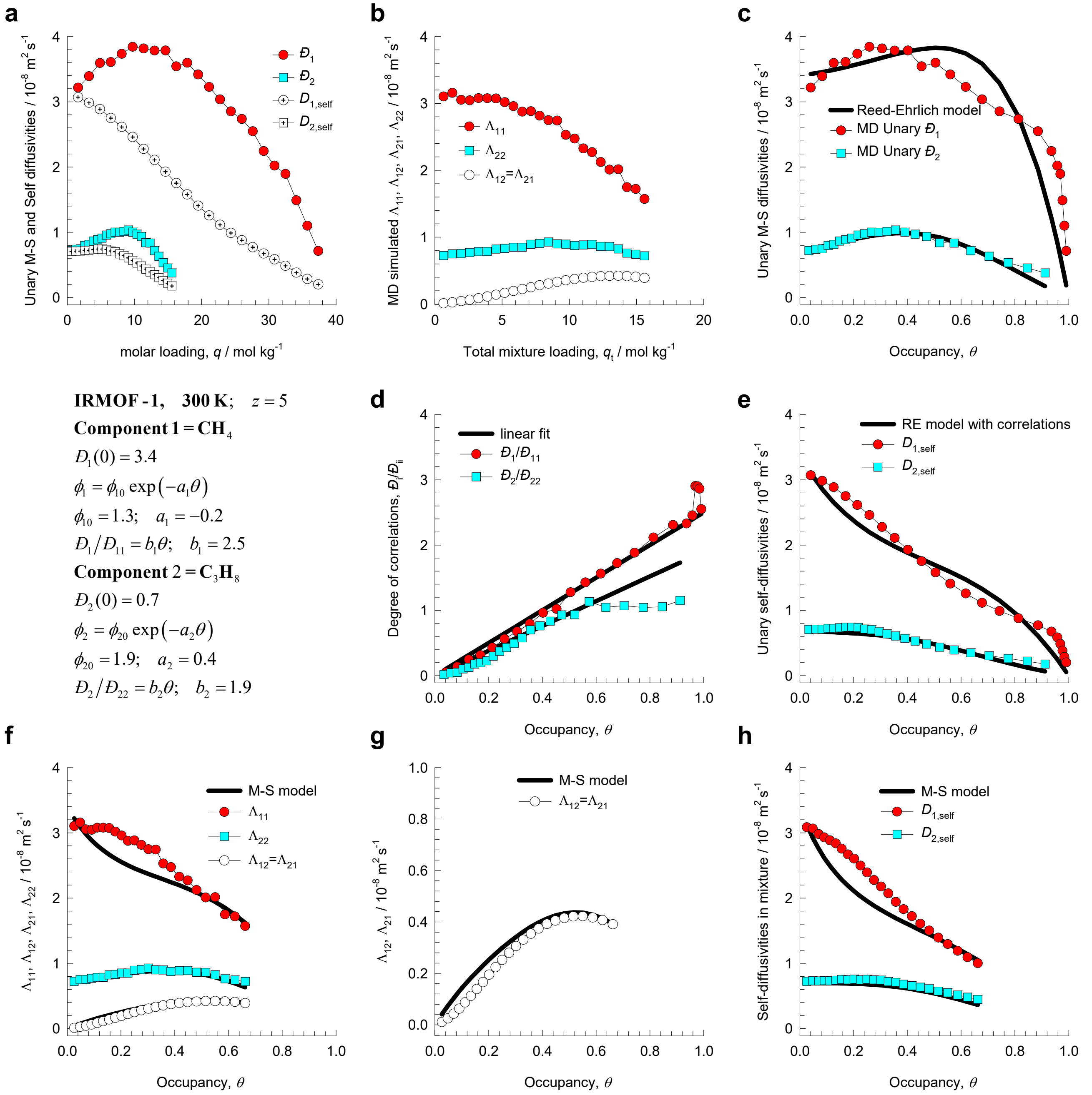

IRMOF-1, 300 K; $z=5$

Component 1 = CH_4

$Đ_1(0)=3.4$

$\phi_1=\phi_{10}\exp(-a_1\theta)$

$\phi_{10}=1.3;\quad a_1=-0.2$

$Đ_1/Đ_{11}=b_1\theta;\quad b_1=2.5$

Component 2 = C_3H_8

$Đ_2(0)=0.7$

$\phi_2=\phi_{20}\exp(-a_2\theta)$

$\phi_{20}=1.9;\quad a_2=0.4$

$Đ_2/Đ_{22}=b_2\theta;\quad b_2=1.9$

Figure S89. (a-h) MD simulated values of $\Lambda_{11},\Lambda_{12},\Lambda_{21},\Lambda_{22}$ for equimolar (q_1=q_2) binary CH_4(1)/C_3H_8(2) mixtures in IRMOF-1 at 300 K, compared with the estimations (continuous solid lines) using the Maxwell-Stefan model, based on fitted data of unary diffusivities, $Đ_1,Đ_2$, and unary degrees of correlations, $Đ_1/Đ_{11},Đ_2/Đ_{22}$.

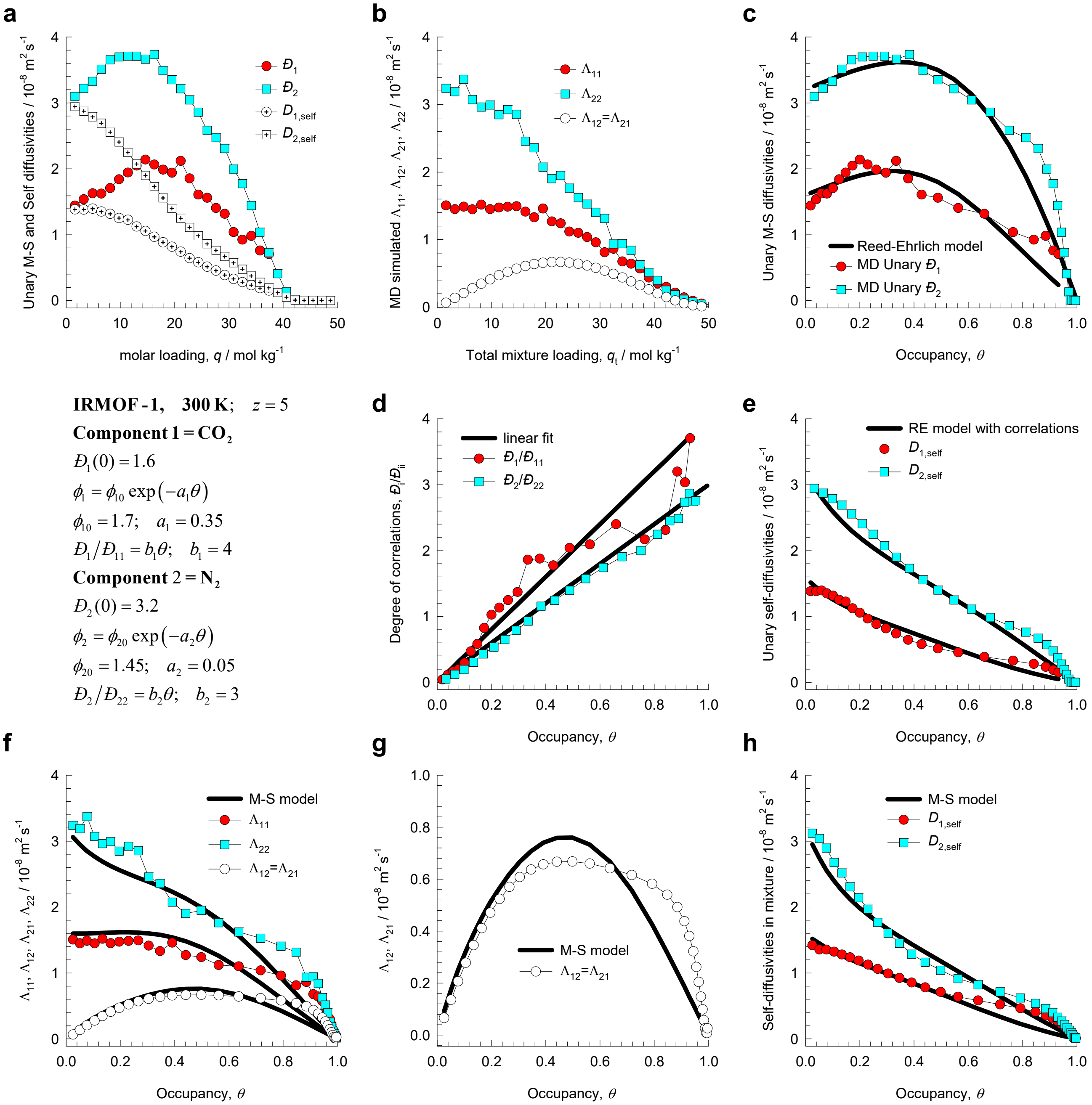

IRMOF-1, 300 K; $z = 5$

Component 1 = CO_2

$Đ_1(0) = 1.6$

$\phi_1 = \phi_{10}\exp(-a_1\theta)$

$\phi_{10} = 1.7; \quad a_1 = 0.35$

$Đ_1/Đ_{11} = b_1\theta; \quad b_1 = 4$

Component 2 = N_2

$Đ_2(0) = 3.2$

$\phi_2 = \phi_{20}\exp(-a_2\theta)$

$\phi_{20} = 1.45; \quad a_2 = 0.05$

$Đ_2/Đ_{22} = b_2\theta; \quad b_2 = 3$

Figure S90. (a-h) MD simulated values of $\Lambda_{11},\Lambda_{12},\Lambda_{21},\Lambda_{22}$ for equimolar (q_1=q_2) binary CO_2(1)/N_2(2) mixtures in IRMOF-1 at 300 K, compared with the estimations (continuous solid lines) using the Maxwell-Stefan model, based on fitted data of unary diffusivities, $Đ_1$,$Đ_2$, and unary degrees of correlations, $Đ_1/Đ_{11}$, $Đ_2/Đ_{22}$.

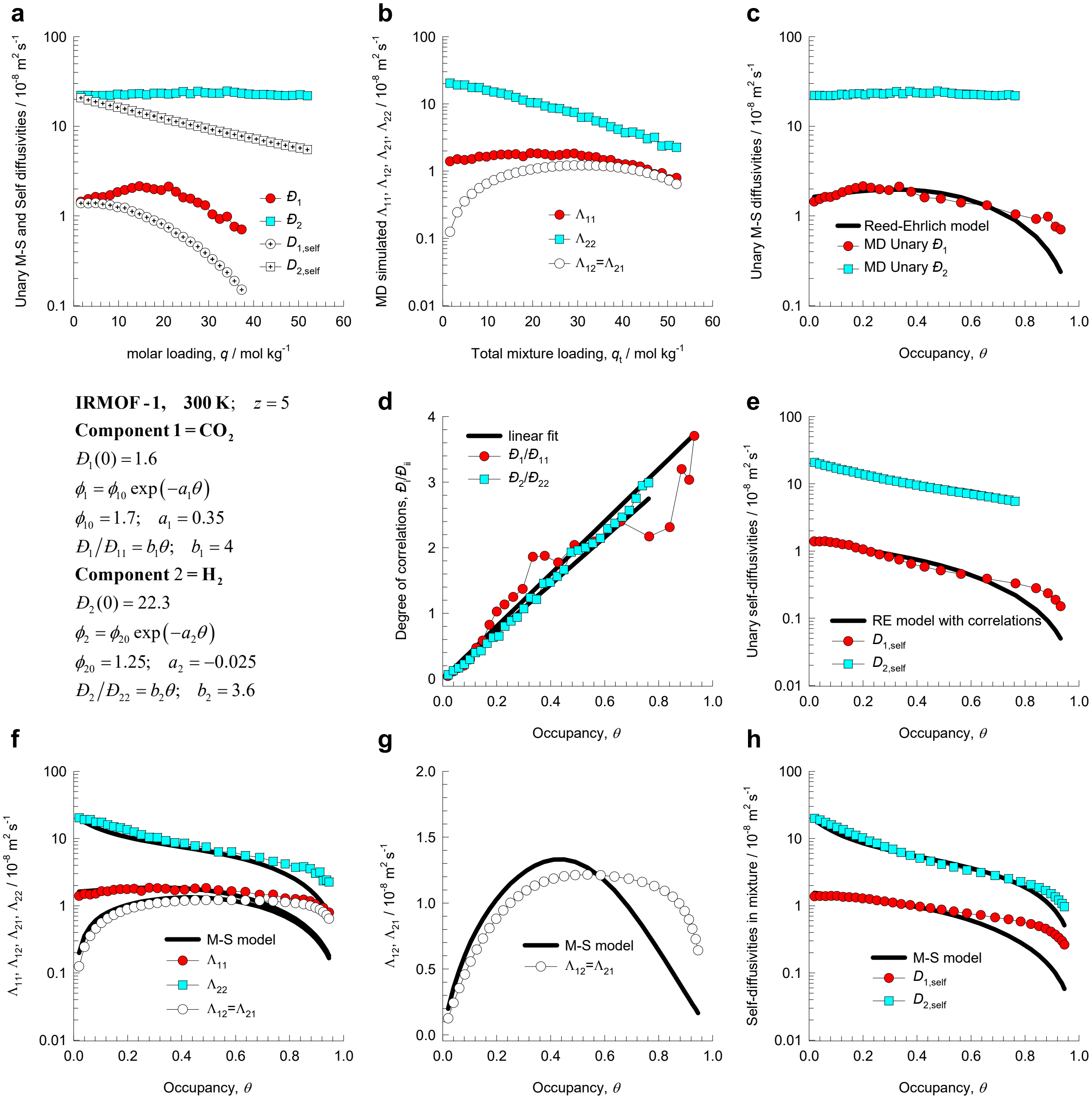

IRMOF-1, 300 K; $z = 5$

Component 1 = CO$_2$

$Đ_1(0) = 1.6$

$\phi_1 = \phi_{10}\exp(-a_1\theta)$

$\phi_{10} = 1.7; \quad a_1 = 0.35$

$Đ_1/Đ_{11} = b_1\theta; \quad b_1 = 4$

Component 2 = H$_2$

$Đ_2(0) = 22.3$

$\phi_2 = \phi_{20}\exp(-a_2\theta)$

$\phi_{20} = 1.25; \quad a_2 = -0.025$

$Đ_2/Đ_{22} = b_2\theta; \quad b_2 = 3.6$

Figure S91. (a-h) MD simulated values of $\Lambda_{11}, \Lambda_{12}, \Lambda_{21}, \Lambda_{22}$ for equimolar (q_1=q_2) binary CO$_2$(1)/H$_2$(2) mixtures in IRMOF-1 at 300 K, compared with the estimations (continuous solid lines) using the Maxwell-Stefan model, based on fitted data of unary diffusivities, $Đ_1, Đ_2$, and unary degrees of correlations, $Đ_1/Đ_{11}, Đ_2/Đ_{22}$.

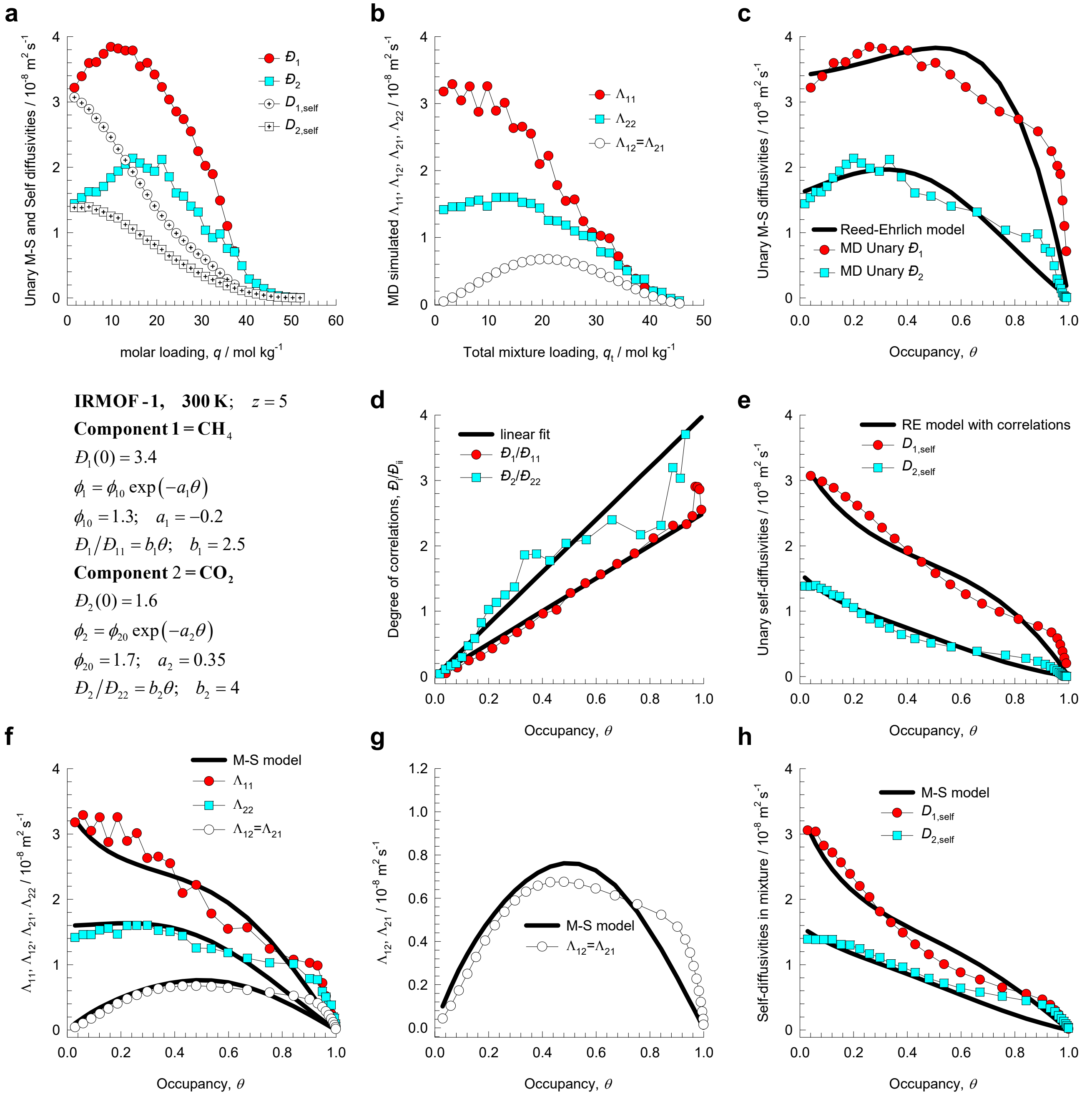

IRMOF-1, 300 K; $z = 5$

Component 1 = CH$_4$

$Đ_1(0) = 3.4$

$\phi_1 = \phi_{10}\exp(-a_1\theta)$

$\phi_{10} = 1.3; \quad a_1 = -0.2$

$Đ_1/Đ_{11} = b_1\theta; \quad b_1 = 2.5$

Component 2 = CO$_2$

$Đ_2(0) = 1.6$

$\phi_2 = \phi_{20}\exp(-a_2\theta)$

$\phi_{20} = 1.7; \quad a_2 = 0.35$

$Đ_2/Đ_{22} = b_2\theta; \quad b_2 = 4$

Figure S92. (a-h) MD simulated values of $\Lambda_{11}, \Lambda_{12}, \Lambda_{21}, \Lambda_{22}$ for equimolar (q_1=q_2) binary CH$_4$(1)/CO$_2$(2) mixtures in IRMOF-1 at 300 K, compared with the estimations (continuous solid lines) using the Maxwell-Stefan model, based on fitted data of unary diffusivities, $Đ_1, Đ_2$, and unary degrees of correlations, $Đ_1/Đ_{11}, Đ_2/Đ_{22}$.

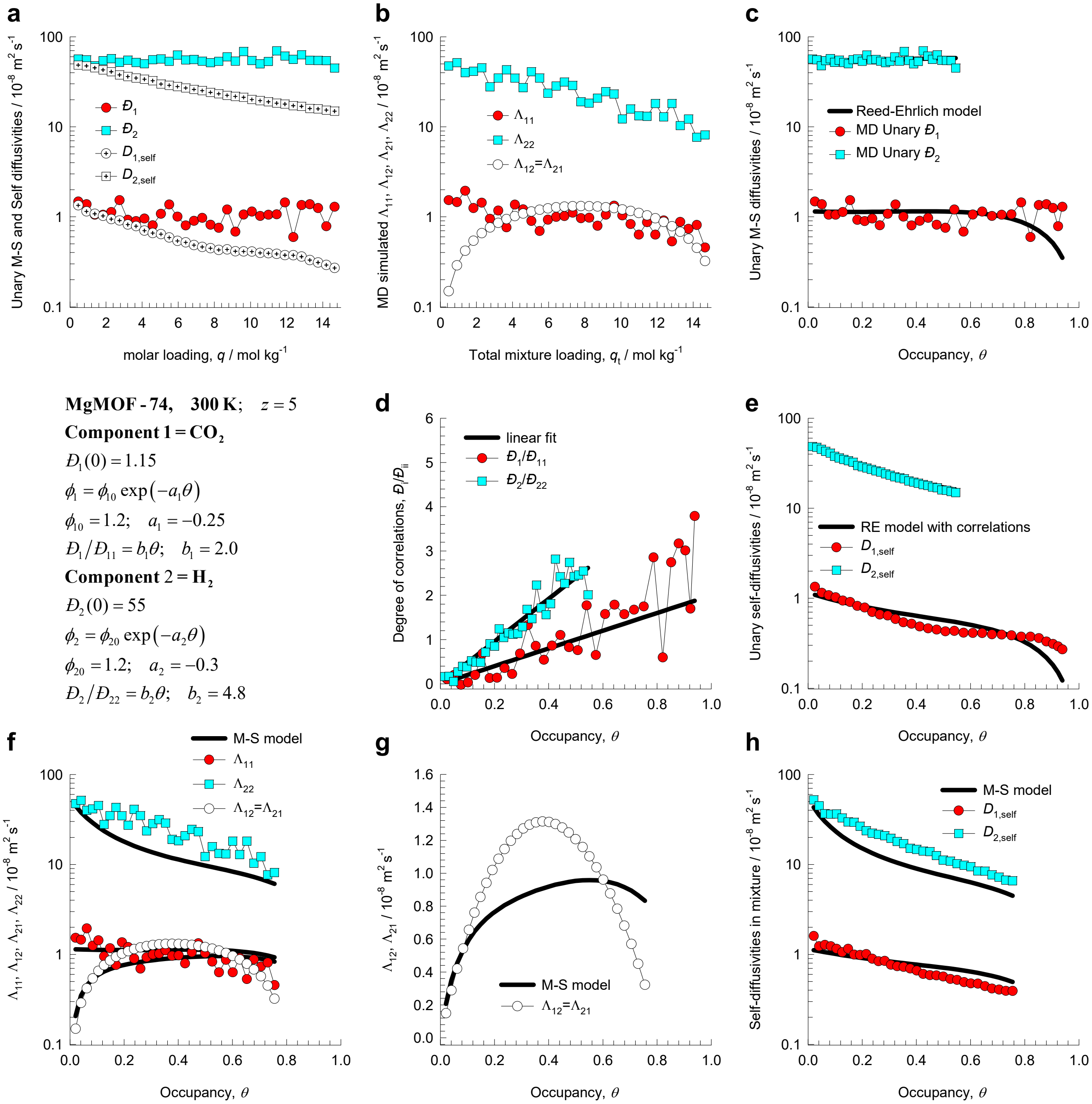

Figure S93. (a-h) MD simulated values of $\Lambda_{11},\Lambda_{12},\Lambda_{21},\Lambda_{22}$ for equimolar (q_1=q_2) binary CO$_2$(1)/H$_2$(2) mixtures in MgMOF-74 at 300 K, compared with the estimations (continuous solid lines) using the Maxwell-Stefan model, based on fitted data of unary diffusivities, $Đ_1, Đ_2$, and unary degrees of correlations, $Đ_1/Đ_{11}, Đ_2/Đ_{22}$.

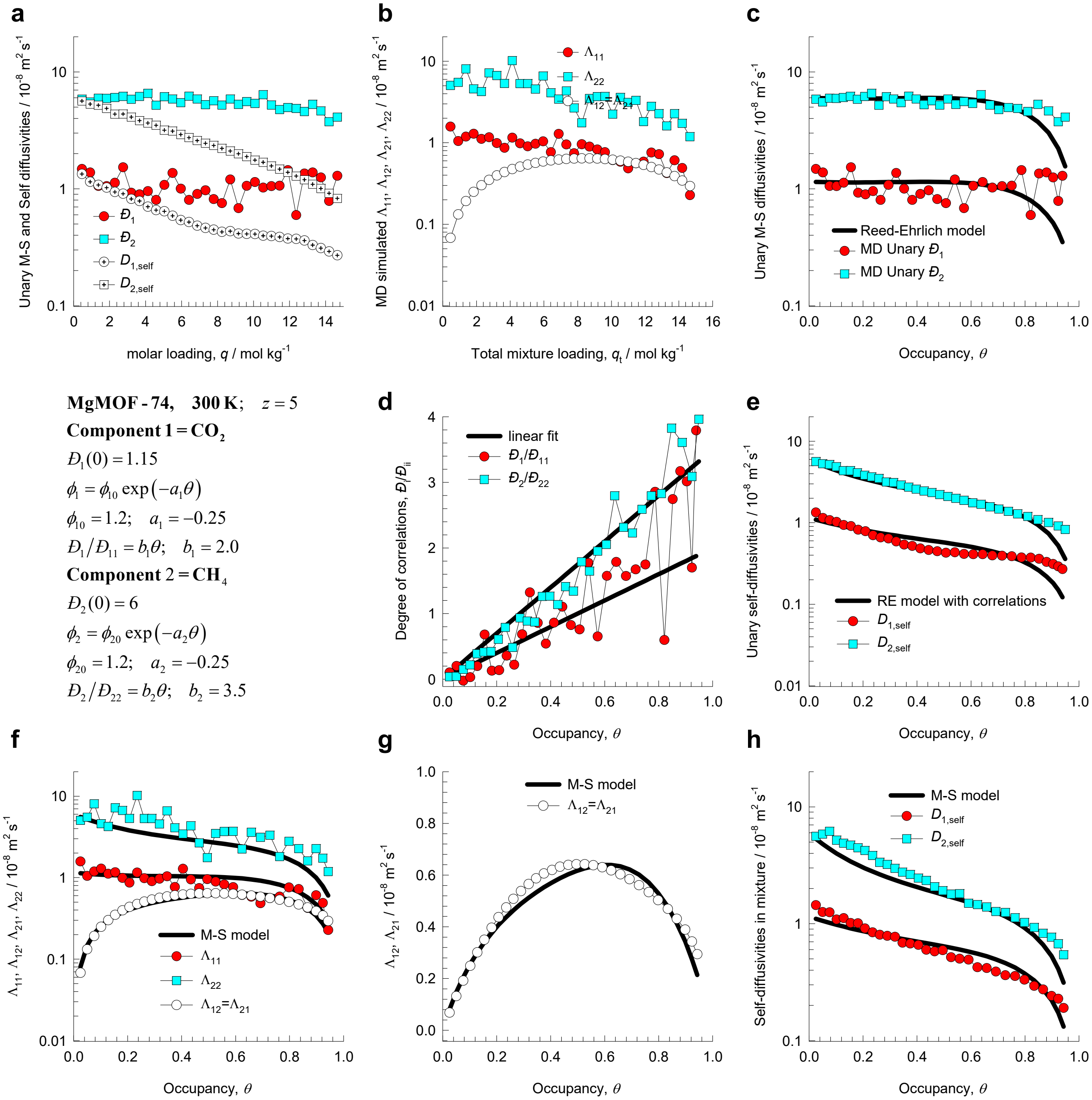

MgMOF-74, 300 K; $z=5$

Component 1 = CO$_2$

$Đ_1(0)=1.15$

$\phi_1=\phi_{10}\exp(-a_1\theta)$

$\phi_{10}=1.2;\quad a_1=-0.25$

$Đ_1/Đ_{11}=b_1\theta;\quad b_1=2.0$

Component 2 = CH$_4$

$Đ_2(0)=6$

$\phi_2=\phi_{20}\exp(-a_2\theta)$

$\phi_{20}=1.2;\quad a_2=-0.25$

$Đ_2/Đ_{22}=b_2\theta;\quad b_2=3.5$

Figure S94. (a-h) MD simulated values of $\Lambda_{11},\Lambda_{12},\Lambda_{21},\Lambda_{22}$ for equimolar ($q_1=q_2$) binary CO_2(1)/CH_4(2) mixtures in MgMOF-74 at 300 K, compared with the estimations (continuous solid lines) using the Maxwell-Stefan model, based on fitted data of unary diffusivities, $Đ_1,Đ_2$, and unary degrees of correlations, $Đ_1/Đ_{11},Đ_2/Đ_{22}$.

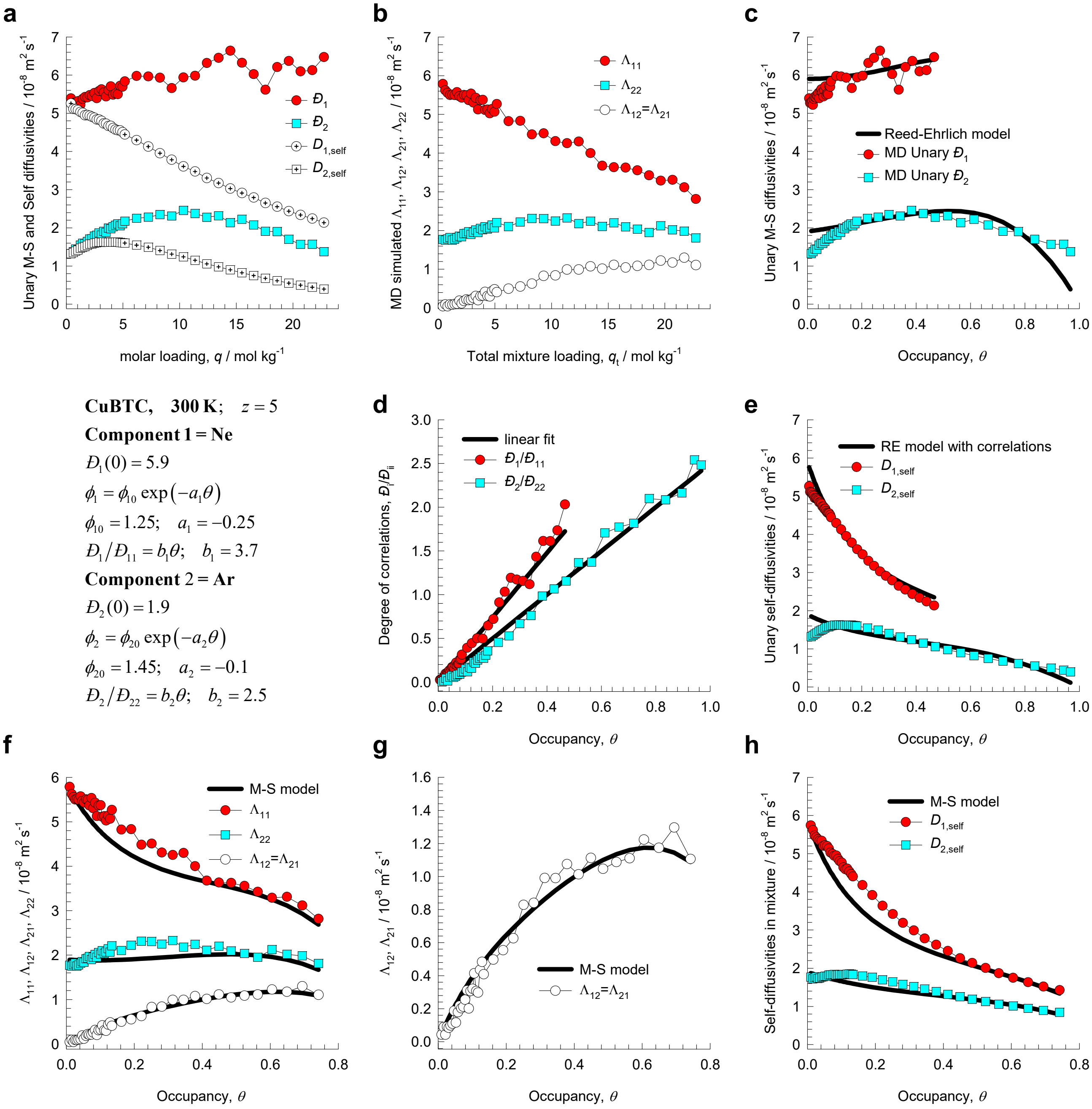

CuBTC, 300 K; $z = 5$

Component 1 = Ne

$Đ_1(0) = 5.9$

$\phi_1 = \phi_{10} \exp(-a_1\theta)$

$\phi_{10} = 1.25; \quad a_1 = -0.25$

$Đ_1/Đ_{11} = b_1\theta; \quad b_1 = 3.7$

Component 2 = Ar

$Đ_2(0) = 1.9$

$\phi_2 = \phi_{20} \exp(-a_2\theta)$

$\phi_{20} = 1.45; \quad a_2 = -0.1$

$Đ_2/Đ_{22} = b_2\theta; \quad b_2 = 2.5$

Figure S95. (a-h) MD simulated values of $\Lambda_{11}, \Lambda_{12}, \Lambda_{21}, \Lambda_{22}$ for equimolar (q_1=q_2) binary Ne(1)/Ar(2) mixtures in CuBTC at 300 K, compared with the estimations (continuous solid lines) using the Maxwell-Stefan model, based on fitted data of unary diffusivities, $Đ_1, Đ_2$, and unary degrees of correlations, $Đ_1/Đ_{11}, Đ_2/Đ_{22}$.

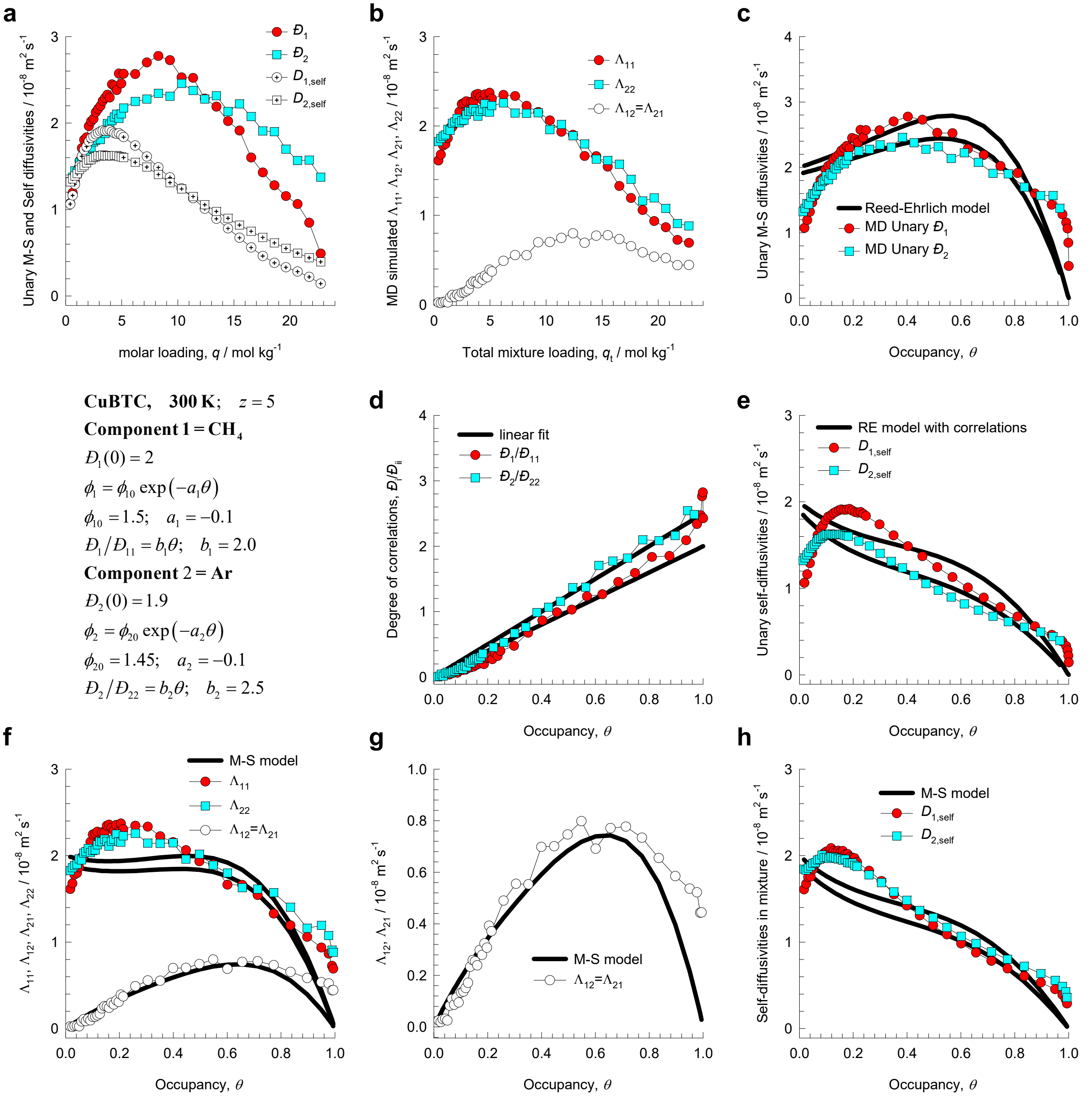

CuBTC, 300 K; $z = 5$

Component 1 = CH$_4$

$Đ_1(0) = 2$

$\phi_1 = \phi_{10} \exp(-a_1\theta)$

$\phi_{10} = 1.5; \quad a_1 = -0.1$

$Đ_1/Đ_{11} = b_1\theta; \quad b_1 = 2.0$

Component 2 = Ar

$Đ_2(0) = 1.9$

$\phi_2 = \phi_{20} \exp(-a_2\theta)$

$\phi_{20} = 1.45; \quad a_2 = -0.1$

$Đ_2/Đ_{22} = b_2\theta; \quad b_2 = 2.5$

Figure S96. (a-h) MD simulated values of $\Lambda_{11}, \Lambda_{12}, \Lambda_{21}, \Lambda_{22}$ for equimolar (q_1=q_2) binary CH$_4$(1)/Ar(2) mixtures in CuBTC at 300 K, compared with the estimations (continuous solid lines) using the Maxwell-Stefan model, based on fitted data of unary diffusivities, $Đ_1, Đ_2$, and unary degrees of correlations, $Đ_1/Đ_{11}, Đ_2/Đ_{22}$.

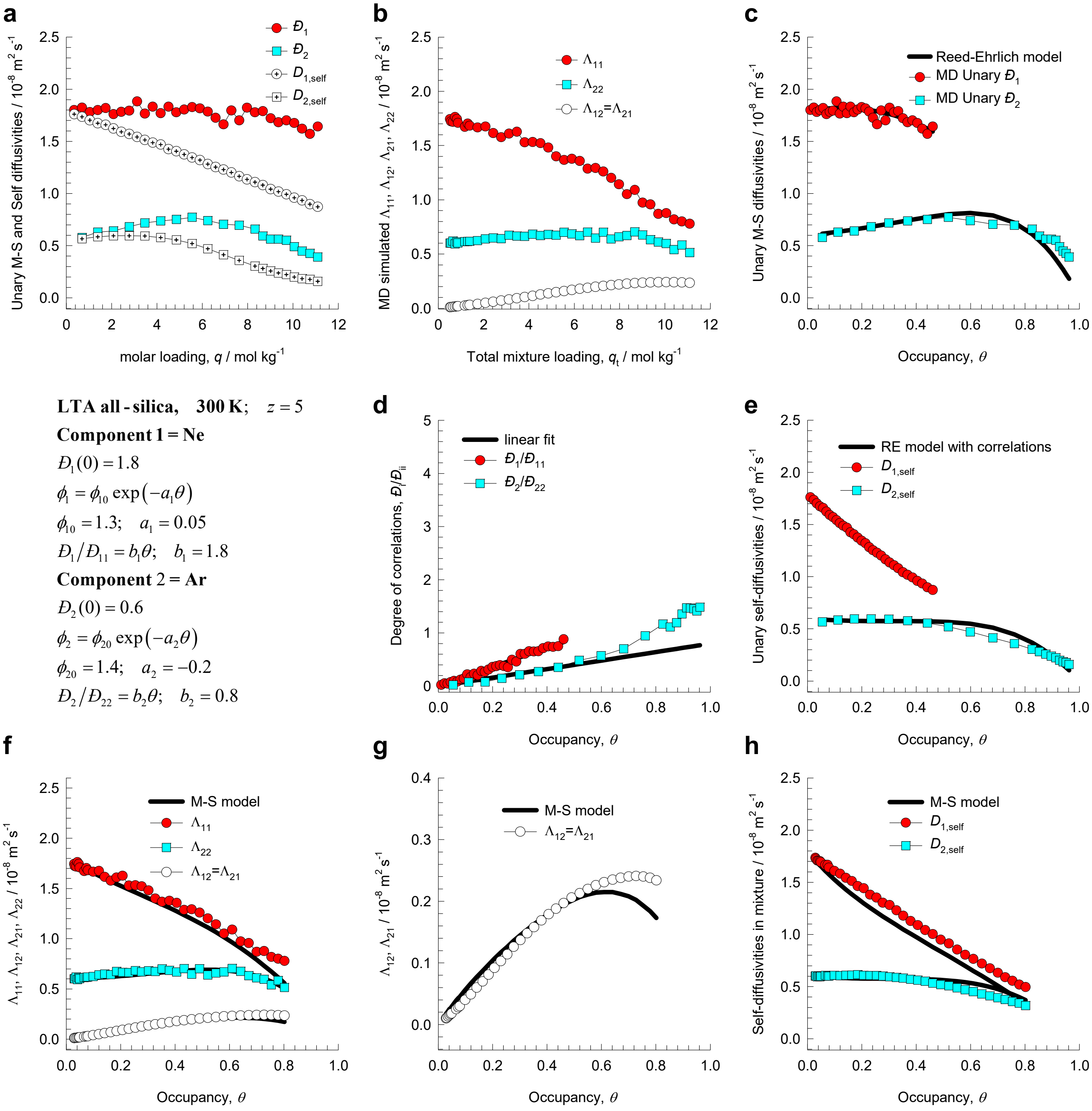

LTA all-silica, 300 K; $z = 5$

Component 1 = Ne

$Đ_1(0) = 1.8$

$\phi_1 = \phi_{10}\exp(-a_1\theta)$

$\phi_{10} = 1.3; \quad a_1 = 0.05$

$Đ_1/Đ_{11} = b_1\theta; \quad b_1 = 1.8$

Component 2 = Ar

$Đ_2(0) = 0.6$

$\phi_2 = \phi_{20}\exp(-a_2\theta)$

$\phi_{20} = 1.4; \quad a_2 = -0.2$

$Đ_2/Đ_{22} = b_2\theta; \quad b_2 = 0.8$

Figure S97. (a-h) MD simulated values of $\Lambda_{11},\Lambda_{12},\Lambda_{21},\Lambda_{22}$ for equimolar (q_1=q_2) binary Ne(1)/Ar(2) mixtures in LTA all-silica zeolite at 300 K, compared with the estimations (continuous solid lines) using the Maxwell-Stefan model, based on fitted data of unary diffusivities, $Đ_1, Đ_2$, and unary degrees of correlations, $Đ_1/Đ_{11}, Đ_2/Đ_{22}$.

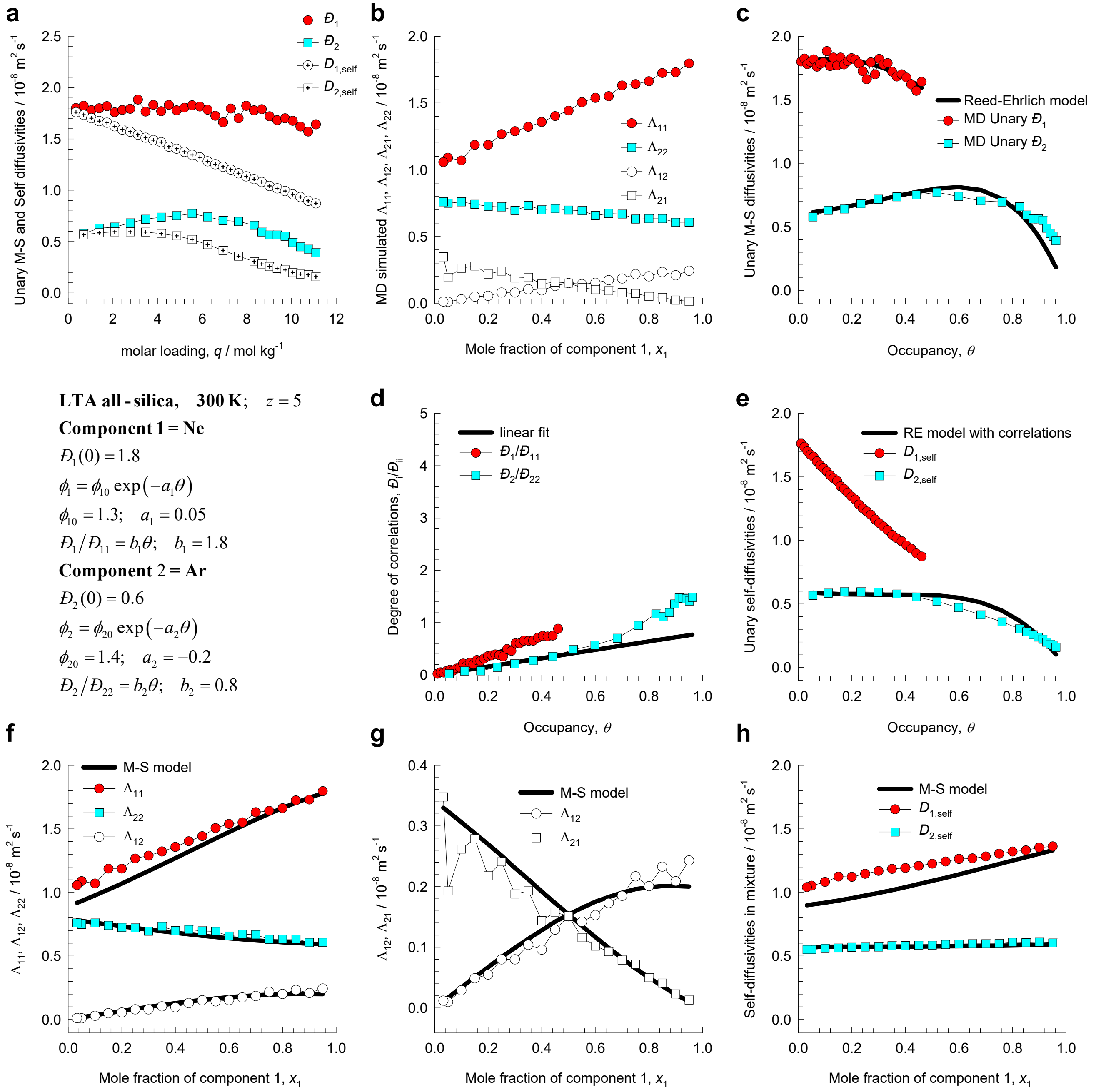

Figure S98. (a-h) MD simulated values of $\Lambda_{11},\Lambda_{12},\Lambda_{21},\Lambda_{22}$ for binary Ne(1)/Ar(2) mixtures of varying composition (total loading = 60 molecules uc^{-1}) in LTA all-silica zeolite at 300 K, compared with the estimations (continuous solid lines) using the Maxwell-Stefan model, based on fitted data of unary diffusivities, $Đ_1, Đ_2$, and unary degrees of correlations, $Đ_1/Đ_{11}, Đ_2/Đ_{22}$.

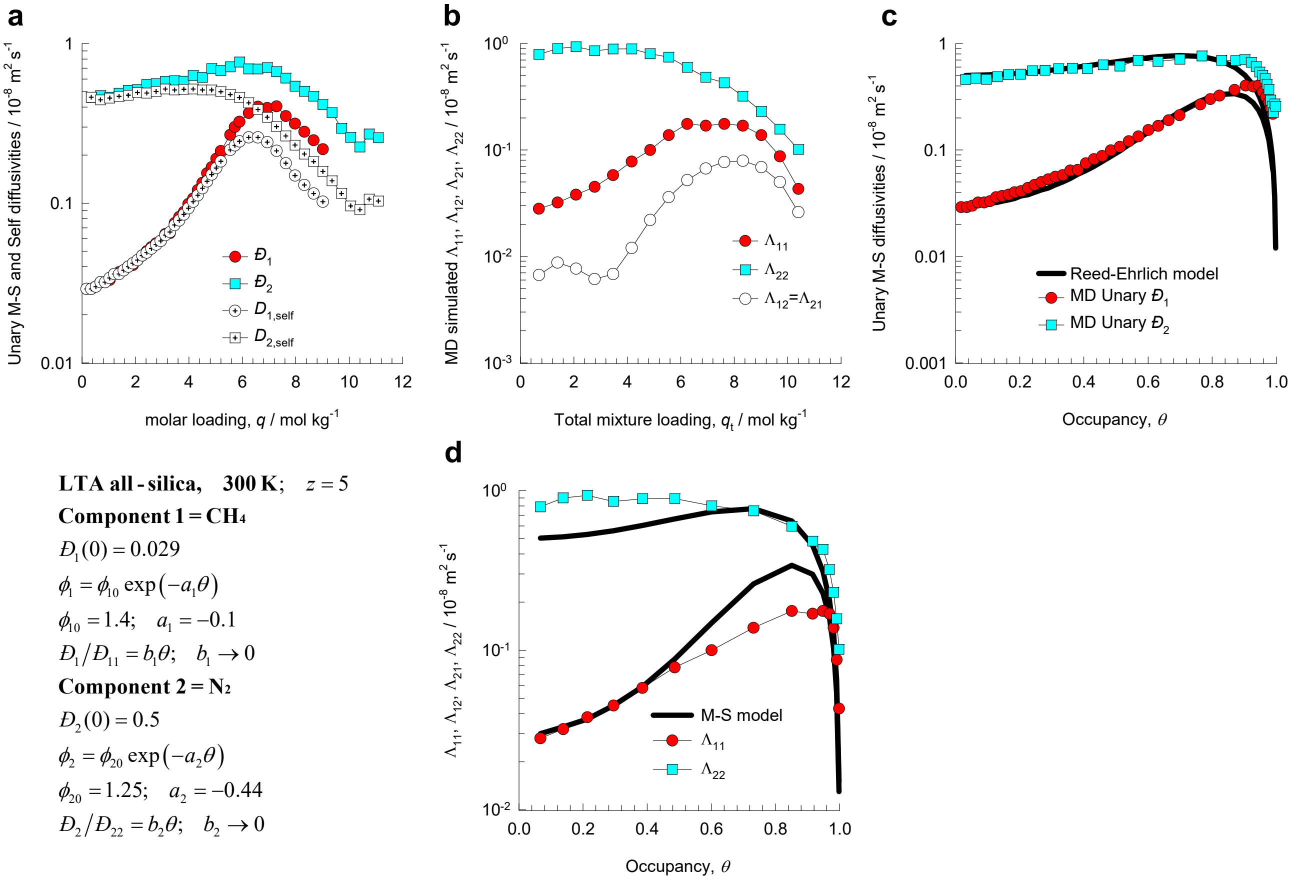

LTA all-silica, 300 K; $z = 5$

Component 1 = CH₄

$Đ_1(0) = 0.029$

$\phi_1 = \phi_{10} \exp(-a_1\theta)$

$\phi_{10} = 1.4; \quad a_1 = -0.1$

$Đ_1/Đ_{11} = b_1\theta; \quad b_1 \to 0$

Component 2 = N₂

$Đ_2(0) = 0.5$

$\phi_2 = \phi_{20} \exp(-a_2\theta)$

$\phi_{20} = 1.25; \quad a_2 = -0.44$

$Đ_2/Đ_{22} = b_2\theta; \quad b_2 \to 0$

Figure S99. (a-d) MD simulated values of $\Lambda_{11},\Lambda_{12},\Lambda_{21},\Lambda_{22}$ for equimolar (q_1=q_2) binary CH_4(1)/N_2(2) mixtures in LTA all-silica zeolite at 300 K, compared with the estimations (continuous solid lines) using the Maxwell-Stefan model, based on fitted data of unary diffusivities, $Đ_1,Đ_2$, and unary degrees of correlations, $Đ_1/Đ_{11}, Đ_2/Đ_{22}$.

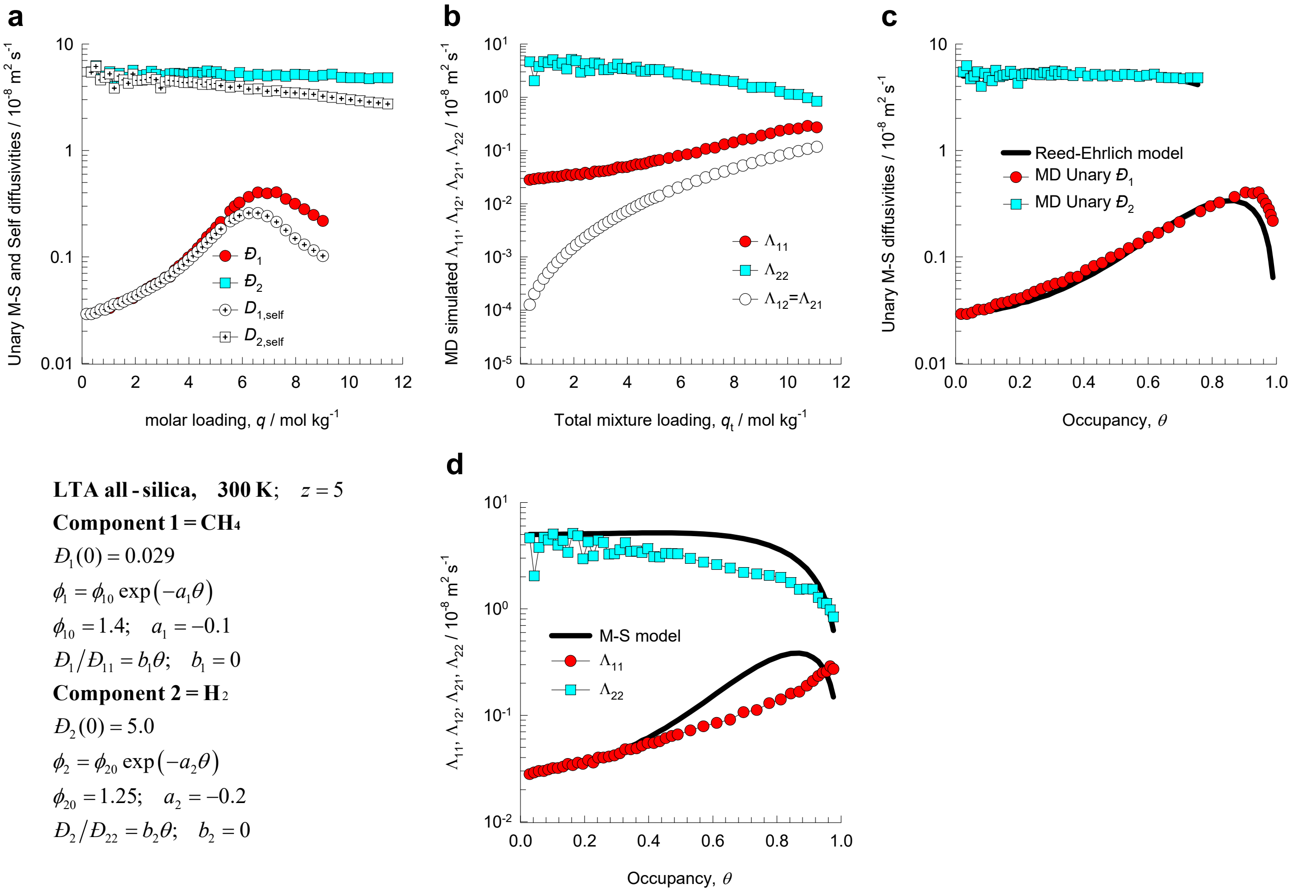

LTA all-silica, 300 K; $z = 5$

Component 1 = CH$_4$

$Đ_1(0) = 0.029$

$\phi_1 = \phi_{10}\exp(-a_1\theta)$

$\phi_{10} = 1.4; \quad a_1 = -0.1$

$Đ_1/Đ_{11} = b_1\theta; \quad b_1 = 0$

Component 2 = H$_2$

$Đ_2(0) = 5.0$

$\phi_2 = \phi_{20}\exp(-a_2\theta)$

$\phi_{20} = 1.25; \quad a_2 = -0.2$

$Đ_2/Đ_{22} = b_2\theta; \quad b_2 = 0$

Figure S100. (a-d) MD simulated values of $\Lambda_{11},\Lambda_{12},\Lambda_{21},\Lambda_{22}$ for equimolar (q_1=q_2) binary CH$_4$(1)/H$_2$(2) mixtures in LTA all-silica zeolite at 300 K, compared with the estimations (continuous solid lines) using the Maxwell-Stefan model, based on fitted data of unary diffusivities, $Đ_1, Đ_2$, and unary degrees of correlations, $Đ_1/Đ_{11}, Đ_2/Đ_{22}$.

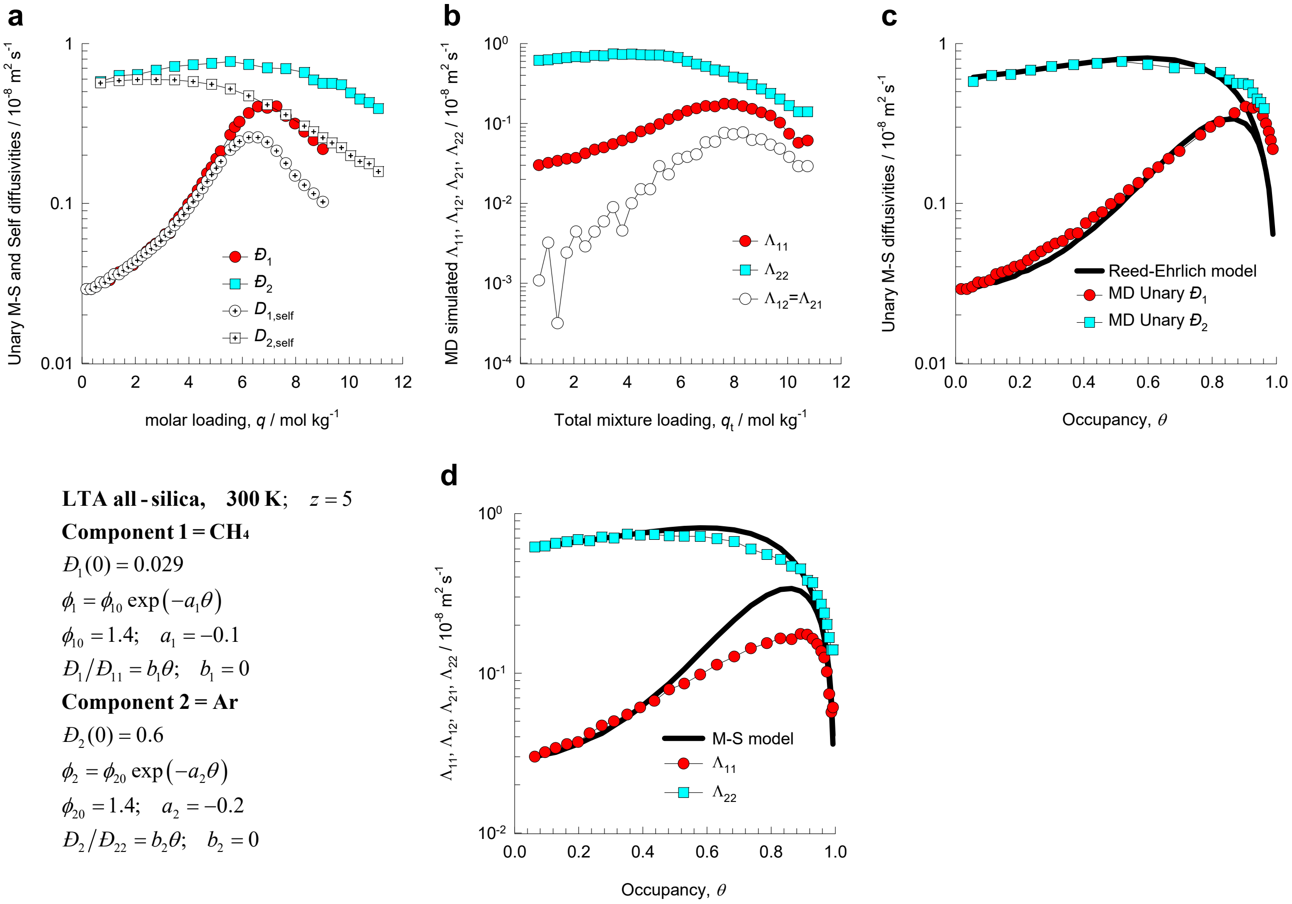

LTA all-silica, 300 K; $z = 5$

Component 1 = CH_4

$Đ_1(0) = 0.029$

$\phi_1 = \phi_{10}\exp(-a_1\theta)$

$\phi_{10} = 1.4; \quad a_1 = -0.1$

$Đ_1/Đ_{11} = b_1\theta; \quad b_1 = 0$

Component 2 = Ar

$Đ_2(0) = 0.6$

$\phi_2 = \phi_{20}\exp(-a_2\theta)$

$\phi_{20} = 1.4; \quad a_2 = -0.2$

$Đ_2/Đ_{22} = b_2\theta; \quad b_2 = 0$

Figure S101. (a-d) MD simulated values of $\Lambda_{11}, \Lambda_{12}, \Lambda_{21}, \Lambda_{22}$ for equimolar (q_1=q_2) binary CH_4(1)/Ar(2) mixtures in LTA all-silica zeolite at 300 K, compared with the estimations (continuous solid lines) using the Maxwell-Stefan model, based on fitted data of unary diffusivities, $Đ_1, Đ_2$, and unary degrees of correlations, $Đ_1/Đ_{11}, Đ_2/Đ_{22}$.

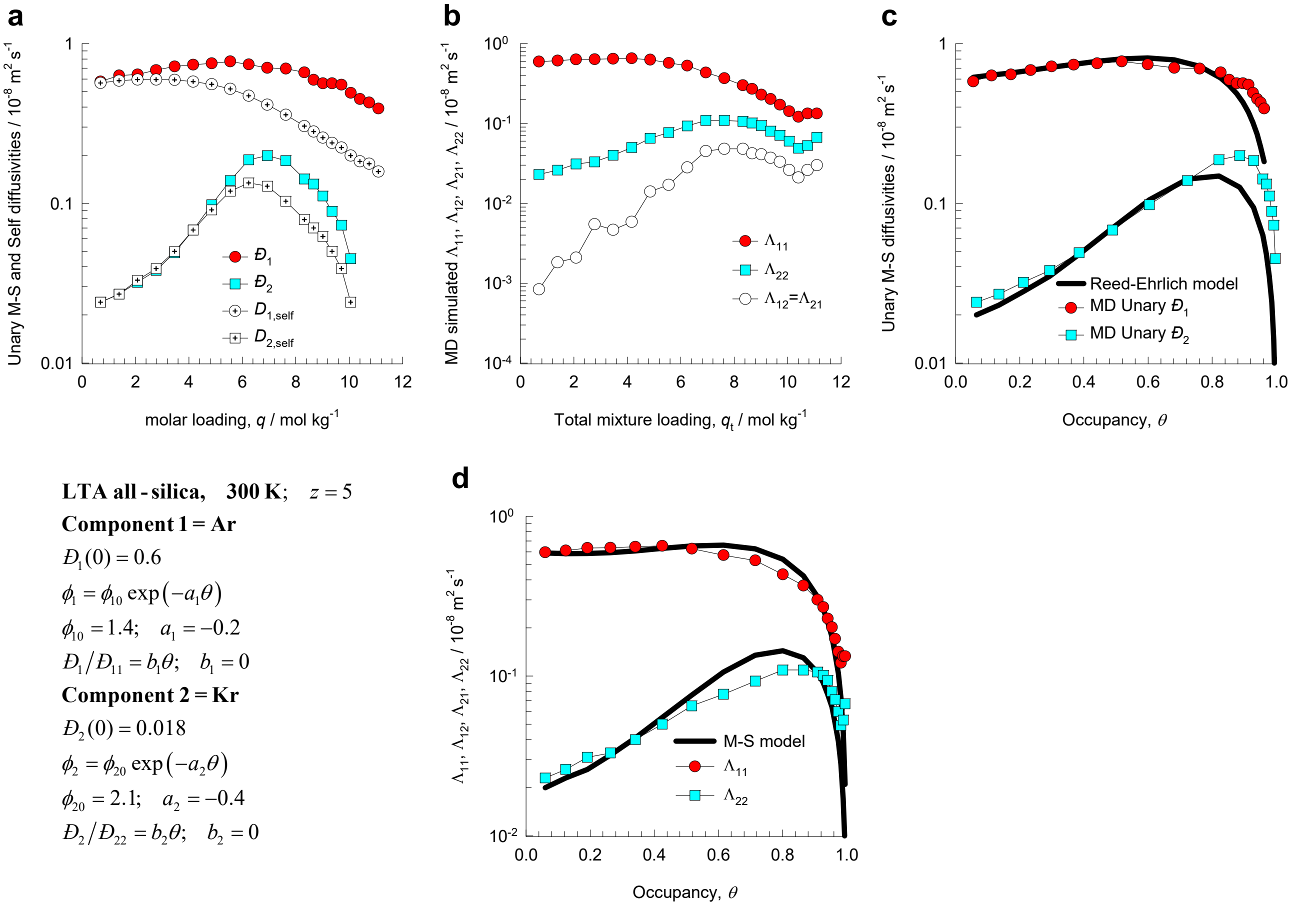

LTA all-silica, 300 K; $z = 5$

Component 1 = Ar

$Đ_1(0) = 0.6$

$\phi_1 = \phi_{10} \exp(-a_1\theta)$

$\phi_{10} = 1.4; \quad a_1 = -0.2$

$Đ_1/Đ_{11} = b_1\theta; \quad b_1 = 0$

Component 2 = Kr

$Đ_2(0) = 0.018$

$\phi_2 = \phi_{20} \exp(-a_2\theta)$

$\phi_{20} = 2.1; \quad a_2 = -0.4$

$Đ_2/Đ_{22} = b_2\theta; \quad b_2 = 0$

Figure S102. (a-d) MD simulated values of $\Lambda_{11}, \Lambda_{12}, \Lambda_{21}, \Lambda_{22}$ for equimolar (q_1=q_2) binary Ar(1)/Kr(2) mixtures in LTA all-silica zeolite at 300 K, compared with the estimations (continuous solid lines) using the Maxwell-Stefan model, based on fitted data of unary diffusivities, $Đ_1, Đ_2$, and unary degrees of correlations, $Đ_1/Đ_{11}, Đ_2/Đ_{22}$.

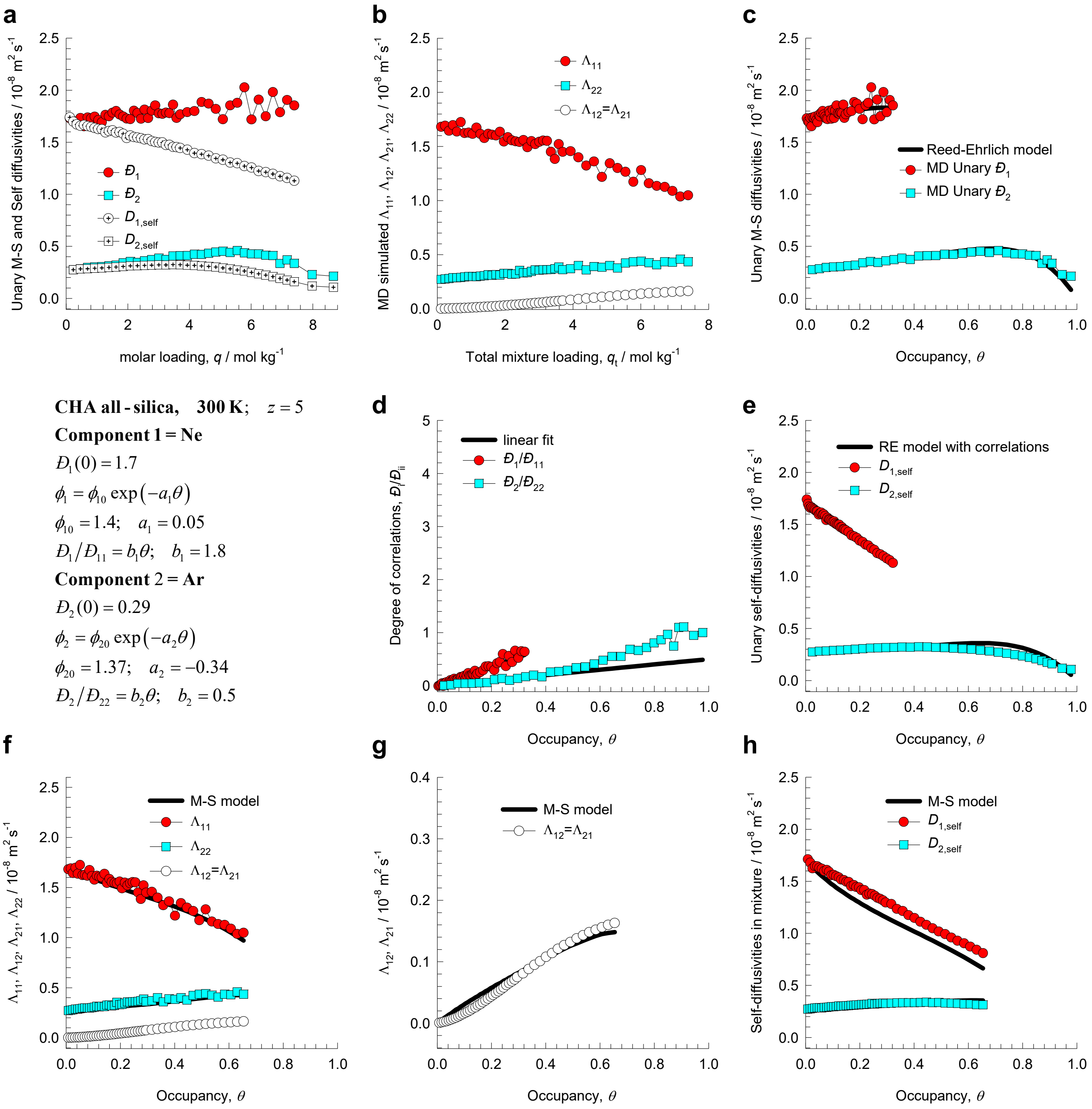

Figure S103. (a-h) MD simulated values of $\Lambda_{11},\Lambda_{12},\Lambda_{21},\Lambda_{22}$ for equimolar ($q_1=q_2$) binary Ne(1)/Ar(2) mixtures in CHA all-silica zeolite at 300 K, compared with the estimations (continuous solid lines) using the Maxwell-Stefan model, based on fitted data of unary diffusivities, $Đ_1, Đ_2$, and unary degrees of correlations, $Đ_1/Đ_{11}, Đ_2/Đ_{22}$.

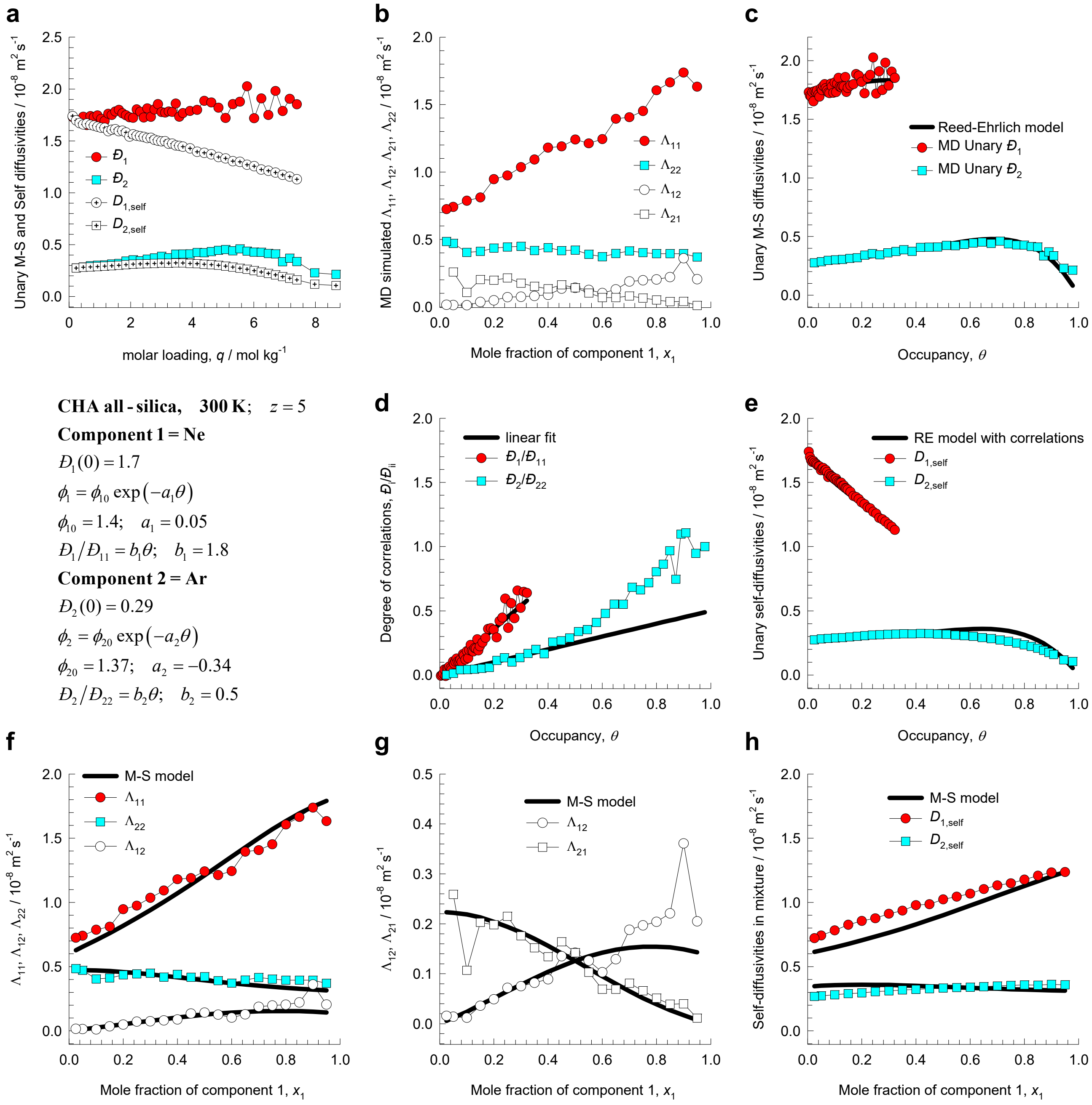

Figure S104. (a-h) MD simulated values of $\Lambda_{11}, \Lambda_{12}, \Lambda_{21}, \Lambda_{22}$ for binary Ne(1)/Ar(2) mixtures of varying composition (total loading = 25 molecules uc^{-1}) in CHA all-silica zeolite at 300 K, compared with the estimations (continuous solid lines) using the Maxwell-Stefan model, based on fitted data of unary diffusivities, $Đ_1, Đ_2$, and unary degrees of correlations, $Đ_1/Đ_{11}, Đ_2/Đ_{22}$.

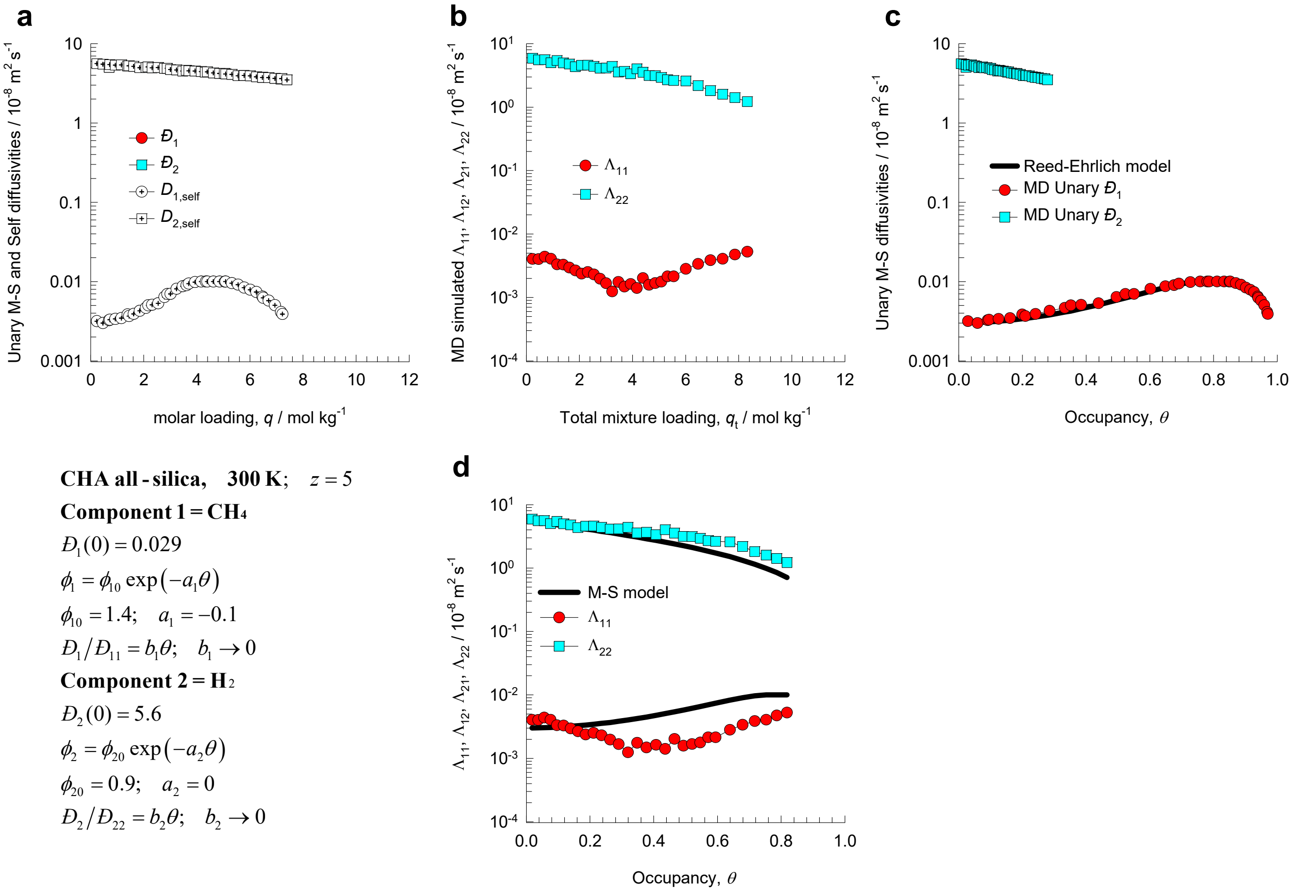

CHA all-silica, 300 K; $z = 5$

Component 1 = CH_4

$Đ_1(0) = 0.029$

$\phi_1 = \phi_{10} \exp(-a_1\theta)$

$\phi_{10} = 1.4; \quad a_1 = -0.1$

$Đ_1/Đ_{11} = b_1\theta; \quad b_1 \to 0$

Component 2 = H_2

$Đ_2(0) = 5.6$

$\phi_2 = \phi_{20} \exp(-a_2\theta)$

$\phi_{20} = 0.9; \quad a_2 = 0$

$Đ_2/Đ_{22} = b_2\theta; \quad b_2 \to 0$

Figure S105. (a-d) MD simulated values of $\Lambda_{11},\Lambda_{12},\Lambda_{21},\Lambda_{22}$ for equimolar (q_1=q_2) binary CH_4(1)/H_2(2) mixtures in CHA all-silica zeolite at 300 K, compared with the estimations (continuous solid lines) using the Maxwell-Stefan model, based on fitted data of unary diffusivities, $Đ_1,Đ_2$, and unary degrees of correlations, $Đ_1/Đ_{11}, Đ_2/Đ_{22}$.

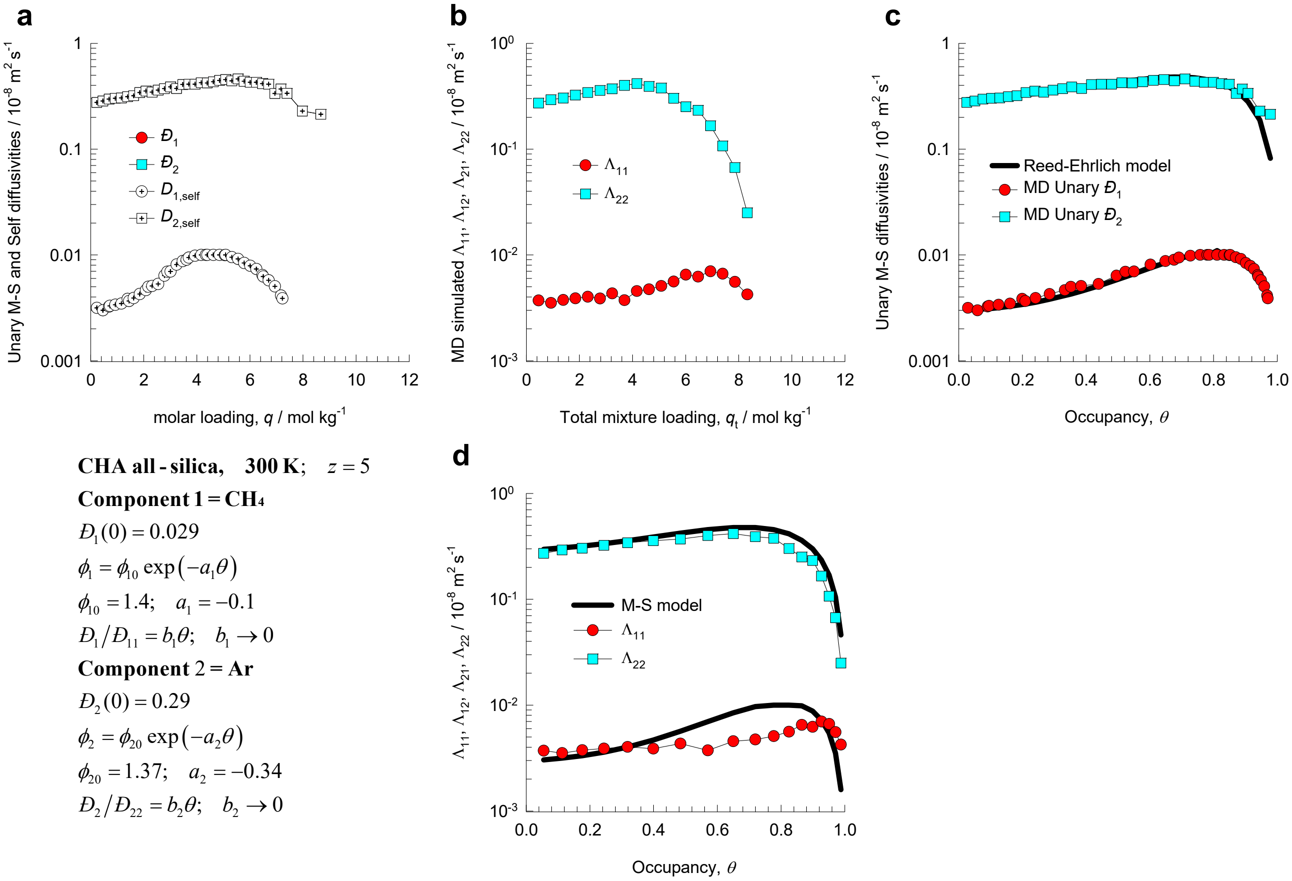

CHA all-silica, 300 K; $z = 5$

Component 1 = CH4

$Đ_1(0) = 0.029$

$\phi_1 = \phi_{10} \exp(-a_1\theta)$

$\phi_{10} = 1.4; \quad a_1 = -0.1$

$Đ_1/Đ_{11} = b_1\theta; \quad b_1 \to 0$

Component 2 = Ar

$Đ_2(0) = 0.29$

$\phi_2 = \phi_{20} \exp(-a_2\theta)$

$\phi_{20} = 1.37; \quad a_2 = -0.34$

$Đ_2/Đ_{22} = b_2\theta; \quad b_2 \to 0$

Figure S106. (a-d) MD simulated values of $\Lambda_{11},\Lambda_{12},\Lambda_{21},\Lambda_{22}$ for equimolar (q_1=q_2) binary CH_4(1)/Ar(2) mixtures in CHA all-silica zeolite at 300 K, compared with the estimations (continuous solid lines) using the Maxwell-Stefan model, based on fitted data of unary diffusivities, $Đ_1$,$Đ_2$, and unary degrees of correlations, $Đ_1/Đ_{11}, Đ_2/Đ_{22}$.

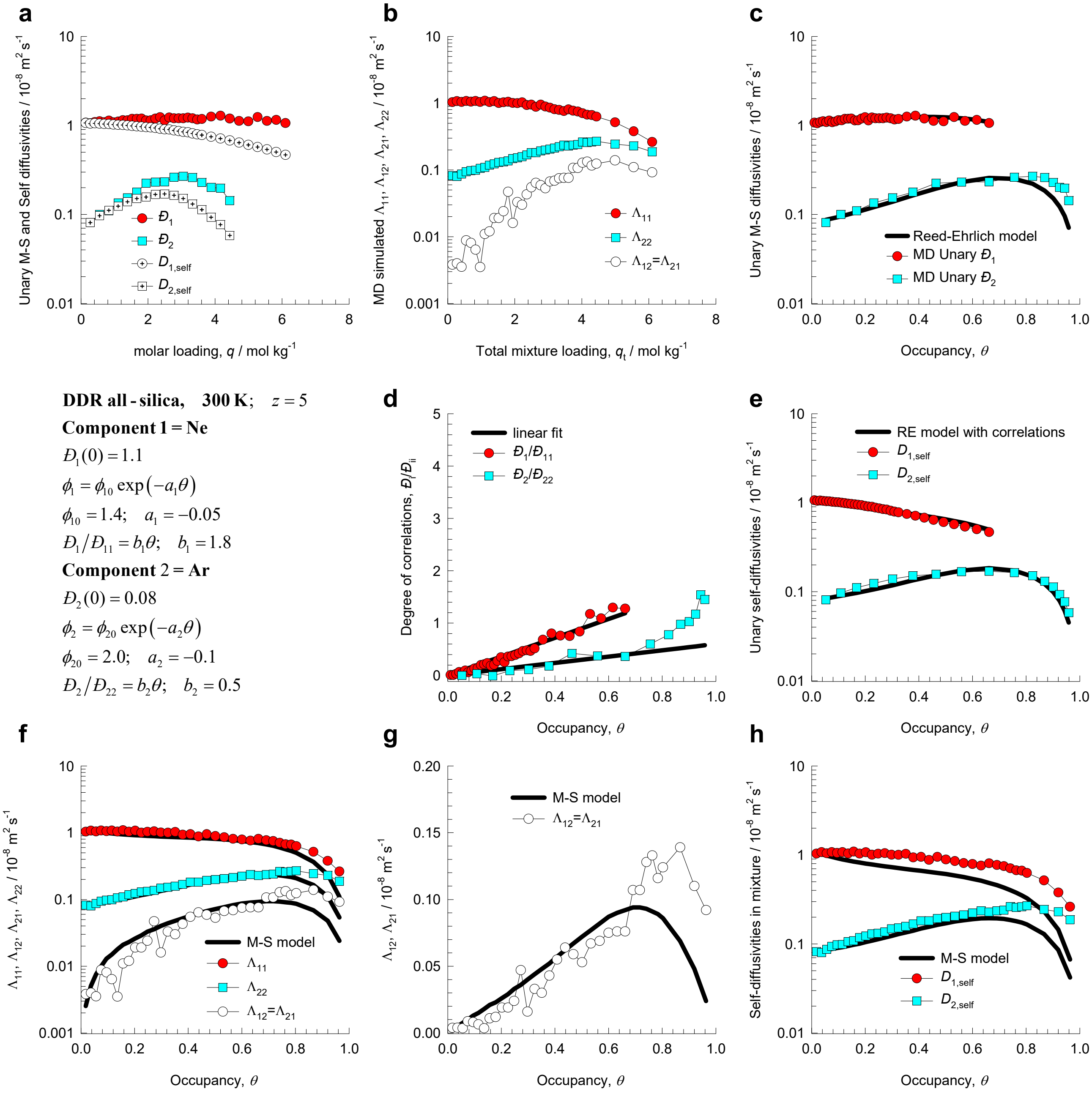

DDR all-silica, 300 K; $z = 5$

Component 1 = Ne

$Đ_1(0) = 1.1$

$\phi_1 = \phi_{10} \exp(-a_1\theta)$

$\phi_{10} = 1.4; \quad a_1 = -0.05$

$Đ_1/Đ_{11} = b_1\theta; \quad b_1 = 1.8$

Component 2 = Ar

$Đ_2(0) = 0.08$

$\phi_2 = \phi_{20} \exp(-a_2\theta)$

$\phi_{20} = 2.0; \quad a_2 = -0.1$

$Đ_2/Đ_{22} = b_2\theta; \quad b_2 = 0.5$

Figure S107. (a-h) MD simulated values of $\Lambda_{11},\Lambda_{12},\Lambda_{21},\Lambda_{22}$ for equimolar (q_1=q_2) binary Ne(1)/Ar(2) mixtures in DDR all-silica zeolite at 300 K, compared with the estimations (continuous solid lines) using the Maxwell-Stefan model, based on fitted data of unary diffusivities, $Đ_1,Đ_2$, and unary degrees of correlations, $Đ_1/Đ_{11}, Đ_2/Đ_{22}$.

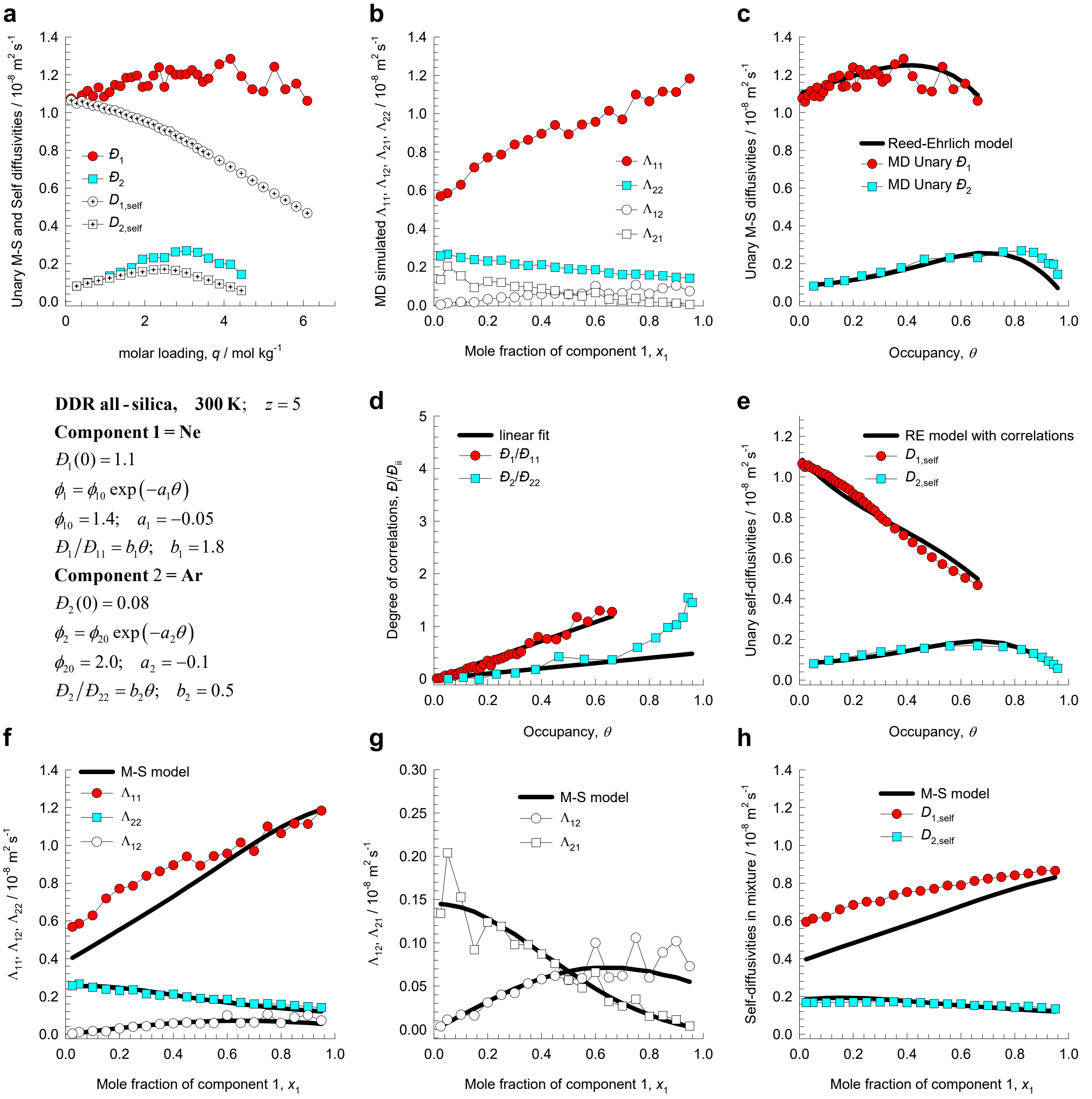

Figure S108. (a-h) MD simulated values of $\Lambda_{11},\Lambda_{12},\Lambda_{21},\Lambda_{22}$ for binary Ne(1)/Ar(2) mixtures of varying compositions (total loading = 40 molecules uc^{-1}) in DDR all-silica zeolite at 300 K, compared with the estimations (continuous solid lines) using the Maxwell-Stefan model, based on fitted data of unary diffusivities, $Đ_1, Đ_2$, and unary degrees of correlations, $Đ_1/Đ_{11}, Đ_2/Đ_{22}$.

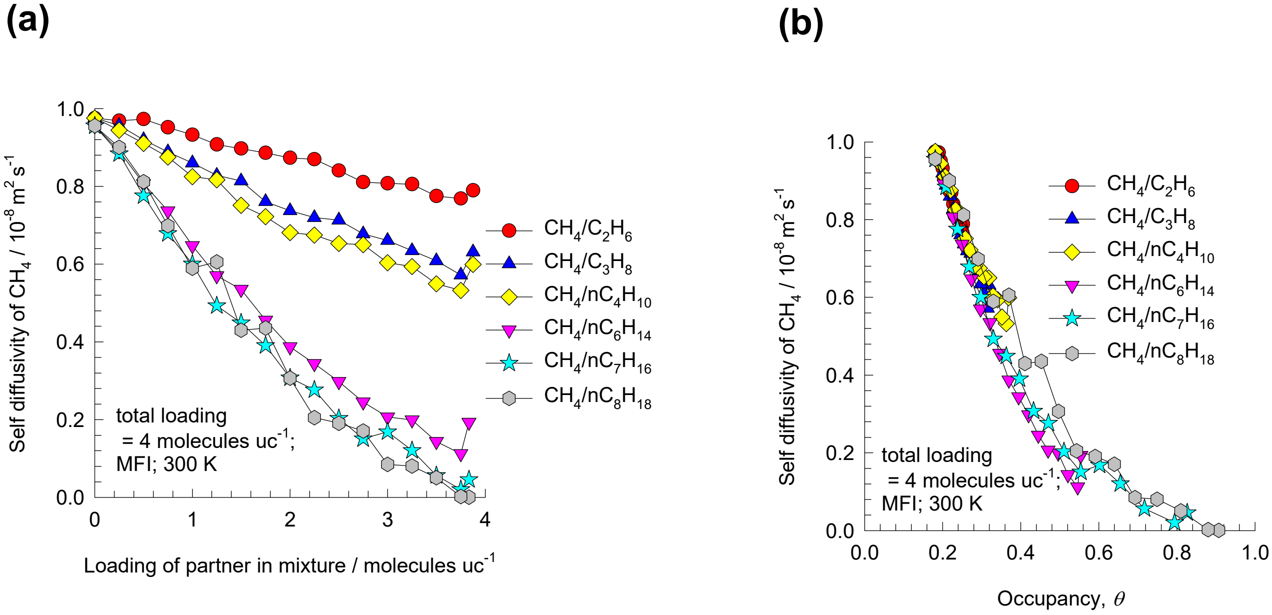

Figure S109. Self-diffusivities of CH_4 in binary mixtures with C_2H_6, C_3H_8, nC_4H_{10}, nC_6H_{14}, nC_7H_{16}, and nC_8H_{18} in MFI zeolite at 300 K at a total loading of 4 molecules per unit cell.The *x*-axes represent the (a) loading of the partner molecules in the mixture, and (b) total mixture occupancy, θ, that are determined using equations (S11), (S12), and (S13). The MD simulations are culled from our previous publications.[46, 47]

10 Preferential Perching of CO_2 at window regions

For diffusion of CO_2-bearing mixtures in cage-type zeolites such as LTA, DDR, and ERI, CO_2 gets preferentially, and strongly, adsorbed at the narrow windows of these zeolites, hindering the diffusion of partner molecules. As a consequence, the Maxwell-Stefan diffusivity of the partner molecule falls significantly below the corresponding value of the unary M-S diffusivity. Evidence of such hindering influences are evident in the following set of nine Figures:

Figure S110: $CO_2(1)/H_2(2)$ mixtures in LTA all-silica zeolite

Figure S111: $CO_2(1)/N_2(2)$ mixtures in LTA all-silica zeolite

Figure S112: $CH_4(1)/CO_2(2)$ mixtures in LTA all-silica zeolite

Figure S113: $CO_2(1)$/Ne(2) mixtures in LTA all-silica zeolite

Figure S114: $CO_2(1)$/Ar(2) mixtures in LTA all-silica zeolite

Figure S115: $CO_2(1)/CH_4(2)$ mixtures in CHA all-silica zeolite

Figure S116: $CO_2(1)$/Ne(2) mixtures in CHA all-silica zeolite

Figure S117: $CO_2(1)$/Ar(2) mixtures in CHA all-silica zeolite

Figure S118: $CO_2(1)$/Ne(2) mixtures in DDR all-silica zeolite

Detailed analysis and explanation of the hindering effects caused by segregated adsorption effects are provided in our earlier works.[22, 48, 49] Hindering effects are not catered for by the Maxwell-Stefan formulation.

10.1 List of Figures for Preferential Perching of CO2 at window regions

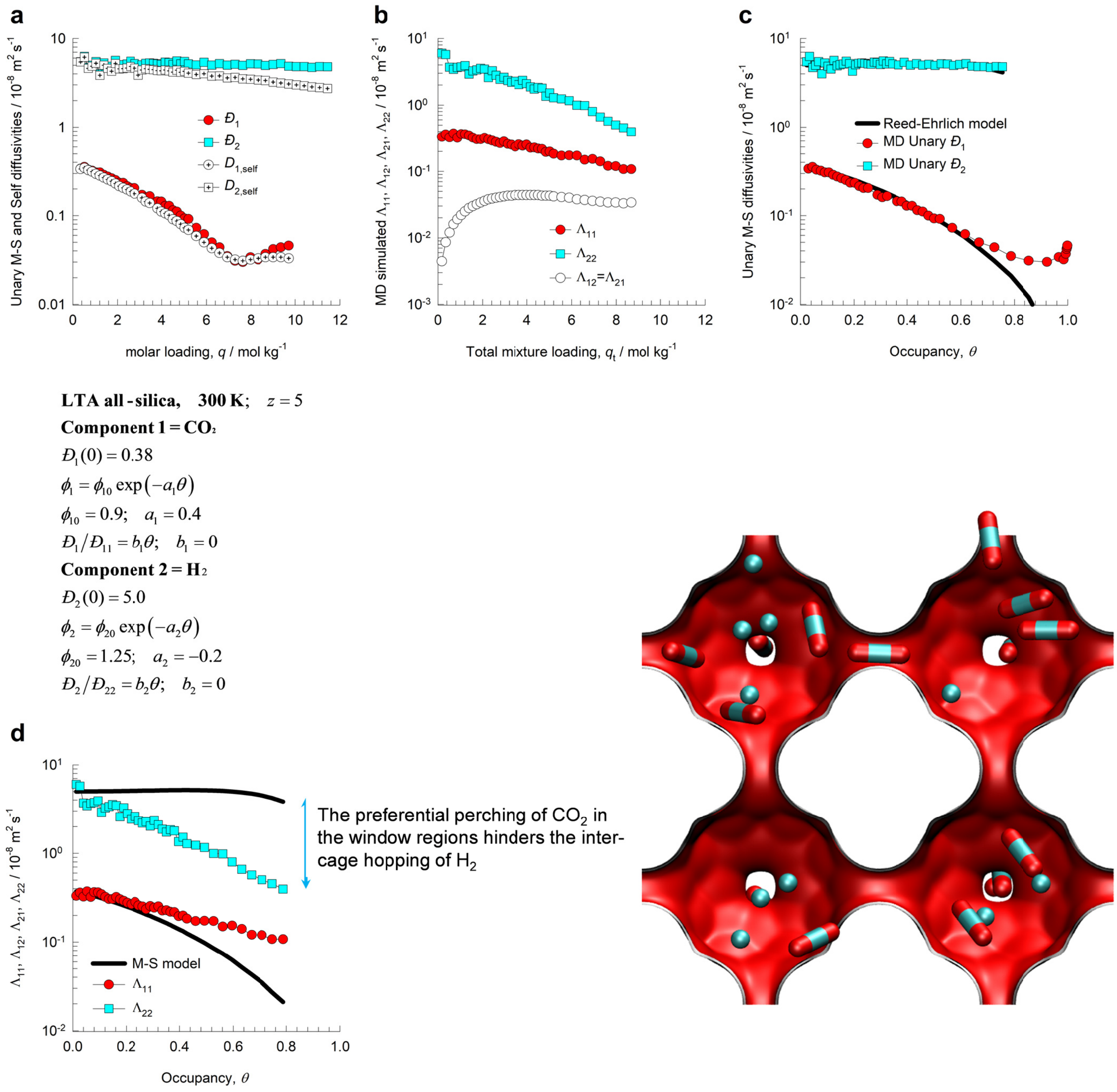

LTA all-silica, 300 K; $z = 5$

Component 1 = CO₂

$Đ_1(0) = 0.38$

$\phi_1 = \phi_{10} \exp(-a_1\theta)$

$\phi_{10} = 0.9; \quad a_1 = 0.4$

$Đ_1/Đ_{11} = b_1\theta; \quad b_1 = 0$

Component 2 = H₂

$Đ_2(0) = 5.0$

$\phi_2 = \phi_{20} \exp(-a_2\theta)$

$\phi_{20} = 1.25; \quad a_2 = -0.2$

$Đ_2/Đ_{22} = b_2\theta; \quad b_2 = 0$

The preferential perching of CO_2 in the window regions hinders the inter-cage hopping of H_2

Figure S110. (a-d) MD simulated values of $\Lambda_{11},\Lambda_{12},\Lambda_{21},\Lambda_{22}$ for equimolar (q_1=q_2) binary CO_2(1)/H_2(2) mixtures in LTA all-silica zeolite at 300 K, compared with the estimations (continuous solid lines) using the Maxwell-Stefan model, based on fitted data of unary diffusivities, $Đ_1$,$Đ_2$, and unary degrees of correlations, $Đ_1/Đ_{11}$, $Đ_2/Đ_{22}$.

Preferential Perching of CO2 at window regions

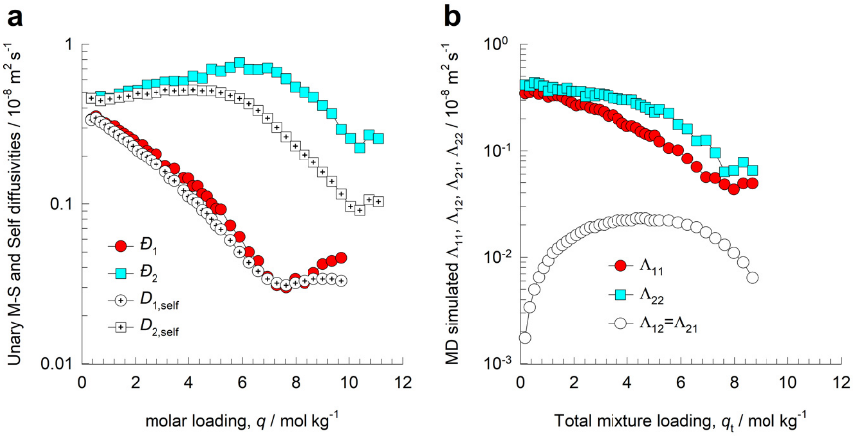

LTA all-silica, 300 K; $z = 5$

Component 1 = CO₂

$Đ_1(0) = 0.38$

$\phi_1 = \phi_{10} \exp(-a_1\theta)$

$\phi_{10} = 0.9; \quad a_1 = 0.4$

$Đ_1/Đ_{11} = b_1\theta; \quad b_1 = 0$

Component 2 = N₂

$Đ_2(0) = 0.5$

$\phi_2 = \phi_{20} \exp(-a_2\theta)$

$\phi_{20} = 1.25; \quad a_2 = -0.44$

$Đ_2/Đ_{22} = b_2\theta; \quad b_2 = 0$

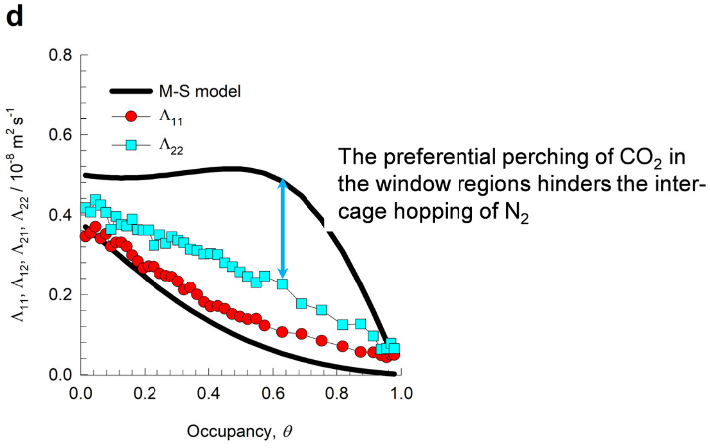

The preferential perching of CO_2 in the window regions hinders the inter-cage hopping of N_2

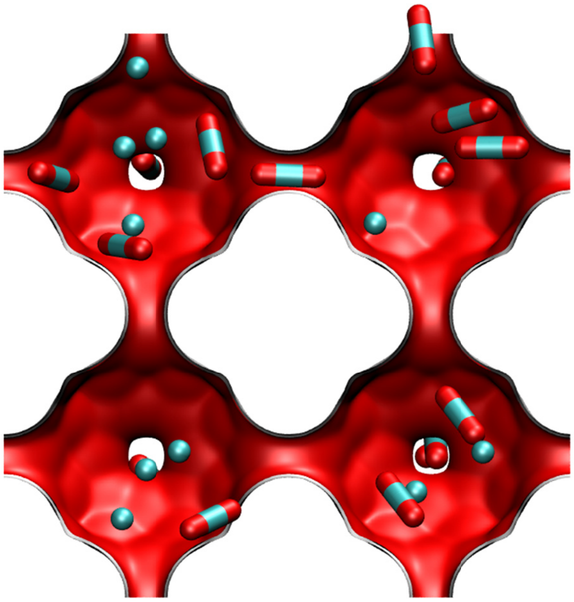

Figure S111. (a-d) MD simulated values of $\Lambda_{11},\Lambda_{12},\Lambda_{21},\Lambda_{22}$ for equimolar (q_1=q_2) binary CO_2(1)/N_2(2) mixtures in LTA all-silica zeolite at 300 K, compared with the estimations (continuous solid lines) using the Maxwell-Stefan model, based on fitted data of unary diffusivities, $Đ_1$,$Đ_2$, and unary degrees of correlations, $Đ_1/Đ_{11}$, $Đ_2/Đ_{22}$.

Preferential Perching of CO2 at window regions

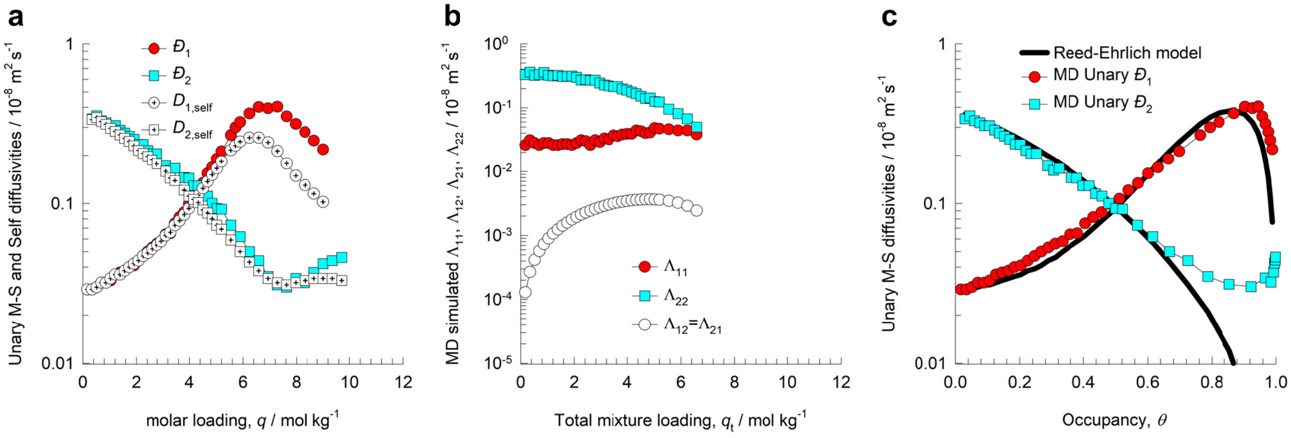

LTA all-silica, 300 K; $z = 5$

Component 1 = CH₄

$Đ_1(0) = 0.029$

$\phi_1 = \phi_{10}\exp(-a_1\theta)$

$\phi_{10} = 1.4; \quad a_1 = -0.1$

$Đ_1/Đ_{11} = b_1\theta; \quad b_1 = 0$

Component 2 = CO₂

$Đ_2(0) = 0.38$

$\phi_2 = \phi_{20}\exp(-a_2\theta)$

$\phi_{20} = 0.9; \quad a_2 = 0.4$

$Đ_2/Đ_{22} = b_2\theta; \quad b_2 = 0$

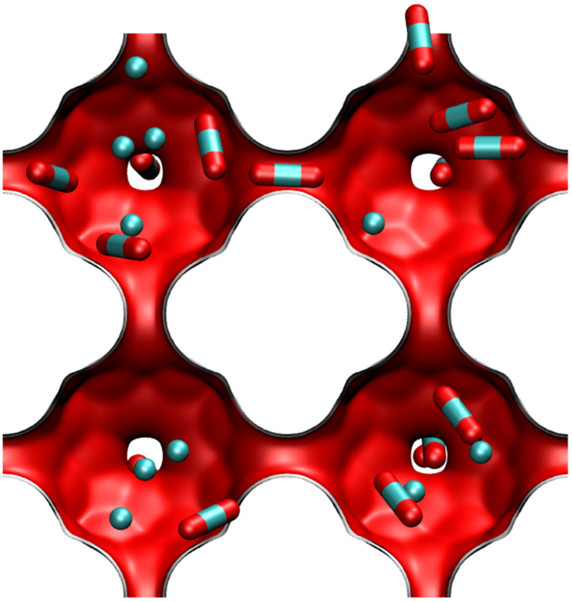

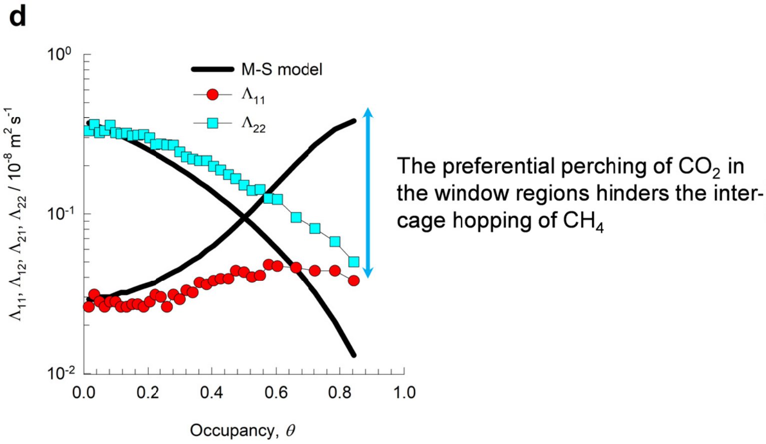

Figure S112. (a-d) MD simulated values of $\Lambda_{11},\Lambda_{12},\Lambda_{21},\Lambda_{22}$ for equimolar (q_1=q_2) binary CH$_4$(1)/CO$_2$(2) mixtures in LTA all-silica zeolite at 300 K, compared with the estimations (continuous solid lines) using the Maxwell-Stefan model, based on fitted data of unary diffusivities, $Đ_1, Đ_2$, and unary degrees of correlations, $Đ_1/Đ_{11}, Đ_2/Đ_{22}$.

Preferential Perching of CO2 at window regions

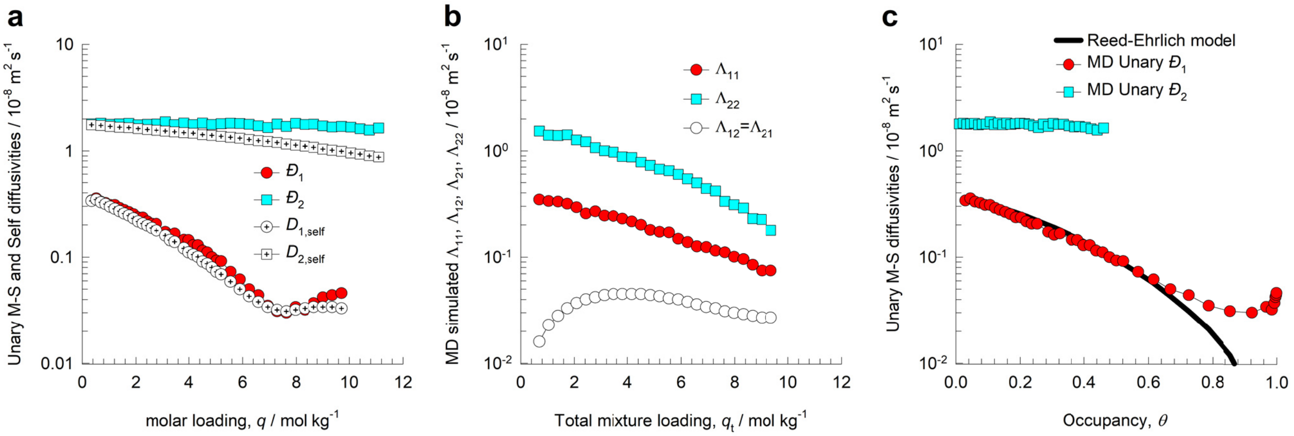

LTA all-silica, 300 K; $z = 5$

Component 1 = CO₂

$Đ_1(0) = 0.38$

$\phi_1 = \phi_{10} \exp(-a_1\theta)$

$\phi_{10} = 0.9; \quad a_1 = 0.4$

$Đ_1/Đ_{11} = b_1\theta; \quad b_1 = 0$

Component 2 = Ne

$Đ_2(0) = 1.8$

$\phi_2 = \phi_{20} \exp(-a_2\theta)$

$\phi_{20} = 1.3; \quad a_2 = 0.05$

$Đ_2/Đ_{22} = b_2\theta; \quad b_2 = 0$

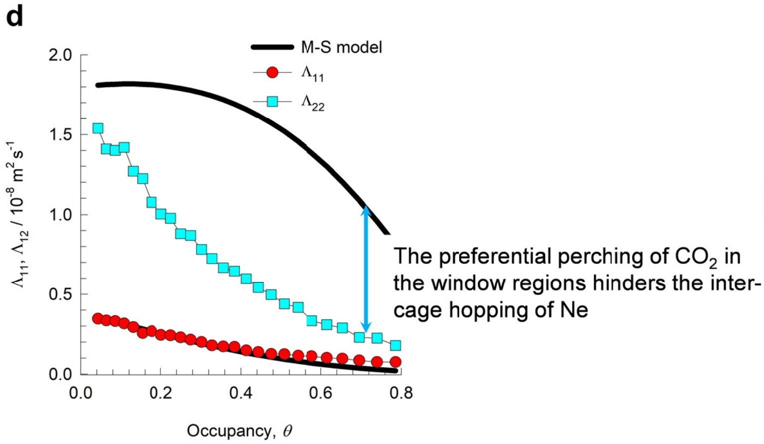

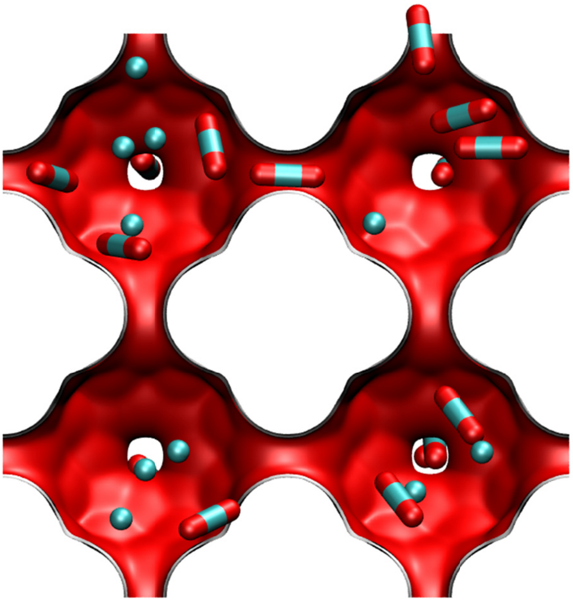

Figure S113. (a-d) MD simulated values of $\Lambda_{11},\Lambda_{12},\Lambda_{21},\Lambda_{22}$ for equimolar (q_1=q_2) binary CO$_2$(1)/Ne(2) mixtures in LTA all-silica zeolite at 300 K, compared with the estimations (continuous solid lines) using the Maxwell-Stefan model, based on fitted data of unary diffusivities, $Đ_1, Đ_2$, and unary degrees of correlations, $Đ_1/Đ_{11}, Đ_2/Đ_{22}$.

Preferential Perching of CO2 at window regions

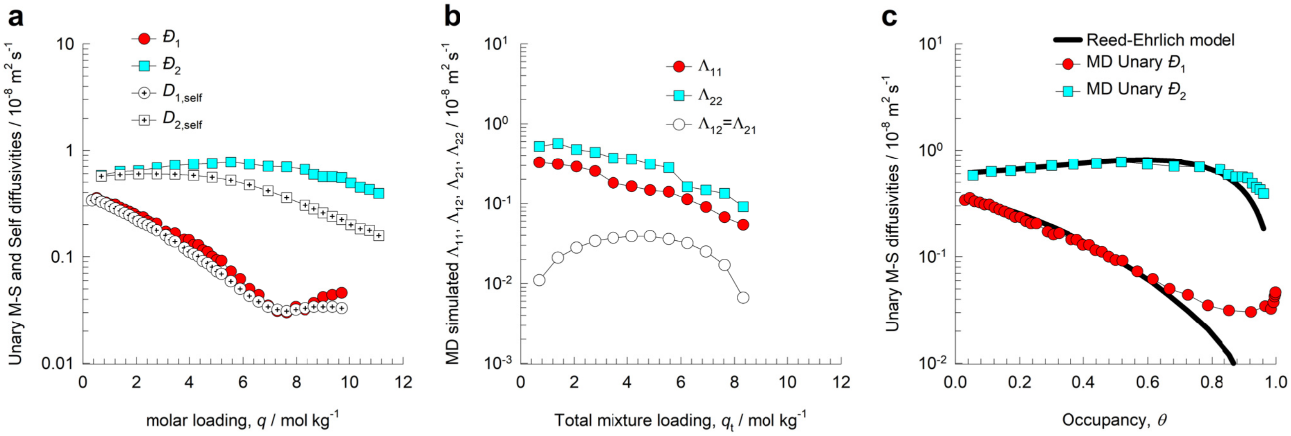

LTA all-silica, 300 K; $z = 5$

Component 1 = CO₂

$Đ_1(0) = 0.38$

$\phi_1 = \phi_{10} \exp(-a_1\theta)$

$\phi_{10} = 0.9$; $a_1 = 0.4$

$Đ_1/Đ_{11} = b_1\theta$; $b_1 = 0$

Component 2 = Ar

$Đ_2(0) = 0.6$

$\phi_2 = \phi_{20} \exp(-a_2\theta)$

$\phi_{20} = 1.4$; $a_2 = -0.2$

$Đ_2/Đ_{22} = b_2\theta$; $b_2 = 0$

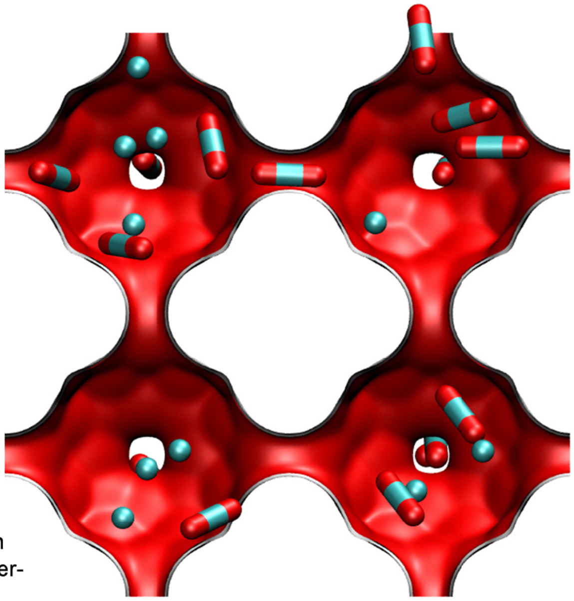

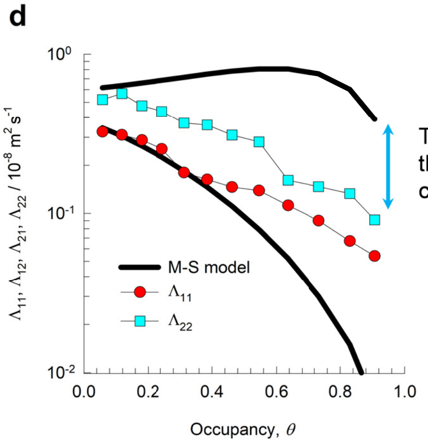

The preferential perching of CO_2 in the window regions hinders the inter-cage hopping of Ar

Figure S114. (a-d) MD simulated values of $\Lambda_{11}, \Lambda_{12}, \Lambda_{21}, \Lambda_{22}$ for equimolar (q_1=q_2) binary CO_2(1)/Ar(2) mixtures in LTA all-silica zeolite at 300 K, compared with the estimations (continuous solid lines) using the Maxwell-Stefan model, based on fitted data of unary diffusivities, $Đ_1$,$Đ_2$, and unary degrees of correlations, $Đ_1/Đ_{11}, Đ_2/Đ_{22}$.

Preferential Perching of CO2 at window regions

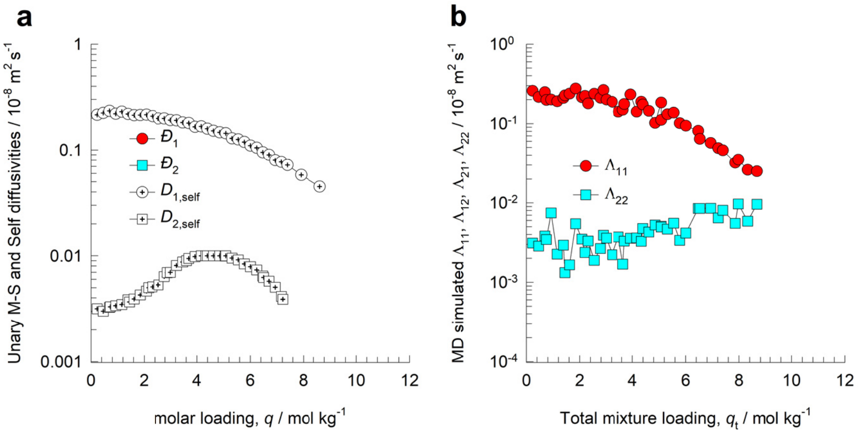

CHA all-silica, 300 K; $z = 5$

Component 1 = CO₂

$Đ_1(0) = 0.24$

$\phi_1 = \phi_{10} \exp(-a_1\theta)$

$\phi_{10} = 1.0; \quad a_1 = -0.28$

$Đ_1/Đ_{11} = b_1\theta; \quad b_1 \to 0$

Component 2 = CH₄

$Đ_2(0) = 0.003$

$\phi_2 = \phi_{20} \exp(-a_2\theta)$

$\phi_{20} = 1.3; \quad a_2 = -0.7$

$Đ_2/Đ_{22} = b_2\theta; \quad b_2 \to 0$

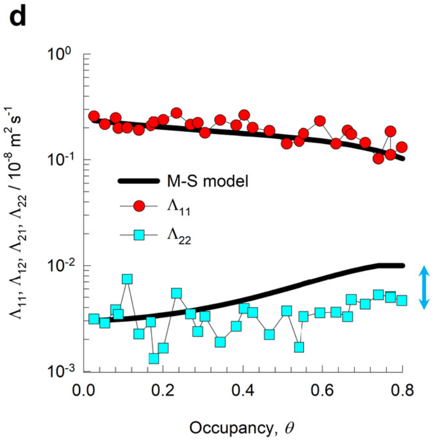

The preferential perching of CO_2 in the window regions hinders the inter-cage hopping of CH_4

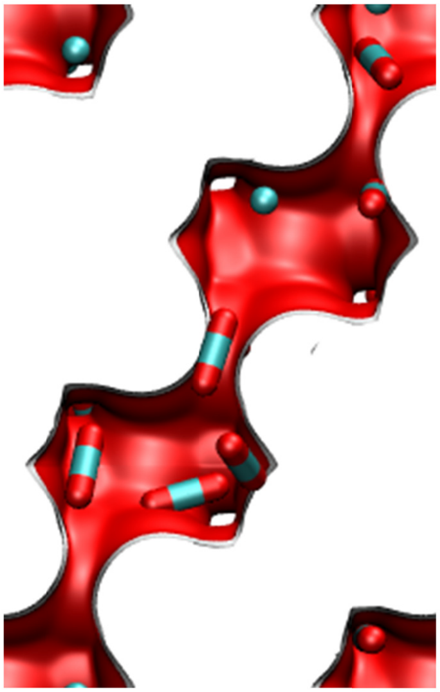

Figure S115. (a-d) MD simulated values of $\Lambda_{11}, \Lambda_{12}, \Lambda_{21}, \Lambda_{22}$ for equimolar (q_1=q_2) binary CO_2(1)/CH_4(2) mixtures in CHA all-silica zeolite at 300 K, compared with the estimations (continuous solid lines) using the Maxwell-Stefan model, based on fitted data of unary diffusivities, $Đ_1, Đ_2$, and unary degrees of correlations, $Đ_1/Đ_{11}, Đ_2/Đ_{22}$.

Preferential Perching of CO2 at window regions

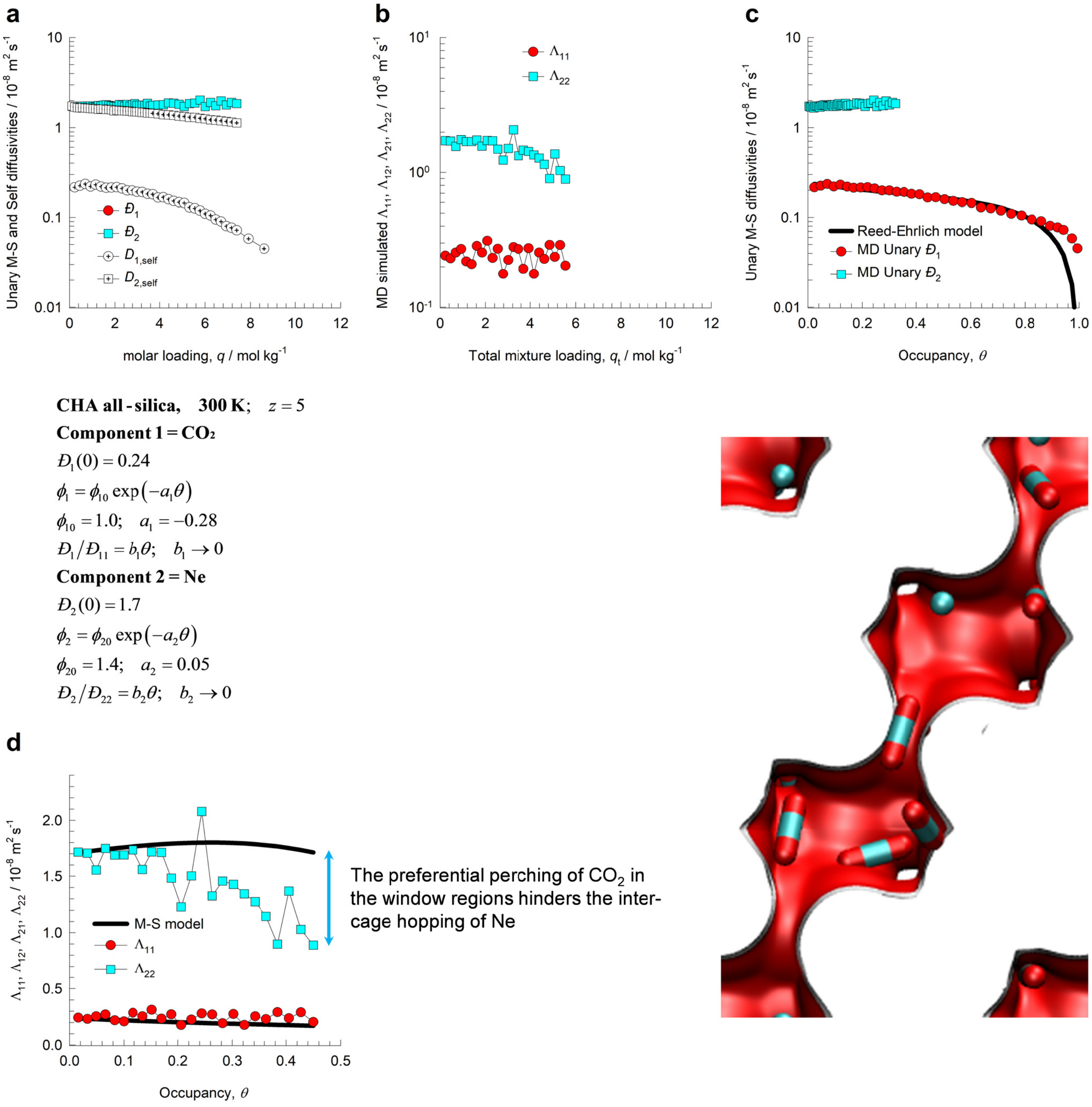

CHA all-silica, 300 K; $z = 5$

Component 1 = CO₂

$Đ_1(0) = 0.24$

$\phi_1 = \phi_{10} \exp(-a_1\theta)$

$\phi_{10} = 1.0; \quad a_1 = -0.28$

$Đ_1/Đ_{11} = b_1\theta; \quad b_1 \to 0$

Component 2 = Ne

$Đ_2(0) = 1.7$

$\phi_2 = \phi_{20} \exp(-a_2\theta)$

$\phi_{20} = 1.4; \quad a_2 = 0.05$

$Đ_2/Đ_{22} = b_2\theta; \quad b_2 \to 0$

Figure S116. (a-d) MD simulated values of $\Lambda_{11}, \Lambda_{12}, \Lambda_{21}, \Lambda_{22}$ for equimolar (q_1=q_2) binary CO$_2$(1)/Ne(2) mixtures in CHA all-silica zeolite at 300 K, compared with the estimations (continuous solid lines) using the Maxwell-Stefan model, based on fitted data of unary diffusivities, $Đ_1, Đ_2$, and unary degrees of correlations, $Đ_1/Đ_{11}, Đ_2/Đ_{22}$.

Preferential Perching of CO2 at window regions

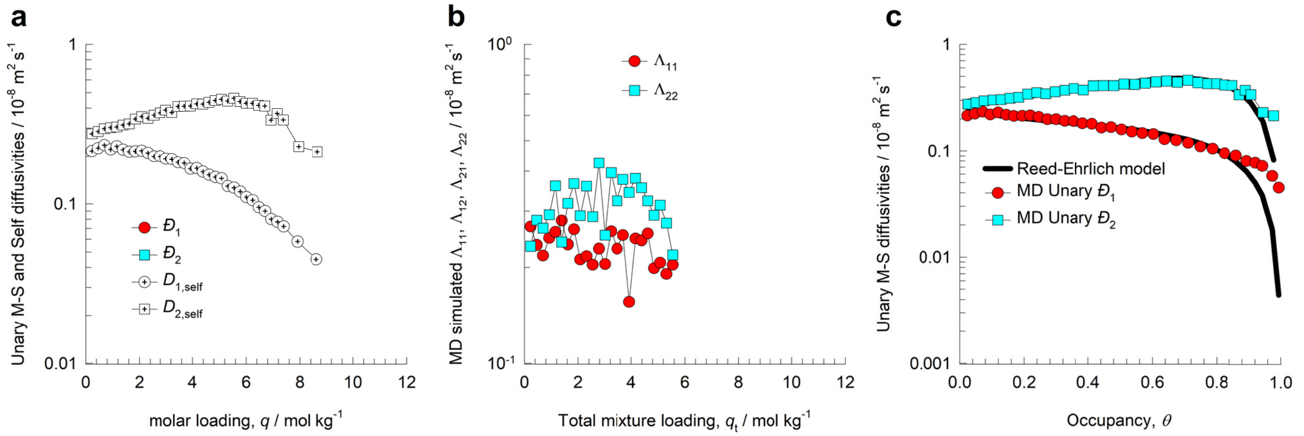

CHA all-silica, 300 K; $z = 5$

Component 1 = CO_2

$Đ_1(0) = 0.24$

$\phi_1 = \phi_{10} \exp(-a_1 \theta)$

$\phi_{10} = 1.0; \quad a_1 = -0.28$

$Đ_1 / Đ_{11} = b_1 \theta; \quad b_1 \to 0$

Component 2 = Ar

$Đ_2(0) = 0.29$

$\phi_2 = \phi_{20} \exp(-a_2 \theta)$

$\phi_{20} = 1.37; \quad a_2 = -0.34$

$Đ_2 / Đ_{22} = b_2 \theta; \quad b_2 \to 0$

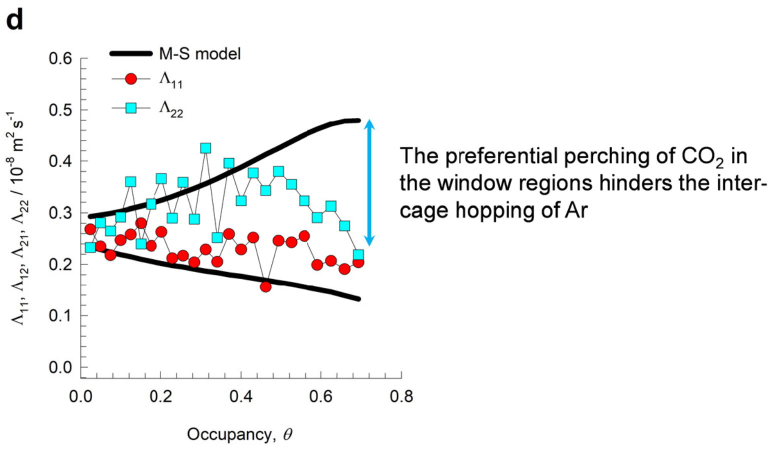

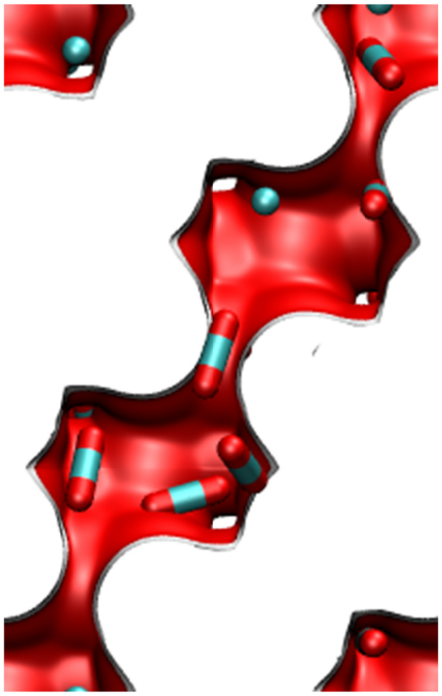

Figure S117. (a-d) MD simulated values of $\Lambda_{11}, \Lambda_{12}, \Lambda_{21}, \Lambda_{22}$ for equimolar (q_1=q_2) binary CO_2(1)/Ar(2) mixtures in CHA all-silica zeolite at 300 K, compared with the estimations (continuous solid lines) using the Maxwell-Stefan model, based on fitted data of unary diffusivities, $Đ_1, Đ_2$, and unary degrees of correlations, $Đ_1/Đ_{11}, Đ_2/Đ_{22}$.

Preferential Perching of CO2 at window regions

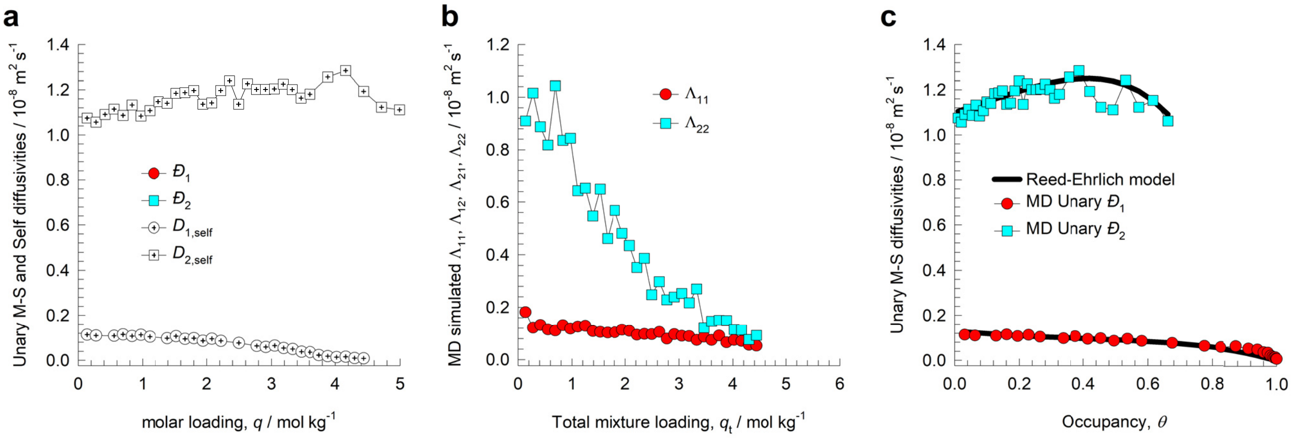

DDR all-silica, 300 K; $z = 5$

Component 1 = CO₂

$Đ_1(0) = 0.13$

$\phi_1 = \phi_{10} \exp(-a_1\theta)$

$\phi_{10} = 1.0$; $a_1 = -0.3$

$Đ_1/Đ_{11} = b_1\theta$; $b_1 = 0$

Component 2 = Ne

$Đ_2(0) = 1.1$

$\phi_2 = \phi_{20} \exp(-a_2\theta)$

$\phi_{20} = 1.4$; $a_2 = -0.05$

$Đ_2/Đ_{22} = b_2\theta$; $b_2 = 0$

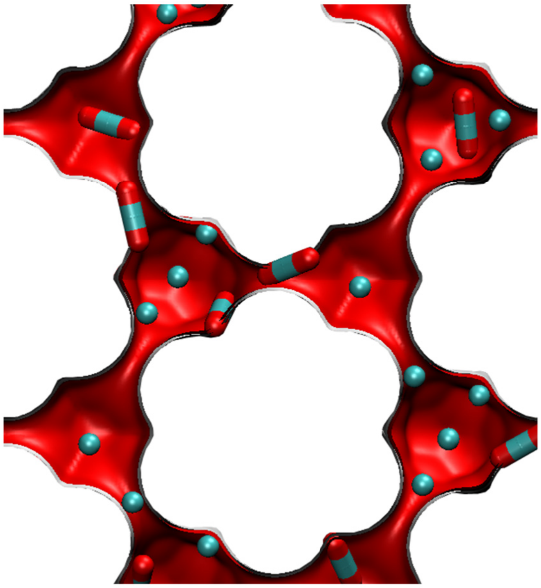

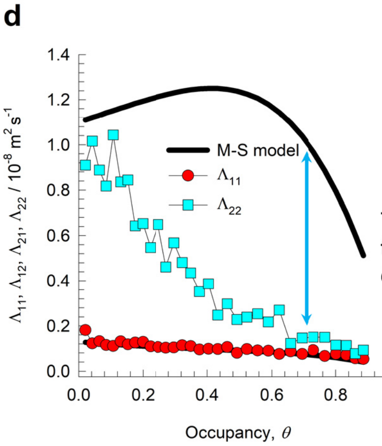

The preferential perching of CO_2 in the window regions hinders the inter-cage hopping of Ne

Figure S118. (a-d) MD simulated values of $\Lambda_{11}, \Lambda_{12}, \Lambda_{21}, \Lambda_{22}$ for equimolar (q_1=q_2) binary CO_2(1)/Ne(2) mixtures in DDR all-silica zeolite at 300 K, compared with the estimations (continuous solid lines) using the Maxwell-Stefan model, based on fitted data of unary diffusivities, $Đ_1, Đ_2$, and unary degrees of correlations, $Đ_1/Đ_{11}, Đ_2/Đ_{22}$.

11 Molecular Clustering and Hydrogen Bonding

Exceptional circumstances prevail in cases of severe molecular segregation[22, 48] or cluster formation [50-53]; in such situations, the coefficients $Đ_1$, and $Đ_2$ in the mixture are significantly different to those determined from unary experiments or simulations. For water/alcohol mixture diffusion, the diffusivity of each component is lowered due to molecular clusters being formed as a consequence of hydrogen bonding. This is illustrated in Figure S119(a,b,c) that present MD simulations of the self-diffusivities $D_{i,self}$, and M-S diffusivities $Đ_i$ for water(1)/methanol(2), water(1)/ethanol(2), and methanol(1)/ethanol(2) and mixture diffusion in FAU all-silica zeolite. The diffusivity of water is reduced with increasing proportion of alcohol. Hydrogen bonding between water and alcohol molecule pairs serves to act as a "flexible leash" linking the motion of the more mobile (water) and tardier (alcohol) species. Remarkably, the alcohol diffusivity is also reduced by increasing addition of water till a minimum value is reached at an alcohol mole fraction of about 0.5; see Figure S119(b,c). For methanol(1)/ethanol(2) mixtures, hydrogen bonding effects are significantly lower, and the diffusivities of methanol and ethanol vary with composition in the same manner as for unclustered molecules.

For MFI zeolite, the diffusivity of methanol is practically independent of composition, while that for water shows a dramatic decrease with increasing methanol concentration (cf. Figure S120(a)); this trend is the same as determined in the NMR experiments data of Caro et al.[54]

For DDR. LTA, and CHA zeolites, each of the diffusivities of water and methanol is lowered due to the presence of its partner species; see Figure S120(b,c,d). Experimental evidence of mutual-slowing down effects are available for water/alcohol permeation across CHA,[55, 56] H-SOD,[57] and DDR[53, 58] membranes. Further research is necessary to generalize the M-S formulation in a manner that explicitly allows for cluster formation, by defining a cluster to be a pseudo-species in the mixture.

11.1 List of Figures for Molecular Clustering and Hydrogen Bonding

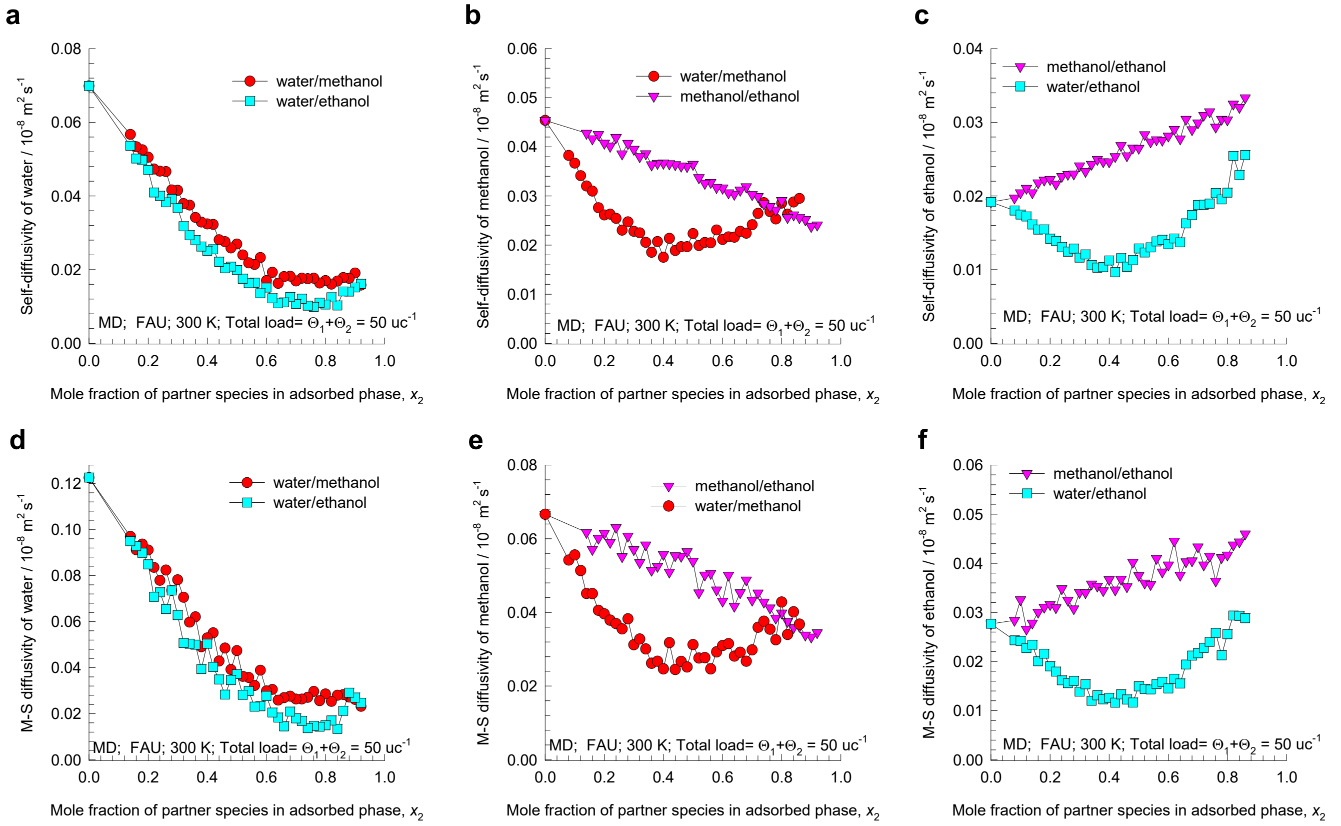

Figure S119. (a-f) MD simulations of self-diffusivities, $D_{i,self}$, and M-S diffusivities, $Đ_i$, in water(1)/methanol(2), water(1)/ethanol(2), and methanol(1)/ethanol(2) mixtures of varying composition in FAU (all-silica) zeolite at 300 K. The MD simulations were carried out under conditions in which the total loading, Θ_t, is held constant at 50 molecules uc^{-1}. The MD data are culled from our previous publications.[52, 59]

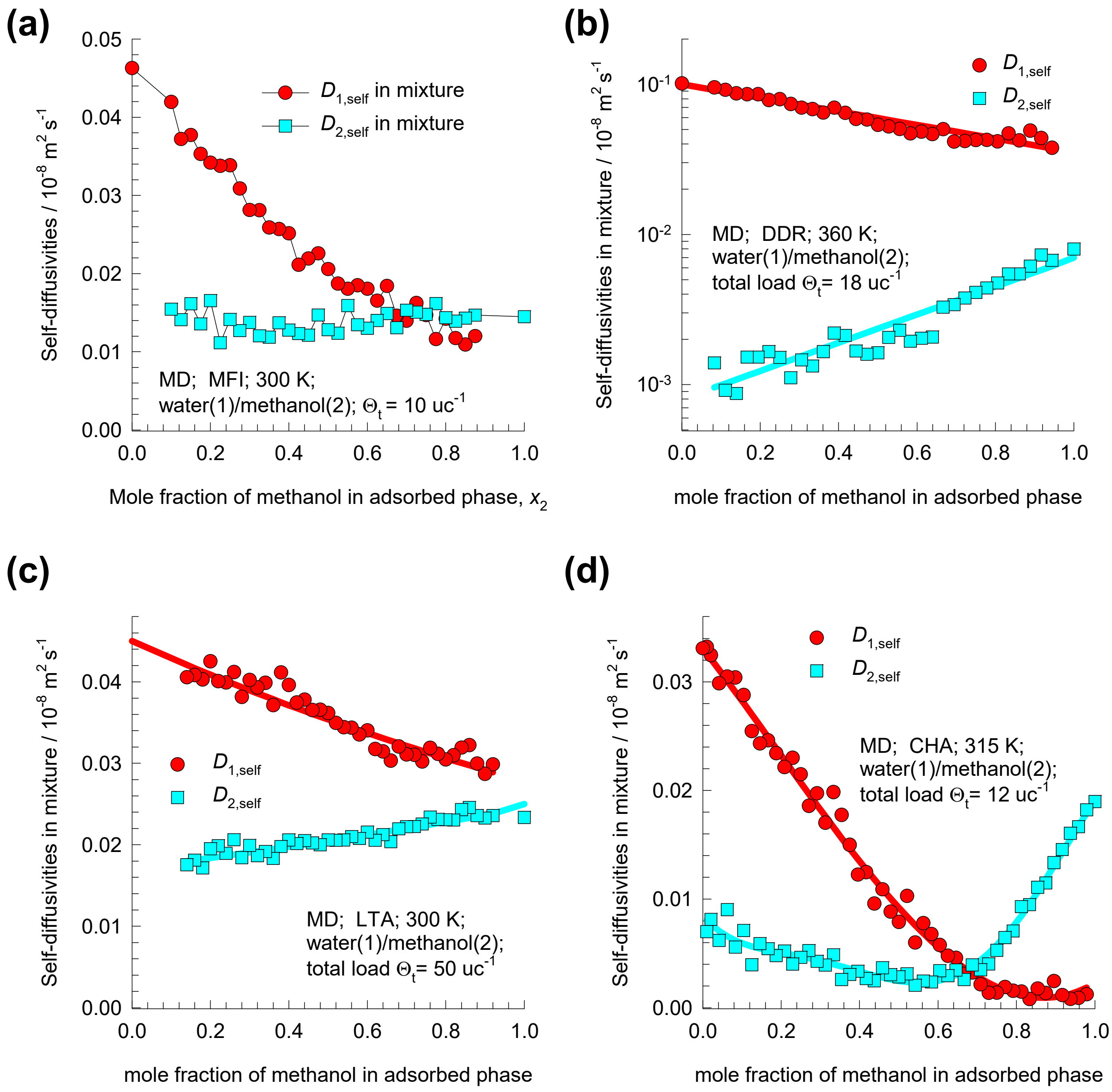

Figure S120. MD simulations of self-diffusivities, $D_{i,\mathrm{self}}$, of water(1)/methanol(2) mixtures of varying composition in (a) MFI, (b) DDR, (c) LTA, and (d) CHA zeolites. In all cases the MD simulations were carried out under conditions in which the total loading, Θ_t, expressed as molecules uc^{-1}, is held constant; the values Θ_t are specified. The MD data are culled from our previous publications.[52, 53, 59]

12 Nomenclature

Latin alphabet

A	surface area per kg of framework, m^{2} kg^{-1}
b_{A}	dual-Langmuir-Freundlich constant for species *i* at adsorption site A, $\mathrm{Pa}^{-\nu_i}$
b_{B}	dual-Langmuir-Freundlich constant for species *i* at adsorption site B, $\mathrm{Pa}^{-\nu_i}$
$[B]$	Maxwell-Stefan matrix, m^{-2} s
$Đ_{\mathrm{i}}$	Maxwell-Stefan diffusivity for molecule-wall interaction, m^{2} s^{-1}
$Đ_{i}(0)$	M-S diffusivity at zero-loading, m^{2} s^{-1}
$Đ_{\mathrm{ij}}$	M-S exchange coefficient, m^{2} s^{-1}
$Đ_{\mathrm{ii,fl}}$	self-diffusivity of species *i* in fluid phase, m^{2} s^{-1}
$Đ_{12}$	M-S exchange coefficient for binary mixture, m^{2} s^{-1}
$Đ_{12,\mathrm{fl}}$	M-S diffusivity in binary fluid mixture, m^{2} s^{-1}
$D_{\mathrm{i,self}}$	self-diffusivity of species *i*, m^{2} s^{-1}
f_{i}	partial fugacity of species *i*, Pa
n	number of species in the mixture, dimensionless
n_{i}	number of molecules of species *i* in simulation box, dimensionless
N_{i}	molar flux of species *i* with respect to framework, mol m^{-2} s^{-1}
p_{i}	partial pressure of species *i* in mixture, Pa
p_{t}	total system pressure, Pa
P_i^0	sorption pressure, Pa
q_{i}	component molar loading of species *i*, mol kg^{-1}

Nomenclature

$q_{\mathrm{i,sat}}$	molar loading of species *i* at saturation, mol kg^{-1}
q_{t}	total molar loading in mixture, mol kg^{-1}
$\mathbf{r}_{\mathrm{l,i}}(t)$	position vector for molecule *l* of species *i* at any time *t*, m
R	gas constant, 8.314 J mol^{-1} K^{-1}
T	absolute temperature, K
u_{i}	velocity of motion of adsorbate species *i* with respect to the framework material, m s^{-1}
V_{p}	accessible pore volume, m^{3} kg^{-1}
w	energy of interaction; see equation (S55), J mol^{-1}
x_{i}	mole fraction of species *i* in adsorbed phase, dimensionless
z	distance coordinate, m

Greek alphabet

β	parameter defined in equation (S55), dimensionless
Γ_{ij}	thermodynamic factors, dimensionless
$[\Gamma]$	matrix of thermodynamic factors, dimensionless
δ_{ij}	Kronecker delta, dimensionless
ε	fractional pore volume of particle, dimensionless
ζ	coordination number defined in equation (S54), dimensionless
λ	jump distance in lattice model, m
$[\Lambda]$	matrix of Maxwell-Stefan diffusivities, m^{2} s^{-1}
μ_{i}	molar chemical potential of component *i*, J mol^{-1}
π	spreading pressure, N m^{-1}
θ	fractional occupancy, dimensionless
Θ_{i}	loading of species *i*, molecules per unit cell
$\Theta_{\mathrm{i,sat}}$	saturation loading of species *i*, molecules per unit cell

Nomenclature

Θ_t	total mixture loading, molecules per unit cage, or per unit cell
ν	jump frequency, s^{-1}
ν	exponent in dual-Langmuir-Freundlich isotherm, dimensionless
ϕ	parameter defined in equation (S55), dimensionless
ρ	framework density, kg m^{-3}

Subscripts

1	referring to component 1
2	referring to component 2
i	referring to component *i*
t	referring to total mixture
sat	referring to saturation conditions
V	vacancy

13 References

(1) Krishna, R. Occupancy Dependency of Maxwell−Stefan Diffusivities in Ordered Crystalline Microporous Materials. *ACS Omega* **2018**, *3*, 15743-15753. https://doi.org/10.1021/acsomega.8b02465.

(2) Kärger, J.; Ruthven, D. M.; Theodorou, D. N. *Diffusion in Nanoporous Materials*. Wiley - VCH: Weinheim, 2012; pp

(3) Krishna, R.; van Baten, J. M. In Silico Screening of Zeolite Membranes for CO_2 Capture. *J. Membr. Sci.* **2010**, *360*, 323-333.

(4) Krishna, R.; van Baten, J. M. In silico screening of metal-organic frameworks in separation applications. *Phys. Chem. Chem. Phys.* **2011**, *13*, 10593-10616.

(5) Thomas, A. Functional Materials: From Hard to Soft Porous Frameworks. *Angew. Chem. Int. Ed.* **2010**, *49*, 8328 – 8344.

(6) Baerlocher, C.; Meier, W. M.; Olson, D. H. *Atlas of Zeolite Framework Types*. 5th Edition, Elsevier: Amsterdam, 2002; pp

(7) Baerlocher, C.; McCusker, L. B. Database of Zeolite Structures. http://www.iza-structure.org/databases/, International Zeolite Association, 10 January 2002.

(8) Krishna, R. Diffusion in Porous Crystalline Materials. *Chem. Soc. Rev.* **2012**, *41*, 3099-3118.

(9) Krishna, R. The Maxwell-Stefan Description of Mixture Diffusion in Nanoporous Crystalline Materials. *Microporous Mesoporous Mater.* **2014**, *185*, 30-50.

(10) Krishna, R. Describing the Diffusion of Guest Molecules inside Porous Structures. *J. Phys. Chem. C* **2009**, *113*, 19756-19781.

(11) Krishna, R.; van Baten, J. M. Investigating the Relative Influences of Molecular Dimensions and Binding Energies on Diffusivities of Guest Species Inside Nanoporous Crystalline Materials *J. Phys. Chem. C* **2012**, *116*, 23556-23568.

(12) Krishna, R.; van Baten, J. M. Investigating the Influence of Diffusional Coupling on Mixture Permeation across Porous Membranes *J. Membr. Sci.* **2013**, *430*, 113-128.

(13) Krishna, R.; van Baten, J. M. Influence of Adsorption Thermodynamics on Guest Diffusivities in Nanoporous Crystalline Materials. *Phys. Chem. Chem. Phys.* **2013**, *15*, 7994-8016.

(14) Krishna, R.; van Baten, J. M. Insights into diffusion of gases in zeolites gained from molecular dynamics simulations. *Microporous Mesoporous Mater.* **2008**, *109*, 91-108.

(15) Krishna, R.; van Baten, J. M. Diffusion of alkane mixtures in MFI zeolite. *Microporous Mesoporous Mater.* **2008**, *107*, 296-298.

(16) Myers, A. L.; Prausnitz, J. M. Thermodynamics of Mixed Gas Adsorption. *A.I.Ch.E.J.* **1965**, *11*, 121-130.

(17) Ruthven, D. M. *Principles of Adsorption and Adsorption Processes*. John Wiley: New York, 1984; pp 1-433.

(18) Siperstein, F. R.; Myers, A. L. Mixed-Gas Adsorption. *A.I.Ch.E.J.* **2001**, *47*, 1141-1159.

(19) PTC MathCad 15.0. http://www.ptc.com/, PTC Corporate Headquarters, Needham, 3 November 2015.

(20) Skoulidas, A. I.; Sholl, D. S.; Krishna, R. Correlation effects in diffusion of CH_4/CF_4 mixtures in MFI zeolite. A study linking MD simulations with the Maxwell-Stefan formulation. *Langmuir* **2003**, *19*, 7977-7988.

(21) Chempath, S.; Krishna, R.; Snurr, R. Q. Nonequilibrium MD simulations of difusion of binary mixtures containing short n-alkanes in faujasite. *J. Phys. Chem. B* **2004**, *108*, 13481-13491.

(22) Krishna, R.; van Baten, J. M. Onsager coefficients for binary mixture diffusion in nanopores. *Chem. Eng. Sci.* **2008**, *63*, 3120-3140.

(23) Hansen, N.; Keil, F. J. Multiscale modeling of reaction and diffusion in zeolites: from the molecular level to the reactor. *Soft Mater.* **2012**, *10*, 179-201.

(24) Krishna, R.; van Baten, J. M. An Investigation of the Characteristics of Maxwell-Stefan Diffusivities of Binary Mixtures in Silica Nanopores. *Chem. Eng. Sci.* **2009**, *64*, 870-882.

(25) Krishna, R.; van Baten, J. M. Unified Maxwell-Stefan Description of Binary Mixture Diffusion in Micro- and Meso- Porous Materials. *Chem. Eng. Sci.* **2009**, *64*, 3159-3178.

(26) Krishna, R.; van Baten, J. M. Describing Mixture Diffusion in Microporous Materials under Conditions of Pore Saturation. *J. Phys. Chem. C* **2010**, *114*, 11557-11563.

(27) Krishna, R.; van Baten, J. M. Diffusion of alkane mixtures in zeolites. Validating the Maxwell-Stefan formulation using MD simulations. *J. Phys. Chem. B* **2005**, *109*, 6386-6396.

(28) van Baten, J. M.; Krishna, R. Entropy effects in adsorption and diffusion of alkane isomers in mordenite: An investigation using CBMC and MD simulations. *Microporous Mesoporous Mater.* **2005**, *84*, 179-191.

(29) Krishna, R.; van Baten, J. M. Describing binary mixture diffusion in carbon nanotubes with the Maxwell-Stefan equations. An investigation using molecular dynamics simulations. *Ind. Eng. Chem. Res.* **2006**, *45*, 2084-2093.

(30) Krishna, R. Adsorptive separation of CO_2/CH_4/CO gas mixtures at high pressures. *Microporous Mesoporous Mater.* **2012**, *156*, 217-223.

(31) Krishna, R.; van Baten, J. M. Investigating the potential of MgMOF-74 membranes for CO_2 capture. *J. Membr. Sci.* **2011**, *377*, 249-260.

(32) Krishna, R.; van Baten, J. M. Maxwell-Stefan modeling of slowing-down effects in mixed gas permeation across porous membranes. *J. Membr. Sci.* **2011**, *383*, 289-300.

(33) Krishna, R.; van Baten, J. M. Investigating the Validity of the Knudsen Prescription for Diffusivities in a Mesoporous Covalent Organic Framework. *Ind. Eng. Chem. Res.* **2011**, *50*, 7083-7087.

(34) Krishna, R.; van Baten, J. M. Investigating the Validity of the Bosanquet Formula for Estimation of Diffusivities in Mesopores. *Chem. Eng. Sci.* **2012**, *69*, 684-688.

(35) Vlugt, T. J. H.; Krishna, R.; Smit, B. Molecular Simulations of Adsorption Isotherms for Linear and Branched Alkanes and Their Mixtures in Silicalite. *J. Phys. Chem. B* **1999**, *103*, 1102-1118.

(36) Chmelik, C.; Heinke, L.; Kärger, J.; Shah, D. B.; Schmidt, W.; van Baten, J. M.; Krishna, R. Inflection in the Loading Dependence of the Maxwell-Stefan Diffusivity of Iso-butane in MFI Zeolite. *Chem. Phys. Lett.* **2008**, *459*, 141-145.

(37) Jobic, H.; Laloué, C.; Laroche, C.; van Baten, J. M.; Krishna, R. Influence of isotherm inflection on the loading dependence of the diffusivities of n-hexane and n-heptane in MFI zeolite. Quasi-Elastic Neutron Scattering experiments supplemented by molecular simulations. *J. Phys. Chem. B* **2006**, *110*, 2195-2201.

(38) Krishna, R.; Baur, R. Modelling Issues in Zeolite Based Separation Processes. *Sep. Purif. Technol.* **2003**, *33*, 213-254.

(39) Krishna, R. The Maxwell-Stefan Description of Mixture Permeation across Nanoporous Graphene Membranes. *Chem. Eng. Res. Des.* **2018**, *133*, 316-325. https://doi.org/10.1016/j.cherd.2018.03.033.

(40) Reed, D. A.; Ehrlich, G. Surface diffusion, atomic jump rates and thermodynamics. *Surf. Sci.* **1981**, *102*, 588-609.

(41) Krishna, R.; Paschek, D.; Baur, R. Modelling the occupancy dependence of diffusivities in zeolites. *Microporous Mesoporous Mater.* **2004**, *76*, 233-246.

(42) Krishna, R.; van Baten, J. M. A molecular dynamics investigation of a variety of influences of temperature on diffusion in zeolites. *Microporous Mesoporous Mater.* **2009**, *125*, 126-134.

(43) Krishna, R.; Wesselingh, J. A. The Maxwell-Stefan Approach to Mass Transfer. *Chem. Eng. Sci.* **1997**, *52*, 861-911.

(44) Vignes, A. Diffusion in binary solutions. *Ind. Eng. Chem. Fundamentals* **1966**, *5*, 189-199.

(45) Krishna, R.; van Baten, J. M. The Darken relation for multicomponent diffusion in liquid mixtures of linear alkanes. An investigation using Molecular Dynamics (MD) simulations. *Ind. Eng. Chem. Res.* **2005**, *44*, 6939-6947.

(46) Krishna, R.; van Baten, J. M. Diffusion of Hydrocarbon Mixtures in MFI Zeolite: Influence of Intersection Blocking. *Chem. Eng. J.* **2008**, *140*, 614-620.

(47) Fernandez, M.; Kärger, J.; Freude, D.; Pampel, A.; van Baten, J. M.; Krishna, R. Mixture Diffusion in Zeolites Studied by MAS PFG NMR and Molecular Simulation. *Microporous Mesoporous Mater.* **2007**, *105*, 124-131.

(48) Krishna, R.; van Baten, J. M. Segregation effects in adsorption of CO_2 containing mixtures and their consequences for separation selectivities in cage-type zeolites. *Sep. Purif. Technol.* **2008**, *61*, 414-423.

(49) Krishna, R.; van Baten, J. M. Influence of segregated adsorption on mixture diffusion in DDR zeolite. *Chem. Phys. Lett.* **2007**, *446*, 344-349.

(50) Krishna, R.; van Baten, J. M. Investigating cluster formation in adsorption of CO_2, CH_4, and Ar in zeolites and metal organic frameworks at sub-critical temperatures. *Langmuir* **2010**, *26*, 3981-3992.

(51) Krishna, R.; van Baten, J. M. Highlighting a variety of unusual characteristics of adsorption and diffusion in microporous materials induced by clustering of guest molecules. *Langmuir* **2010**, *26*, 8450-8463.

(52) Krishna, R.; van Baten, J. M. Hydrogen Bonding Effects in Adsorption of Water-alcohol Mixtures in Zeolites and the Consequences for the Characteristics of the Maxwell-Stefan Diffusivities. *Langmuir* **2010**, *26*, 10854-10867.

(53) Krishna, R.; van Baten, J. M. Mutual slowing-down effects in mixture diffusion in zeolites. *J. Phys. Chem. C* **2010**, *114*, 13154-13156.

(54) Caro, J.; Bülow, M.; Richter-Mendau, J.; Kärger, J.; Hunger, M.; Freude, D. Nuclear Magnetic Resonance Self-diffusion Studies of Methanol-Water Mixtures in Pentasil-type Zeolites. *J. Chem. Soc., Faraday Trans.* **1987**, *83*, 1843-1849.

(55) Hasegawa, Y.; Abe, C.; Nishioka, M.; Sato, K.; Nagase, T.; Hanaoka, T. Formation of high flux CHA-type zeolite membranes and their application to the dehydration of alcohol solutions. *J. Membr. Sci.* **2010**, *364*, 318-324.

(56) Sato, K.; Sugimoto, K.; Shimosuma, N.; Kikuchi, T.; Kyotani, T.; Kurata, T. Development of practically available up-scaled high-silica CHA-type zeolite membranes for industrial purpose in dehydration of N-methyl pyrrolidone solution. *J. Membr. Sci.* **2012**, *409-410*, 82-95.

(57) Khajavi, S.; Jansen, J. C.; Kapteijn, F. Application of hydroxy sodalite films as novel water selective membranes. *J. Membr. Sci.* **2009**, *326*, 153-160.

(58) Kuhn, J.; Castillo-Sanchez, J. M.; Gascon, J.; Calero, S.; Dubbeldam, D.; Vlugt, T. J. H.; Kapteijn, F.; Gross, J. Adsorption and Diffusion of Water, Methanol, and Ethanol in All-Silica DD3R: Experiments and Simulation. *J. Phys. Chem. C* **2009**, *113*, 14290-14301.

(59) Krishna, R.; van Baten, J. M. Highlighting Pitfalls in the Maxwell-Stefan Modeling of Water-Alcohol Mixture Permeation across Pervaporation Membranes. *J. Membr. Sci.* **2010**, *360*, 476-482.